# Agent-based modeling of growing cell populations and the regenerating liver based on image processing

Von der Fakultät für Mathematik und Informatik

der Universität Leipzig

angenommene

## D I S S E R T A T I O N

zur Erlangung des akademischen Grades

DOCTOR RERUM NATURALIUM

(Dr. rer. nat.)

im Fachgebiet

Informatik

vorgelegt

von Dipl. Inf. Stefan Höhme

geboren am 7.10.1978 in Leisnig

Die Annahme der Dissertation wurde empfohlen von:

1. Prof. Dr. Gerik Scheuermann (Universität Leipzig)
2. Privatdozent Dr. Dirk Drasdo (INRIA Paris)

Die Verleihung des akademischen Grades erfolgt mit Bestehen der Verteidigung am 3.3.2010 mit dem Gesamtprädikat magna cum laude.

# Acknowledgement

First and foremost, I would like to thank my advisor Dr. Dirk Drasdo for his advice, his persistent and generous support, and inspiring and enlightening discussions. It was always a pleasure to work with him and I deeply appreciated his helpful suggestions.
I also would like to express my gratitude to Professor Jan G. Hengstler from the Leibnitz Research Centre (IfADo) in Dortmund. Without him and his co-workers, the exiting research on liver regeneration in this work would not have been possible. I always enjoyed working with him and I am sure that there will be many fascinating projects ahead. Furthermore, I very much thank Professor Stadler, head of the Bioinformatics Group at the University of Leipzig, for his straightforward support which I truly appreciated.

I also thank my colleagues from the Research Group Multicellular Systems at the Interdisciplinary Centre for Bioinformatics (IZBI) in Leipzig and at the Institut National De Recherché En Informatique Et En Automatique (INRIA) in Paris. I appreciated the discussions and work with Axel Krinner, Nick Jagiella and William Weens. Furthermore, I would like to thank Dr. Jörg Galle (IZBI), Dr. Hans Binder (IZBI), Petra Pregel (IZBI) and Professor Löffler (IMISE) from the University of Leipzig for their support.
For motivating collaborations and helpful discussions I would like to acknowledge Dr. Marc Brulport, Alexander Bauer, Dr. Iris von Recklinghausen, Dr. Essam Bedawy, Wiebke Schormann, Dr. Matthias Hermes, Marc Schäfer (IfADo), Markus Rohrschneider (IfI) and Anne-Céline Boulanger. Especially, I would like to thank Professor Rolf Gebhardt and Dr. Sebastian Zellmer from the Institute of Biochemistry and Professor Gerik Scheuermann, head of the Image and Signal Processing Group at the University of Leipzig, for making fruitful collaborations possible.
Especially, I would very much like to express my gratitude to Dr. Irène E. Vignon from INRIA Paris for her inspiring and friendly support.

I acknowledge the financial support from the German Federal Ministry of Education and Research (HepatoSys) and the European Commission (PASSPORT).

Furthermore, I would like to thank all those people that helped to successfully complete this thesis but whom I forgot to mention.

Finally, I would like to especially thank my family, especially my parents Marlies and Volker Höhme and my grandparents Liselotte and Alfred Hebenstreit, for their continuous support throughout this thesis and last but not least, I would like to express my gratitude and affection to Franziska Bach. I truly appreciated her support and patience, and on many occasions she shed light on the mysteries of mathematics.

# Table of Contents

# 1. Introduction

## 1.1. Motivation

In the last decades research in the life sciences had to face a rapidly increasing amount of data resulting from improved experimental methods. An example is the large amount of data from the high-throughput methods in molecular biology. However, these data were found to be not sufficient to fully understand the complicated behavior of biological systems. In a recent and much-noticed paper Hiroaki Kitano trenchantly summarized the problem by noting that "identifying all the genes and proteins in an organism is like listing all the parts of an airplane" [Kitano, 2002a] which - metaphorically speaking - certainly is a precondition but not sufficient to fly. It became more and more clear that biological systems are composed of "a large number of functionally diverse, and frequently multifunctional, sets of elements that interact selectively and nonlinearly to produce coherent rather than complex behaviors" [Kitano, 2002a]. A system level understanding therefore requires insights in four major aspects:

(1) The structure of a system which includes the physical properties of its intracellular and multicellular components.
(2) The system dynamics which summarizes the behavior of the system over time and under particular conditions.
(3) The mechanisms that passively control or actively regulate the state of the system and thereby help to identify potential targets for therapeutic treatments of diseases.
(4) Strategies to modify and construct biological systems guided by predictive tools such as computer simulation models.

Essentially, a system level understanding of biological entities in physiological and especially pathological states is required in order to deploy the full potential of modern life sciences.
The scientific discussion of a holistic understanding of biological systems had been a recurrent subject since over half a century [Wiener, 1948]. However for a long time, due to the inherent complexity of such systems it seemed impossible to be realized. The extraordinary advances of computer science in the last two decades in combination with the steadily expanding abilities to measure biological systems parameters on all spatial and temporal scales are expected to help mastering this complexity. One of the most important contributions of contemporary computer science are computational models that allow to test novel hypotheses by *in silico* simulations whose predictions can be validated by experiments *in vitro* and *in vivo* [Kitano, 2002b]. The pluralism of causes in biological systems requires simultaneous measurements of system parameters across various scales. Computational models permit to stepwise integrate the different components on different scales and thereby

gradually understand their role in the context of all other components [Sauer et al., 2007].

The challenge to construct realistic computational models of biological systems typically requires an interdisciplinary effort integrating contributions from many different disciplines including biology, chemistry, physics, mathematics, engineering, and computer science. For example, mathematics typically serves as a unifying theoretical framework to construct biophysical and biochemical models whereby computer science lays the technological foundation [Maler, 2008]. In the last decade, this interdisciplinary approach increasingly facilitated a new holistic perspective onto biological entities and their interactions. This new perspective has been termed “systems biology” [Snoep & Westerhoff, 2005].

Until today systems biology already has made important contributions to many fields of science and has proven to be especially useful in cancer research [Manoussaki, 2006] [Marcus, 2008]. Nevertheless, cancer is still one of the most frequent causes of death in modern societies. Recent studies of the American Cancer Association estimate the probability of developing invasive cancer at least once to be over 43% for males and over 37% for females [www, 18]. Therefore, the search for effective therapies is one of the major challenges for science today. Computational models contribute to the understanding of the underlying principles and mechanisms of this complicated multi-scale disease [Drasdo et al., 1995] [Chaplain, 1996] [Byrne et al., 2001] [Anderson, 2005] [Jiang et al., 2005] [Block et al., 2007] [Aebersold et al., 2009].

Nevertheless, despite extensive studies it is still not fully understood which factors determine the growth kinetics and spatial structure of tumors in different growth stages and in different environments, both *in vitro* and *in vivo*. In the first part of this thesis we establish a three-dimensional computational model for multicellular growth in order to elucidate the mechanisms that determine avascular tumor growth. For example, we study how far tumor growth is controlled by biomechanics or active regulatory processes by modeling monolayers and multicellular tumor spheroids embedded in liquid suspension, granular medium or host tissue. We shed light on universal biomechanical mechanisms that, as we show by comparison of computer simulations with published experimental data, largely determine the morphologies and growth dynamics of tumors.

Moreover, computational models not only facilitate the investigation of pathological processes but also allow us to study mechanisms that determine biological systems under physiological conditions. Accordingly, in this thesis we also present an interdisciplinary approach to combine microscopic imaging, image processing and analysis and computational modeling - all in three dimensions. The integration of results from different scientific fields like in this case cell biology, physics and computer science enables us to meticulously study the fascinating process of liver regeneration. On the basis of the model for tumor growth developed in the first part of this thesis, we construct the first quantitative three-dimensional model of liver regeneration and use it to elucidate a yet unknown key mechanism of liver

regeneration. Moreover, we consider the presented interdisciplinary approach and the corresponding process chain exemplary for the study of tissues in general and especially in cancer research.

## 1.2. Structure of the thesis

The presented thesis is subdivided in six chapters. After this introduction, the second chapter focuses on the software that was developed as a part of this work. We discuss the cornerstones of its design and implementation, and summarize its features. The software implements the computational models for multicellular growth and liver regeneration developed later in this work together with elaborated visualization, image processing and image analysis techniques. Thereby it lays the foundation for the results presented in the subsequent chapters.

In chapter three we construct an agent-based model for the growth of multicellular populations and use it to elucidate the biomechanical mechanisms that determine their morphologies and growth kinetics. We model different biological settings from two-dimensional monolayers to three-dimensional tumor spheroids realistically embedded in granular medium and host tissue. Thereby, we continuously increase the complexity of the described biological systems. We establish concrete predictions that allow for the validation of our model.

In the fourth chapter, we develop an extended version of this model to study the complex processes during liver regeneration. We elaborate how the liver model was parameterized in close collaboration with experimentalists using images obtained by bright field microscopy and high resolution volume data generated by confocal laser scanning microscopy. We discuss in detail the image processing and analysis techniques that were used to obtain a statistically representative liver lobule as an initial state for our model simulations. We describe how in an iterative and interdisciplinary process the predictions of our model simulations stimulated new experiments whose results are used to further refine the model. Finally, we elaborate how this approach led to the elucidation of a novel cellular mechanism that we found to be crucial for successful liver regeneration and that may also play a role in the development of hepatocellular carcinoma.

The fifth chapter comprehensively summarizes the results presented in this thesis and leads over to chapter six, where we conclude with a brief outlook to future work.

# 2. Cellsys software

## 2.1. Introduction

In the last decades, computer science has played an increasingly important role for the advancement of the life sciences. In medical and biological research the amount of data that is obtained by large-scale technologies for example DNA microarrays or genome sequencers has by far exceeded the human capacity to analyze it [Fisher & Henzinger, 2007]. Computational methods are required to create a coherent picture based on this data. However, in addition to pure data mining and analysis, the construction of models for biological entities on all length scales – from single molecules to whole organs - has become more and more important to better understand the complex behavior of biological systems. As elaborated in section 1.1, mathematics and computer science serve as unifying framework and lay the technological foundation for such models [Maler, 2008].

In general, there are two basic modeling approaches: (1) mathematical models and (2) computational models [Fisher & Henzinger, 2007]. Mathematical models that are sometimes also called continuum-based models use a collection of transfer functions for example a system of differential equations to relate different numerical quantities to each other. Mathematical models can sometimes be solved analytically. In more complicated situations for example if the differential equations are non-linear or stochastic they can only be numerically approximated.

In contrast, computational models are constructed as a composition of state machines which often directly represent biological entities such as cells. State machines react on events by state transformations. Events are often triggered locally by neighboring state machines. Except for very simple cases, computational models generally are highly non-linear and non-deterministic and thus are not amenable for analytical solution. In order to gain insight into the behavior of the modeled biological system, computational models are executed or in other words - simulated.

Essentially, modern computers are very complex state machines and therefore are ideally suited for the simulation of computational models.

In this thesis we developed a special kind of computational model termed “agent-based model” (ABM). A widely-used acronym for ABM is “individual-based model”. In ABMs the complex behavior of a system arises from actions and interactions of autonomous elements called “agents” [Axelrod, 1997]. An agent is a discrete entity with its own behavior and the capability to modify this behavior based on local information. Typically, in ABMs no central authority controlling the agents exists. In general, agents interact with each other based on a spatial topology. In this work we use free, continuous Euclidean space in two or three dimensions. However, other spatial topologies for example regular grids or complex networks are also widely used in ABMs.

The history of ABMs origins in the Von Neumann machine (also called Universal Assembler), a theoretical, self replicating machine. Inspired by Stanislaw Ulam, who

was von Neumann's colleague at the Los Alamos National Laboratory in the 1940s, von Neumann abstracted his approach using a mathematical framework that later was termed "cellular automata" (see section 3.1.2).
Today, agent-based modeling integrates ideas from several fields of computer science for example artificial intelligence, complex systems, game theory and computational sociology [Emonet et al., 2005]. ABMs have been used in an extraordinarily broad range of applications for example to model the stock market [Arthur et al., 1997], to evaluate human behavior in complex societies [Epstein & Axtell, 1996], to predict the spread epidemics [Bagni et al., 2002] or civil violence [Epstein, 2002], or potential terrorist activity [Krause, 2003]. A comprehensive and detailed introduction to ABMs can be found in [Axelrod, 1997].
The modular structure of agent-based models makes them very suited to study biological systems [Hartwell et al., 1999] [Emonet et al., 2005] [Griffin, 2006] [Thorne et al., 2007] and additionally simplifies their implementation. For example, [Jennings, 2000] noted the similarities of agent-based modeling and the object oriented paradigm in software engineering that we utilized for the implementation of software in this work (section 2.3).
In order to fully exploit the rapidly increasing capabilities of recent computer hardware, specialized software is required that on the one hand implements the agent-based model and on the other hand is able to simulate, analyze and visualize it. In this chapter we illustrate the process of design and implementation of such software that we later use to study the systems biology of growing cell populations (chapter 3) and the regenerating liver (chapter 4).

## 2.2. Software design

Software design is an integral part of software engineering that encompasses the process of problem specification and the strategical planning of a corresponding software solution [Wiegers, 2003]. This includes an architectural view that structures the organization of software into units and describes their behavior and interactions. A key component of software design is a requirements analysis which approaches user-, functional- and performance requirements that depend on the specific field of application [Abran et al., 2004]. In the following, we elaborate the requirements for the software developed in this work.

### 2.2.1. Requirements analysis

In this thesis we study active and passive processes on molecular and cellular length scales that lead to the formation of complex multicellular structures on tissue level in two or three dimensions. We encounter situations that involve many interdependent and interacting objects (for example cells) with specific properties and behavior.
For example in section 3.6 we simulate three-dimensional tumor spheroids embedded in tissue, a situation that involves more than a million individual cells with

potentially very different intracellular and biophysical properties. Biomechanical interactions among these model cells are implemented in lattice-free three-dimensional Euklidean space utilizing complex models of elastic body interaction (refer to section 3.2 for details). Thereby, the model depends on a large system of equations whose solution is computationally intense and requires significant amounts of memory.
In section 4.3 we further increase this complexity by modeling liver cells (hepatocytes) that are additionally organized in a specific spatial architecture. Furthermore, these hepatocytes interact with a dense blood vessel network comprised of lobule veins and sinusoids and respond to various extracellular signals and chemicals. Diffusion and consumption of these chemicals are implemented by complex reaction-diffusion equations on three-dimensional lattices of fine granularity (see section 3.5).
The software developed in this work has a number of purposes including the implementation of all model elements in the outlined complexity. Furthermore, the software is used to visualize and analyze the simulated multicellular systems that are a result of the model simulations. Additionally, the software implements certain problem-specific image processing and analysis techniques to integrate experimental data and modeling as elaborated in chapter 4.
Accordingly, this leads to specific requirements in software design that involve considerations for example on the general architecture of the implementation (section 2.2.2), efficient ways to manage software workflows (section 2.2.3) and specific technical considerations to optimize computation performance, portability and scalability (section 2.3). Additionally, an ergonomic user interface is required to provide access to the wide variety of functionality of the software (chapter 2.4) including its visualization features (chapter 2.5).
Therefore, we specify the following cornerstones of software design to meet the described requirements. These cornerstones will guide all major technological choices during the implementation of software in this work.

(1) **Structure and modularity**
During its development we expect our software to reach a size and complexity where the addition of new or the modification of existing functional components becomes increasingly complicated due to potential interdependencies with existing components. In order to minimize this effect, we implement our software as a composition of encapsulated modules that have only limited and strictly defined dependencies on each other. Furthermore, we impose a strict semantic hierarchy on this composition of software components to facilitate a perspicuous structure that also improves efficient development and maintenance.

(2) **Efficiency and parallelism**
We anticipate the performance of our computer simulations to be a major limiting factor for the maximal granularity of our model. Therefore all parts of the software that are critical to the overall performance are subject to intense optimization. This includes the implementation of parallel algorithms that are required to take advantage of modern multiprocessing systems.

(3) **Portability**
The possibility to use our software on different platforms and operating systems is essential for its flexible use. For example portability is an important precondition for the efficient utilization of parallel computing as in a typical academic environment highly parallel workstations and dedicated compute clusters often involve heterogeneous host platforms.

(4) **Usability**
We anticipate our model for complex biological systems to include a large number of parameters and associated settings regarding simulation, analysis and visualization. Therefore we integrate a flexible, ergonomic and graphical user interface in order to manage access to all relevant features of the software.

(5) **Integration of experimental data**
Images obtained by bright field microscopy (in 2D) and volumetric data sets obtained by confocal laser scanning microscopy (in 3D) lay the foundation for our model of the regenerating liver lobule (see chapter 4). The direct integration of methods to process and analyze such experimental data into our software enables us to merge information from experiment and model in a very effective way. Thereby we are able to directly use experimental data to set up model structures for example to parameterize patient-specific models.

(6) **Code reuse**
The reuse of source code is a common technique in software engineering that attempts to save time and work by reducing redundant implementations. We impose a strict module hierarchy on our implementation (see cornerstone 1) which in general facilitates code reuse for example by class inheritance. Furthermore, we implement abstract server modules for general purposes that are used by many other client modules. As a general principle, whenever an efficient solution for an encountered problem already has been implemented and is accessible we attempt to reuse this solution for example by utilizing libraries or implementing interfaces to external software.

These cornerstones of software design guide the entire process of implementation throughout this thesis and result in a flexible and efficient software tool that we named Cellsys. We use Cellsys for all model simulations and analysis in this work.

### 2.2.2. Software architecture

In general, the term "software architecture" designates the specific structure of a software system, which comprises its components, the externally visible properties of these components, and the relationships among them [Brown & Mcdermid, 2007]. The strategical planning of the architecture of software simplifies its stringent organization on a high level of abstraction which is an important precondition to manage complex software (refer to section 2.2.1 cornerstone 1) [Posch et al., 2007].
The architectural foundation of Cellsys is a strict functional partitioning. Thereby the functionality of Cellsys is subdivided (partitioned) into subsets according to a contentual grouping. For example all software components that implement functionality related to the simulation of our model, like the components that solve equations of motion, are associated to the functional partition "model simulation", whereas all software components that implement image processing algorithms, for example the component that implements median filtering, are associated to the functional partition "image/volume processing". Thereby software components within each partition realize a content-wise similar functionality and thus are associated to the same data structures (Table 1).
Cellsys consists of 8 major functional partitions whereby one half concerns modeling and the other half concerns images and volumetric data. In general, functional partitions on modeling refer to the data structure "Model state" while functional partitions on images or volumetric data process specific data structures for images and volumetric data sets (Table 1). The relationships between the functional partitions and their associated data structures are illustrated in Fig.1.

**Table 1: Cellsys software functional partitioning**

| | **Modeling** | **Images/volumes** |
|---|---|---|
| **Functional partitions** | ▪ Model parameterization<br>▪ Model simulation<br>▪ Model analysis (observation)<br>▪ Model visualization | ▪ Image/volume parameterization<br>▪ Image/volume processing<br>▪ Image/volume analysis<br>▪ Image/volume visualization |
| **Associated data** | ▪ Model state | ▪ Images (2D)<br>▪ Volumes (3D) |

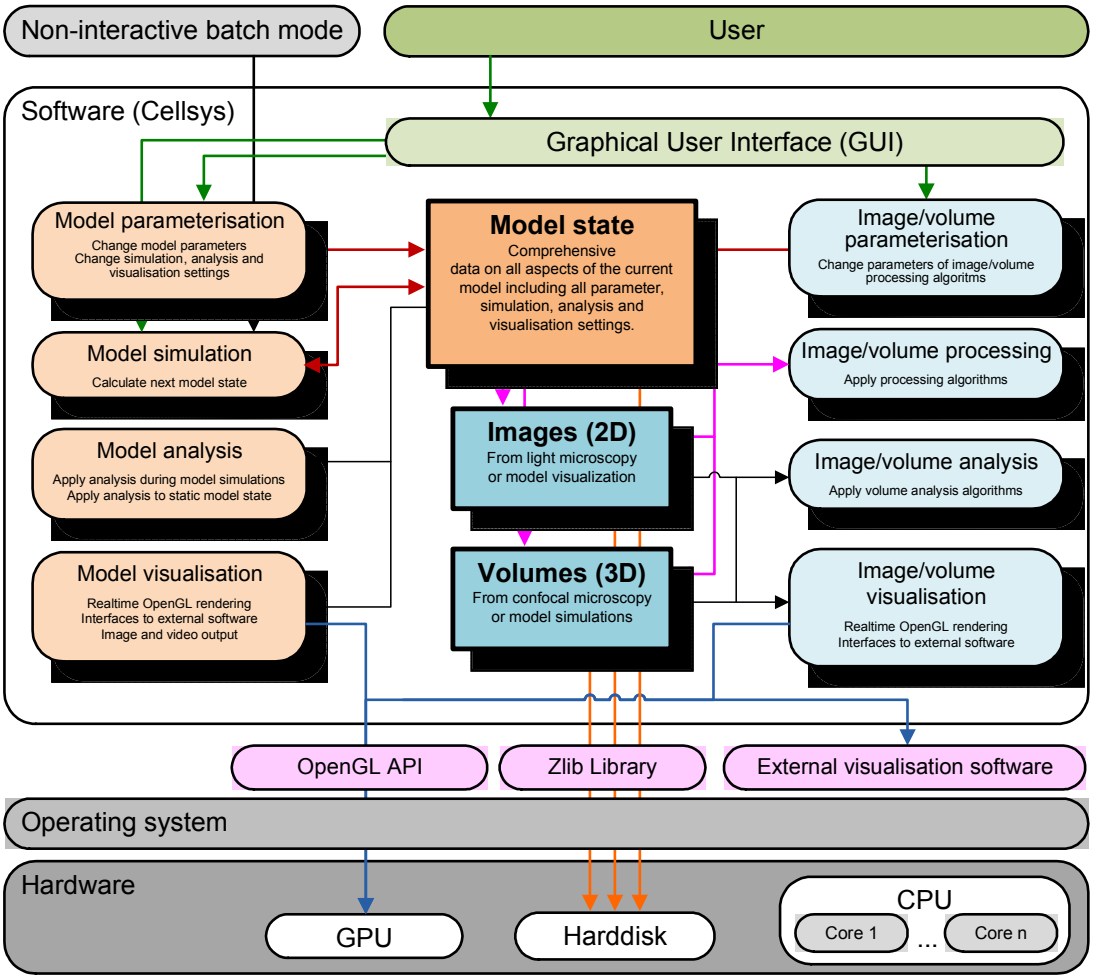


**Fig. 1: Cellsys software architecture.**
Illustration of the relationships between the functional partitions of Cellsys and associated data structures including their interactions with users and hardware.

The data structure model state is a key component of the Cellsys software. It contains the current multicellular configuration and all associated data. For example a particular model state includes not only all properties of each model cell, but also all parameters that control the simulation, analysis and visualization of these cells. Additionally, a model state integrates the current parameterization of the image and volume processing algorithms. Thereby it represents a comprehensive description of all current settings of Cellsys. The model state is effectively stored in a binary and compressed form (orange arrow in Fig.1) using a specific file format.
In general, the model state can only be modified by software components associated to the functional partitions model parameterization, model simulation or image/volume parameterization (dark red arrows in Fig.1). Typically, these components are controlled via the interactive graphical user interface (green arrows in Fig.1). Nevertheless, model simulations can alternatively be triggered using the batch mode (black arrow in Fig.1, for details see section 2.2.3).

The data structures “Images” and “Volumes” are used to store images or stacks of images (volumetric data) supplemented with additional information in a binary and compressed form (orange arrows in Fig.1). Typically, both data structures contain experimental data obtained by either bright field microscopy or confocal laser scanning microscopy. In some situations, however, we use the current multicellular configuration stored in the model state data structure to generate a volumetric data set (magenta arrows in Fig.1). Thereby, we are able to directly compare the results of model simulations and the corresponding experimental data sets (see chapter 4). In general, the content of the data structures images and volumes is modified only by image/volume processing algorithms for example to facilitate image/volume analysis or visualization which both typically only access and not modify these data structures.

All three data structures (model state, images and volumes) represent the main resource of Cellsys for analysis and visualization (black and blue arrows in Fig.1).

During the incremental implementation of our software, this strict definition of the architecture of Cellsys has considerably helped maintain an organized and structured application despite the steady addition of new functional components.

### 2.2.3. Workflow

The functionality of the Cellsys software can be accessed either (1) interactively via the graphical user interface or (2) non-interactively by a batch processing system. Both ways to use the software implicate specific workflows that are outlined in this section and illustrated in Fig.2.

Whether Cellsys starts in interactive or batch mode is determined by command line parameters. However, only the interactive mode allows the user to access the full set of functionality of Cellsys, while in batch mode the accessible functionality of the software is limited to a few frequently used tasks. In interactive mode (blue area in Fig.2) a user can for example create, load and modify the model state via the graphical user interface. All changes are immediately visualized. Additionally, the user can manually invoke methods for example to analyze or persistently save the current model state or start a model simulation (green area in Fig.2). In contrast, in batch mode (red area in Fig.2) the software automatically loads a particular model state that is specified by command line parameters and then directly starts a model simulation (green area in Fig.2) without further interaction with the user. During such simulations the software remains in a non-interactive state and consecutively conducts previously specified measurements, persistently saves the model and calculates the next model state until the specified simulation target has been reached. In this case, if the model simulation was started in interactive mode, the software returns control to the user and reenters an interactive state (blue arrow in Fig.2).

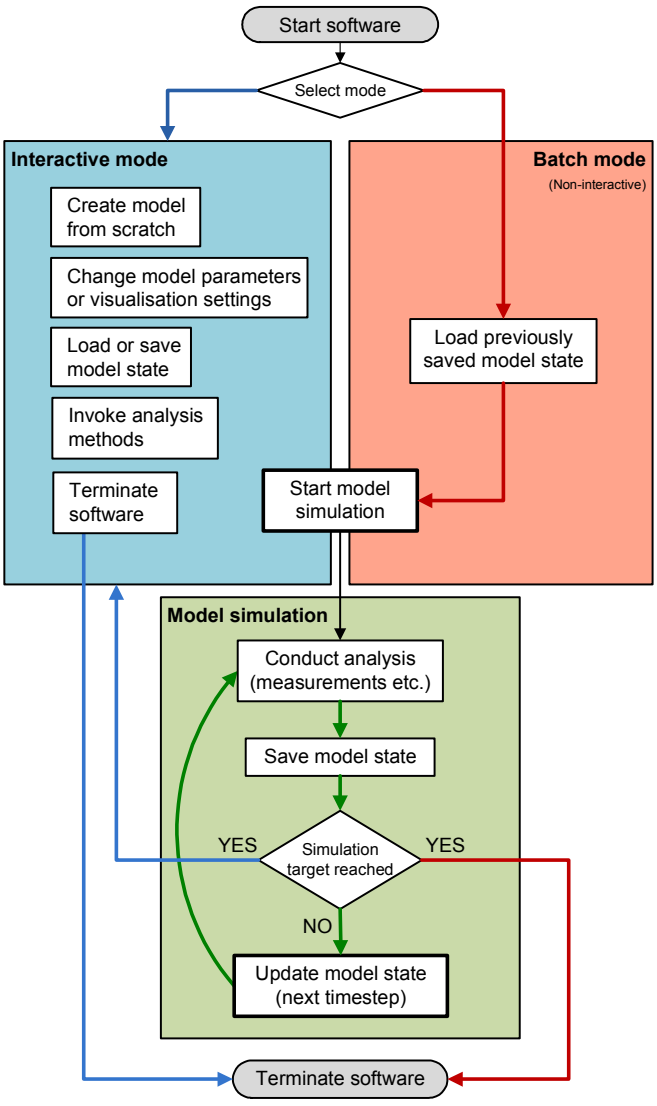


**Fig. 2: Cellsys common workflows.**
Illustration of the interplay of interactive (blue) and non-interactive (red) modes to execute model simulations (green).

In batch mode the software immediately terminates (red arrow in Fig.2). The graphical user interface is only initialized in interactive mode which enables Cellsys in batch mode to run on host architectures without display capabilities for example dedicated compute clusters.
In summary, the interactive mode is typically used to prepare model simulations which later are carried out using batch mode. The results of these simulations are then visualized and analyzed again using the interactive mode.

## 2.3. Implementation

In the preceding sections, we outlined the design and architecture of Cellsys on an abstract and implementation-independent level and specified cornerstones to guide the implementation phase. The next sections substantiate these considerations and discuss concrete technological choices to meet the requirements defined by these cornerstones.

### 2.3.1. Methodology: Object oriented paradigm

The object oriented paradigm (OOP) is a software development methodology that lays the foundation for the modular and reusable implementation of Cellsys (refer to section 2.2.1 cornerstones 1 and 6) by providing a conceptual framework to manage the software lifecycle by applying several ideas and implementation principles. The main idea is to strictly encapsulate software components into self sufficient objects whose functionality is exclusively accessible through precisely defined interfaces.

#### 2.3.1.1. History

The roots of the OOP can be traced to the 1960s where early ideas [Dahl, 1968] of object oriented concepts can be found in the Simula67 programming language which strongly influenced later languages especially Smalltalk and Pascal. Smalltalk was developed at Xerox PARC in the 1970s and first introduced the phrase “object-oriented programming” [Kay, 1993]. In the 1980s further extensive pioneering research on software development methodologies [Cardelli & Wegner, 1985] [Nygaard, 1986] [Stroustrup, 1988] [Wegner, 1987] [Madsen & Moller-Pedersen, 1988] was published. Since the early 1990s the object oriented approach became increasingly popular. Comprehensive textbooks [Booch, 1991] [Rumbaugh et al., 1991] described the OOP as permeating the entire software lifecycle including analysis, design and implementation phases. Today, OOP has become the most widespread approach for the development of large software systems [Capretz, 2003].

#### 2.3.1.2. Key concepts

The main elements of an object-oriented software system are objects and classes. In this context a class describes the abstract characteristics of an idea or physical component in a particular domain whereas an object represents the concrete realization of these characteristics. Every object is derived from a particular class and is termed its instance. In a platonic sense, a class is an ideal, archetypal object.
When modeling a biological system, classes and objects often directly refer to biological or biophysical components of that system. For example, in chapter 3 we model avascular tumor spheroids whose main components are cancerous cells. In our software each of these cells is implemented by an individual object. However, each of these objects is an instance of the same class *TumorCell* that defines its characteristics.
The internal state of an object is represented by its attributes. For example, objects instantiated from class *TumorCell* store their current age, volume and position in model space. In general, the internal state of an object can be manipulated only by its methods. When modeling biological systems, such methods often directly represent a particular biological functionality. For example, objects instantiated from class *TumorCell* include methods to model cellular growth, cell division, migration, differentiation or death.
The object management group (OMG), a well-known international computer industry consortium dedicated to the development of standards for object oriented systems, recapitulatory defined an object as an “entity that has a unique identity, a set of operations that can be applied to it and a state that stores the effect of the operations" [www, 13].
Traditional imperative programming separates data from the operations to manipulate data. Object oriented programming transcends this approach by considering objects a composition of data (attributes) and associated operations (methods). While traditional programming is strictly causal, object oriented programming is intentional. Instead of defining a specific response for every possible program action, an object oriented approach defines functionality of interacting objects which leads to complex program behavior.
Classes support the modeling of a complex domain by providing the possibility to construct class hierarchies. This concept is termed class inheritance. In a hierarchy of classes, a class of a more specific level (termed subclass) adopts attributes and methods from classes of a more abstract level (termed superclass). However, a subclass is able to redefine this inheritance and add its own individual attributes and methods. For example in Cellsys the most abstract class is termed *BiophysicalEntity* and describes a generic biophysical component. A typical attribute of this class is for example its position in model space. An exemplary subclass of *BiophysicalEntity* is the class *Cell* which itself is superclass for the classes *HepatocyteCell*, *SinusoidalCell* or the already mentioned class *TumorCell* that each describe specific cell types. While the generic class *Cell* only includes common attributes of cells as cell volume or cell surface area, the more concrete classes add further attributes that

are specific for the particular cell type. In order to maintain a clear class hierarchy, in Cellsys objects are instantiated only from the most specific classes. In general, class inheritance is a key concept of the object oriented paradigm which imposes modularity and structure (refer to section 2.2.1 cornerstone 1) to an object oriented implementation.
A further basic principle in object oriented programming is termed message passing. Message passing designates the process by which an object communicates to another object by either sending data or asking to invoke a method [Armstrong, 2006]. For example an object instantiated from class *TumorCell* may receive messages from another object instantiated from class *NutrientEnvironment* that implements glucose diffusion in model space (see section 3.5). For low glucose concentrations, this messages may invoke methods to trigger apoptosis (cell death) thereby encouraging a model tumor cell to die. Nevertheless, the functional details of the object that receives the message are strictly concealed from the sending object. This principle of object oriented programming is termed encapsulation which means that the methods of an object are accessible exclusively through an interface hiding the details of the implementation. This approach enables client objects of such interface to be independent of details of the implementation that may change in the future. Thereby such changes can be made more easily without interdependence between objects.
Essentially, programming within the object oriented paradigm means organizing software as a community of objects instantiated from and structured by a hierarchy of classes that interact and communicate to each other using precisely defined interfaces.

#### 2.3.1.3. Discussion

The object oriented software development methodology offers several advantages over traditional techniques especially for the implementation of agent-based models for complex systems [Booch, 1991] [Hartwell et al., 1999] [Emonet et al., 2005] [Griffin, 2006] [Thorne et al., 2007]. Object oriented programming imposes simplicity to an implementation by directly relating objects to components of the modeled system. This reduces the complexity of the abstraction and facilitates a clear structure and modularity of the implementation (refer to section 2.2.1 cornerstone 1).
In principle object oriented software is modified by adapting the internal implementation of particular objects and extended by adding new objects. Due to the encapsulation of the implementation of objects and the resulting strict modularity in general such changes do not require a complete revision of the source code. Especially for large scientific software this local modifiability leads to an invaluable easing of software maintenance that is a key advantage over traditional techniques.
Object oriented programming also facilitates software reuse (refer to section 2.2.1 cornerstone 6) as classes can be used to instantiate objects for different functional subsets of Cellsys. This code reuse is multiplied by class inheritance as the definition of an abstract class potentially lays the foundation for many subclasses each instantiating many objects.

From a purely technical perspective a disadvantage of object oriented programming results from a small inherent performance und memory overhead as objects are normally referenced by pointers whose memory is allocated dynamically at runtime. A further performance overhead results from the time to find space on the heap to store objects. However, these efficiency penalties are very limited and of little importance in comparison with the benefits of object oriented programming with regard to software engineering.

### 2.3.2. Programming language: C++

In principle object oriented software can be implemented in a wide variety of modern programming languages. However, for computationally intense scientific problems application performance must be optimized. Together with other major factors as compiler efficiency and especially algorithmic optimality (refer to section 2.2.1 cornerstone 2) the overall performance of the programming language has significant impact on the time that is required to solve a particular problem on a given host architecture. Thereby application performance effectively constrains the range of problems that can be addressed by a particular implementation.
Unfortunately a precise and exhaustive performance comparison of all relevant programming languages is not available and may due to the wide variety of influence factors hardly ever been accomplished. However, there is a broad consensus that C++ [Stroustrup, 2000] is among the fastest languages currently available [Eckel, 2003] [www, 01].
C++ is a portable (refer to section 2.2.1 cornerstone 3) and widespread programming language that supports object oriented programming and that rests upon a solid standardization by a joint ANSI/ISO committee [www, 03].
A further important advantage of C++ over other programming languages is the unrivaled availability of libraries that in many cases considerably simplify and accelerate software development (refer to section 2.2.1 cornerstone 6).
Today, many C/C++ compilers including the widespread GCC (GNU Compiler Collection) contain implementations of OpenMP facilitating the easy introduction of shared-memory parallel computing into an application (refer to section 2.3.5). This enables Cellsys to scale with its host architecture and considerably gain performance on a multi-processor or multi-core system.
Despite these advantages C++ has some disadvantages that are often a tribute to its high performance. For example deficient type safety and the possibility to implement unverified address pointers may lead to serious and difficult to debug coding errors.
Nevertheless the C++ programming language meets all theoretical (support for effective object oriented programming, portability, reusability) and practical (performance) requirements for the implementation of Cellsys.

### 2.3.3. 3D graphics: OpenGL

Besides the execution of model simulations, a key feature of Cellsys is the visualization of simulated multicellular assemblies and related image and volume data sets. Such graphical representations of the model are of great value for verifying and presenting simulation results. Moreover, often visualization is the most effective way to identify sometimes subtitle flaws of a model and its implementation for example by comparison with experimental images.

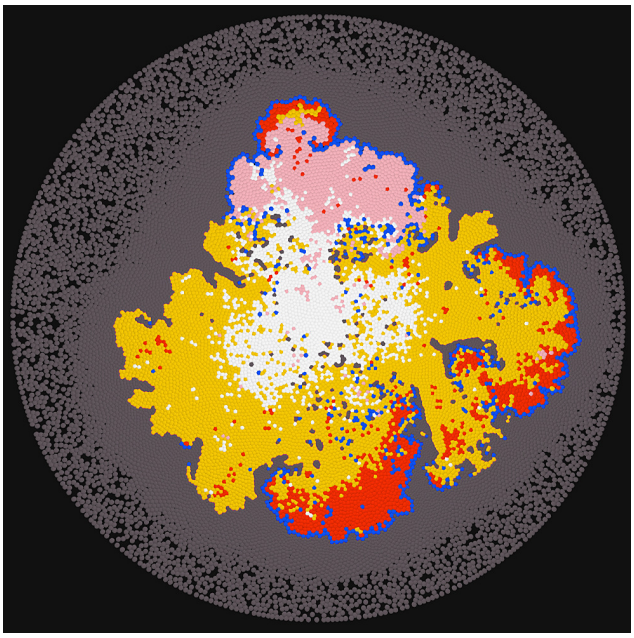

**Fig. 3: OpenGL in Cellsys.**
Typical OpenGL-based rendering of a two-dimensional multicellular assembly in Cellsys. Here, cell color indicates specific intracellular properties.

Today, the rendering of complex three-dimensional graphics is supported by widely available graphics accelerator cards of great computational power. For example the 240 parallel stream processors of a Nivida GeForce GTX 285 card theoretically exhibit a peak performance of more than a TFlop and are able to render over $20^{10}$ pixels per second. Additionally, this particular hardware provides a memory bandwidth of more than 159 GB per second [www, 12]. By exploiting this computational power we are able to render a very detailed and yet interactive representation of our complex three-dimensional models in real time.

By now only two major application-programming interfaces (APIs) are available to access the features of graphics accelerator cards: (1) Microsoft DirectX and (2) the Open Graphics Library (OpenGL). Both APIs represent a mediation layer between graphics hardware and software and thus can be considered software-based abstractions of hardware. In the following we refer to version 10.1 of Microsoft DirectX and version 2.1 of OpenGL.

While Microsoft DirectX is frequently used in computer games, OpenGL is the standard API for high performance visualization in engineering especially in computer aided design and is widely used for scientific visualization. Scientific software is often required to be executed on heterogeneous host architectures, therefore the most striking advantage of OpenGL is its portability (refer to section 2.2.1 cornerstone 3). In contrast to Microsoft DirectX that is only available for Windows operating systems, OpenGL implementations are available on all major platforms for example all recent Windows operating systems (98, ME, 2000, XP,

Vista, 2003), all Linux distributions, Unix, Irix, Solaris and all recent Apple Mac OS X operating systems. Additionally, OpenGL is licensed and supported by all major graphics hardware manufacturers (Nvidia, ATI, Intel and S3). The software developed in this work utilizes OpenGL to display three-dimensional graphics.
Basically an OpenGL implementation transforms geometrical primitives and image data (e.g. textures) into pixels on a screen by utilizing a graphics pipeline that includes image and geometry paths. The image path (red in Fig.4) consists of pixel operations, texture assembly and rasterization, while the geometry path (blue in Fig.4) includes evaluation, per-vertex operations (including viewing transformations and primitive assembly) and rasterization. Both paths merge at rasterization stage and allow subsequent per-fragment operations. Since the graphics pipeline provides access to both image data and geometric primitives, it facilitates the implementation of low-level graphics functionality.

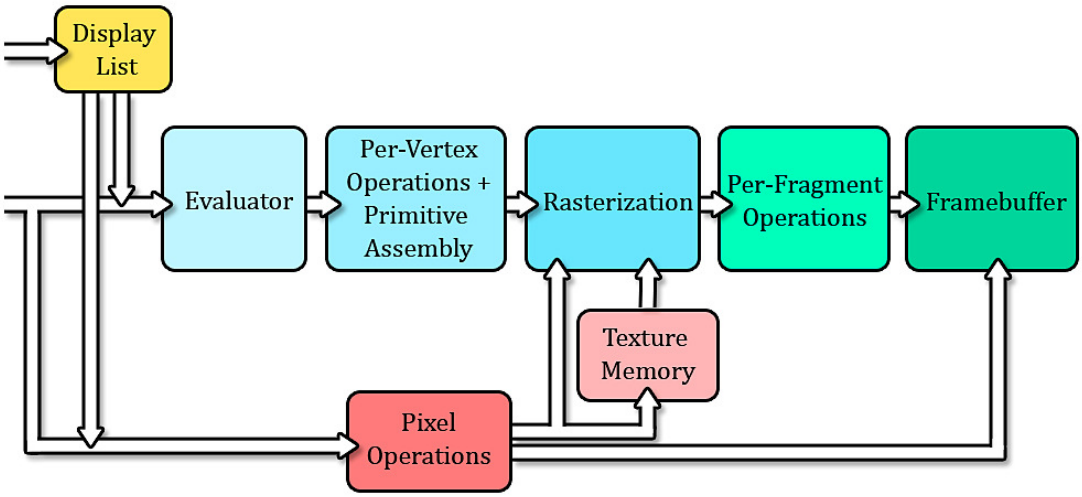


**Fig. 4: OpenGL rendering pipeline.** Simplified block diagram of the OpenGL rendering pipeline illustrating its components and their succession.

A standard implementation of the OpenGL specification includes the base graphics library (GL) and the graphics library utilities (GLU). While the GL library only features simple geometric primitives as points, lines, triangles and polygons, GLU provides higher-level drawing routines and additional geometric primitives including quadric surfaces. A quadric surface is an n-dimensional hypersurface defined by the locus of zeros of a quadratic polynomial [Venit & Bishop, 1996] by:

$$\sum_{i,j=0}^{n} M_{ij} x_i x_j + \sum_{i=0}^{n} V_i x_i + C = 0 \qquad (1)$$

where $M$ is a $(n+1)\times(n+1)$ matrix, $V$ is a $(n+1)$-dimensional vector and $C$ a constant. Quadric surfaces can describe various geometric shapes for example

spheres, ellipsoids and cylinders which are utilized in Cellsys as flexible basis for real time visualization of multicellular assemblies (see Fig.3).
Another very useful extension of OpenGL is the graphics library utility toolkit (GLUT) that provides portable window management and routines for mouse and keyboard input [Kilgard, 1996]. Especially its open source implementation freeglut (freeglut.sourceforge.net) lays a foundation for the portability of Cellsys and its graphical user interface (refer to section 2.2.1 cornerstone 3).

### 2.3.4. User interface: GLUI

The GLUT extension (refer to previous section) also represents the technological basis for the OpenGL user interface library (GLUI) [www, 07]. GLUI provides all important elements for the construction of a portable and flexible graphical user interface (refer to section 2.2.1 cornerstones 3 and 4). GLUI is implemented in C++ and integrates a wide variety of standard base components as buttons to trigger actions, checkboxes to change Boolean states, radio buttons to select mutually exclusive options and editable text boxes to input variables of different types for example strings or floating point values. Furthermore, GLUI integrates very convenient components especially for the visualization of complex three-dimensional structures (e.g. multicellular assemblies). These special rotation and translation controllers allow a direct manipulation of the position and orientation of an object in 3D.
Additionally, GLUI includes panels and rollout elements for grouping sets of controls which considerably helps structuring an extensive user interface. Especially for complex applications a well structured and ergonomic user interface considerably increases productivity and helps to prevent errors due to invalid user input. For these reasons we use the GLUI library to implement the graphical user interface of Cellsys (also refer to section 2.4 for a brief description of its concrete realization).

### 2.3.5. Parallelism: OpenMP

In 1965 Gordon Moore (a co-founder of Intel) observed a long-term trend in the history of computing hardware. He proposed that since the invention of integrated circuits in 1958 the number of transistors that can be placed on an integrated circuit without exceptional cost has increased exponentially, doubling approximately every two years [Moore, 1965]. This empirical trend commonly designated as “Moore’s law” has roughly held true since then and is expected to last at least for another decade. In correlation to Moore’s law, most capabilities of electronic digital devices have also improved at approximately exponential rate including general processing speed and memory capacity.
During the last years however, the computational power of CPUs mainly has been improved by constructing processors that contain multiple computation cores. Recent

Intel desktop processors for example typically contain four processing cores (Intel Core 2 Quad). Multi-core processor architectures are becoming dominant in most areas of computing [Bliss, 2007]. To exploit the advantages of such parallel machines software is required to support parallel computing.
Cellsys utilizes OpenMP (Open Multi Processing) to implement parallel processing on shared memory machines. OpenMP is a standardized, scalable and portable application program interface (API) that uses the Fork-Join Model of parallel execution [Quinn, 2004]. In its current version 3.0 there are specifications for C/C++ and FORTRAN which have been included into compilers on all major platforms (including Microsoft Windows XP/Vista and most Linux distributions).
Other widespread approaches to implement parallel processing are POSIX threads and the message passing interface (MPI). In contrast to these methods that use explicit threading, OpenMP is specified by a small set of special compiler directives and library routines that can easily be embedded in existing C/C++ source code. This support for an incremental implementation is a key advantage of OpenMP. Furthermore OpenMP is capable of implicit communication to compensate irregular communication patterns and includes an advanced dynamic load balancing approach [Chapman et al., 2007].
According to Amdahl's law the theoretical maximum speed up $S_{\max}$ on a parallel machine with $N$ processors (or cores) is:

$$S_{\max} = \left( (1-P) + \frac{P}{N} \right)^{-1} \tag{2}$$

with $P$ the partition of the application that can be parallelized [Amdahl, 1967]. For Cellsys $P \approx 0.95$ (estimated from empirical $S_{\max}$) which allows an effective implementation of parallel computing. Thereby OpenMP lays the foundation for the high computational scalability of Cellsys (refer to section 2.2.1 cornerstone 2).

## 2.4. Graphical user interface

In general a graphical user interface (GUI) represents a mediation layer between user and application that enables that user to interact with the application using graphical symbols and pointing devices for example a computer mouse. In Cellsys the GUI provides a hierarchically organized access to a wide variety of functionality. In case Cellsys is used in interactive mode, all aspects of model parameterization, simulation, analysis and visualization and image/volume processing and analysis are controlled via the GUI. The hierarchical organization of the GUI corresponds with the software architecture elaborated in section 2.2.2. Accordingly, each functional partition is represented by a particular window that realizes a flexible and structured interface to the corresponding functional partition using predefined components of

the GLUI library (for further details refer to section 2.3.4). Such components include panels, rollouts (collapsible panels), checkboxes, spinners, text fields or radio buttons. The approach of organizing the GUI of an application corresponding to its functionality and common workflows considerably increases productivity and facilitates extensibility [Shneiderman & Plaisant, 2004].

Fig.5 shows the user interface of Cellsys in its fully unfolded form that reveals all GUI components. However, in general only a small fraction of these components is simultaneously visible. In the following we briefly outline the functionality within each particular window (Fig.5A-F) to sketch the GUI of Cellsys.

Fig.5A shows variations of the "Create" window. This window summarizes functionality to create and adapt the model and corresponds to the functional partition for model parameterization. For example GUI components in this window are used to load and save model states or adjust model parameters. Initial configurations with a specific spatial structure or chemical environment can be created and the prospective behavior of cells (for example state transitions or intracellular responses) can be specified.

The "Visualization" window shown in Fig.5B is used to adjust the visual depiction of model and image/volume data and corresponds to the functional partitions for model and image/volume visualization. All major properties of individual cells can be illustrated together with the current spatial structure of the multicellular population. Concentrations of chemicals in model space can be visualized along with further technical information for example the direction and strength of particular biomechanical forces. Additionally users can select from a wide variety of options to determine what components of the model should be shown or hidden. All changes of visualization settings are immediately reflected in the "Viewport" window illustrated in Fig.5C.

Here, along with general information on the currently rendered cell population (in the upper left corner) model cells are visualized by geometric primitives and quadric surfaces (refer to section 2.3.3). Fig.5C shows a typical example for the depiction of model cell properties by a specific color coding: in the left half of the monolayer in Fig.5C cells are colored according to their current contact area to adjacent cells, while in the right half cells are colored to reflect their age. In this particular case the color coding reveals a decreased contact area at the monolayer border and a complex non-trivial distribution of cells of different age within the population. The arrows at the brink of the monolayer additionally illustrate the strength and direction of the biomechanical forces that result from cell-cell interactions. This reveals that for cells at the monolayer border these forces are exerted mainly in outward direction which later in this work is shown to play an important role in cultured cell growth (see section 3.3).

The interactive and often real time display of the current model state is very helpful to explore and analyze multicellular structures that resulted from model simulations. The window "Simulate and Observe" shown in Fig.5D is used to prepare and start such simulations and corresponds to the functional partitions for model simulation

and analysis. Here, the objective of a simulation (for example growth to a specific number of cells) and the frequency and type of measurements during a simulation can be specified. For static model states various additional analyses (for example cell property distribution histograms) can be triggered. The “Simulate and Observe” window also provides functionality for obtaining screenshots and recording videos.
Screenshots as well as microscopic images and volumetric data sets from external sources (for example from laser scanning microscopy) may be further processed utilizing the “Image and Volume processing” window shown in Fig.5E that corresponds to the functional partitions for image/volume processing and analysis. This window provides access to various specialized algorithms that can be used to enhance and analyze images and volumetric data sets. For example volume data sets can be improved by an adaptive histogram equalization filter, a median filter and further, more complex morphological operators (elaborated in detail in section 4.3.2).
All major commands that are triggered using the Cellsys GUI are reflected on the “System console” window shown in Fig.5F. The textual output in this window displays important technical information (for example errors and warnings) and additionally could be used to journalize model modifications and simulations.
In conjunction all GUI windows form a flexible (regarding both content and arrangement on screen) and organized interface to all features of the Cellsys software.

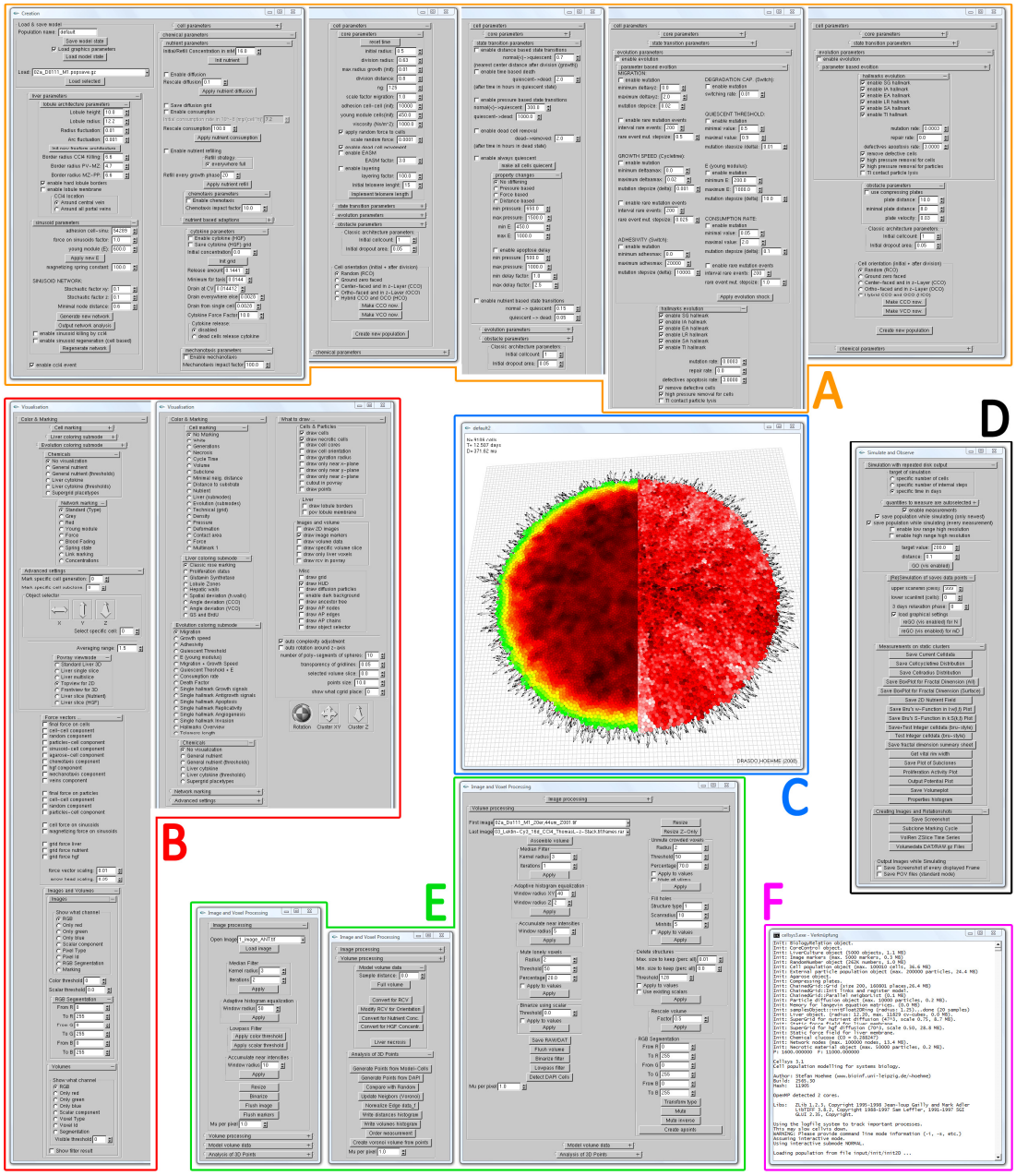


**Fig. 5: The graphical user interface (GUI) of Cellsys.**
A: Create window. B: Visualization window. C: Viewport window. D: Simulate and Observe window. E: Image and volume processing window. F: System console. Multiple windows shown for A-E represent different unfolding states. For an exemplary magnification see Supporting Fig.1

## 2.5. Visualization

The Cellsys software developed as part of this thesis integrates two main possibilities to visualize our model and associated data. On the one hand primary visualization is directly integrated into the graphical user interface (refer to section 2.4) and implements hardware-accelerated polygon-based 3D graphics utilizing OpenGL (refer to section 2.3.3). On the other hand, secondary visualization implements interfaces to external software that integrates ray tracing or direct volume rendering functionality. Considering different fields of application, both possibilities of visualization have specific advantages and disadvantages that are discussed in the following sections.

### 2.5.1. Primary visualization: OpenGL

The primary visualization component of Cellsys directly utilizes OpenGL to render all model elements and associated data by polygonal representations of geometric primitives and quadric surfaces. On adequate hardware this OpenGL rendering provides a fast and often real time display. In our context the term “real time” implicates a minimal reaction time of 40 ms which is equivalent to a screen refresh rate of 25 frames per second [Liu & Layland, 1973].
The depiction of complex model structures in real time is a main advantage of primary visualization. Typically, the polygonal shapes that are used to represent a particular model element are determined by their type while the color of the shape is often encoded by a selected property of the model element it represents. Thereby OpenGL rendering directly reflects changes of the model state and for example can be used to verify parameter changes or explore the results of model simulations. Fig.6 illustrates typical examples of OpenGL rendering. Additional textual displays of key parameters of the current model state and dynamic legends that elucidate the current color encoding complement primary visualization. The coloring of frequently used shapes according to a subset of their properties is supported by a number of predefined color-schemes implemented in Cellsys in form of visualization classes. These classes allow the fast integration of sophisticated coloring for new model elements. For example in Fig.6A each model cell is represented by a sphere that illustrates its position and size while the color of the sphere encodes the pressure that is currently exerted on that particular cell (also see magnification of Fig.6A).
A major weakness of OpenGL-based visualization in Cellsys arises from its missing support for realistic shadow-casting. This deficiency leads to restrictions regarding the perceptibility of spatial relationships between objects in 3D. Unfortunately, the complex three-dimensional structure often is an important property of multicellular assemblies. For example recent studies suggest that even minor differences in the surface roughness of a tumor spheroid could have major impact on its invasiveness [Guiot et al., 2007], also refer to section 3.6). The main reason why realistic shadow casting has not been implemented in Cellsys is that in most cases it impedes real time

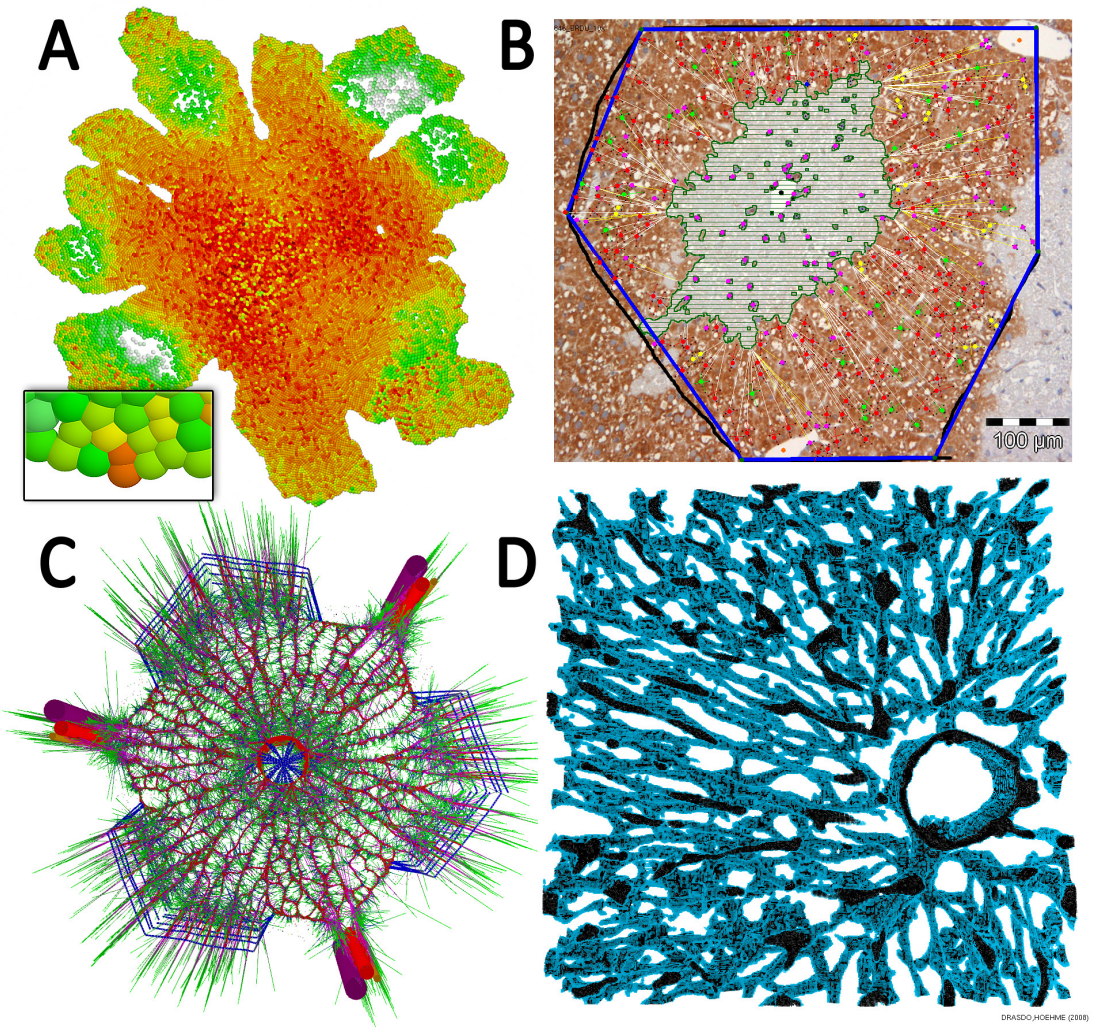


**Fig. 6: Examples of primary OpenGL rendering.**
A: Cell monolayer embedded in tissue (not shown). Cell color indicates the pressure that is exerted on particular cells (red=high, white/green=low). B: 2D image of a liver lobule for example showing the automatically detected necrotic area (green lines) which was rendered using OpenGL orthogonal projection. C: Partition of the sinusoidal blood vessel network with additional force visualization. Green lines indicate direction and strength of biomechanical forces that affect the cells (not shown). D: Volume visualization of a confocal data set containing lobule blood vessels. Light blue voxels are marked to be removed by a generalized erosion operator (details: A: section 3.6, B-D: section 4.3).

rendering by introducing computationally complex visibility tests to the rendering process. The most common techniques to implement high quality shadows are shadow mapping [Williams, 1978] [Reeves et al., 1987] [Segal, 1992] and stenciled shadow volumes [Crow, 1977] [Everitt & Kilgard, 2002]. In principle both techniques require visibility tests for each light source at each rasterized fragment. A typical representation of a multicellular assembly in Cellsys is composed of $10^5$ cells that together are represented by approximately $10^7$ polygons (before level-of-detail optimizations) which on current hardware are impossible to render in real time using

accurate shadows. In order to overcome this limitation of the primary visualization we implemented interfaces to external software that either approximates shadows by geometrical simplifications for example isosurfaces (refer to section 2.5.3) or that uses ray tracing to render accurate shadows (refer to section 2.5.2.). Ray tracing software supports even more sophisticated lighting techniques as photon mapping [Jensen, 2001] but always completely abandons real time rendering.
In addition to the visualization of the current model state, we use primary OpenGL rendering to display images (Fig.6B) and volumetric data (Fig.6D) for example to verify the results of image processing algorithms that improve or analyze such data. This visualization of images and volumetric data is directly integrated into the graphical user interface and utilizes OpenGL orthographic projection for the rendering images and slices through volumetric data in2D and display lists of geometric primitives for the three-dimensional display of volumetric data. However, the visualization of large volumetric data sets ($> 2 \cdot 10^6$ Voxels) is slow without further optimizations. Fortunately, external software dedicated to the direct rendering of volumetric data often includes sophisticated optimizations to handle such large high-resolution volume data sets. Therefore, we utilize the interface of Cellsys to such volume rendering software (refer to section 2.5.3) for the visualization of large volume data sets.
In summary we use primary OpenGL rendering for an immediate and interactive real time visualization of the current model state and associated data and compensate its main deficiencies (the lack of realistic shadow casting and real time rendering of large volume data sets) by using interfaces to external software (secondary visualization).

### 2.5.2. Secondary visualization: Ray tracing

In order to complement the primary visualization capabilities of Cellsys we implemented interfaces to external ray tracing software. Ray tracing is a method of contemporary computer graphics that basically generates an image by tracing rays of light through pixels in an image plane [Shirley & Morley, 2001]. In the last two decades many sophisticated image synthesis techniques based on that idea have been developed. Methods as diffuse ray tracing [Cook, 1984], path tracing [Kajiya, 1986], Metropolis light transport [Veach & Guibas, 1997] or photon mapping [Jensen & Christensen, 1995] provide a high degree of photorealism for example by approximating global illumination. Modern ray tracing software has become a powerful visualization tool by implementing these lighting techniques along with further helpful features as constructive solid geometry [Atherton, 1983] and freeform surface modeling for example using isosurfaces of scalar fields. In order to utilize such ray tracing applications we integrated VRML 2.0 (virtual reality markup language) and POV-Ray (persistence of vision) interfaces in Cellsys by supporting the corresponding file formats.

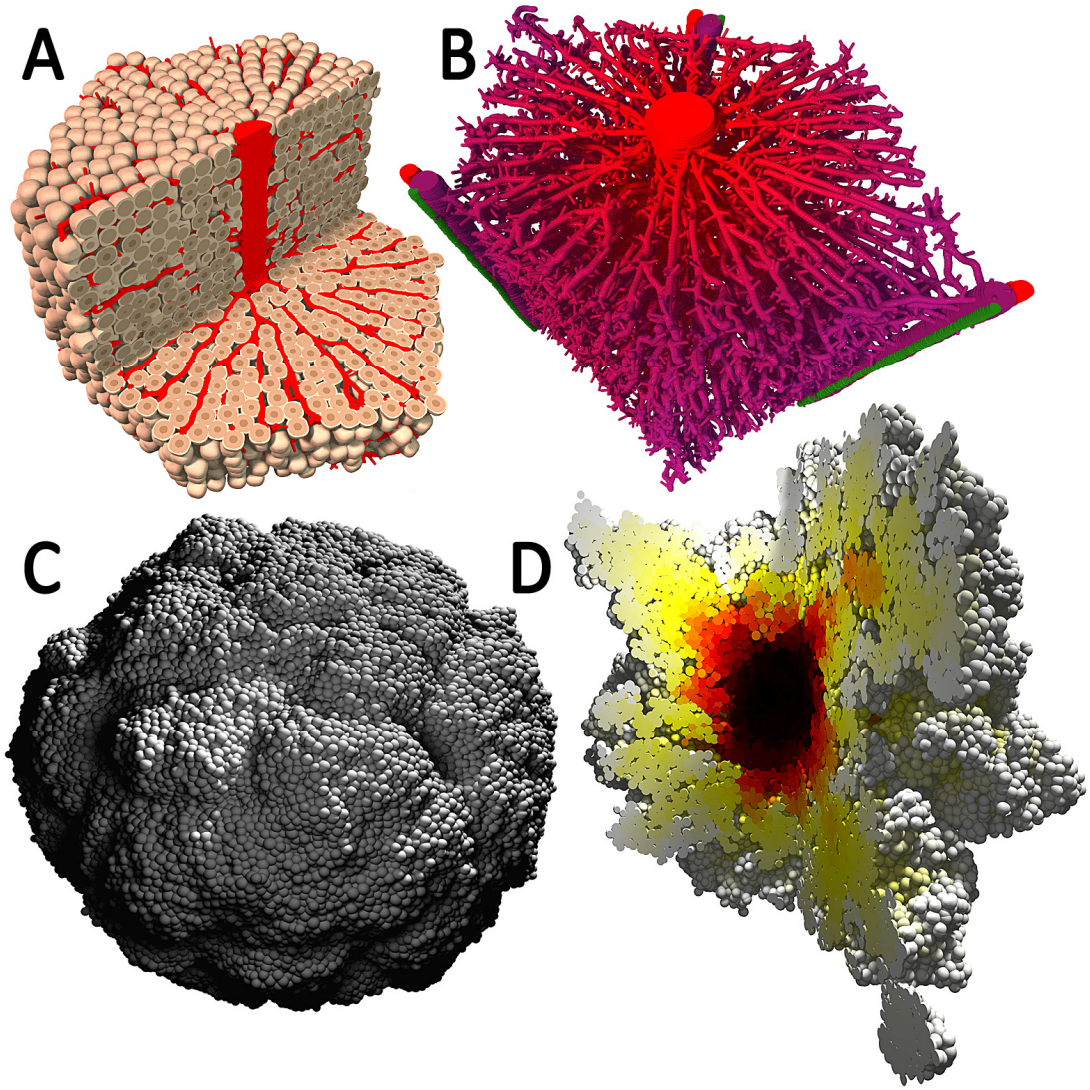


**Fig. 7: Examples of secondary ray tracing visualization.**
A: 3D model of a liver lobule including hepatocytes (ochre) and blood vessels (red). A quarter of lobule has been cut out to reveal its internal structure. B: Blood vessel network within a model liver lobule. Vessel color indicates oxygen concentration (violet = high, red=low). C: 3D model of a tumor spheroid embedded in tissue (not shown) exhibiting a complex surface structure. D: Model tumor spheroid grown in a low oxygen environment showing pronounced surface fingering. Brightness of cell coloring indicates proliferation activity (black=low, white=high). (details: A-B: section 4.3, C-D: section 3.6)

The VRML interface precisely wraps all geometric primitives that are used by the primary OpenGL visualization to display model elements into associated VRML objects. This VRML representation of the model can then be accessed by compatible rendering software including commercial packages as Autodesk Maya, Autodesk 3DS Max (both: [www, 04]) or free and open-source software as Rayshade [www, 15]. Therefore such software can be used to generate images similar to the primary visualization but with more sophisticated lighting for example accurate shadow casting (Fig.7C).

The interface to the free and open-source POV-Ray software [www, 14] advances this approach by translating many model elements into more realistic shape descriptions in POV-Ray SDL (scene description language). Fig.7A/B shows examples for this kind of visual enhancement using the freeform surface modeling capabilities that have been integrated in POV-Ray. For example, Fig.7A shows a liver lobule (see chapter 4) where the shape of the hepatocytes (liver cells) is visualized by cuboidal objects rather than the simple spheres used in the primary OpenGL visualization. This more complex cuboidal shape more realistically mimics the shape of hepatocytes *in vivo*. In another example, Fig.7B shows the sinusoidal blood vessel network within a liver lobule. In this ray traced image the surface of the blood vessels is defined by the isosurface of a scalar field generated by overlapping spheres along the vessels. This visualization of blood vessels by smooth tubes that cast accurate shadows is again much more realistic than the overlapping spheres used by primary OpenGL rendering.

Besides the more realistic representation of model elements, another major advantage of the POV-Ray interface is its capability to easily visualize cutouts of complex geometry. Partitions of arbitrary shape may be excluded from model structures to reveal otherwise hidden information for example within a compact population of cells. Fig.7 illustrates the benefits of such cutouts by exemplarily revealing the architecture within a lobule in Fig.7A and decreased proliferation activity in the interior of a compact model cell population in Fig.7D that both could not be recognized from the outside without cutouts.

A further important advantage of ray tracing software is its inherent capability to render images with correct shadow casting. For example, Fig.7C shows a tumor spheroid rendered with accurate shadows that represents a typical example where due to a complex (rough) surface an optimal depth perception becomes important to fully recognize a three-dimensional structure. The capability of ray tracing software to render correct shadows thereby compensates the corresponding limitation of primary OpenGL visualization.

Unfortunately, today ray tracing of complex structures using cutouts, multiple light sources and realistic shadows is not possible in real time as the superior visual quality is computationally expensive. Images of only moderately complex structures (for example model cell populations of $\leq 10^4$ cells without slicing) can be rendered within a few seconds on recent hardware. However, images of more complex structures that for example include slicing or a high number of cells ($> 10^4$) may take hours to render. In many situations for single images this may be acceptable, but if a large number of images have to be rendered for example to generate videos, rendering speed rapidly becomes a limiting factor. Nevertheless, ray tracing can easily be parallelized and therefore multiprocessing can effectively be used to accelerate the calculations. Furthermore, ray tracing requires high amounts of memory which additionally introduces an upper limit for the complexity of structures that can effectively be rendered on particular host architectures.

In summary we use the interface of Cellsys to ray tracing software to generate images and videos that depict the model state in superior visual quality whenever a fast (or even real time) rendering is not required.

### 2.5.3. Secondary visualization: Volume rendering

A further complement to primary visualization in Cellsys is the interface to external volume rendering software. Volume rendering is a technique to construct a 2D projection of a 3D volume data set [Levoy, 1988] [Drebin et al., 1988]. This projection is calculated by evaluating a volume rendering integral [Engel et al., 2001] for a continuous scalar field $s(\bar{x})$ and viewing rays $\bar{x}(\lambda)$:

$$I = \int_0^{\lambda_{\max}} \tilde{c}\left(s\left(\bar{x}(\lambda)\right)\right) \cdot \exp\left[-\int_0^{\lambda} d_{ext}\left(s\left(\bar{x}(\lambda')\right) d\lambda'\right)\right] d\lambda \qquad (3)$$

where $\lambda$ is the distance and $\lambda_{\max}$ the maximal distance to the viewpoint. $\tilde{c}(s)$ is a transfer function for color densities and $d_{ext}(s)$ are extinction densities. Because an analytical evaluation of the volume rendering integral is often not possible, in most cases it is numerically approximated by substituting the integral by the Riemann sum [Anton, 1999]. The continuous scalar field $s(\bar{x})$ is generated from discretely sampled volume data sets typically by trilinear interpolation [www, 17].

Today volume rendering is commonly used for example in medicine for the visualization of data obtained by computer tomography (CT) and magnetic resonance imaging (MRI) or in computational fluid dynamics. In this work we use volumetric data obtained by a confocal laser scanning microscope to extract quantitative information from experimental data on regenerating liver lobules (refer to chapter 4).

Methods for volume rendering can be subdivided in indirect and direct techniques. Indirect volume rendering generally includes methods that further process and analyze the volume data set and then construct the image using this secondary information. A common indirect volume rendering technique is to utilize the marching cubes algorithm [Lorensen & Cline, 1987] to extract isosurfaces within a volume and then render a polygonal representation of this isosurface using traditional polygon-based rendering [Montani et al., 1994].

By contrast, direct volume rendering directly derives an image from the information within a volume data set. A common image-based direct volume rendering technique based on Eqn.3 is termed volume ray casting. Here, a viewing ray is generated for each image pixel of the projection plane. Volume ray casting is widely considered the volume rendering technique that provides best visual results, but it is also one of the most computationally complex methods [Lichtenbelt et al., 1998]. However, in the last years the performance of ray casting algorithms has been significantly improved by exploiting the massive parallelism and programmability of recent graphics hardware [Kruger & Westermann, 2003]. Additional optimizations as pre-

integrated volume rendering [Engel et al., 2006] [Lum et al., 2004] reduce sampling artifacts and thereby further improve visual quality.
Despite volume rendering software is not yet a down-market product, there are several powerful applications as PIVR (pre-integrated volume renderer) [Engel et al., 2001], VOXX [Clendenon et al., 2006] and SPVOLREN [Stegmaier et al., 2005] available. Cellsys integrates interfaces to all three applications by supporting specific compatible RAW/DAT and multilayer TIFF file formats.
We use PIVR to visualize large volume data sets using direct pre-integrated volume rendering. PIVR supports an arbitrary number of isosurfaces with diffuse and specular lighting without explicitly extracting a polygonal representation. The rendering of isosurfaces can be mixed with volume shading and semi-transparent volumes. Fig.8A shows a typical rendering of the sinusoidal blood vessel network (white) and hepatocyte nuclei (blue) within a liver lobule after several processing steps (elaborated in chapter 4.3).
VOXX is especially useful to render and explore large multi-channel data sets. Fig.8B shows a typical multi-channel volume data set of a liver lobule obtained by a confocal laser scanning microscope that has been fluorescently stained by three different antibodies. This data set represents a typical unprocessed input volume whereas Fig.8A shows the corresponding resulting data set after volume processing.
In addition to secondary visualization based on direct volume rendering we use indirect volume rendering implemented in SPVOLREN to render polygonal isosurfaces that cast shadows (Fig.8C). However, the quality of the calculated shadows is not comparable to those obtained by ray tracers (refer to previous section). Nevertheless, the capability of SPVOLREN to render such shadows in real time is a striking advantage which enables us to efficiently explore large volume data sets with complex surface structures. This real time shadow casting is especially useful for volume data sets directly generated from model cell populations (as exemplified in Fig.8C) and thereby allows compensating this main deficiency of primary OpenGL visualization in Cellsys.

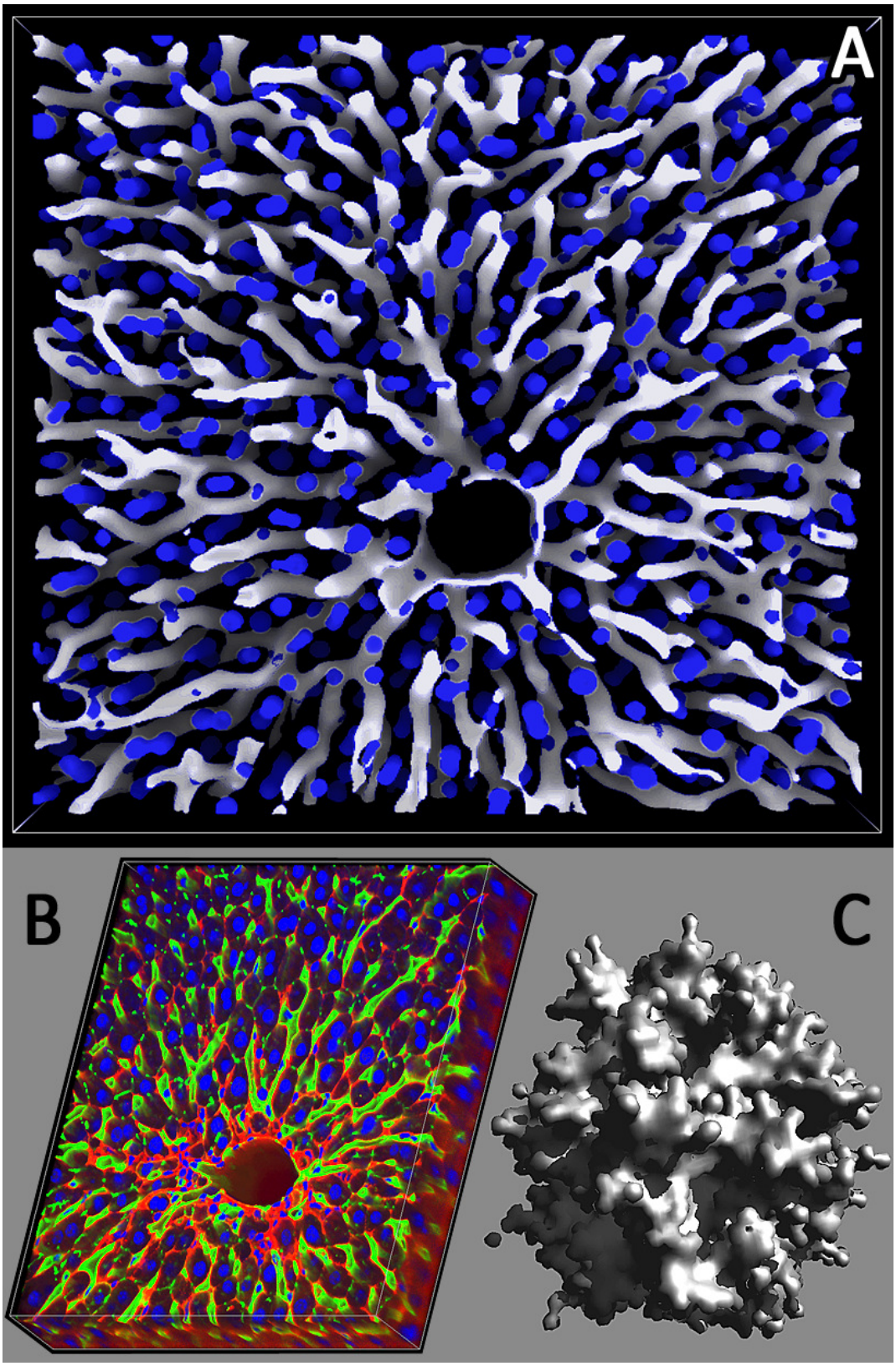


**Fig. 8: Examples of secondary volume visualization.**
A: Example for a processed volume data set revealing the sinusoidal blood vessels (white) and hepatocyte nuclei (blue) (PIVR). B: Corresponding multichannel data set as obtained by a confocal laser scanning microscope (VOXX). C: Isosurface of model tumor spheroid rendered with shadow casting (SPVOLREN). (details: A-B: section 4.3, C: section 3.6)

## 2.6. Discussion and Summary

In this chapter we illustrated the design and implementation of specialized software for the computational three-dimensional modeling, simulation, visualization and analysis of growing cell populations. The developed software allows the processing and analysis of experimental images in 2D and volumetric data sets in 3D. This facilitates a tight coupling of experiments and modeling that we consider an important precondition for tissue modeling in systems biology. We set up design principles and outlined a structured and hierarchical architecture that we consider exemplary for software engineered to implement computational models. Furthermore, we recommended concrete technologies for example regarding the software development methodology and the efficient implementation of 3D visualization.

There exist several software approaches that facilitate the modeling of cell populations. The most prominent are VirtualCell, E-Cell and CompuCell. VirtualCell is developed by NRCAM (National Resource for Cell Analysis and Modeling), USA [www, 11] and represents a remote user modeling and simulation environment. The software is implemented in Java and allows to create models, specify simulations and analyze the simulation results. Additionally a mathematical framework allows the stand-alone modeling of reaction-diffusion systems. E-Cell is developed at the Institute for Advanced Biosciences in Tsuruoka, Japan [www, 06] and represents a software platform for modeling, simulation and analysis of complex, heterogeneous and multi-scale systems. E-Cell also integrates numerical simulation algorithms and mathematical analysis methods. One of the most comprehensive approaches is CompuCell [www, 05], an open source software modeling environment that can be used for cellular modeling. CompuCell is based on the Cellular Potts Model (CPM) and includes a PDE solver. The software is developed at the Biocomplexity Institute, USA and provides a framework for the simulation of the development of multicellular populations and corresponding gene regulatory networks.

However, none of these existing approaches implement a computational lattice free single-cell-based model that can be directly coupled with experimental data. Cellsys is the first software that integrates computational modeling, real time visualization of model results and image processing into one framework. Additionally, all these components are entirely supported in two and three spatial dimensions. Thereby we are able to set up models directly from experimental data for example volumetric data sets in 3D obtained by laser scanning microscopy of *in vivo* tissue. This unique capability of Cellsys lays the foundation for patient-specific computational modeling that in the near future will likely be of direct medical relevance.

# 3. Modeling growing cell populations

## 3.1. Introduction

### 3.1.1. Cell biology

The cell is a basic structural and functional unit of all known organisms. It is the smallest unit that typically is considered living. Multicellular organisms such as plants, animals or humans are composed of a large number of cells (humans: $\approx 10^{14}$) that are often grouped in specialized tissues and organs [Maton et al., 1997].
In 1665 cells were first discovered by Robert Hooke who observed cork plant cells (Fig.9) and described strangely looking cellulae in his book *Micrographia* [Hooke, 1665]. Etymologically, the modern term cell was derived from the Latin cellula and means small room. Cornerstones of modern cell theory were first proposed in 1839 by Matthias Schleiden and Theodor Schwann [Schwann, 1839] who realized that cells are the basic units of both plants and animals. This was later complemented by Rudolph Virchow's theory *Omnis cellula e cellula* that suggested that every cell originates from another existing cell [Virchow, 1858]. Together, these ideas forever changed biological research.
Since then cell biology aspired deeper and deeper insights into the processes and mechanisms that define biological systems especially on a cellular level. Aided by

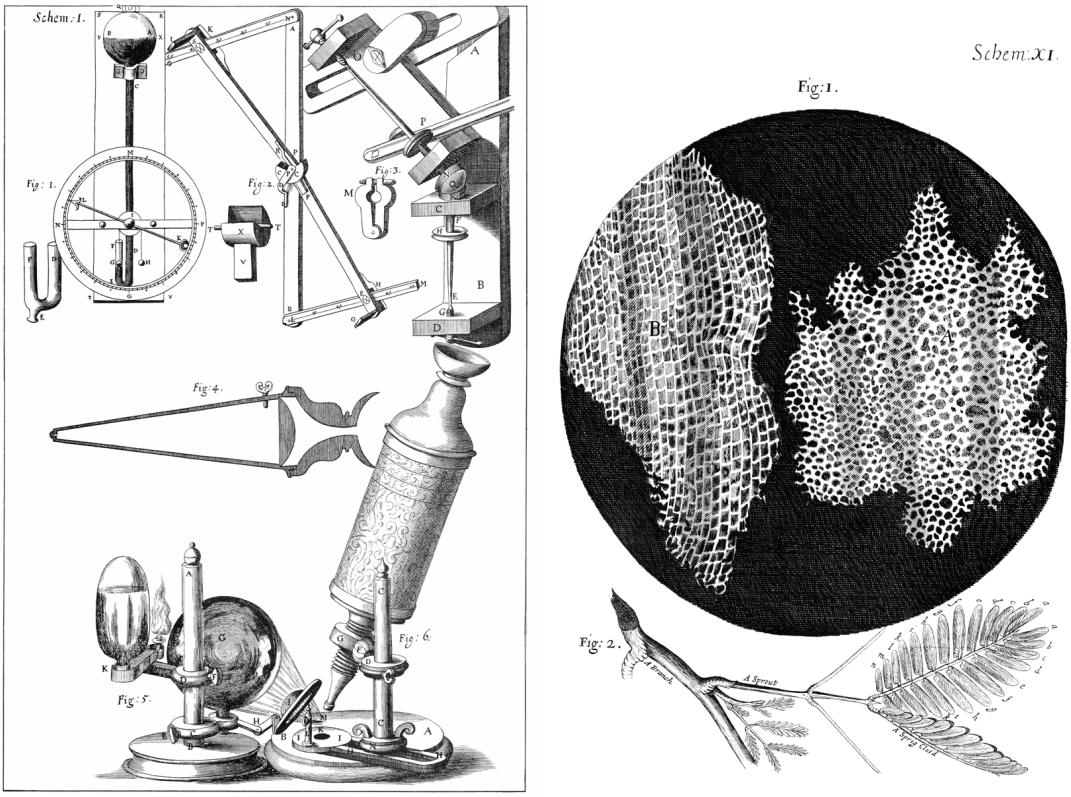


**Fig. 9: The origins of cell biology.**
Drawings of the microscope (left) that Robert Hooke used to first discover cells in cork plants (right). Both drawings are reproduced from his book *Micrographia* [Hooke, 1665].

technological advances as the invention of electron microscopy in 1931, since the 1950's, biological science has made immense progress. For example, the first continuous cell line was cultured by Otto Gey and co-workers in 1951. This significant breakthrough made it possible to maintain, grow, and manipulate cells outside of living organisms [Fedoroff, 1971].
Nowadays modern microscopes allow the observation of living cells down to molecular scales which tremendously increased knowledge of cellular and subcellular structures. The inner mechanisms of cellular movement, growth and replication are more and more elucidated which lays the foundation for effective therapies of diseases that root in cellular dysfunction. A large class of these diseases in which cells display uncontrolled growth and division is designated as cancer. For decades an immense scientific effort has targeted cancer in order to understand the disease and discover possible therapies. However, today cancer is still the leading cause of deaths [www, 16].
During the last decades biology and medicine have become more and more interdisciplinary. Collaborations with other traditional disciplines of science like mathematics, physics and computer science have led to new fields called mathematical biology, physical biology, bioinformatics and computational biology. Emergent new disciplines such as computer science facilitated high-throughput data analysis and spatio-temporal modeling that greatly fueled research in the life sciences.

### 3.1.2. Models

Since the first pioneering publications [Thomlinson & Gray, 1955] [Burton, 1966] [Iyer & Saksena, 1970] [Greenspan, 1976] on mathematical and computational models in cancer research, experimentalists became increasingly aware of the fascinating opportunities opened up by these models.
For example, current experimental approaches are often unable to distinguish between various possible mechanisms underlying important aspects of tumor development [Araujo & McElwain, 2004]. Accordingly, more and more models for multicellular morphogenesis and growth are considered to gain novel insights into this domain [Drasdo et al., 1995] [Byrne et al., 2001] [Chen et al., 2001] [Schwarz et al., 2002] [Byrne & Preziosi, 2003] [Bischofs & Schwarz, 2005] [Drasdo & Hoehme, 2005] [Drasdo et al., 2007] [Hoehme & Drasdo, 2009a].
The role of mechanics and physical interactions in the control of growth and pattern formation in multicellular systems is also attracting increasing interest [Huang & Ingber, 1999] [Salazar-Ciudad et al., 2003] [Tschumperlin, 2004] [Neagu et al., 2005] [Forgacs & Newman, 2005] [Hoehme & Drasdo, 2009b]. Here, models can contribute to distinguish between experimentally observed effects that can be explained purely by physical interactions and those effects that require active regulatory changes of cell behavior or cell properties.

3.1.2.1. Model validation

However, the possible benefit of model simulations largely depends on in how far they can be experimentally validated.
A couple of years ago the validation of predictions from computational models of multicellular systems was generally impossible. This situation is rapidly improving now. The experimental abilities to collect information on cell-biophysical, cell-biological and cell-kinetic properties have improved significantly in the last years. For example, cell proliferation (cell division) activity can be determined by the markers Ki-67 [Schiffer et al., 2003], BrdU or Thymidin [Alison & Sarraf, 1998], apoptosis (programmed cell death) by Tunnel assays [Schiffer et al., 2003] [Sayan et al., 2001] and diffusion constants of cells can be measured by tracking labeled cells [Mombach & Glazier, 1996]. The elastic modulus of cells can be determined by optical stretchers [Guck et al., 2001], atomic force microscopy (AFM) [Alcaraz et al., 2003] or acoustic microscopy [Laforsch et al., 2005] and the strength of cell-cell and cell/substrate adhesion can be measured by AFM [Chesla et al., 1998] [Zhang et al., 2004]. Confocal laser scanning microscopy (CLSM) [Claxton et al., 2008] which allows a direct, noninvasive, serial optical sectioning of intact, thick ($\leq 150\mu m$), living specimen with a minimum of sample preparation has become increasingly popular among biologists [Fellers & Davidson, 2007]. For example in this work (chapter 4.3) optical serial sections obtained by a confocal laser scanning microscope were used to reconstruct and analyze liver lobules in 3D [Hoehme et al., 2008] [Hoehme et al., 2009]. In addition, also traditional serial sections are used for the reconstruction of tissues in 3D [Levinthal & Ware, 1972] [Kay et al., 1996].
Together with recent cytometric analyses [Galle et al., 2006] these methods facilitate the quantification of the experimentally obtained spatio-temporal information from tissue morphotypes that is necessary for the comparison with the results of computational models. Moreover, the technical capabilities are crossing the borders between different disciplines. For example, methods that previously had only been used by cell-biologists such as cell-cycle labeling are now also used by other disciplines such as engineering science and for example are combined with measurements on the mechanical stress within cell layers to identify the active and passive properties within multicellular systems [Nelson et al., 2005] [Cheng et al., 2009]. This facilitates the construction of models for cells and tissue that vice versa help to further analyze biological experiments given these models properly represent the relevant parameters. On the level of individual cells these are for example cell-biological parameters such as the cycle time, the control of cell cycle passage, apoptosis (programmed cell death) and cell-biophysical parameters such as cell material parameters, cell shape, and the strength and specificity of cell-cell and cell-substrate adhesion.

3.1.2.2. Model classification

In general, models for growing cell populations can be subdivided in:

1. Phenomenological, macroscopic growth laws [Marusic et al., 1994]
2. Continuum models [Byrne & Preziosi, 2003] [Araujo & McElwain, 2004] [Byrne & Drasdo, 2009] [Christini et al., 2009]
3. Agent-based models
   3.1. Lattice-based [Moreira & Deutsch, 2002] [Alber et al., 2002]
   3.2. Lattice-free [Drasdo, 2003] [Drasdo & Hoehme, 2005] [Galle et al., 2006] [Hoehme et al., 2009]

Macroscopic growth laws and continuum models describe locally averaged quantities and thus are often well suited for large scale phenomena [Adam & Bellomo, 1997] [Araujo & McElwain, 2004] where spatial properties change smoothly over a length scale of several cell diameters [Byrne & Drasdo, 2009]. Continuum models include those that represent a tumor as an elastic continuum [Jones et al., 2000], a fluid [Byrne & Preziosi, 2003] or kinetic equations such as the Fisher-KPP equation (the logistic equation extended by a diffusion term) [Swanson et al., 2000] [Drasdo, 2005]. The Fisher-KPP equation predicts that the cell population size initially grows exponentially fast, and crosses over to a linear expansion of the population diameter at advanced stages. The exponential growth of the population size is accompanied by an expansion of its diameter $L$ according to $L \propto \sqrt{t}$ , which we believe is not appropriate for compact tumors in the initial growth phase (refer to section 3.5). Most of the continuum approaches are deterministic. These are neither able to cover the correct system behavior if stochastic fluctuations become important, nor to detect information that is reflected only in stochastic fluctuations.
As introduced in section 2.1, in agent-based models complex behavior of a system arises from actions and interactions of autonomous elements. Agent-based models, however, provide a higher spatial resolution and thus can be used in situations where tissue properties change on the scale of single cells. Most agent-based models can be characterized as either lattice-based or lattice-free models (for reviews, see [Moreira & Deutsch, 2002], [Alber, 2003], [Cickovski et al., 2005], [Merks & Glazier, 2005], [Anderson et al., 2007]).
In many lattice-based models, each lattice site can be occupied by at most one cell [Dormann & Deutsch, 2002], [Anderson, 2000], [Alarcon et al., 2004], [Drasdo, 2005], [Lee & Rieger, 2006], [Block et al., 2007]. These models are usually called cellular automaton (CA) models. Their dynamics is based on rules that are hoped to reflect the relevant physics. Cellular automata represent a fictitious oversimplified microworld [Rivet & Boon, 2001] and are based on a set of rules. Nevertheless, cellular automata can show a remarkable correspondence to real systems on mesoscopic length scales much larger than the cell diameter. However, effects such as cell size changes, and mechanical deformation or compression of cells or cell

aggregates are difficult to represent by a cellular automaton [Galle et al., 2009]. For example, recent measurements show that the elastic modulus of cancer cells is often smaller than those of normal cells [Guck et al., 2001], and therefore may be an important model parameter that cannot be represented in CA models in which each cell is represented by a single lattice site.
A second class of lattice-based models are those in which a cell may span many lattice sites [Graner & J.Glazier, 1992], [Stott et al., 1999], [Hogeweg, 2000]. This approach permits to mimic complex cell shapes, and the cell migration dynamics is modeled by a stochastic dynamics controlled by a generalized energy function.
A third class of lattice models is that in which a lattice site can be occupied by many cells [Radszuweit et al., 2009]. Such models are also rule-based but they permit to simulate growing cell populations up to the centimeter scale and thereby mimic growing *in vivo* tumors.
Lattice-free models are not confined by any lattice symmetry and thus are able to represent arbitrarily small displacements. Therefore, they are particularly appropriate to model the dynamics of cells in complex spatial architectures in which cell positions can gradually change and biomechanical influences may affect cell migration and proliferation. Therefore, lattice free models are well suited to describe spatio-temporal multicellular organization processes that are difficult to represent using a fixed lattice. Furthermore, intracellular processes may easily be integrated into single cell-based models [Hogeweg, 2000] [Alarcon et al., 2004].
Within the class of lattice-free models, cells have been parameterized by measurable cell-biophysical and cell-biological parameters and approximated by quasi-spherical particles [Drasdo, 2003] [Drasdo & Hoehme, 2005] [Galle et al., 2006] [Hoehme & Drasdo, 2009a], deformable ellipsoids [Palsson & Othmer, 2000], Voronoi polygons [Meineke et al., 2001], or, more recently, networks of spheres in a so called “multi-center approach” [Newman, 2005].

Different from physical particles, cells can change their parameters such as the cycle time, the micro-motility and the material parameters. As long as the rules that underlie these parameter changes, e.g. by cell regulation or differentiation have not been fully understood, the predictive power of models of multicellular systems remains limited. Nevertheless, as we will show below, even models that assume static parameters i.e., that do not include the regulatory machinery that controls the cell parameters can already explain many experimental observations. Moreover, points where the predictions of model simulations and experimentally observed behavior start to diverge may demarcate active changes of cell behavior or cell properties by regulation or differentiation. The ambition to attune model and experimental observations could iteratively stimulate informative experiments and model refinements that together may shed light on the studied processes. In chapter 3 we consider different experimental situations to mimic aspects of tumor growth. The simulation results will be compared directly to data. In chapter 4 we use a similar

iterative approach to elucidate organization processes of liver regeneration in close iteration with experiments.

In the following sections we elaborate the lattice-free model that was used in this thesis to study the growth of multicellular populations and the mechanisms of liver regeneration in detail. Therefore we introduce relevant biological aspects together with their representation in the model. The main idea for the model has been introduced in [Drasdo et al., 1995] and has been advanced in [Drasdo & Hoehme, 2003] [Drasdo & Hoehme, 2005], [Hoehme & Drasdo, 2009a] and [Hoehme & Drasdo, 2009b].

## 3.2. Basic model

### 3.2.1. The cell

The cell is the smallest structural and functional unit of a tissue [Alberts et al., 2008] and thus also represents the basic unit in our lattice-free agent-based model. Cells have different abilities and, to a certain degree, are self-contained and self-maintaining. They can migrate, reproduce by cell division, respond to external and internal stimuli such as temperature, nutrient concentrations, pH levels or stress and are capable of metabolism. Cells are able to extract and use chemical energy stored in organic molecules. This energy is released and then used in metabolic pathways. Each cell stores a set of instructions for carrying out these activities. A typical cell size is 10 µm (bacteria: 1-5 µm, plant cells: 100µm) and a typical cell mass is 1 ng. All intracellular components are contained within a cell surface membrane that consists of a lipid bilayer with proteins embedded in it.

There are two basic types of cells: prokaryotic and eukaryotic. Prokaryotic cells are relatively simple since they lack a nuclear envelope, a cell nucleus and most of the intracellular organelles and structures that are found in eukaryotic cells. They are often found in unicellular organisms for example bacteria and archaea.

Almost all multicellular organisms, however, are composed of eukaryotic cells which include a variety of complex internal membrane-bound compartments, termed organelles, in which specific metabolic activities take place. Eukaryotic cells also have a cytoskeleton composed of microtubules, microfilaments, and intermediate filaments that play an important role in defining the cell's shape. Another major difference to prokaryotic cells is the presence of a cell nucleus, a membrane-delineated compartment that envelops the eukaryotic cell's DNA that is divided into several linear bundles called chromosomes. Fig.10 shows prokaryotic and eukaryotic cells as schematic illustration and under the microscope.

In the following we only consider eukaryotic cells and limit ourselves to a few basic, yet fundamental, structural and functional aspects. A detailed introduction to the broad fields of cell and molecular biology can for example be found in the monograph “Molecular Biology of the Cell” [Alberts et al., 2008].

The basic idea of the model presented in this work is to approximate complex cells by isotropic, elastic and adhesive objects of limited compressibility and deformability. These model cells are capable of active migration, growth and division and are defined by cell-kinetic, biophysical and cell-biological parameters that can be experimentally measured. Model cells can interact with each other and respond to changes in their environment. This especially includes biomechanical influences that, as we show in this work, play an important role in morphogenesis and growth kinetics of multicellular populations.

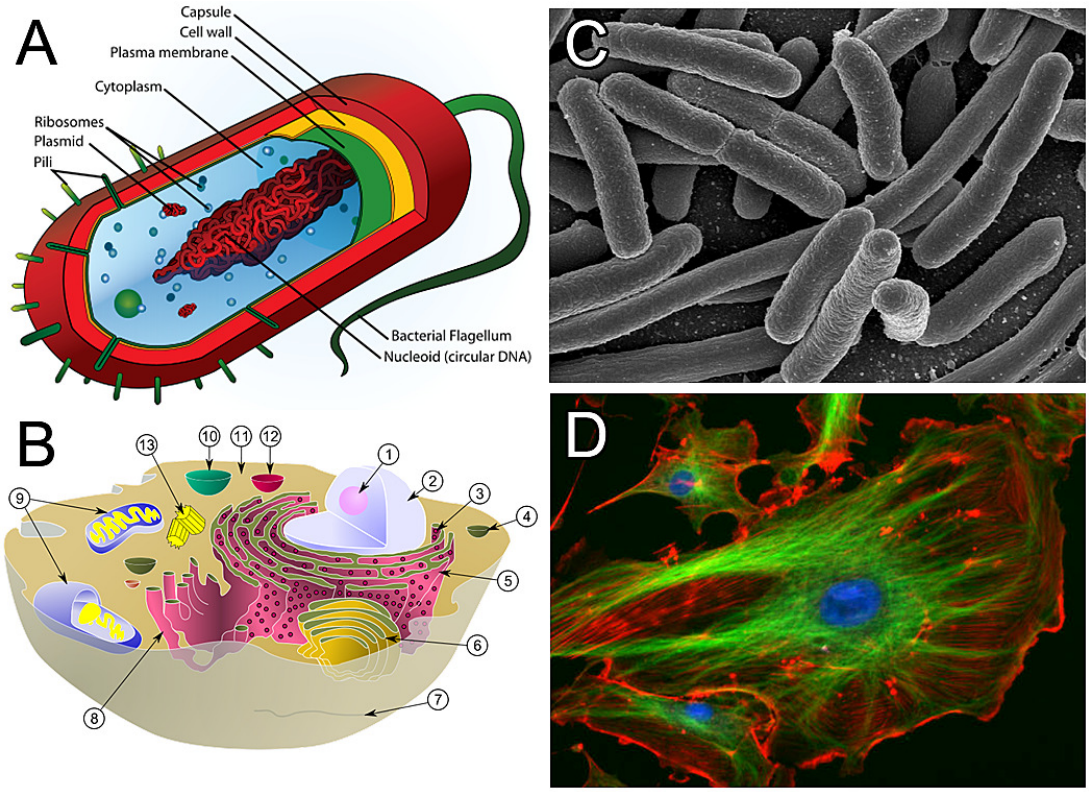


**Fig. 10: Procaryotic and eukaryotic cells.**
A: Schematic illustration of a typical procaryotic cell. B: Illustration of a typical eukaryotyic cell. Organelles are labelled as follows: (1) Nucleolus, (2) Nucleus, (3) Ribosome, (4) Vesicle, (5) Rough endoplasmic reticulum, (6) Golgi apparatus, (7) Cytoskeleton, (8) Smooth endoplasmic reticulum, (9) Mitochondrion, (10) Vacuole, (11) Cytosol, (12) Lysosome and (13) Centriole. C: Scaning electron micrograph of a procaryotic cell (Escherichia coli) grown in culture. D: Example of an eukaryotic (endothelial) cell under a confocal laser scanning microscope. Cell nuclei are stained with DAPI (blue), microtubules are marked by an antibody (green) and actin microfilaments are labelled with phalloidin (red). Images from Wikimedia Commons (public domain).

For example, experiments suggest that cells may grow and divide faster if situated at positions of large local tissue curvature. This has been experimentally observed for cells growing on flat substrates [Nelson et al., 2005] and in epithelial cell layers for example in the lung [Ingber, 2005] [Ingber, 2006] or the pancreas [Horb & Slack, 2000]. Cells may also sense mechanical stress to adjust their growth rate to the growth rate of other cells in a tissue sheet [Shraiman, 2005]. There are different ways in which a cell can control its physical properties and biomechanically communicate with its environment depending on its state of differentiation, its type and on the properties of its environment [Huang & Ingber, 1999]. For example, a cell can reorganize its cytoskeleton and thereby change its shape and mechanical rigidity. Furthermore, cells can control the number, placing and specificity of adhesion molecules which it uses to anchor in a substrate or to form contacts to its neighbor cells thereby controlling the strength and specificity of its substrate and neighbor-cell contacts [Lodish et al., 2004].

## 3.2.2. Cell growth and division

Cells reproduce by dividing into two daughter cells. This process of cell division during which cells pass their genetic heritage to the next generation is embedded into an ordered sequence of events designated as “the cell cycle”. In eukaryotic cells, a complex network of regulatory proteins governs the progression of the cell in the cell cycle. The essence of this system is a series of biochemical switches that respond to various signals from inside and outside the cell and control the main events of the cell cycle.

The cell cycle consists of four distinct phases termed $G_1$-phase, S-phase, $G_2$-phase (together designated as interphase) and M-phase. Fig.11 illustrates the succession of these phases. In $G_1$-phase (short for gap-1-phase) cells primarily increase their volume and synthesize various enzymes that are required for DNA replication in S-phase. Additionally, $G_1$-phase includes a restriction point (also designated as $G_1$ checkpoint) that further regulates cell cycle progression. For example the restriction point ensures that the cell is large enough for division and that enough nutrients for the daughter cells are available in the cells environment. At this point in the cell cycle cells can enter a resting state known as $G_0$ and remain there permanently or for long time periods before resuming cell cycle progression. A cell in $G_0$ is often called “quiescent”.

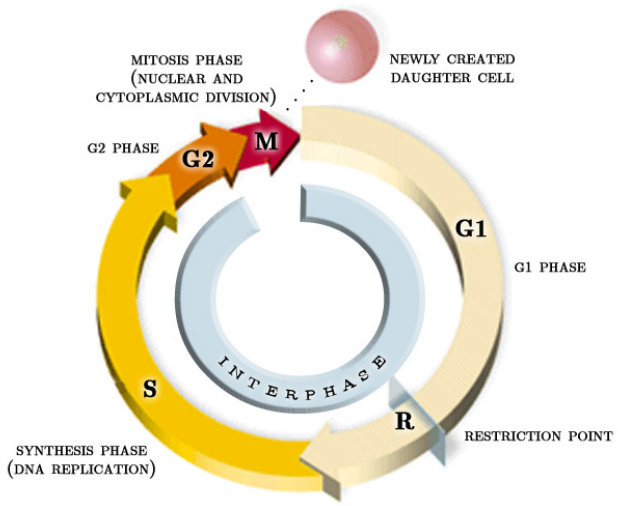


**Fig. 11: The cell-cycle.**
Illustration of the succession of the four distinct phases of the cell cycle and the restriction point.

DNA replication takes place in the subsequent S-phase (short for synthesis-phase) wherein cells duplicate all their chromosomes. Damage to the DNA often takes place during this phase. Thus after completion of replication DNA repair is initiated.

The cell then enters $G_2$-phase which mainly involves the production of microtubules, which are required during mitosis.

The following relatively brief M-phase (short for mitosis-phase) includes karyokinesis (the division of the cell nucleus) and cytokinesis (cytoplasmic division). Furthermore, the M-phase consists of several distinct sub-phases, known as prophase, metaphase, anaphase and telophase.

In prophase the chromosomes condense, the centrioles form and move towards the cell poles, the nuclear membrane dissolves and the mitotic spindle forms. In metaphase the centrioles complete their movement to the cell poles and the

chromosomes line up at the cell equator. In anaphase the spindles begin to shorten which pulls apart the sister chromatids thereby ensuring that each daughter cell includes an identical set of chromosomes. In telophase the chromosomes decondense and the nuclear envelope forms. In this phase cytokinesis completes and thereby creates two distinct daughter cells. A more detailed description of the cell cycle can be found in [Alberts et al., 2008].

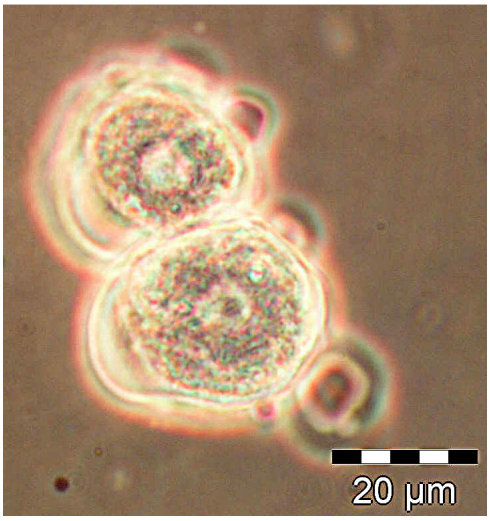


**Fig. 12: Typical shape of isolated cells**
(Image by [Hengstler, 2007]).

In our model we abstract from most of the details of the cell cycle and the process of cell division and focus on the biomechanical aspects of cell growth and division. Since isolated cells in cultures or suspensions often have a spherical shape [Drubin & Nelson, 1996] (Fig.12) we assume each model cell after cell division to be spherical with radius $R_0$. During cell cycle and especially in the $G_1$ and $G_2$-phases cells deform and grow by biosynthetic activity [Saucedo & Edgar, 2002].

We implement the increase of cellular volume and the corresponding deformations during cell cycle by two distinct model variants.

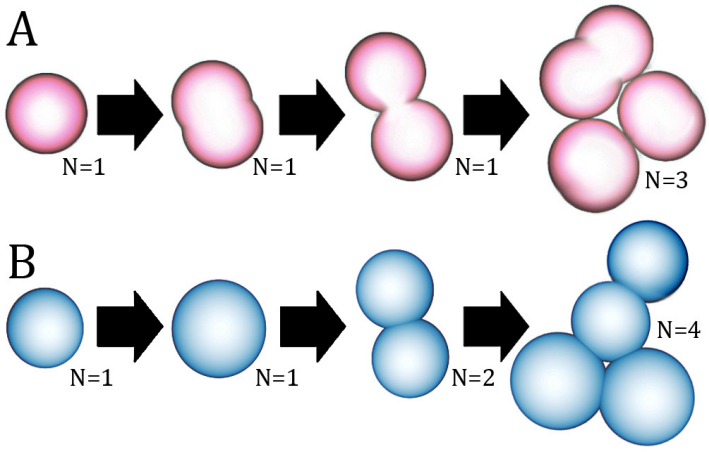


**Fig. 13: Model cells during growth and division**
either A: deform into a dumb-bell shape or B: grow maintaining a spherical shape (also see Supporting video 1).

In variant 1 every model cell consists of two overlapping spherical components each of radius $R_0$ (Fig.13A). During cell cycle, a growing model cell $i$ deforms into an axis-symmetrical dumb-bell by increasing the distance $d_i$ of its spherical components in small steps $\Delta d \ll R_0$. The current volume $V_i$ of model cell $i$ can be calculated by:

$$V_i(d_i) = 2\left(\frac{4}{3}\pi R_0^3 - \frac{\pi \cdot h_i^2}{3}(3R_0 - h_i)\right) \tag{4}$$

with $h_i = R_0 - 0.5 \cdot d_i$. Once $d_i \geq 2R_0$, the model cell divides into two daughter cells. Directly after cell division $d_i = 0$.

In the alternative model variant 2 each cell consists of only one spherical component that directly after cell division has the radius $R_0$. During cell cycle we increase the radius $R_i$ of a model cell $i$ in small steps $\Delta R \ll R_0$. In this case the volume $V_i$ of model cell $i$ can be calculated by:

$$V_i(R_i) = \frac{4}{3}\pi R_i^3 \tag{5}$$

During growth the cell remains spherical until it has doubled its initial volume ($V^{DIV} = 2 \cdot V(R_0), R^{DIV} \approx 1.26 \cdot R_0$). Then the model cell divides into two daughter cells of radius $R_0$ that immediately after division are arranged as a dumb-bell that occupies the same volume as the mother cell directly before division (Fig.13B). Supporting video 1 illustrates the process of cell division in the model.

Both division algorithms were originally introduced in [Drasdo et al., 1995]. In agreement with the experimental observations [Fidorra et al., 1981], we mimic a linear increase of cell volume during the passage of a cell through the cell cycle by appropriately choosing (A) $\Delta d(R_i)$ and (B) $\Delta R(R_i)$.

### 3.2.3. Cell-cell interactions

During the growth of a multicellular population, cell-cell interactions play an important role for tissue organization and the development of functions. These interactions include the communication between cells by complex biochemical signals and biomechanical interactions between adjacent cells. Biomechanical interactions often significantly stress cell membranes and especially the cytoskeleton. The term cytoskeleton was first introduced in 1931 by the embryologist Paul Wintrebert [Wintrebert, 1931] and designates a dynamic, three-dimensional structure that is contained within the cytoplasm [Frixione, 2000]. In eukaryotic cells, the cytoskeleton is composed of microfilaments, microtubules and intermediate filaments (see Fig.10D). The cytoskeleton maintains mechanical stability and shape of the cell and additionally plays an important role in cellular movement, intracellular transport and cell division.

Cells in contact can form adhesive bonds that anchor in the cytoskeleton. With decreasing distance between cells, for example upon compression, the contact area between them increases and with it the number of adhesive bonds which typically results in an increasing attractive interaction. On the other hand, if cells in isolation are spherical, an increase of the contact area is accompanied by an increasing deformation which results in a repulsive interaction. Furthermore cells under

physiological conditions have only a moderate compressibility [Mahaffy et al., 2000].
The first contact models appeared in the 1930s in surface physics and chemistry [Bradley, 1932] [Derjaguin, 1934]. These pioneering publications still influence current research in this area [Barthel, 2008]. In this work we used two alternative contact models:

3.2.3.1 Extended Hertz model

In a number of cases, we model the combination of attractive and repulsive interactions by a modified Hertzian contact model. We extended the classical Hertz-model [Hertz, 1882] [Landau, 1975] by a term that takes into account cell-cell adhesion [Galle et al., 2005] [Schaller & Meyer-Hermann, 2005]. Thereby we are able to describe the contact behavior of two elastic and adhesive objects with a circular contact area (Fig.14). The Hertz model describes the potential $V_{ij}^{HER}$ of any two model cells of radius $R_i$ and $R_j$ by:

$$V_{ij}^{HER} = (R_i + R_j - d_{ij}^{HER})^{5/2} \frac{1}{5\tilde{E}_{ij}} \sqrt{\frac{R_i R_j}{R_i + R_j}} + \varepsilon_k \tag{6}$$

The first term of the equation summarizes the repulsive interaction while $\varepsilon_k$ adds the contribution from the adhesive interaction. $d_{ij}^{HER}$ is the distance between the centers of model cells *i* and *j* and the composite Young's modulus $\tilde{E}_{ij}$ is related to the elastic moduli $E_i$, $E_j$ and the Poisson's ratios $\nu_i$, $\nu_j$ of the model cells *i* and *j* by:

$$\tilde{E}_{ij}^{-1} = \frac{3}{4}\left( \frac{1-\nu_i^2}{E_i} + \frac{1-\nu_j^2}{E_j} \right) \tag{7}$$

This relies on the fact that a homogeneous, isotropic elastic body is completely characterized by two independent material constants, for example its Young modulus *E* and its Poisson ratio $\nu$. Due to the limited compressibility of cells, the Poisson ratios are chosen close to 0.5 [Alcaraz et al., 2003]. The adhesive contribution is approximated by:

$$\varepsilon_k \approx \varsigma_m W_s A_{ij}^{HER} \tag{8}$$

where $\varsigma_m$ is the density of surface adhesion molecules in the contact area and $W_s$ is the energy of a single bond. $\varsigma_m \approx 10^{15} m^{-2}$ [Chesla et al., 1998] [Piper et al., 1998] and

$W_s \approx 25 k_B T$ (T: temperature, $k_B$: Boltzmann constant). $k_B \approx 1.38 \cdot 10^{-23} JK^{-1}$. $A_{ij}^{HER}$ is the contact area between cell *i* and *j* that can be calculated by:

$$A_{ij}^{HER} = \pi \left( \frac{R_i R_j}{R_i + R_j} \right) \cdot \left( R_i + R_j - d_{ij}^{HER} \right) \tag{9}$$

Thereby the contribution of the adhesive interaction $\varepsilon_k$ is proportional to the surface density of receptor-ligand bonds and the receptor-ligand interaction energy [Moy et al., 1994].

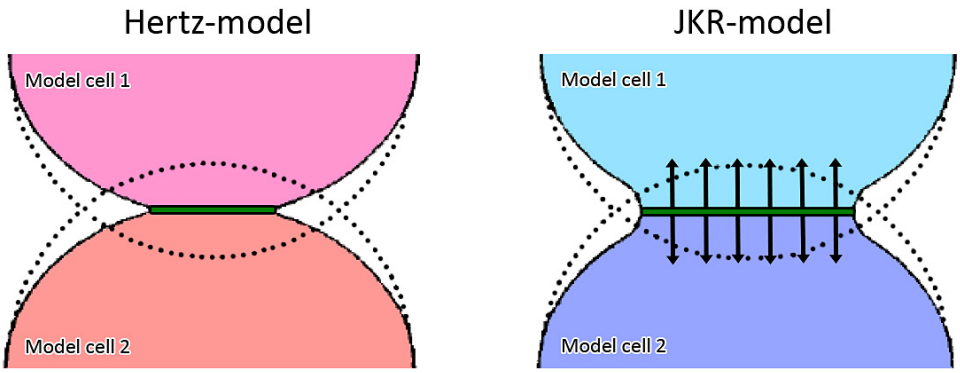


**Fig. 14: Deformations due to cell-cell interactions.**
Note the significant difference of Hertz- (left) and JKR-model (right) considering model cell shape and contact area (green) (image based on illustrations in [Johnson, 1985])

The interaction force results from the negative gradient of the potential energy:

$$\underline{F}_{ij}^{HER} = -\left( \frac{\partial V_{ij}^{HER}}{\partial d_{ij}^{HER}} \right) \left( \frac{d(d_{ij}^{HER})}{dx}, \frac{d(d_{ij}^{HER})}{dy}, \frac{d(d_{ij}^{HER})}{dz} \right) \tag{10}$$

3.2.3.2. Johnson-Kendall-Roberts model

However, in some situations, for example for cell-detachment, the extended Hertz-model is not appropriate. An improved theory was published by [Johnson et al., 1971]. The proposed Johnson-Kendall-Roberts (JKR) model directly includes adhesion and correlates the contact area to the elastic material properties and the adhesion strength [Carpick et al., 1999]. The JKR-model has been validated for S180-cells [Chu et al., 2005] and has independently been proposed to model cells in [Drasdo & Hoehme, 2005]. The JKR-model includes a negative loading regime that takes into account the hysteresis effect that occurs due to cell elongation if cells are

pulled apart (Fig.14). Here, we calculate the interaction force $F_{ij}^{JKR} \equiv \left| \underline{F}_{ij}^{JKR}(d_{ij}^{JKR}) \right|$ numerically from the implicit equation:

$$\delta = \frac{a^2}{\tilde{R}_{ij}} - \sqrt{\frac{16\pi\hat{\gamma}a}{3\tilde{E}_{ij}}} \tag{11}$$

whereby the contact radius $a$ is determined by:

$$a^3 = \frac{2\tilde{R}_{ij}}{\tilde{E}_{ij}} \left[ F_{ij}^{JKR} + 3\pi\hat{\gamma}\tilde{R}_{ij} + \sqrt{6\pi\hat{\gamma}\tilde{R}_{ij}F_{ij}^{JKR} + \left(3\pi\hat{\gamma}\tilde{R}_{ij}\right)^2} \right] \tag{12}$$

The composite radius $\tilde{R}_{ij}^{-1}$ is given by $\tilde{R}_{ij}^{-1} = R_i^{-1} + R_j^{-1}$, the distance between model cell $i$ and $j$ is given by $d_{ij}^{JKR} = R_i + R_j - \delta$ where $\delta = \delta_i + \delta_j$ is the sum of the deformation along the axis between the centers of these cells. $\tilde{E}_{ij}$ is the composite Young modulus as defined in the previous section and we approximate $\tilde{\gamma} \approx \varsigma_m W_s$. Eqn.12 has to be solved implicitly to derive $a(F_{ij}^{JKR})$ .The value of $a$ is then inserted into Eqn.11 to give $\delta(a)$ and, by $d_{ij}^{JKR} = R_i + R_j - \delta$, $d_{ij}^{JKR}(a)$. Plotting $F_{ij}^{JKR}$ vs. $d_{ij}^{JKR}$ yields $F_{ij}^{JKR}(d_{ij}^{JKR})$ which is not amendable to an explicit solution but can be easily fitted by a polynomial. We use a polynomial of degree three:

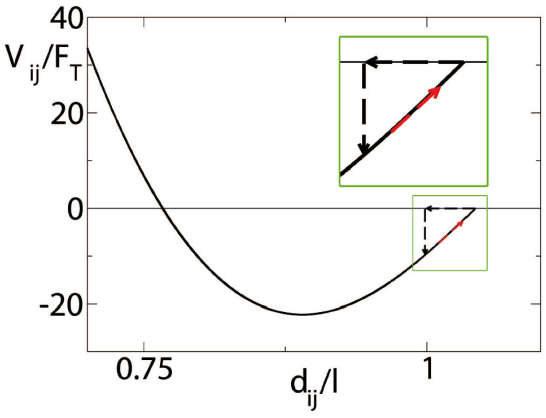


**Fig. 15: Scaled interaction energy** $V_{ij} / F_T$ vs. scaled distance $d_{ij}$ for two interacting spheroidal cells $i, j$ according to the JKR-model. Note the hysteresis behavior (magnification).

$$F_{ij}^{JKR}(d_{ij}^{JKR}) \approx a_3(d_{ij}^{JKR})^3 + a_2(d_{ij}^{JKR})^2 + a_1(d_{ij}^{JKR}) + a_0 \tag{13}$$

The force vector denoting the force of cell $j$ on cell $i$ results from

$$\underline{F}_{ij}^{JKR} = F_{ij}^{JKR}(d_{ij}^{JKR}) \frac{\underline{r}_i - \underline{r}_j}{|\underline{r}_i - \underline{r}_j|} \tag{14}$$

From this, the potential $V_{ij}^{JKR}$ (Fig.15) can again be investigated by:

$$\underline{F}_{ij}^{JKR} = -\left(\frac{\partial V_{ij}^{JKR}}{\partial d_{ij}^{JKR}}\right)\left(\frac{d(d_{ij}^{JKR})}{dx}, \frac{d(d_{ij}^{JKR})}{dy}, \frac{d(d_{ij}^{JKR})}{dz}\right) \tag{15}$$

In comparison to the extended Hertz-model, the most important advantage of the JKR-model is the appropriate integration of the hysteresis effect by the negative loading regime which includes a negative deformation. When two spheres of radius $R_0$ approach each other they spontaneously form a contact area of finite size at a distance $d_{con} = 2R_0$ while at $\lim_{\varepsilon \to \infty}(2R_0 + \varepsilon)$ they had no contact. If later they are pulled apart they still have contact at distance $d_{ij}^{JKR} \geq d_{con}$ and exert a pull-off force that models hysteresis. This leads to a difference in situations in which cell detachment becomes important as we show in section 3.4 where we consider a piling up of monolayers. Note also, that for $\zeta_m$=0 the JKR-model results in the classical Hertz model without adhesion.

### 3.2.4. Cell migration

Cell migration is a key process in the development and maintenance of every organism. In multicellular tissues individual cells employ a variety of mechanisms to move through spaces in the extracellular matrix and over the surfaces of other cells [Horwitz & Parsons, 1999]. In general, cell migration is a dynamic and cyclical process that, in most situations, is initiated by external signals (for example by chemotaxis related molecules that act as chemoattractants or chemorepellents). These signals are sensed and communicated into the cell interior by specialized receptor proteins in the cell membrane stimulating the cell to extend protrusions by polymerizing actin. These protrusions seek out new terrain and in the direction into which the cell intends to move. Once the direction for movement is established, the machinery for enabling movement assembles. With regard to the direction of the migration, adhesive complexes that are needed for traction accumulate at the front of the protrusion, tethering the protrusion to the substratum. Actomyosin filaments contract at the front of the cell and pull the cell towards the protrusion. Finally, the adhesive connections in the rear of the cell are released and retraction of the tail completes the cycle [Webb et al., 2005]. The control of this complex process is based on many molecules that for example serve to distinguish the front of a cell from its rear and whose actions are carefully timed [Lauffenburger & Horwitz, 1996].
The inability of cells to migrate or the pathological migration of cells to inappropriate locations can result in life threatening consequences for example congenital defects prominent in the brain. Pathological cell migration also contributes to widespread diseases including vascular disease, chronic inflammatory diseases, and tumor formation and metastasis [Horwitz & Webb, 2003]. Furthermore,

cell migration is central to homeostatic processes for example an effective immune response or the repair of injured tissues.
In the absence of chemotactic signals, isolated cells in suspension or culture medium have been observed to perform an active random-walk-like movement [Schienbein et al., 1994] [Mombach & Glazier, 1996]. Accordingly, in our model we characterize the observed random-walk-like movement of isolated cells by the cell diffusion constant $D_0 \approx 10^{-12} cm^2 s^{-1}$. More motile cells are assumed to have a larger $D_0$. Hence $D_0$ quantifies the micromotility of model cells.
While in mechanical contact with other cells, proliferating cells exert a pressure on their neighbors. The neighboring cells try to escape this pressure by moving against the friction caused by the other neighbor cells and extracellular material for example the extracellular matrix [Rosen & Misfeldt, 1980]. The movement could be partly passive, due to pushing, and active [Nelson et al., 2005], if cells migrate into the direction into which they escape the mechanical stimulus. We model the complex dynamics of cell migration as a friction-dominated over-damped motion with a stochastic contribution. In order to simplify the biomechanical interactions we leave aside the complex deformations of the cytoskeleton described above and model cell migration by Langevin-type stochastic equations of motion for each cell.

The velocity of cell *i* is determined by:

$$\zeta \underline{v}_i(t) = \sum_j \left( \zeta_{ij}^C (\underline{v}_j(t) - \underline{v}_i(t)) + \underline{F}_{ij}^C \right) + \sqrt{2\zeta_i^2 D^C} \cdot \underline{\eta}_i(t) \tag{16}$$

where $\underline{v}_i(t)$ is the velocity of cell *i*, $\zeta_{ij}^C$ denotes the friction between cells *i* and *j*, $\underline{F}_{ij}^C$ denotes the JKR or extended Hertz – force (refer to section 3.2.3) between cells *i* and *j*. $\zeta_i$ denotes an effective friction between cell *i* and the extracellular matrix. $\underline{\eta}_i(t)$ is an uncorrelated noise term with amplitude:

$$\left\langle \eta_{in}(t) \eta_{jm}(t') \right\rangle = \delta_{ij} \delta_{mn} \delta(t - t') \tag{17}$$

whereby *i* ,*j* denote different cells, and *n*,*m* ϵ (x, y, z) denote the coordinates. In general, cells can actively control the noise amplitude *A*. However, the size of *A* has not been found to have a significant effect on the observed dynamics. Besides the noise term, the driving forces in this approach emerge from dividing cells. During cell division (refer to section 3.2.2) cells increase their volume and thereby exert biomechanical forces to cells in their neighborhood which are compressed and deformed and migrate in order to escape these forces.

### 3.2.5. Cell death

In the human body, every day more than 50 million cells die [Zhivotovsky, 2004]. In almost all cases, cells die by either one of only two distinct mechanisms [Kanduc et al., 2002] [Feinstein-Rotkopf & Arama, 2009].
On the one hand cells may die by necrosis which designates a pathological process that occurs if cells are exposed to serious physical or chemical insult. On the other hand cells may die by apoptosis which is often also termed "programmed cell death". In contrast to necrosis, apoptosis is a physiological process by which cells are eliminated for example during development and other normal biological processes. Apoptosis designates a well ordered and organized sequence of morphological

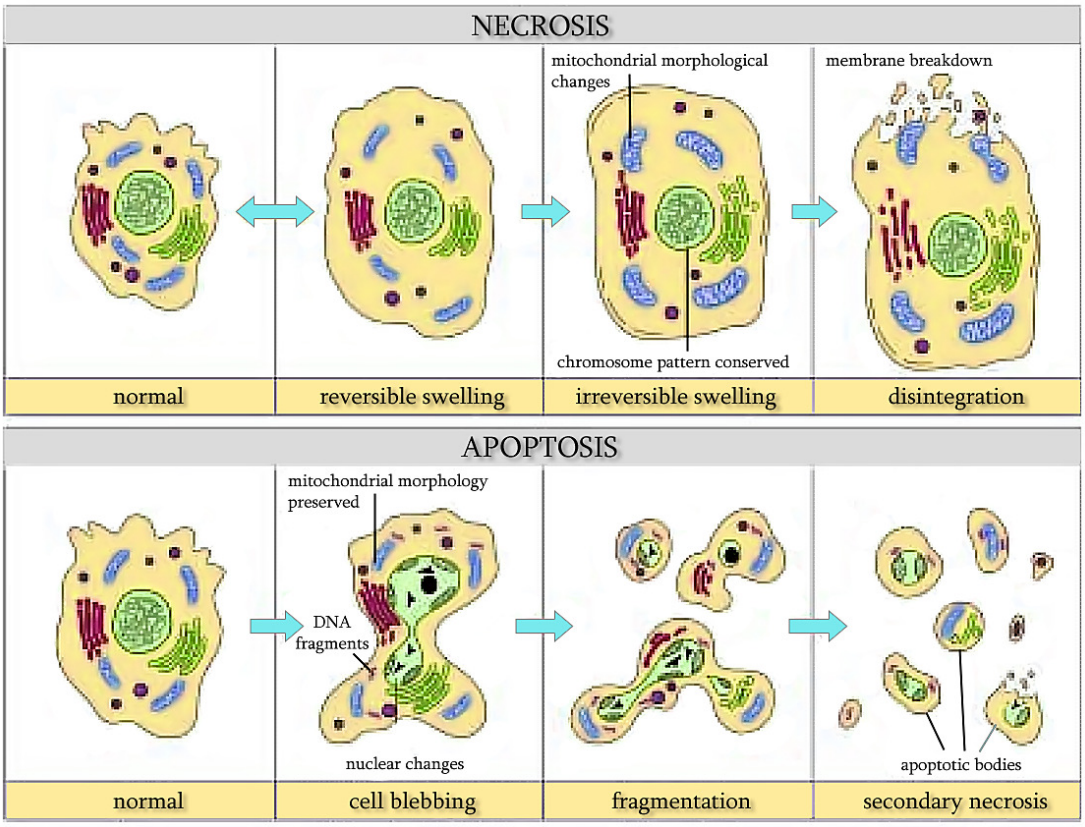


**Fig. 16: Morphological features of cell death**
(Images from [Rode et al., 2004])

events. In addition to apoptosis and necrosis, several further forms of cell death, for example autophagic cell death [Kourtis & Tavernarakis, 2009] or cornification [Lippens et al., 2009] are known.
The major morphological differences between apoptosis and necrosis are summarized in Fig.16. Necrosis typically occurs if cells are exposed to an extreme variance of normal physiological conditions that potentially damage the plasma membrane for example infections, toxins, lack of oxygen, radiation or trauma.

Necrosis commences with an impairment of the cell's ability to maintain homeostasis which leads to an influx of water and extracellular ions. This results in swelling of the intracellular organelles and the entire cell that, if not reversed, leads to cell rupture and disintegration (cell lysis). Due to the breakdown of the plasma membrane, cytoplasmic contents are released into extracellular fluid. By this reason, necrosis of cells *in vivo* is often accompanied by extensive damage to adjacent tissue.
Apoptosis, in contrast, is a variant of cellular death that occurs under physiological conditions. Cells that are no longer required undergo apoptosis by activating strictly regulated intracellular machinery that orchestrates their suicide. Apoptotic cells show characteristic morphological and biochemical features for example chromatin aggregation, nuclear and cytoplasmic condensation and the formation of membrane bound vesicles also termed apoptotic bodies. In the final phase of apoptosis, these apoptotic bodies as well as the remaining cell fragments swell and lyse in a process termed "secondary necrosis" (refer to Fig.16). In general cells decide to undergo apoptosis when cellular signals that normally indicate the need for continued survival withdraw or when signals that indicate the need for apoptosis arise [Lauffenburger & Horwitz, 1996]. Apoptosis may also occur if a cell is irreparably damaged as a regulatory mechanism intrinsically embedded in the cells.
In contrast to necrosis, during apoptosis cellular contents are not released and therefore inflammation typically does not occur. Apoptosis is essential for the development and maintenance of multicellular organisms [Orrenius et al., 2003]. It plays a vital role in embryogenesis and for example eliminates cells infected with viruses or cells with DNA damage. Interestingly, failure of apoptosis is also believed to be a major factor in the cell kinetics of tumors, both growing and regressing [Rode et al., 2004].
In our computer simulations we model necrosis and apoptosis using state transitions. Model cells undergo necrosis if the pressure that is exerted on them exceeds a specific pressure threshold $p^{NECR}$. Since we do not calculate the volume of the cells explicitly, and since the movement of cells is strongly friction-limited so that calculations of the pressure by the root-mean-square-velocity (as used for gases) are not suitable, we define as an (approximate) measure for the pressure $p_i$ that is exerted on model cell *i* by all adjacent cells *j* within interaction range by:

$$p_i = -\sum_j \left( \frac{\tilde{F}_{ij}}{A_{ij}} \right) \tag{18}$$

where $A_{ij}$ is the contact area between cells *i* and *j* and $\tilde{F}_{ij}$ is the force in the direction of the normal vector of the surface of cell *i* (in case of adhesion: $\tilde{F}_{ij} < 0$, in case of repulsive interaction $\tilde{F}_{ij} > 0$ and in equilibrium distance $\tilde{F}_{ij} = 0$). If $p_i > p^{NECR}$, model cells change their internal state from proliferating or quiescent (further

explained in the next section) to necrotic. Under normal conditions, necrotic cells are physically removed from the simulation which models cell lysis. In section 3.5 we additionally introduce state transitions that are based on the local nutrient concentration. In this case cells may become necrotic due to a lack of nutrient.

## 3.3. Monolayer cultures

A commonly used cell culturing technique to study growing cell populations *in vitro* is the monolayer culture. In a monolayer culture cells are seeded to grow in a Petri dish coated with proteins and liquid media containing specified quantities of small molecules such as salts, glucose, amino acids, and vitamins, and furthermore growth factors and transferrin, which carries iron into cells [Eagle, 1955] [Ham, 1965] [Hayashi & Sato, 1976] [Sato et al., 1982]. Monolayers mainly form two-dimensional colonies [Bru et al., 1998] [Bru et al., 2003] and thus are easy to manipulate and easy to observe [Werner & Noé, 1993] [Castell & Gómez-Lechón, 2009]. Fig.17A shows a typical example of a monolayer culture.

Despite recent advances in cell culturing techniques (see for example section 3.5), two-dimensional *in vitro* cell cultures remain an important experimental tool in understanding and analyzing the mechanisms involved in the growth dynamics of cell populations. Treatment strategies for a number of diseases may be tested *in vitro* with respect to their efficiency and their toxicity before being applied to *in vivo* systems. This in particular involves drug testing, radiation, and chemotherapy strategies against cancer [Santini et al., 1999].

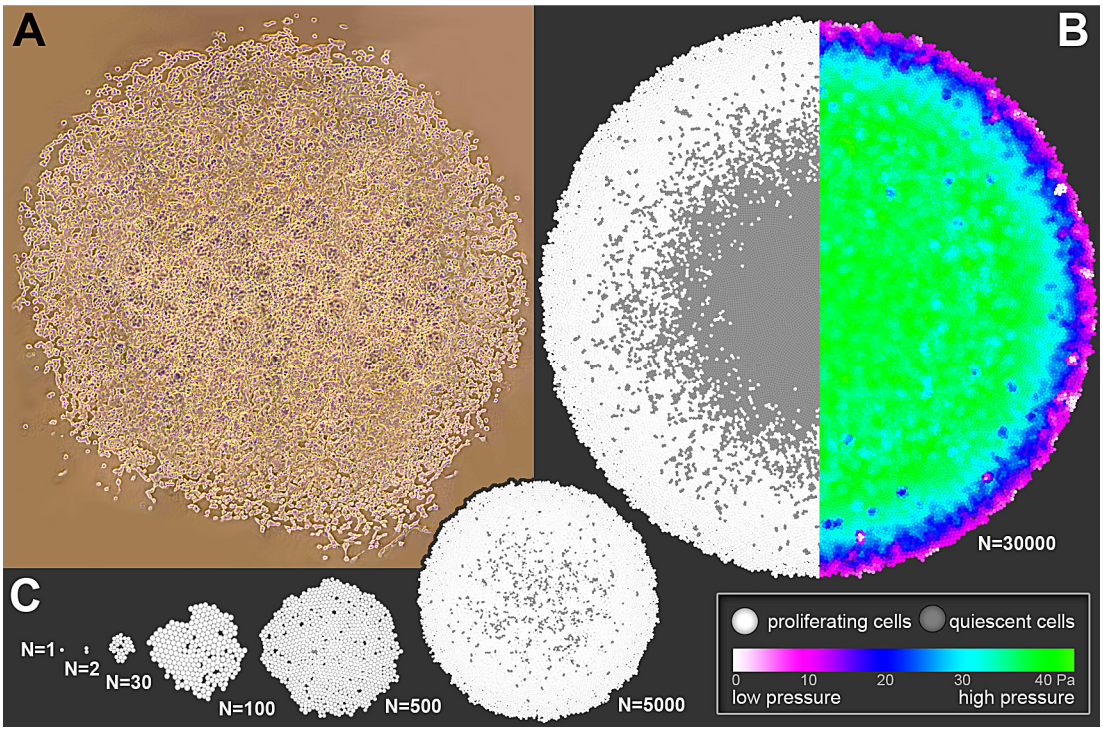


**Fig. 17: Monolayer cultures *in vitro* and *in silico***

A: Typical monolayer culture *in vitro* [Hoehme, 2007], B: Typical monolayer in the model. C: Monolayer growth scenario. Shown are snapshots at N = 1, 2, 30, 100, 500, 5000 and 30000 cells, respectively. B/C: Above a certain monolayer size the main cell proliferation (left half of B, also see Supporting video 2) is suppressed by a form of contact inhibition in the interior of the monolayer due to an increased pressure (right half of B)

Many types of normal cells need anchorage to grow and proliferate. When normal fibroblasts or epithelial cells, for example, are cultured in suspension they round off and usually do not divide [Burrige, 1986]. In order to commence division they need to be anchored in the substrate by focal contacts. Focal contacts are links of the actin cytoskeleton by cell-surface matrix receptors (integrins) to extracellular matrix (ECM) molecules, such as laminin or fibronectin. The binding of ECM molecules to integrins leads to the local activation of intracellular signaling pathways that can promote the survival, growth and division of cells. As a consequence, normal cells usually stop division at confluence whereby the cells form a closed layer on the floor of the Petri dish.
We model monolayer cultures by constraining cell growth and division to a plane that represents the floor of a Petri dish. The growing cell population is thereby restricted to two dimensions which compared to the three-dimensional situation significantly reduces the computational complexity of a number of important calculations in the model for example the detection of the interaction partners or the computation of Euclidean distances. Additionally and in analogy to the experimental situation, simulated monolayer cultures are easy to observe and thus represent a very useful tool for example to test the implementation of new algorithms or to directly compare to experimental data.

### 3.3.1. Monolayer growth kinetics

[Bru et al., 1998] have grown two-dimensional tumor monolayer cultures from C6 rat astrocyte glioma cells. Surprisingly, they observed a linear growth of the tumor diameter $L$ with time $t$ (Fig.19A) even if the monolayer was covered with additional nutrient medium. Despite all cells were in contact to the nutrient medium and hence no shortage of glucose (or oxygen) supply occurred, the growth was not exponential but linear. Moreover, above a certain population size a characteristic proliferation pattern formed with the highest proliferation activity close to the tumor boundary [Bru et al., 2003]. This suggests that the division of cells in the interior of the monolayer culture may be repressed by a form of contact inhibition. This finding has stimulated us to study whether the growth kinetics and spatial growth pattern could be explained by a mechanical form of contact inhibition [Drasdo & Hoehme, 2005]. As long as a monolayer is sufficiently small the number of cells that have to rearrange if a cell in the monolayer interior grows or divides remains small. Accordingly a growing cell in the monolayer interior is in general able to exert a sufficiently strong force on its neighbors to push them aside or stimulate them to actively migrate away. Since glucose and oxygen are not limiting, in such initial phase cells divide everywhere in the monolayer hence the cell population size grows exponentially fast. Above a certain monolayer size cells sufficiently far in the monolayer interior should become jammed between so many surrounding cells that they are neither capable of pushing their neighbors aside nor is active migration of

surrounding cells fast enough to generate sufficient space for interior cells to divide. This would result in a large pressure inside the monolayer which would relax towards the boundary only within a limited number of surface cell layers where cells still have sufficient space for migration. In this regime, $dL/dt = v \approx 2\Delta L/\tau$, where $\Delta L$ is the width of the proliferating rim (white in Fig.17B) and τ is the cycle time.

Alternatively to this biomechanical approach, one may think of contact inhibition as initiated by the interaction of cell surface receptor molecules. In this case, if cell-cell attraction is present, only the outermost cells of the monolayer would be able to divide in which case the growth velocity would be $2l/\tau \approx 1\mu m/h$ ($l$: cell diameter) that is considerably smaller than the value of 5.8 μm/h found by [Bru et al., 2003]. Note that this case corresponds to the assumption of the Eden model [Eden, 1961] in which cells occupy sites of a lattice, at most one cell per lattice site, and cell division can only occur onto adjacent free lattice sites.

Another possible alternative would be that the boundary cells detach from the monolayer and freely migrate away from compact monolayer compound. Such behavior can be observed for invading tumor cells [Weinberg, 2007] and is also shown in Fig.17A. In this case the boundary of the monolayer would not be sharp but disperse. Such a behavior is qualitatively modeled by the Fischer-KPP-equation in which the local density of cells is assumed to change by logistic growth and diffusion (e.g. [Xin, 2000], [Swanson et al., 2000]). However, the shape of the cell aggregates observed by Bru and co-workers suggests that at least for C6 rat astrocyte cells [Bru et al., 1998] and for HT-29 cells [Bru et al., 2003] it is not the migration of detached cells that is responsible for the observed linear growth regime.

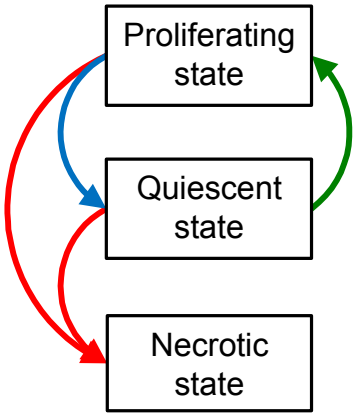


**Fig. 18: State transitions in the model**

In order to model contact inhibition we defined further state transitions that complement the ones already defined in section 3.2.5 (Fig.18, red arrows). In the extended model used in this section cells stop to proliferate if they are surrounded by too many adjacent cells, i.e., if the pressure $p_i$ (Eqn.18) that is exerted on model cell $i$ exceeds a certain threshold $p^{QUIES}$. In this case cells change their state from proliferating to quiescent (Fig. 18, blue arrow). However, this state transition was only evaluated right after cell division which models the experimental observation that cell only switch to $G_0$ phase (quiescent state) at a certain restriction point in the cell cycle (Fig.11). If later $p_i < p^{QUIES}$ cells are able to reenter the cell cycle and resume proliferation. This was modeled by a transition back to proliferating state (Fig.18, green arrow).

Alternatively to pressure-based state transitions we modeled contact inhibition by deformation-based state transitions. In this case we approximated the deformation of

a cell *i* by the Euclidean distance $d_{ij}^{HER}$ (as defined in section 3.2.3.1) to its nearest neighbor cell *j*. Based on this measure a cell *i* comes quiescent if $d_{ij}^{HER} \leq \zeta$ (Fig.18, blue arrow) and resumes proliferation if $d_{ij}^{HER} > \zeta$ (Fig.18, green arrow), where $1-\zeta$ is a critical deformation (or compression) threshold. Again, the model cells either become quiescent immediately after cell division or are committed to complete the cell cycle.

Since in the monolayer experiments by [Bru et al., 1998] nutrients were equally accessible to all cells, it was not necessary to model glucose or oxygen explicitly.

Fig. 17B/C shows typical morphologies of a simulated growing monolayer culture using the described model and illustrates the formation of a layer-like proliferation pattern due to the described state transitions (also see Supporting videos 2 and 3). When the simulated monolayer reached a certain size, proliferation was mainly restricted to outer cell layers while in the interior almost no proliferation can be found due to contact inhibition in agreement with the experimental observations [Bru et al., 1998] [Bru et al., 2003]. As shown in Fig.19A the time development of the monolayer diameter in our model was also in good agreement with the experimental observations.

We also tested the situation where in this surface growth regime cells in the interior became apoptotic due to a too long lasting extensive pressure and were removed from the simulation modeling cell lysis. In this scenario the monolayer expansion velocity *v* decreased only negligibly since the space left by apoptotic cells was immediately refilled by dividing neighbor cells. Hence apoptosis did not affect the total cell number in our simulations.

Our explanation of the specific monolayer growth kinetics by proposing a form of mechanical contact inhibition is supported by the observation of [Bru, 2004] that almost each cell was in close contact to its neighbors. The inherent coupling of mechanical stress and cell kinetics is also supported by experiments in a number of publications (e.g. [Boucher et al., 1990], [Boucher et al., 1997], [Helmlinger et al., 1997], [Gutmann et al., 1992]).

Our model predicts that the expansion velocity can be changed by mechanisms that either modify the thickness of the proliferation layer $\Delta L$ or modify the cell cycle time $\tau$. Our computer simulations suggest that an increase of (1) the cell motility which can be achieved by increasing *D* or, analogously, by decreasing the friction between cells and their environment or (2) the cell's Young-modulus *E* (the cell elasticity) delays the cross-over from exponential to linear growth of *L* and increases the monolayer expansion velocity in the surface growth regime (Fig.19 A-D). A larger cell motility or smaller cell-environment friction facilitates relaxation of the mechanical stress in the proliferating rim. However, migration over distances large compared to the cell diameter was not observed within the viable rim in our simulations. A larger *E* increases the force necessary to cause the critical cell deformation at which a stop of cell growth is triggered. Hence both result in a larger

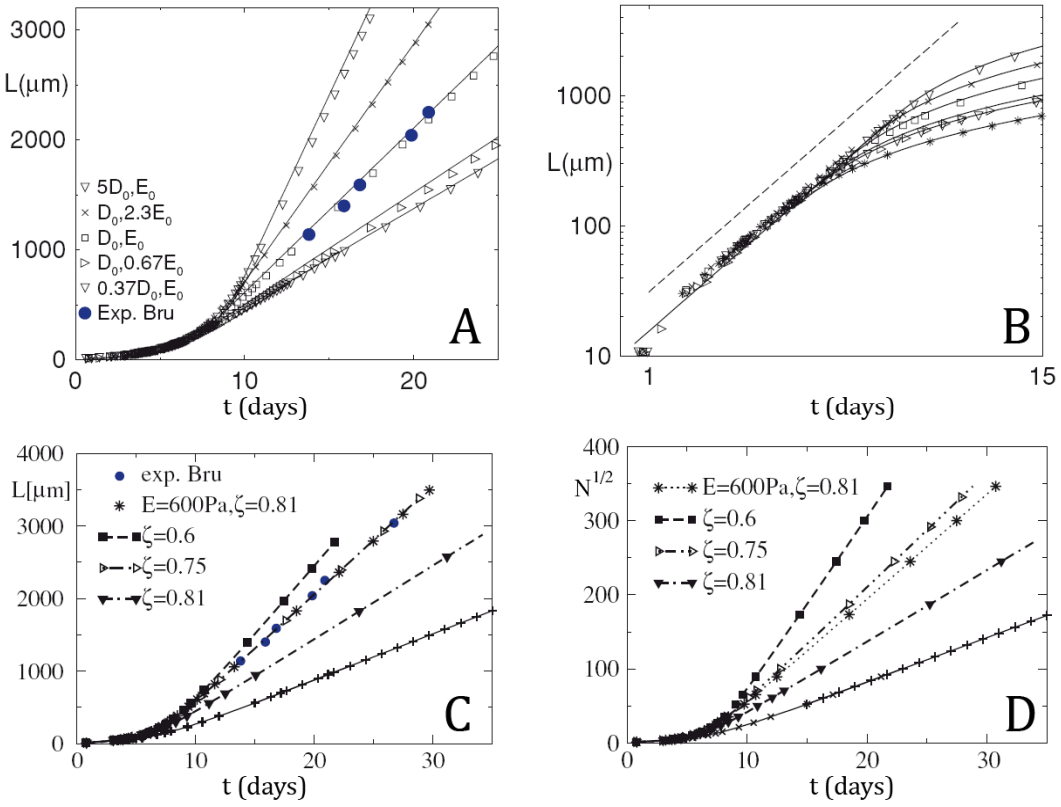


**Fig. 19: Monolayer growth dynamics.**

A: Growth of monolayer diameter $L(t)$ (filled circles: experimental data from [Bru et al., 1998], other symbols: model simulations). An increase of the cell motility (via $D$), or of the Young modulus E result in an increase of the expansion velocity $v = dL/dt$, and B: extends the initial exponential growth regime. $E_0 = 400$ Pa, $D_0 = 1.27 \times 10^{-11}$ cm$^2$ s$^{-1}$ is the reference parameter set for the simulations of Bru's data. C: Expansion for $0.6 \le \zeta \le 0.81$. For larger $\zeta$ the growth velocity $v = dL/dt$ decreases since the cells become quiescent at a smaller degree of deformation. For the curves denoted by the star ('*') in (C) and (D), E = 600 Pa, $\zeta$= 0.81. For the curves denoted by '+', E = 600 Pa. For all other curves E = 400 Pa. D: $dN^{1/2}/dt$ shows a monotonic increase with decreasing $\zeta$. Note, that $90\,\mu m/d \le v \le 320\,\mu m/d$ is within the range observed for different cell lines in [Bru et al., 2003].

size $\Delta L$ of the proliferating rim. Also a decrease of the critical deformation (or compression) threshold $1-\zeta$ reduced $v$ (Fig.19 B-D). An inhibition of cell division triggered by a limitation of growth factors (e.g. [Alberts et al., 2002]), for example, would not show the predicted behavior.

### 3.3.2. Subclone analysis

We also studied clones of cells that originate from the same mother cell. The size of these so called subclones reflects the capability of each cell to create a significant offspring which we believe reveals information on the competition of cells for free space. Our model predicts that adjacent cells in the monolayer with identical properties can form subclones of largely different size as a consequence of a competition of growing and dividing cells for free space (Fig.20). Those cells which are under slightly smaller compression can, on the average, more easily grow and divide than other cells which are under larger compression. At the monolayer border, usually the cells at outermost, convex positions are under smaller compression (arrow in the magnification of Fig.20A) which often allows them to outcompete clones which are formed by cells at concave positions. One way to experimentally verify this observation of clonal competition found in our computer simulations is to label individual cells by markers such as BrdU [Alison & Sarraf, 1998]. Once BrdU has been integrated into the cell's DNA, it is passed on to its daughter cells in case the cell divides. Thereby it could be used to label cell subclones.
We measure the size of the subclones by enumerating all cells in chronological order (based on their time of birth) from $k = 1,...,N$ and count the offspring $N_k(t)$ (Fig.20B) that arose from cell $k$ ($N_1 = N$ by definition). The average clone size was expected to behave as:

$$\langle N_m \rangle = \frac{q(N-m)}{N_p} \tag{19}$$

where $m$ enumerates all cells in chronological order from $m = 1,...,N_p$ the number of proliferating cells and $q$ is a fit parameter. $N_p = m$ in the exponential ($m \propto exp(t/\tau)$) and $N_p = m^{d_s/d}\Delta L/l$ in the surface growth ($m \propto t^d$) regime, where $d_s$ is the global surface dimension, and $d$ the dimension into which the tumor is expanding (for monolayers, $d_s = 1$, $d = 2$). Hence, for the three subclones labeled red, green and blue in Fig.20A approximately the same clone sizes would be expected while the observed clone sizes show significant differences. For monolayers in the surface growth regime the gliding average $\bar{N}_{m,\Delta m}$, where $\Delta m$ denotes the window size (here $\Delta m = 100$) obeys the relation:

$$\bar{N}_{m,\Delta m} \approx \frac{q_s(N-m)}{\sqrt{m}(\Delta L/l)} \tag{20}$$

This is illustrated in Fig.20C, where we have drawn:

$$Y \equiv \bar{N}_{m,\Delta m} \times \frac{(\Delta L / l)\sqrt{m}}{(N-m)} \approx q_s \tag{21}$$

where we have approximated $\langle N_m \rangle$ by $\bar{N}_{m,\Delta m}$ with $\Delta m = 100$ and $N = 10^5$. The smaller the proliferating rim (or equivalently the expansion velocity $v$), the larger is the fluctuation of the subclone sizes given all cells have the same average $\tau$. The decay of Y for small m's (m < ~5000) in Fig.20C indicates the exponential growth regime.

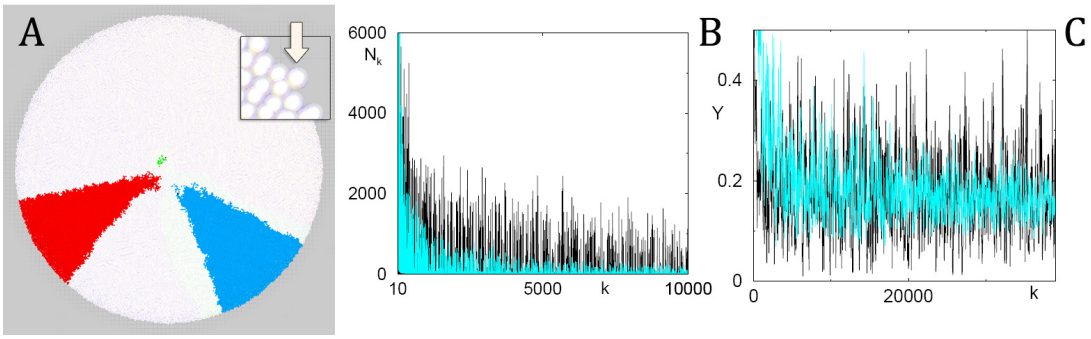


**Fig.20: Subclone statistics.**

A: Simulated monolayer culture where the subclones of three different cells have been labeled in red, blue and green. The arrow within the magnification shows a cell at a locally convex position of the monolayer border that has a larger probability to form a large clone. B: Sub-clone statistics $N_k$ for a typical monolayer simulation for the parameters $D=5D_0$ (cyan), $D=0.37D_0$ (black). C: Y as defined in Eqn.21 for the same monolayer.

## 3.4. From 2D towards 3D: Detachment from substrate

Two-dimensional monolayer cultures are an important experimental tool to study growing cell populations *in vitro*. However, tumor cells are often able to grow and divide anchorage-independent and hence do not stop to grow after confluence. Whether cell lines grow as monolayers or also expand perpendicular to the substrate depends on whether certain mechanisms that control growth and apoptosis work properly. Different cell lines originating from the same tissue may grow very differently. For example, while HCT116 cells, a human colon carcinoma cell line, grow mainly as a monolayer, WiDr cells, a human colon adenocarcinoma cell line, quickly expand into the direction perpendicular to the plane of the substrate [Noguchi et al., 1979] [Lachmann et al., 1988]. After studying the morphology and growth kinetics of two-dimensional monolayers in the previous section we now explore the effect of simulated knockouts of growth control mechanisms and show that the phenotype in this case can dramatically change. In this section we study cell detachment and thereby take first steps towards the simulation of growing cell populations in 3D.

Epithelial cells, which typically form the inner and outer surfaces of the body [Junqueira & Carneiro, 2005], are often subject to proliferation that depends on cell-substrate contact and anoikis (a special type of selective programmed cell death). Therefore in cell cultures they typically grow to confluent cell monolayers [Li et al., 2003] [Warchol, 2002] [Klekotka et al., 2001] forming a one-cell-thick layer which covers the total area of the culture dish. Often epithelial cells establish a cell polarity.

The introduction of different oncogenes into cultured epithelial cell lines affects their signal transduction pathways [Orford et al., 1999] [Yan et al., 1997] [Lu et al., 1995]. In cell lines which normally would form cell monolayers this can result in a breakdown of epithelial cell polarity due to changes of the cellular adhesion properties [Yan et al., 1997]. Additionally, oncogenes may prevent anoikis that normally occurs if cells loose contact to the substrate [Stupack & Cheresh, 2002] by interrupting apoptotic signaling pathways [Lu et al., 1995]. Thereby the introduction of oncogenes may enable anchorage independent growth, which is characteristic for many tumor cell lines [Bates et al., 2000] [Santini et al., 2000]. The accumulation of such altered cells at confluence can lead to the formation of multilayers [Yan et al., 1997] or to the formation of spheroidal aggregates [Lu et al., 1995]. In order to explain these phenotypic differences between non-altered and altered cells, biologists mainly have been focusing on the molecular mechanisms to understand how molecular signals from other cells or the substrate are transduced from the cell surface into the cell and affect the genetic control of cell proliferation and death [Orford et al., 1999] [Yan et al., 1997] [Lu et al., 1995]. However, epithelial cells are also able to recognize changes within the local microenvironment by sensing the degree of their own extension or compression, and thereby couple cell shape changes to cell migration and proliferation [Gloushankova et al., 1997]. Thus cell shape may

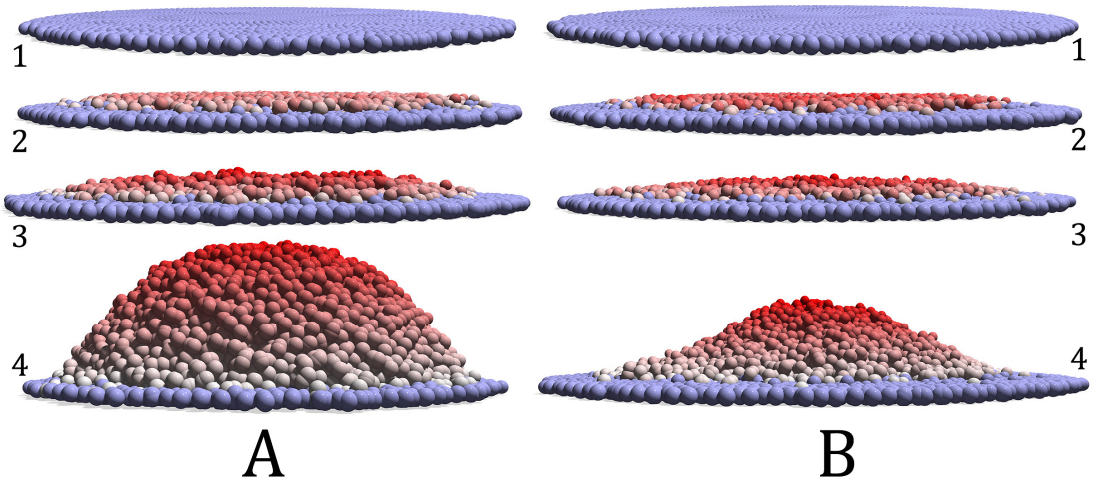


**Fig. 21: Destabilization scenario of a growing monolayer**
Simulations use extended Hertz model (A) or JKR model (B). Blue color indicates direct substrate contact. (1) denotes no knockout, the further numbers denote knocked-out control mechanisms, namely, the knockout of (2) contact inhibition (3) anchorage-dependent proliferation and contact inhibition, and (4) anoikis (anchorage-dependent apoptosis), anchorage-dependent proliferation and contact inhibition. The parameters in A and B are the same (for details see Appendix 5). As the consequence of the hysteresis in the JKR model, much less cells detach from the substrate for the JKR model than for the extended Hertz model (4). For growth in perfect one-cell-thick monolayers (1) the differences are negligible.

be another critical factor that influences cell proliferation, quiescence and death[Chen et al., 1997]. Hence, some aspects of multicellular tissue organization in epithelial cells can be directly attributed to the physical interaction between individual cells and their neighbors, and between individual cells and the substrate [Galle et al., 2005].Monolayer cultures in experiments are not completely flat but show small spatial fluctuations as a consequence of stochastic growth and re-arrangement processes. In order to reflect this situation and facilitate cell growth that is not confined to a purely two-dimensional setting, we remove the explicit limitation to two-dimensional space that was used in the previous section to represent a well-functioning contact inhibition of growth.

Cells within monolayers experience forces from adjacent cells due to cell micromotility and proliferation that are not completely parallel to the substrate but have a component perpendicular to the plane of the substrate. If this perpendicular component of the force exerted on a cell is directed outwards, away from the substrate, and if it overcomes the cell-substrate adhesion force then this cell may be pushed out of the one-cell-thick layer that is in contact with the substrate (Fig.21). This situation is most likely to occur in the interior of the monolayer because of high local pressure as we showed in section 3.3 (Fig.17B). The probability of cell-

substrate detachment further increases for cell lines which are either insensitive to contact inhibition or for which contact inhibition has completely been switched off.
Usually cells that loose contact to the substrate do not proliferate anymore (anchorage-dependent proliferation) and after a period of several hours undergo apoptosis (anchorage-dependent apoptosis termed anoikis). In Fig.21 we study (1) normal monolayers (as described in section 3.3) in comparison to successive knock-outs of (2) contact inhibition, (3) anchorage-dependent proliferation in addition to (2) and (4) anoikis in addition to (3). Model cells with a knocked out contact inhibition mechanism (2) are assumed to not stop proliferation even if a critical compression or deformation threshold has been overcome. Cells with additionally knocked out anchorage-dependent proliferation (3) do not stop to proliferate even if they have lost substrate contact and if furthermore anoikis (4) has been knocked out, the cells are assumed to not undergo apoptosis after they lost substrate contact while cells under normal conditions die a few hours after loss of substrate contact.
As long as anoikis was still present (we assume an apoptotic rate of 4 $h^{-1}$ according to [Galle et al., 2005]) a quasi-monolayer was maintained and again a surface growth regime with $L \propto t$ formed. As long as anoikis did not affect cells in the proliferating rim, also the monolayer growth kinetics remained unaffected.
Only if anoikis was knocked out, a significant piling up perpendicular to the plane of the substrate occurred (Fig.21-4).
Furthermore, we studied the influence of the contact model and therefore compared the results obtained with the extended Hertz-model and the JKR-model (both elaborated in section 3.2.3). The qualitative results were the same independently of whether the extended Hertz- or JKR-model was used. However, the hysteresis effect that occurs in the JKR-model led to a delay in the detachment process of cells from the substrate compared to the extended Hertz-model (Fig.21-A/B4). Nevertheless, the qualitative results in our simulations are very robust against changes of model details [Galle et al., 2005].

## 3.5. Tumor spheroids

In early stages of cancer, cells in many cases suffer from a loss of growth control mechanisms as elaborated in the previous section. Such tumor cells are often able to grow and divide anchorage-independent thereby forming three-dimensional cell populations. It became more and more apparent that two-dimensional monolayer cultures, despite being a valuable experimental tool regarding important aspects of multicellular growth, are not suitable as a convincing *in vitro* model for complex three-dimensional cell assemblies for a number of reasons [Santini & Rainaldi, 1999]. Solid *in vivo* tumors for example typically grow as three-dimensional aggregates embedded in tissue of other cells, are influenced by external biophysical stress and are exposed to non-uniform distributions of oxygen and nutrient concentrations. Obviously, these complex variations in a three-dimensional tumor

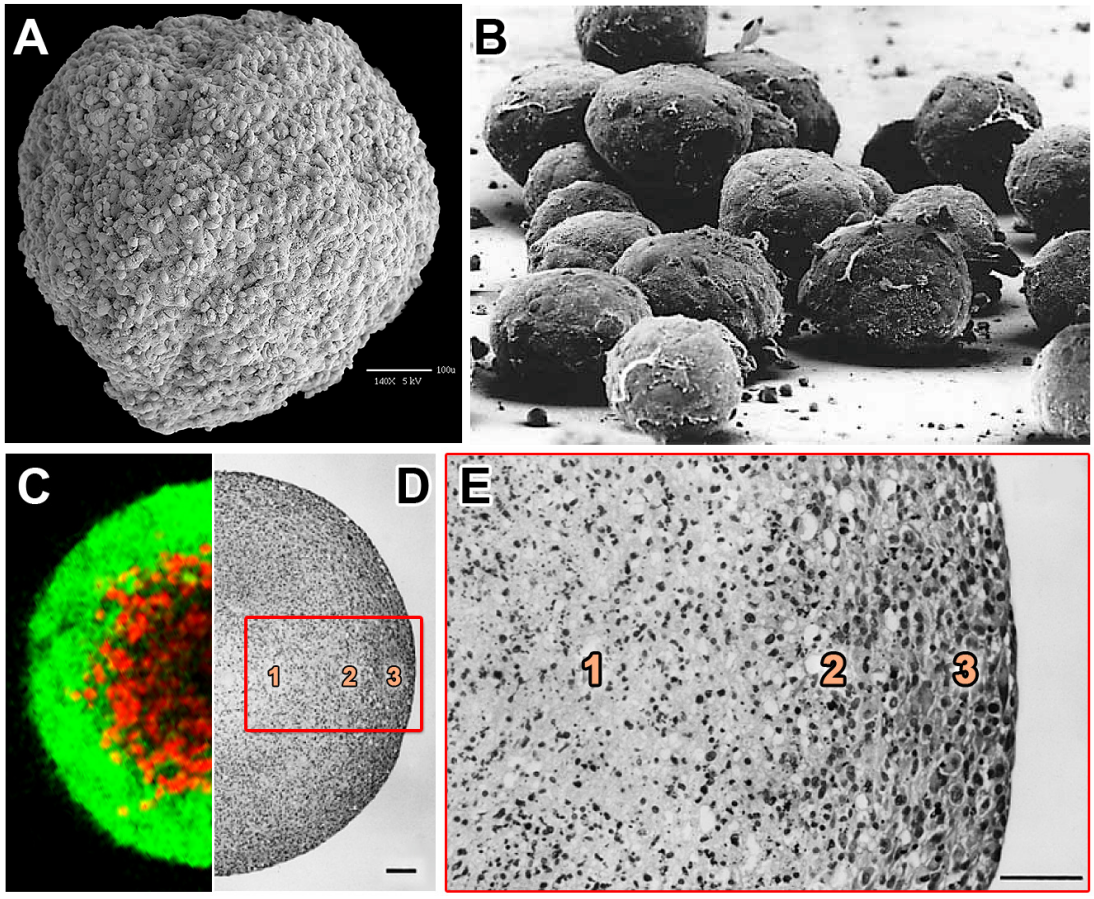


**Fig. 22: Multicellular tumor spheroids (MCTS).** A: Scanning electron micrograph of a single MCTS [Yu et al., n.d.] B: Scanning electron micrograph of A431 MCTS grown for 6 days using the gyratory rotation method. Spheroids appear regular in shape and have a smooth surface [Santini & Rainaldi, 1999]. C: Tumor spheroid (green) with internal cell death (red) [Cheng et al., 2009] D: Representative HE stained paraffin section through the center of a MCTS [Kunz-Schughart, 1999]. Bar = 150 µm. E: Magnification of D. Numbers indicate location of necrotic core (1), quiescent layer (2) and viable rim (3).

microenvironment cannot be reflected by two-dimensional monolayers in which for example all cells are equally exposed to oxygen and nutrients.
In order to overcome the limitations of monolayer cultures, multicellular tumor spheroids (MCTS) have been developed (Fig.22). After the pioneering work of [Holtfreter, 1944] and [Moscona, 1952] who studied embryonic cell aggregates to examine the development of amphibians, the technique of culturing cells in three-dimensional aggregates was later also applied to cancer research [Halpern et al., 1966] [Schleich, 1967] [Sutherland et al., 1971]. MCTS are easy to handle in the laboratory and provide a much more realistic *in vitro* model for the three-dimensional structure and microenvironmental conditions of *in vivo* tumors [Santini & Rainaldi, 1999]. Technically, MCTS can be cultured by various experimental methods for example the liquid-overlay technique [Carlsson & Yuhas, 1984], the spinner flask method [Sutherland & Durand, 1984] or the gyratory rotation system [Santini et al., 1987]. Due to the cultivation as spherical aggregates MCTS restore many functional and morphological features of the original tissue and for example were found to be similar to avascular tumor nodules or microregions of solid in-situ tumors regarding growth kinetics and internal spatial structure [Kunz-Schughart, 1999]. They may also contain an extensive extracellular matrix that often differs in the relative amount and assembly from those of the corresponding monolayer cultures. In the following, we therefore extend our model in order to simulate three-dimensional tumor spheroids and compare our results to experimental data for example by Freyer and Sutherland who studied the effect of glucose and oxygen on the growth of MCTS [Freyer & Sutherland, 1985] [Freyer & Sutherland, 1986].

### 3.5.1. Spheroid morphology

In contrast to monolayer cultures, in avascular tumor spheroids glucose and oxygen can penetrate the tumor only through its surface. Therefore, the farther a cell is situated in the tumor interior the less glucose and oxygen are available because those cells which are closer to the surface have already consumed parts of the penetrating glucose and oxygen. For this reason above a certain tumor diameter of about 400–600 µm (crossover-size) MCTS usually consist of an outer shell of proliferating (dividing) cells, an intermediate layer of quiescent (resting) cells and an inner core of necrotic (dead) cells (Fig.22C-E) [Folkman & Hochberg, 1973] [Kunz-Schughart, 1999]. Typically, the outermost viable rim measures 100 - 300 µm. [Sutherland, 1988].
In order to study the potential impact of this specific morphology on tumor growth kinetics, we extended our model by explicitly implementing nutrient diffusion and consumption. We assumed glucose to be the limiting nutrient. However, in a situation where oxygen is the limiting factor for the growth of MCTS, the corresponding model could be formulated analogously. In the following we study the typical experimental environment in which a fixed glucose concentration $c_0$ is

maintained outside the tumor [Macleod & Langdon, 2004]. The glucose diffuses with a diffusion coefficient $D_{glc}$ and is locally consumed by the model cells with a rate $g_{glc}$. We included this in the model by a reaction-diffusion equation (Eqn.22) that we solved using the explicit Euler Forward Method [Press & Vetterling, 1992]. Because we fulfill the Courant-Friedrichs-Lewy condition [Courant & Lewy, 1967], this technique combines a simple implementation with reasonable accuracy and stability. We use a discrete and regular lattice where each lattice cube had an edge length of $2R$ (cell diameter):

$$\frac{\partial c(\underline{r},t)}{\partial t} = \sum_i D_{glc} \frac{\partial^2 c(\underline{r},t)}{\partial r_i^2} - g_{glc}\Theta\big(c(\underline{r},t)\big)n(\underline{r},t) \tag{22}$$

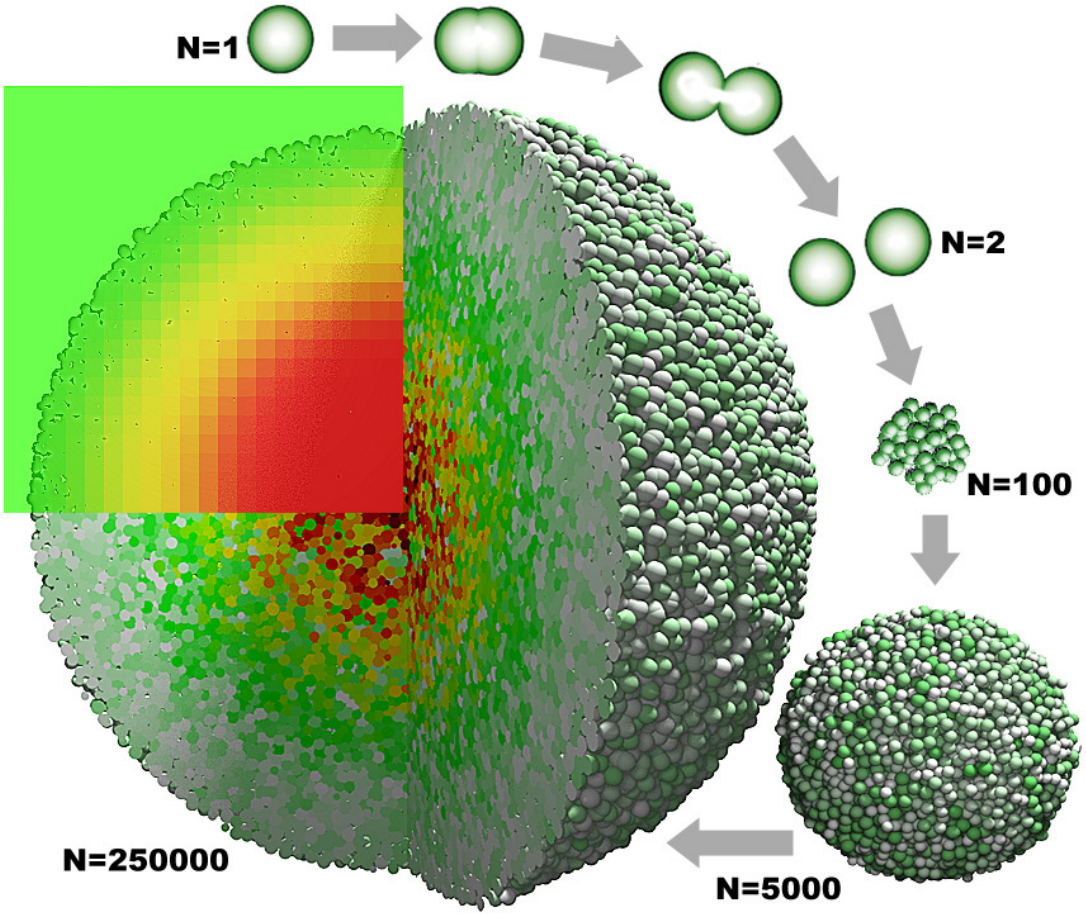


**Fig. 23: Simulated multicellular tumor spheroid**.
Typical tumor growth scenario from N(t = 0d) = 1 until N(t = 22d) = 250000 cells in the last picture (also see Supporting video 4). The arrows indicate the time direction. Cells in the outer boundary layer (white / light grey / light green) form a proliferating rim enclosing a layer of quiescent cells (green) and a necrotic core (yellow, red, black), where glucose has been depleted. The concentration of glucose is illustrated in the upper left corner of the last image (green = high, red = low glucose concentration).

where $n(\underline{r},t)$ is the local density of cells at position $\underline{r}$ at time $t$. $\Theta(x) = 1$ for x > 0 and $\Theta(x) = 0$ otherwise. We further assumed that cells can only proliferate if the local glucose concentration $c(\underline{r},t)$ exceeds a certain threshold $c^{QUIES}$. Otherwise they enter a quiescent state. Moreover, if $c(\underline{r},t)$ falls below a second threshold $c^{NECR}$ ($c^{QUIES} \geq c^{NECR}$) cells undergo necrosis. In contrast to apoptosis [Alison & Sarraf, 1998], cells undergoing necrosis first swell and then lyse by fragmentizing into pieces (for details also see section 3.2.5 and Fig.16). Accordingly, necrotic cells were usually not included in the cell count *N*. We studied the case in which lysis is very fast and therefore immediately removed necrotic cells from the simulation.
These nutrient-based state transitions complement the biomechanical state transitions defined in section 3.3.1 (refer to Fig.18).
Fig.23 shows a typical time series of the tumor morphology and illustrates the layer-like proliferation pattern of MCTS in our model simulations. In agreement with the experimental observations [Folkman & Hochberg, 1973] [Sutherland, 1988] [Kunz-Schughart, 1999], we found the highest proliferation activity close to the tumor boundary where the local concentration of glucose is the highest, while inside the tumor beneath an intermediate layer of quiescent cells a necrotic core formed (Fig.23).

## 3.5.2. Spheroid growth kinetics

Freyer and Sutherland investigated the effect of glucose ($C_6H_{12}O_6$) and oxygen ($O_2$) on the growth of EMT6/Ro mouse mammary carcinoma cell spheroids [Freyer & Sutherland, 1985] [Freyer & Sutherland, 1986]. They reported that during the first 3–4 days the number of cells *N* grew exponentially fast [Freyer & Sutherland, 1985]. After 4 days, *N* continued to increase only sub-exponentially (Fig.24A-C) accompanied by a linear growth of the tumor diameter *L* (Fig.24D). Guided by the Gompertz growth law, which is characterized by exponential growth in early stages and saturation at later stages [Laird, 1964], Freyer and Sutherland concluded that the sub-exponential regime of *N* indicates saturation [Freyer & Sutherland, 1985].
In reanalyzing that data we found that plots of log(*N*) vs. log(*t*) (Fig.24A) and $\sqrt[3]{N}$ vs. *t* (Fig.24B) (*t* denotes time) suggest a power-law-like behavior $N \propto t^3$ rather than a saturation as long as the glucose and oxygen medium concentrations were not too small [Drasdo & Hoehme, 2005]. This indicates that curve fitting by purely phenomenological growth laws, such as the Gompertz law, can be misleading.
The time developments of the tumor diameter and population size in our model both showed a very good agreement with the experimental findings (Fig.24B-D). After an initial exponential increase of the cell population size (Fig.24C), we found that our computer simulations suggest that asymptotically $\sqrt[3]{N(t)} \propto t$ that is $N(t) \propto t^3$ (Fig.24A). Note, that although the spread of the curves for $N(t)^{1/3}$ for the two glucose

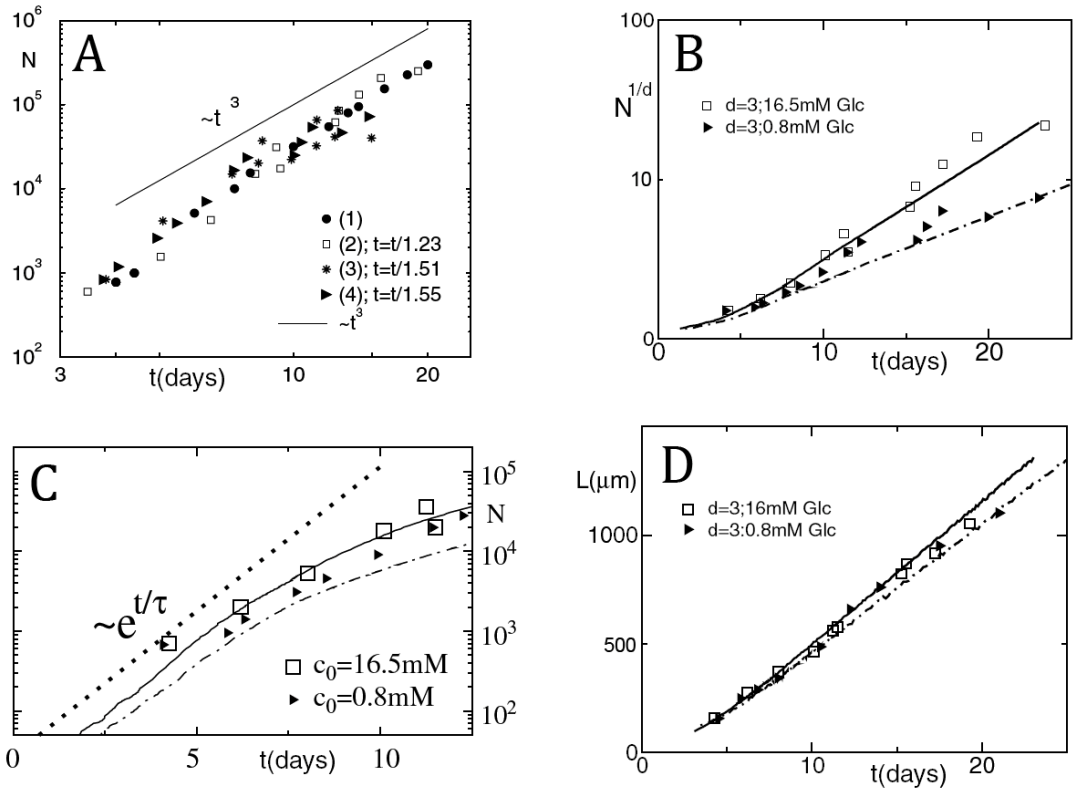


**Fig. 24: Tumor spheroid growth kinetics.**

A: Population size $N$(t) for tumor spheroids in experiments [Freyer & Sutherland, 1985] [Freyer & Sutherland, 1986] in a log-log plot for different medium glucose $c_0$ and oxygen concentrations $o_0$. (1): $c_0$, $o_0$ not known [Freyer & Sutherland, 1985] (2): $c_0$ = 16.5 mM, $o_0$ = 0.28 mM, (3): $c_0$=16.5 mM, $o_0$=0.07 mM, (4): $c_0$=0.08 mM, $o_0$=0.28 mM. The time axis for the data sets (2)-(4) has been rescaled as indicated in the legend to show a power-law behavior in all data sets. B: Model simulations (lines) to the data sets (2) and (4) (symbols). Shown is $N^{1/d}$ vs. $t$ (d = 3 for spheroids). C: Initial phase of growth of population size $N$ for the data sets (2) and (4) in a lin-log plot. D: Corresponding plots of the tumor diameter $L$ vs. $t$ for the simulations in (B).

medium concentrations $c_0$ = 0.8 mM and $c_0$ = 16 mM was significant (Fig.24B shows that $N(t)$ grows much faster for $c_0$ = 16 mM than for $c_0$ = 0.8 mM), there was almost no spread in the corresponding $L(t)$-curves (Fig.24D). Apparently, $L(t)$ was almost unaffected by the 20-fold change of the glucose medium concentration while $N(t)$ was not. Hence, glucose medium concentrations in the range 0.8 mM $\leq c_0 \leq$ 16 mM seem to have no influence on the growth of the tumor diameter $L$ which therefore cannot be determined by glucose control in this case. Since the cell population size $N$ did change significant for different nutrient medium concentrations, it must be the size of the necrotic core that is controlled by $c_0$. Along this line of argument, our model suggests the same mechanical form of contact inhibition that was already able to explain the existence of the linear expansion regime of the monolayers diameter (in section 3.3) to be a likely mechanism that could play an important role in the control of tumor growth.

Note that despite the existence of a (cell-free) necrotic core $N \propto t^3$, $L \propto t$ and thus $N \propto L^3$ which seems to be a contradiction at least for large necrotic core sizes, because in case the average cell size remains the same for all $L$, one obtains $N \propto L^3$ only if the total cell count includes the necrotic cells. In this case $N \propto L^3$ would denote cells distributed over the tumor volume $V = 4\pi/3 \cdot (L/2)^3$. If cells in the necrotic core were not included in the cell count, $N \propto L^2$ as long as neither the average cell size nor the average cell density changes. This, however, is in contrast to the experimental data that suggests $N \propto L^3$.

However, this pretended contradiction can be resolved by taking into account that the median cell volume $\bar{V}_c$ has been observed to decrease with increasing tumor diameter as $\bar{V}_c \propto L^{-1}$ [Freyer & Sutherland, 1985]. This can immediately be seen in case the size $\Delta L$ of the viable rim is much smaller than the tumor diameter $L$. Here:

$$\bar{V}_c N \propto V = \frac{4}{3}\pi(r^3 - r_i^3) \approx \pi L^2 \Delta L \Leftrightarrow N \propto L^3 \tag{23}$$

where $\bar{V}_c \propto L^{-1}$ has been used. Here $r_i = r - \Delta L$ is the inner radius of the viable rim, $r = L/2$ the tumor radius and $V$ is the tumor volume. Accordingly, for the model simulations shown in Fig.24 we removed the necrotic core and hence did not include it in the total cell count. Furthermore, we modeled a decrease of the median cell volume with $L$ ($\bar{V}_c \propto L^{-1}$) as observed by [Freyer & Sutherland, 1985] by assuming that daughter cells are slightly smaller than their mother cell. Thereby $N \propto L^3$ even if the viable cells $N$ are confined to a surface layer of constant width. So interestingly, the decrease of the median cell size and the cell loss due to necrosis in the center of the tumor spheroid occur in such a way, that still $N \propto L^3$ is maintained. In a more recent model [Hoehme & Drasdo, 2009a] we suppressed the assumption that daughter cells are smaller than the mother cell and assumed instead, that most of the cell growth occurs after the cell has passed the restriction point. This is sufficient to observe the correct relation of the median cell volume versus the tumor diameter.

The growth velocity $v \approx 2\Delta L/\tau_e$ increases with the effective thickness $\Delta L$ of the proliferating rim. $\tau_e$ denotes the effective cycle time which was determined from the cycle time distribution [Drasdo & Hoehme, 2005]. The small effect of $c_0$ on $v$ suggests that $c_0$ has almost no effect on $\Delta L$ in agreement with the conjecture by [Mueller-Klieser, 2000]. Moreover, we eliminated the quiescence threshold from our simulation for $c_0$ = 16 mM (by choosing $c^{QUIES} = c^{NECR}$) and found $v$ to remain almost the same. The explanation for this observation could be that the quiescent cells are already under considerable pressure (Fig.23) and hence have a significantly larger than average cycletime. Therefore they hardly contribute to the tumor expansion velocity. Since most cell divisions occur close to the boundary, a quiescent threshold has to be sufficiently close to $c_0$ to have a major impact on $\Delta L$.

On the other hand we found the necrotic core at the same $L$ to be larger for smaller $c_0$: the width of the viable rim $\Delta L$ was about 140 μm for $c_0$ = 16.5 mM and about 80 μm for $c_0$ = 0.8 mM respectively. In order to verify our prediction that $v$ may largely be triggered by a biomechanical form of contact inhibition due to mechanical stress rather than by nutrient limitation, we studied $c_0 \to \infty$ (no nutrient limitation). In this case we obtained a growth velocity $v$ which was only ~15% above the value for $c_0$ = 16.5 mM, whereby the minor increase of $v$ with $c_0$ likely resulted from a small contribution of expansion forces from cells in slightly larger viable rims for $c_0 \to \infty$. Nevertheless, this observation supports our prediction that the growth kinetics of MCTS could be largely determined by the same biomechanical form of contact inhibition that also determined the growth of monolayer cultures.

### 3.5.3 Discussion

Recently, agent-based models of multicellular spheroids have been studied by different authors. For example [Schaller & Meyer-Hermann, 2005] assumed that cells move deterministically by being pushed by dividing cells. The authors obtained a good agreement of their results with the experimental observations of the population size but unfortunately did not consider the tumor diameter. Lattice-based models of tumor spheroid growth have been considered for example by [Dormann & Deutsch, 2002], [Stott et al., 1999] [Jiang et al., 2005] [Radszuweit et al., 2009].
[Dormann & Deutsch, 2002] considered a cellular automaton model in which each cell was represented by one lattice site and included the effect of nutrients. [Stott et al., 1999] used a generalized Potts model in which each cell was represented by many lattice sites but did not include the effect of nutrients. Both models are two-dimensional and in both models the authors qualitatively compared their findings to the diameter growth observed by [Folkman & Hochberg, 1973] but did not compare to data on the population size. [Jiang et al., 2005] established a multiscale stochastic Monte-Carlo simulation model also based on the generalized Potts model. Here, each cell occupied up to 64 nodes on a three-dimensional lattice. The authors include an intracellular regulatory Boolean network that controlled the $G_1$-S-phase transition of the cell cycle. Their results show a good agreement with the experimental data. However, they did not adjust their biophysical parameters to experimental observations. For example, the cell-cell and cell-matrix-interaction strengths were taken from simulations about cell-sorting scenarios in [Glazier & Graner, 1993] and seem to be significantly too large. [Byrne & Drasdo, 2009] derived a continuum-based model from the agent-based model elaborated in this work. For dense aggregates, the authors achieved a remarkable agreement of the two model types.
Nevertheless, models of multicellular tumor spheroids are slowly converging. Off-lattice models of MCTS like the one presented in this work have the advantage that they permit the use of the same models for cell-cell and cell-matrix interactions as experimentalists utilize to analyze their measurements on cells [Chu et al., 2005].

## 3.6. Tumor growth into host tissue

### 3.6.1. Introduction

During the avascular stages of tumor growth that we considered in this work, an *in vivo* tumor typically expands into space that is already occupied by the surrounding tissue. A growing tumor must thus overcome the forces and mechanical stress exerted by the host tissue (the tumor microenvironment). The biophysical properties of this tissue are therefore likely to influence the development of tumor spheroids.
A number of hypotheses have been proposed on the question of how and to what extent the physical interaction of tumor and host tissue influences tumor morphology and growth kinetics during cancergenesis [Gartner et al., 1992] [Vaage, 1992]. Nevertheless, many aspects of these complex interactions still remain to be experimentally elucidated [Gordon et al., 2003].

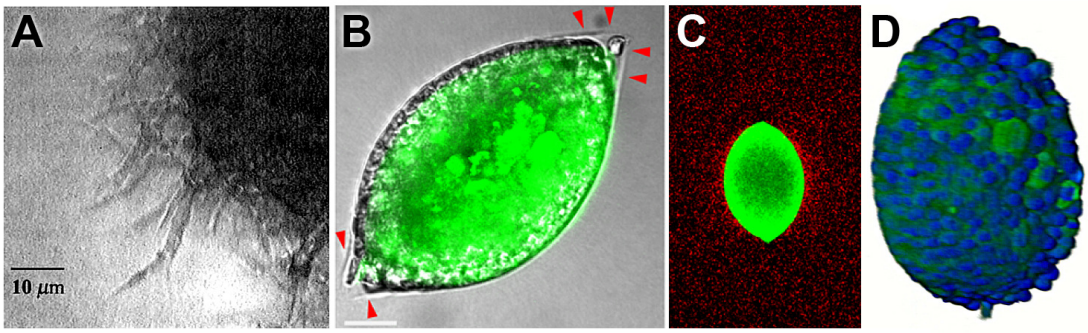


**Fig. 25: Influence of the tumor microenvironment**.
A: Tumor spheroid (dark grey) with invasive branches generated from U87MGmEGFR glioblastoma cell line placed in a cube filled with gel [Gordon et al., 2003]. B: Spheroid (green) with anisotropic shape influenced by mechanical stress (bright field image, scale bar: 50 µm). Red arrowheads show the edge of planar cracks in the agarose gel. C: Stress field visualized by micro beads (red) D: 3D visualization of spheroid in B/C (images from [Cheng et al., 2009]).

[Helmlinger et al., 1997] conducted the first quantitative experimental study of spheroid growth inhibition by mechanical stress. The authors illustrated the biomechanical influence of the tumor microenvironment by growing tumor spheroids embedded in agarose gels of different concentration and thus rigidity. Regardless of host species and tissue of origin, increased mechanical stress led to significantly decreased maximal tumor spheroid sizes which for example in human colon carcinoma decreased from a diameter of 400 µm (in 0.5% agarose) to 50 µm (in more rigid 1% agarose). More recently, another group demonstrated that also the shape of tumor spheroids is dictated by the shape of the solid stress field (Fig.25) by using agarose gels and co-embedding fluorescent micro-beads [Cheng et al., 2009]. Further analysis revealed that that one reason for this observation was suppression of proliferation and induction of apoptosis in regions of high mechanical stress.

Additionally, the shape of a multicellular tumor spheroid may have a secondary impact on its growth dynamics. As elaborated in section 3.5, in avascular stages of tumor growth, glucose and oxygen can only enter the tumor through its surface. This leads to multi-layer tumor morphologies since cells in the tumor interior die because of nutrient lack. Therefore the diameter of an avascular spherical tumor is typically limited to 2-4 mm [Macklin & Lowengrub, 2007]. However, if the tumor surface is non-spherical as experimentally observed in [Bredel-Geissler et al., 1992] [Mueller-Klieser, 1997] [Hedlund et al., 1999] [Enmon et al., 2001] [Frieboes et al., 2006], additional nutrients would be available in the tumor interior because of the increased ratio between the tumor surface and volume. This could lead to a prolonged tumor growth. Along this line of argument, a compact, spherical tumor shape would be favorable from a therapeutical point of view.

In order to model the biomechanical influence of an embedding host tissue on the kinetics and morphologies of growing tumor spheroids, we simulated multicellular aggregates (cell type A) as elaborated in the previous sections growing either within a microenvironment of other cells (cell type B) that we considered tumor host tissue, or in a granular medium of cell-like behavior.

Regarding the model, the only difference between the growing tumor cells of type A and their environment of cells of type B was that we assumed the latter to always remain quiescent (non-dividing). An embedding granular medium was modeled by host tissue of no intrinsic motility ($D_0 = 0$). In contrast to an embedding tissue of cells that may be further influenced in complex ways by signaling and interactions with enzymes, the biomechanical properties of granular medium can be precisely controlled and thus are more directly verifiable in experiments. In the following the term “host tissue” encompasses both models of the embedding tissue.

We assumed the embedding material to be adhesive. As explained in section 3.2.3, the strength of adhesion was defined by the density of adhesion molecules $\zeta_m$. In general, we assumed $\zeta_m = \zeta_{AA} = \zeta_{BB} = \zeta_{AB} = 10^{15} m^{-2}$ , where $\zeta_{AA}$ ($\zeta_{BB}$) denotes the density of adhesion molecules in case of an interaction between two cells of type A (B) and $\zeta_{AB}$ denotes the density of adhesion molecules in case of an interaction between a cell of type A and another cell of type B or an element of the granular medium. In this section, we used pressure based state transitions as described in section 3.3.1.

We believe the introduction of an embedding granular medium and moreover of host tissue with additional micromotility to be a significant steps towards a more realistic modeling of an *in vivo* situation. In order to study the detailed impact of the biophysical properties of the embedding host tissue (granular cell-like medium or type B model cells) on growing cell clones, we modified the properties of the embedding material. We systematically varied its motility (section 3.6.2.), initial density (section 3.6.3.), elasticity (section 3.6.4), adhesion properties (section 3.6.5.) and average cell size (section 3.6.6.). Furthermore, we studied the impact of non-uniform stress induced by a anisotropic environment (section 3.6.7) and additionally

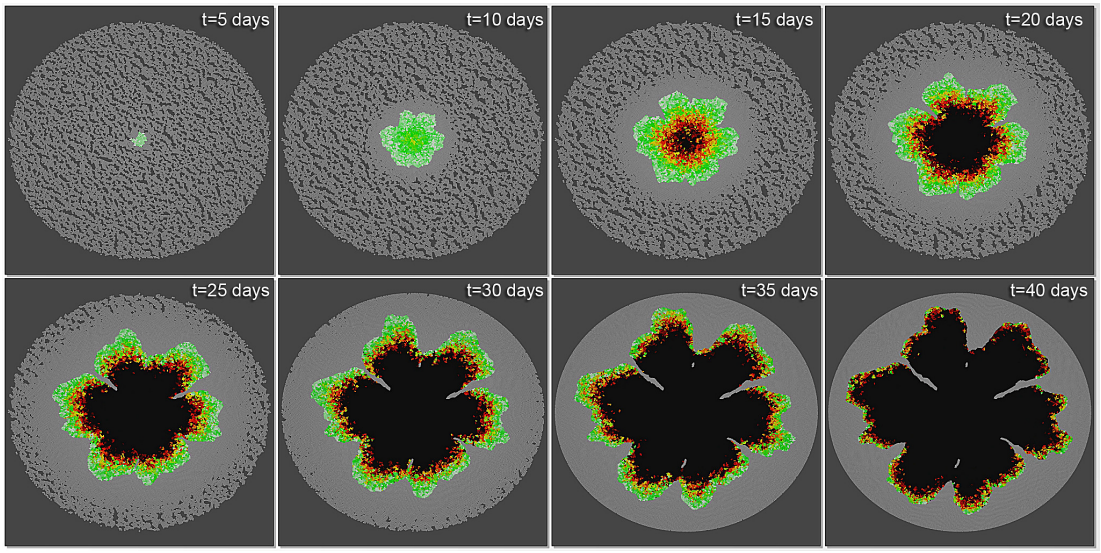


**Fig. 26: Illustration multicellular growth embedded in tissue**.
The coloring of the growing tumor (cell type A) reveals the distribution of proliferation activity: cells of white color have divided within the average cell cycle time, whereas green cells have not divided for two times the average cycletime (yellow = 4 times, red = 6 times, black = more than 10 times). The coloring shows that proliferation mainly takes place at the population border. The embedding tissue (cell type B) is colored light grey. The dynamics of this growth process are also illustrated in Supporting Video 5.

verified our findings in a highly regenerative situation considering cytolysis (section 3.6.8). After analyzing fractal and branching properties of certain dendritic morphologies (section 3.6.9) we compared our findings to experimental data by [Helmlinger et al., 1997] and [Galle et al., 2006] (section 3.6.10.). We always analyzed two- and three-dimensional populations to further improve the robustness of our results.

We started our simulations with a single cell of type A embedded in $2 \cdot 10^4 - 4 \cdot 10^5$ particles of the granular medium or cells of type B. The exact number of elements of the embedding material depended on their initial density and the spatial dimension of the simulation. All elements of the embedding material (granular particles or cells of type B) were randomly arranged (uniform distribution) in a circular (2D), spherical (3D) or anisotropic environment (Fig.26). During a particular simulation, the initial volume of this outer environment was constant and enclosed by an impermeable wall. Therefore the growing cell clone of cells of type A (the multicellular tumor spheroid) pushed away and more and more compressed the constant number of elements of the embedding material (the surrounding host tissue). Considering pressure-based state transitions as elaborated in section 3.3, this ultimately led to a saturation of growth.

We studied in how far biomechanical influences of the host tissue could explain experimentally observed tumor morphologies and growth kinetics. Furthermore by using the inverse information, we were able to predict situations wherein active regulation mechanisms were likely to control the behavior of the cells.

### 3.6.2. Variation of host tissue motility

In a first study, we analyzed the impact of the motility of cells in an embedding tissue on tumor morphology and growth. Variations of cellular motility can be caused for example by molecular changes in the complex coordinated cytoskeletal actions that are required for active cell movement [Walsh & Young, 2008].
In our model we varied cell motility in the embedding tissue by modifying the cell diffusion constant $D_T$ for cell type B. In the following sections $D_0$ designates a reference cell diffusion constant which also was used for cells of type A. In this section no granular medium was considered because granular particles were assumed to have no intrinsic motility ($D_T = 0$).
We found a variation of the motility of the embedding cells of type B to have a strong impact on the surface properties and growth kinetics of the expanding multicellular population. All described influences were found in both, two-dimensional (Fig.27C-E) and three-dimensional (Fig.27A-B) settings. For example, a

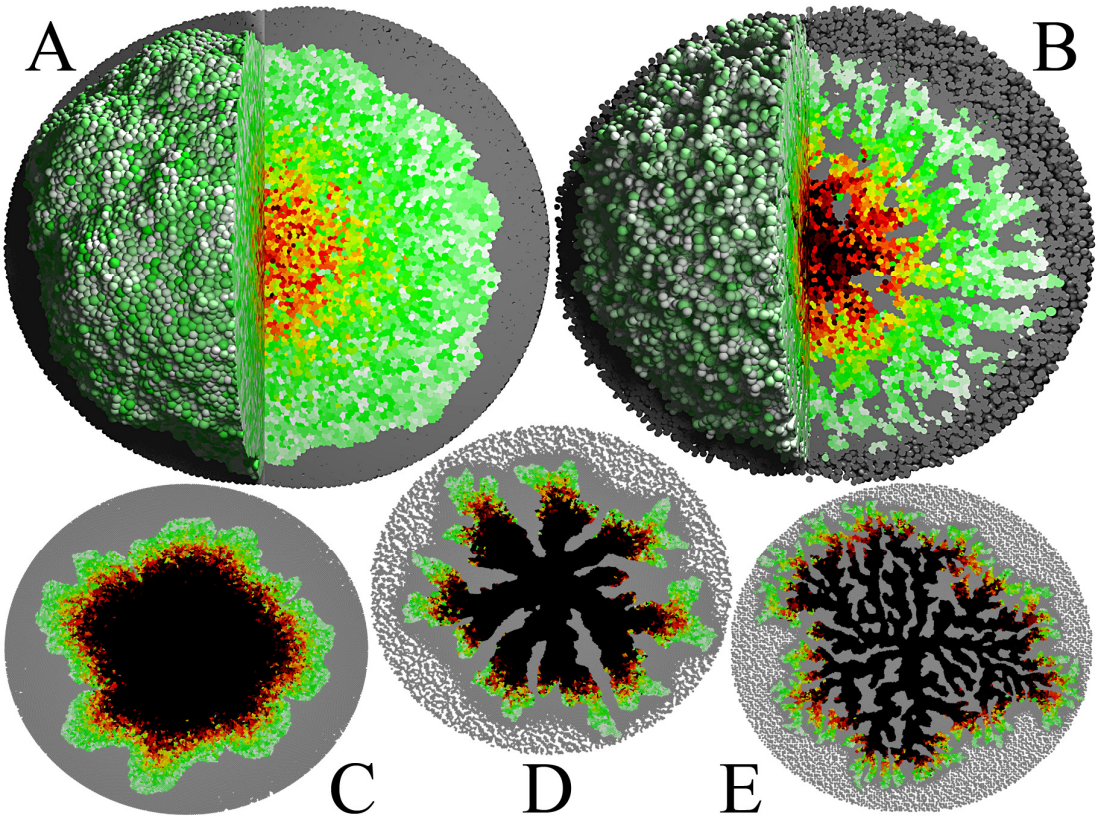


**Fig. 27: Impact of host tissue motility**.
A: Compact tumor cell population (cell type A) growing into embedding tissue (cell type B, colored gray) in 3D ($D_T$=$D_0$). One quarter of both was cut out. Tumor cell coloring as described in Fig.26. B: A decreased motility of cells in the embedding tissue ($D_T$=0.05$D_0$) led to a dendritic tumor morphology. C: Compact tumor monolayer in 2D ($D_T$=$D_0$), D: Intermediate morphology in 2D ($D_T$=0.25$D_0$), E: Dendritic tumor monolayer in 2D ($D_T$=0.05$D_0$). Also see Supporting videos 6-9.

decreased motility of cells of type B ($D_T = 0.05D_0$) resulted in a significantly rougher spheroid surface (Fig.27B) or monolayer border (Fig.27E). Effectively such decrease of motility of the host tissue increased the viscosity of the tumor microenvironment which indicated a Saffman-Taylor-like instability [Saffman & Taylor, 1958]. Consistent with this assumption, in the model a continuously decreased motility led to continuously increased dendritic structures of increasing ramification, refinement and surface roughness (Fig.27C-E). The expanding clusters tended to grow only at the tip of their dendritic fingers where the local stress was smaller than in the interior. This led to local fluctuations of small wavelength on the scale of single cells. Surprisingly, we found this variation of motility to have only minor impact on the width of the proliferating rim. Nevertheless, decreased motility of the embedding cells reduced the expansion velocity of the embedded cell population (Fig.31) because the total number of proliferating cells located at tips of dendritic fingers was smaller compared to the continuous proliferating front of non-dendritic populations. We also found populations with dendritic morphologies to be less dense regarding the number of cells in a given volume which on the one hand resulted in saturation of growth at a lower total number of cells. On the other hand, however, compared to compact tumors, dendritic populations showed significantly (+50%) increased saturation radii which reflects the increased capability to biophysically invade a highly compressed embedding medium (Fig.31) since for a given number of cells the radius of gyration is larger for branching structures than for compact cell aggregates. If this prediction could be experimentally verified it would have direct therapeutic relevance because an important aspect of tumor treatment is to minimize tumor invasiveness.

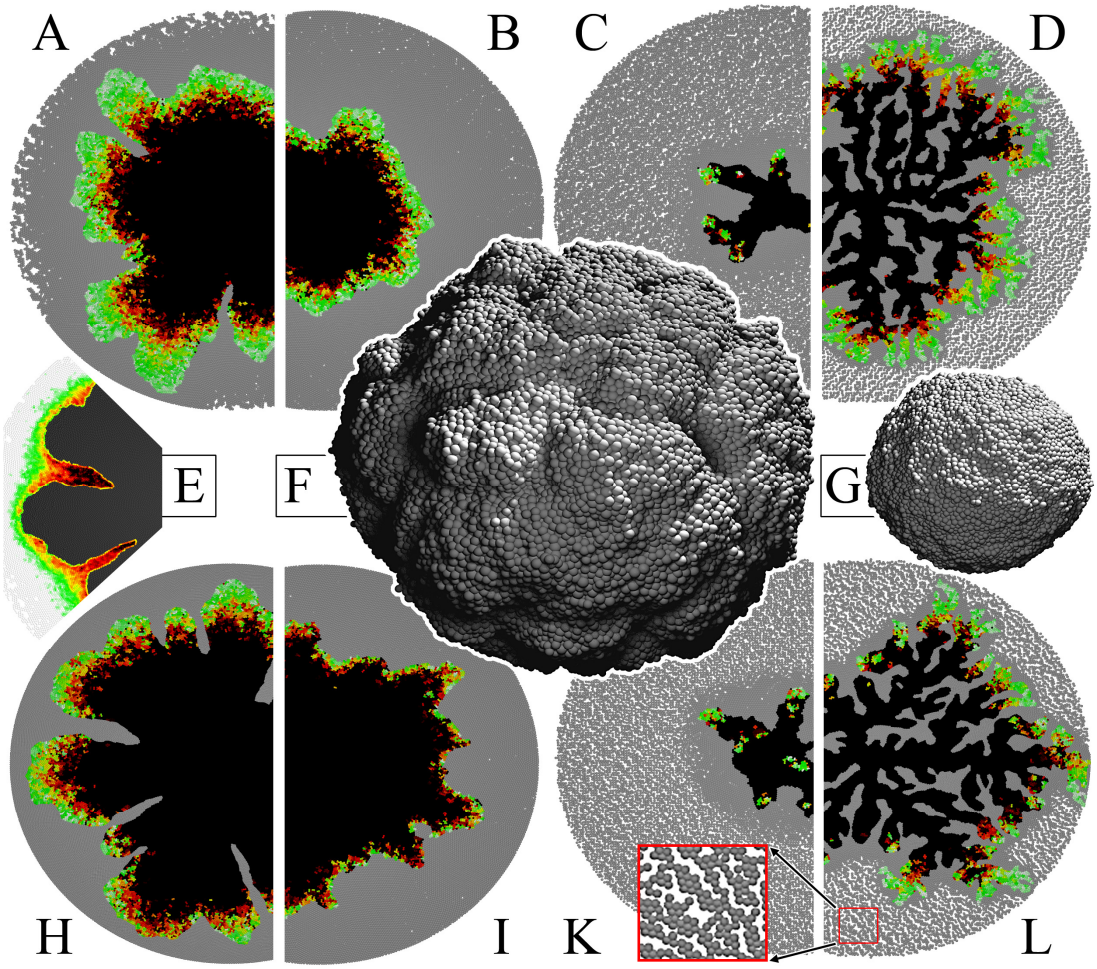


**Fig. 28: Impact of initial cell density and elasticity of tumor host tissue.**
A: Tumor monolayer growing embedded in tissue (colored grey) of decreased initial cell density ($\rho_T$ ~3500 cells per mm²), B: Tissue of increased density ($\rho_T$ ~7000 cells per mm²), C: Same setting as (B) only with additionally lowered motility of the embedding cells ($D_T = 0.05D_0$), D: Same as (A) but with lowered host tissue motility ($D_T = 0.05D_0$), E: Alternative coloring of a section of (H) where tumor cells were colored black and embedding cells were colored according to the pressure (Eqn.18, p.55) exerted on them (black/red=high, yellow=medium, green=low), F: Tumor growing into host tissue (not shown here) in 3D (~$5*10^5$ cells). Host tissue of decreased density ($\rho_T = 0.8\rho_0$). Also see Supporting videos 10 and 11. G: Same as (F) only with increased host tissue density ($\rho_T = 1.2\rho_0$, $10^5$ cells). Also see Supporting videos 12 and 13. H: Tumor monolayer ($E$=450 Pa) growing into host tissue of lowered elasticity ($E_T$=300 Pa), I: Same as (H) only with increased tissue elasticity ($E_T$=1000 Pa), K: Same setting as (I) only with additionally lowered tissue motility ($D_T = 0.05D_0$). Red framed inset: magnification of embedding tissue. L: Same setting as (H) only with additionally lowered tissue motility ($D_T = 0.05D_0$). The coloring of tumor cells (A-D, H-L) shows their proliferation activity and corresponds to the description in the caption of Fig.26.

### 3.6.3. Variation of host tissue cell density

A second important biophysical property of the tumor host tissue is its initial cell density. Both *in vitro* and *in vivo*, the average cell density varies from cell line to cell line and additionally depends on environmental factors for example the local nutrient concentration or cytoxic substances [Blomquist et al., 1993] [Johansson & Granéli, 1999] [Alberts et al., 2008].
In our simulations we model different cell densities by changing the number of embedding cells or granular objects initially seeded into the free volume. Thereby, we studied initial cell densities ($\rho_T$) between 3500 and 7000 cells per mm² whereby the reference cell density ($\rho_0$) was 5250 cells per mm².
An increase of the initial cell density in the host tissue ($\rho_T$ = 7000 cells per mm²) led to a significantly reduced expansion velocity of the growing tumor, an earlier saturation of growth at a smaller diameter and a proliferating rim of smaller width during growth (Fig.28B, Fig.31). Interestingly, if we decreased the initial cell density in the host tissue ($\rho_T$ = 3500 cells per mm²) we observed the formation of large wavelength border fluctuations indicating the formation of fingers. We believe the fingers (Fig.28A) form if cells at the surface of the growing clone are able to establish sprouts between the bodies of embedding cells (or granular particles) thereby invading the environmental material. At smaller densities of the surrounding matter the formation of sprouts is more likely than at high densities because the pressure on the surface is smaller and therefore it is more likely that at some locations the pressure is below the critical pressure $p^{QUIES}$ at which cells cannot enter the cell cycle. Once the cell has entered the cell cycle it can more easily find locations between cell (particle) bodies if the density of the extracellular material is small. This favors finger formation. Between neighboring branches the pressure is elevated because the material is squeezed. Accordingly, we found the hypothesized increased pressure in concave areas of the growing tumor (Fig.28E), where we calculated the pressure as elaborated in section 3.2.5. (Eq.18).
Additionally, we studied the impact of the tumor host tissue in case $\rho_T$ and $D_T$ were simultaneously varied. We found the influence of the discussed variations of $\rho_T$ to be consistent regarding the expansion velocity (Fig.31), saturation size and width of the proliferating rim (Fig.28C,D). Surprisingly, we found the growth of a tumor cell population embedded in host tissue of simultaneously decreased motility ($D_T$ = $0.05D_0$) and increased initial cell density ($\rho_T$ = 7000 cells per mm²) to be highly inhibited (Fig.28C). If this finding could be verified in experiments where the properties of the tumor host tissue were modified as described, the predicted suppression of tumor growth could have direct therapeutical implications.
The small wavelength Saffman-Taylor-like instability that we described for growing populations embedded in tissue of (solely) lowered motility remained unaffected by variations of the initial density (Fig.28D). Again, tumor cell populations developed dendritic morphologies and showed an increased capability to biophysically invade a highly compressed embedding host tissue.

As in the previous section, all described influences changed continuously as we continuously varied $\rho_T$ and were found in both, 2D and 3D (Fig.28F,G, see Supporting Video 10-13).

### 3.6.4. Variation of host tissue elasticity

Another important property of the tumor host tissue is its elasticity. For example, it has been found that tumors and their associated stroma have a lower elasticity than normal tissue [Gieni & Hendzel, 2008] which enables them to more effectively compress and eventually collapse blood and lymphatic vessels in their vicinity [Padera et al., 2004].
In general, cell elasticity is largely determined by the biophysical properties of the cytoskeleton, a complex and dynamic cross-linked protein network anchored to the inner surface of the fluid lipid bilayer (refer to section 3.2.1). Experiments suggest that cellular elasticity can be influenced by substances that depolymerize the cytoskeleton [Safran et al., 2005]. Furthermore, cellular elasticity is closely coupled to dynamic cell behavior as cell movement, cell shape changes or cell division. However, the highly non-linear elastic properties of a living cell are difficult to study and a detailed, experimentally validated model still remains elusive. Nevertheless, the elasticity of the cytoskeleton can be measured by an increasing number of experimental techniques as bulk rheology, traction force microscopy or atomic force microscopy. In our model we introduced cell elasticity using the contact models described in section 3.2.3. In corresponding computer simulations we found the variation of elasticity of granular particles or type B cells of the embedding tissue to

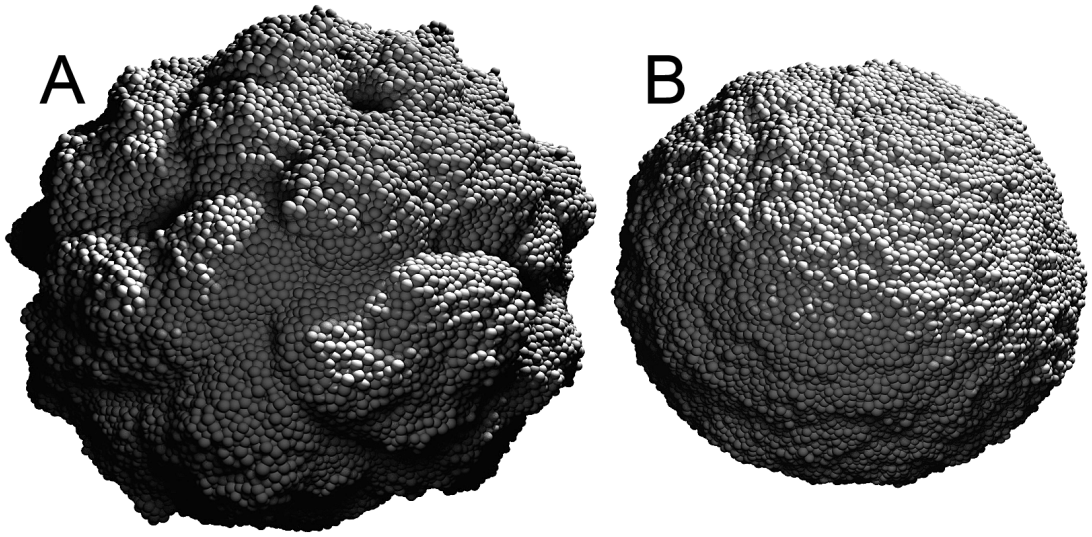


**Fig. 29: Impact of the elasticity of the tumor host tissue in 3D.**
. A: An increase of the elasticity of the embedding tissue ($E_T$ = 300 Pa) led to large wavelength fluctuations (see Supporting video 14) whereas B: a decrease ($E_T$ = 1000 Pa) had an inverse, smoothening effect on the tumor surface.

have a complex influence on a growing cell population. In previous simulations, the elasticity of the embedding tissue $E_T$ was chosen to be equivalent to the elasticity of the growing tumor (type A) for which we assumed a Young's modulus of elasticity $E$ = 450 Pa [Davidson et al., 1995] [Lekka et al., 1999]. However, an increase of elasticity of the host tissue from a Young's modulus of elasticity $E_T$ = 450 Pa to $E_T$ = 300 Pa) led to a proliferating rim of increased width and an amplification of large wavelength fluctuations (Fig.28H, Fig.29A), whereas a decrease of the elasticity of the embedding tissue ($E_T$ = 1000 Pa) had the inverse effect (Fig.28I, Fig.29B).
Furthermore, an increase of host tissue elasticity also led to an increased growth velocity of the tumor accompanied with saturation at an increased population size (Fig.31).
If additionally to the variation of $E_T$ in the type B cells also the motility was decreased ($D_T$ = 0.05 $D_0$) we observed a further amplification of the described influences (Fig.28K,L). Interestingly, in case the elasticity and motility of the tumor microenvironment were both decreased ($E_T$ = 1000 Pa, $D_T$ = 0.05 $D_0$), the growth of the embedded tumor spheroid was found to be highly inhibited (Fig.28K). If experimentally validated, this finding may have direct therapeutical implications.
The small wavelength Saffman-Taylor-like instabilities and the corresponding increased capability of the tumor to biophysically invade highly compressed host tissue that we already observed for cells embedded in tissue of lower motility ($D_T$ = 0.05 $D_0$) were not influenced by changes of the host tissue elasticity.

### 3.6.5. Variation of tumor and host tissue adhesivity

We further studied the impact of selective cell-cell adhesion [Takeichi, 1987] [van der Linden, 1996] whereby cells of a specific type adhere exclusively to cells of the same type rather than to other cells. In general, intercellular adhesion is mediated by transmembrane proteins (selectins, integrins, cadherins and the immunoglobulin (Ig) superfamily). Except for the last all of them require $Ca^{2+}$ and $Mg^{2+}$ in order to work properly. Therefore, many adhesive interactions are $Ca^{2+}$ or $Mg^{2+}$ dependent [Alberts et al., 2008]. Moreover, in tumor spheroids a greatly increased adhesion was found for $CoCl_2$ induced hypoxia, while ionizing radiation had an inverse effect [Indovina et al., 2006].
In the past decades many techniques have been developed to measure cellular adhesion, for example [Benoit et al., 2000] used a modified version of atomic force microscopy to measure adhesion forces between living cells and surfaces at the molecular level.
In our model the strength of the adhesive forces was determined by the density $\zeta$ of the corresponding receptors on the cell surface (section 3.2.3). As introduced before, we typically chose $\zeta_{AA} = \zeta_{BB} = \zeta_{AB} = 10^{15} m^{-2}$ [Chesla et al., 1998] [Piper et al., 1998]. In addition to this reference situation, we studied two cases: (1) elements of the embedding tissue (granular particles or cells of type B) selectively adhered

among each other $\zeta_{AA} = \zeta_{BB} = 10^{15} m^{-2}$ and $\zeta_{AB} = 0$ and (2) elements of the embedding tissue were not adhesive $\zeta_{AA} = 10^{15} m^{-2}$ and $\zeta_{BB} = \zeta_{AB} = 0$ . In both cases the growing tumor cells were assumed to be selectively adhesive. In both cases, there was no adhesion between growing tumor cells and the embedding tissue ($\zeta_{AB} = 0$).
In case (1) adhesion led to the local formation of patches of larger cell density within the embedding tissue (red framed inset in Fig.28). The expanding clone of tumor cells then preferably grew between these patches. We found this to have an amplifying effect on the formation of large wavelength surface fluctuations. The locally smaller density of the host tissue also increased the expansion velocity of the growing cell population and its saturation radius. We found the width of the proliferating rim to almost remain the same. Therefore the patch formation is likely to be responsible for the described changes of morphology and growth dynamics. In case (2), where embedding cells (or granular particles) are not coherent, no local patch formation occurred which left cells of the host tissue uniformly distributed. This resulted in an approximately constant cell density within the embedding tissue. We found this uniform density of the tumor microenvironment to lead to decreased large wavelength surface fluctuations and a decreased growth velocity (Fig.31). Nevertheless, the formation of small wavelength Saffman-Taylor-like instabilities in case of simultaneously lowered embedding tissue motility ($D_T = 0.05 D_0$) remained unaffected by variations of the embedding tissue adhesivity.

### 3.6.6. Variation of average cell size of host tissue

In the preceding sections the size (diameter) $l$ of the growing tumor cells (type A) and the size $l_T$ of the elements of the embedding tissue (granular particles or type B cells) were identical ($l_T = l$). However, cell size is known to vary significantly between different cell types and tissues and even within the same cell type. Nevertheless, the average cell size of a specific cell line or tissue is often well known due to its straightforward accessibility with bright field and electron microscopy. Most eukaryotic cells, for example, have an average size (diameter) of 10 - 25 µm. However, the average cell size is not a constant. It can be influenced by various factors for example cytoxic substances [Alberts et al., 2008] or genes involved in growth control [Saucedo & Edgar, 2002].
Cell size may become important for example if a tumor grows into a tissue which is mainly composed of (in the average) smaller or larger cells ($l_T \neq l$).
In order to study the influence of the size of elements of the tumor host tissue (granular particles or type B cells) on the growth kinetics and morphologies of a growing tumor cell population, we analyzed its growth into an embedding tissue composed of elements of different size ($l_T \neq l$). Thereby we studied sizes in the range of typical eukaryotic cells (10 µm – 25 µm).

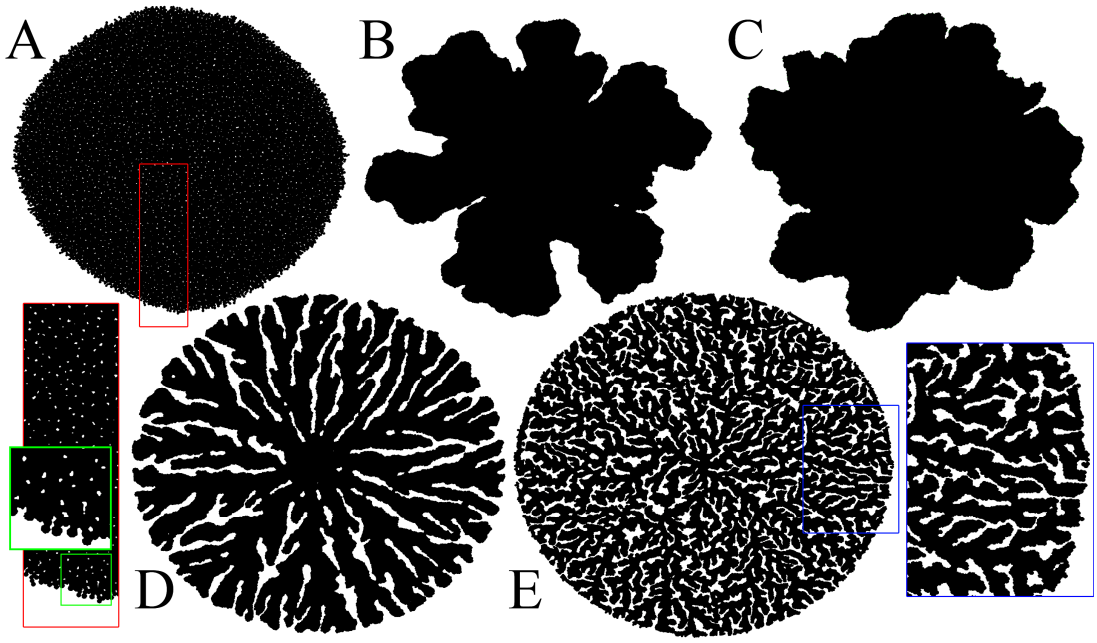


**Fig. 30: Impact of cell size in the embedding tissue**.
A: Morphology of a monolayer tumor cell population (black) growing embedded in cells (not shown) of decreased size ($l_T$=10µm). Note the red/green-framed magnifications showing the encasement of the small host tissue cells. B: Growth into host tissue of increased cell size ($l_T$=25µm), C: Reference population with unchanged cell size ($l_T = l$ = 15µm), D: Decreased cell size ($l_T$=10µm) and simultaneously increased adhesivity between embedding cells ($\zeta_T = 5\zeta_m$), E: Same setting as (D) but with decreased motility of $D_T$=0.05$D_0$. Note the blue-framed magnification illustrating the strong branching (Saffman-Taylor) in this situation.

For example, if we decreased the element size in the host tissue to $l_T$ = 10 µm ($l$ = 15µm), we found large wavelength border fluctuations to nearly vanish along with an increased probability for embedding objects to be encased by the growing tumor cell population (Fig.30A). This amalgamation of growing cells and embedding objects is likely to cause the observed surface smoothening, because if we increased the adhesivity among the embedding objects, which largely prevented their commixture with the growing tumor cells, we again found large wavelength surface fluctuations (Fig.30D). Note, that the smaller wavelength of these fluctuations (compared to previous sections) corresponds to the decreased element size in the host tissue.
If we additionally decreased the motility of the host tissue ($D_T$ = 0.05$D_0$), we again found the small wavelength Saffman-Taylor-like instability. The repeated observation of this low-motility induced instability indicates that it is a very robust influence of the host tissue on a growing tumor (Fig.30E).
For an increased average element size in the host tissue ($l_T$ = 25 µm, $l$ = 15 µm), we found an increase of large wavelength border fluctuations (Fig.30B) regardless of the adhesivity of the embedding objects. We assume that host tissue that is composed of elements of larger or even the same size (compared to the tumor cells) inherently

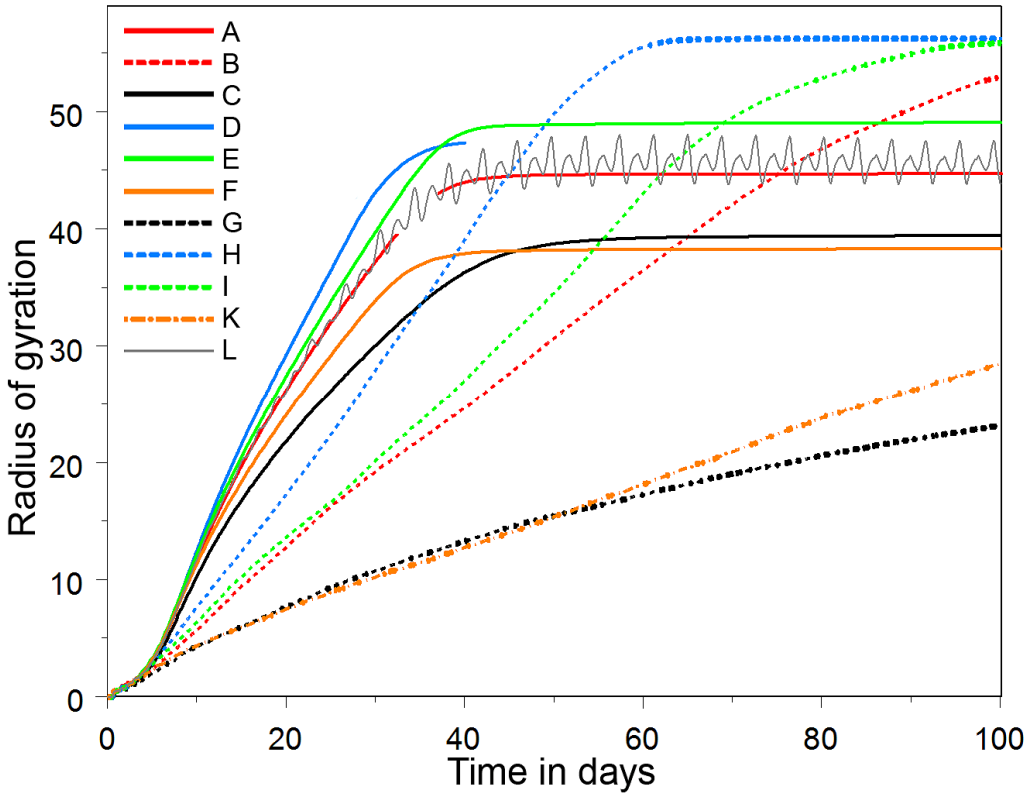


**Fig. 31: Comparison of growth kinetics in 2D**.
A (red line): Reference simulation. $D_T = D_0$, $\rho_T = \rho_0 = 5250$ cells per mm², $E = 450$ Pa, $E_T = 450$ Pa, no selective adhesion was assumed and no cytolysis occurred, B (red dotted line): Lowered host tissue motility ($D_T = 0.05\ D_0$), C (black line): Increased initial cell density in the embedding tissue ($\rho_T \sim 7000$ cells per mm²), D (blue line): Decreased initial cell density in the host tissue ($\rho_T \sim 3500$ cells per mm²), E (green line): Increased host tissue elasticity ($E_T$=300 Pa), F (orange line): Decreased host tissue elasticity ($E_T$=1000 Pa), G (black dotted line): Increased initial cell density and decreased motility ($\rho_T \sim 7000$ cells per mm², $D_T = 0.05\ D_0$), H (blue dotted line): Decreased initial cell density and motility ($\rho_T \sim 3500$ cells per mm², $D_T = 0.05\ D_0$), I (green dotted line): Increased host tissue elasticity ($E_T$=300 Pa) and lowered motility ($D_T = 0.05\ D_0$), K (orange dotted line): Decreased host tissue elasticity ($E_T$=1000 Pa) and lowered motility ($D_T = 0.05\ D_0$), L (grey line): Reference simulation (A) with cytolysis.

biophysically hampers the encasement of embedding objects that we observed for smaller embedding objects ($l_T$ = 10 µm). Furthermore, we found larger embedding objects ($l_T$ = 25 µm) to result in a slightly decreased expansion velocity, whereas smaller embedding objects led to a slightly increased growth velocity. In both situations, the width of the proliferating rim and the saturation size of the growing population remained unchanged.

### 3.6.7. Non-uniform stress

In an *in vivo* situation it seems unlikely that mechanical stress induced by the host tissue that encloses a growing tumor cell population is uniformly distributed across its surface. In order to experimentally model such non-uniform stress, [Helmlinger et al., 1997] grew multicellular spheroids of different cell lines (LS174T, BA-HAN-1, rhabdomyosarcoma and MCaIV) *in vitro* in cylindrical glass capillary tubes with an internal diameter of 1 mm. The authors found a reversible modulation of the spheroid shape induced by non-uniform stress. The radial stress increased faster than the axial stress and thus an orthotropic stress field established.
In another, more recent study [Cheng et al., 2009] used agarose gels and fluorescent micro-beads to demonstrate that the shape of tumor spheroids is dictated by the shape of a solid stress field (see Fig.25) and to analyze this effect in more detail.
In our model, we exemplarily studied the same experimental setting as in [Helmlinger et al., 1997] by changing the shape of the environment of the embedding objects (granular particles or type B cells) into a tube (Fig.32B) of a diameter of 1 mm. In this case, we found the same anisotropic growth (Fig.32C) as it had been observed experimentally by [Helmlinger et al., 1997]. Beyond this phenomenological similarity, the biomechanical cell-cycle control in our model simulations (section 3.3) was able to provide an explanation for the observed stress dependent modulation

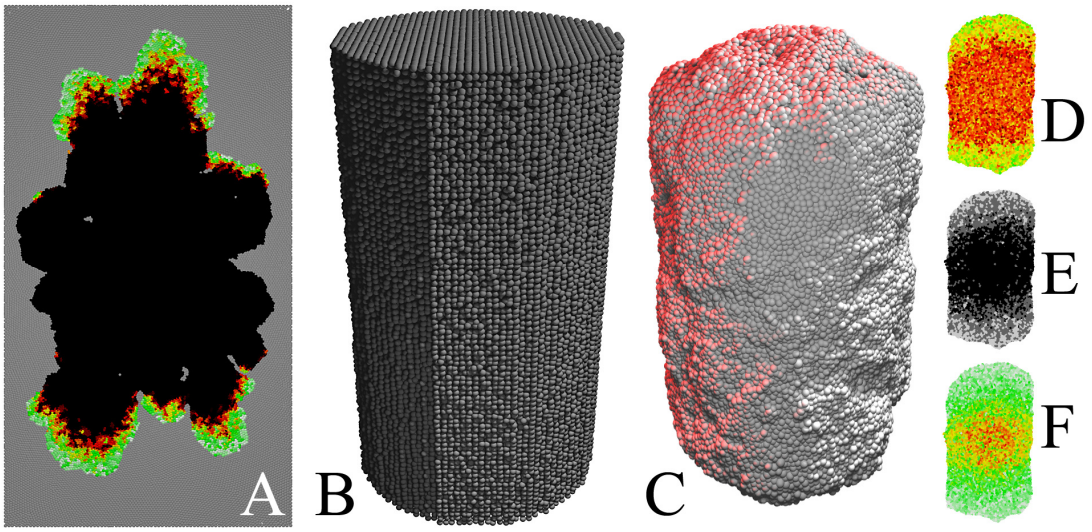


**Fig. 32: Impact of non-uniform stress.** A: 2D monolayer population growing within a rectangular area of embedding cells (grey), coloring of the tumor cells is the same as in Fig.27, also see Supporting video 15, B: Outer view of cylindrical environment (diameter = 1mm) inducing non-uniform stress as described in [Helmlinger et al., 1997] C: 3D multicellular spheroid of $2.5*10^5$ cells grown inside (B) with a anisotropic shape. D: Cross-section of (C) showing the pressure exerted on tumor cells (red=high pressure, green=low) E: Cell cycle state (white= in cell cycle, grey=quiescent, black=necrotic), F: Proliferation activity (colors as in Fig.27).

of the tumor shape. We found cells in positions close to center height to be under increased stress (Fig.32D) induced by the cylindrical environment, which locally triggered an increasing number of cells to remain in $G_0$ (quiescence) (Fig.32E). These cells then did not contribute to cellular proliferation anymore (Fig.32F) which led to the experimentally observed anisotropic axial growth (Fig.32A/C). In the recent study of [Cheng et al., 2009], our prediction that cell proliferation might be suppressed in regions of high mechanical stress was convincingly experimentally validated.

If we compared the length of the radial axis (a) of the cell populations with the length of their longitudinal axis (b), we found values similar to those measured by [Helmlinger et al., 1997]. For example, for the monolayer shown in Fig.32A we found $\omega = b/a = 1.73$, while for the cell clone shown in Fig.32C we found $\omega = 2.11$. In the corresponding experiment Helmlinger measured $\omega = 2.23$ for LS174T spheroids in 0.7% agarose.

In case the anisotropic cell population was released from its glass capillary, after 15 days [Helmlinger et al., 1997] observed a significantly reduced variation of radial and longitudinal axis of $\omega = 1.05$. This suggests that anisotropic growth mostly vanishes if the non-uniform stress is alleviated which was also successfully captured by our model as after 15 days we found $\omega = 1.13$.

In summary and in correspondence with experimental findings [Helmlinger et al., 1997] [Cheng et al., 2009] our model suggests that non-uniform stress strongly but reversibly influences morphogenesis of growing cell populations. In addition to purely biomechanical interactions that are amplified for example by contact inhibition, stress may be sensed at the molecular level also leading to variations in intracellular growth parameters. [Cheng et al., 2009], for example, found that the mitochondrial pathway [de Freitas et al., 2006] [Adams & Cory, 2007] regulates solid stress induced apoptosis.

### 3.6.8. Cytolysis of apoptotic cells

Cytolysis, which is also designated as osmotic lysis, is a degenerative cellular process that involves the destruction of the outer cell membrane. This causes excess water to move into the cell and ultimately leads to the dissolution of the affected cell. A majority of current assays for measuring cytolysis are based on the detection of changes in plasma membrane permeability and either the subsequent leakage of components (e.g. cytoplasmic enzymes) or uptake of dyes which are normally not able to enter the cell (e.g. Trypan blue or propidium iodide).

In our model we introduced cytolytic processes to validate the robustness of our findings from preceding sections in a more dynamic and regenerative environment. In order to model cytolysis, we assumed that after a certain time $\Delta t_{cl}$ apoptotic tumor cells were dissolved without any remains. In comparison to the preceding sections, where the main fraction of cell proliferation took place at the borders of the

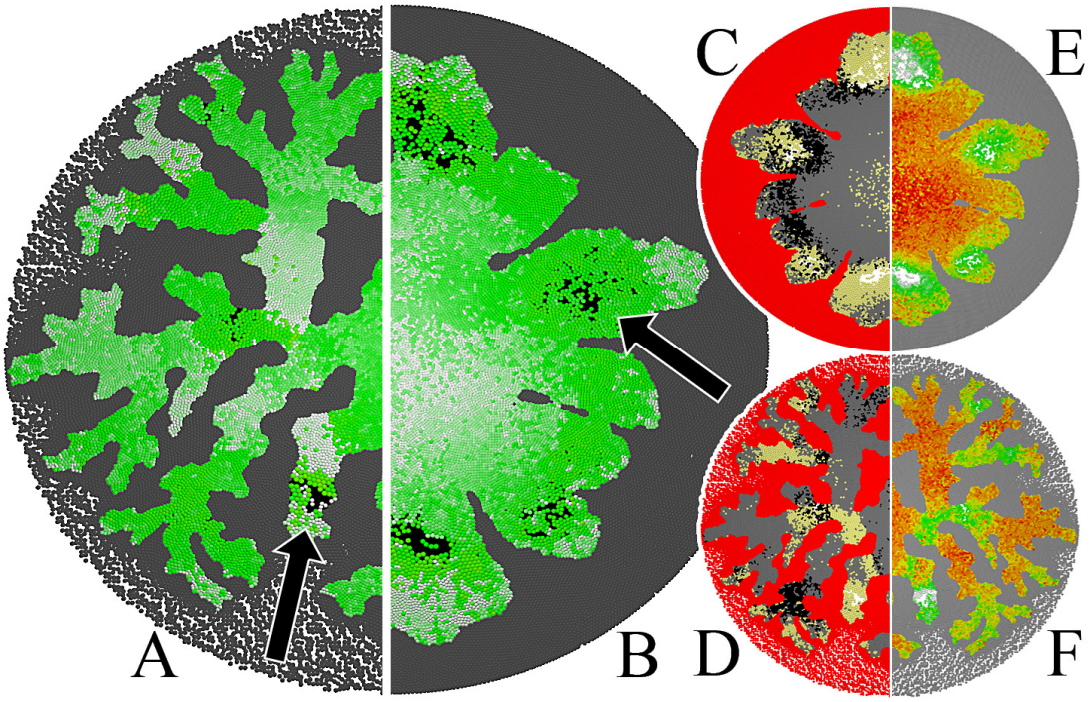


**Fig. 33: Impact of cytolytic cell renewal.**

A: Tumor cell population growing into host tissue (grey) of lowered motility ($D_T = 0.05D_0$) with cytolysis ($\Delta t_{cl}$ = 12h) (see Supporting video 17). B: Reference simulation ($D_T = D_0$, see Fig.27) but with cytolysis (see Supporting video 16). Black patches indicate areas, where recently cells were dissolved and the empty space had not yet been filled by growing cells (black arrows). The coloring is equivalent to Fig.27. C/D: Alternative stainings of (A/B) where the host tissue is colored red, proliferating cells are colored ochre, quiescent cells are grey and apoptotic cells (before cytolysis) are black, empty space remains white. E/F: Alternative stainings of (A/B) where cells are colored according to their compression (red=high, green=low compression). Also see Supporting videos 18 and 19 where $\Delta t_{cl}$ = 4d.

population, the introduction of cytolysis led to much more complex and highly dynamic proliferation activity patterns (Fig.33A,B). We suggest considering the corresponding Supporting videos 16 and 17 as only these fully reveal the dynamics of the changing proliferation patterns. Nevertheless, snapshots of Supporting video 17 shown in Fig.33A/B reveal proliferating regions (colored white) even in the interior of the tumor cell cluster. In this situation of constant cell renewal no tumor cells remained arrested in $G_0$ for a long time (as for example those colored red or black in Fig.27, 28 or 32). The reason for this was that densely packed cells in $G_0$ became apoptotic and then were removed by cytolysis after $\Delta t_{cl}$. Thereafter surviving tumor cells in vicinity of recently dissolved cells (black in Fig.33A/B, see arrows) were able to migrate into the freed space and reenter the cell-cycle because of temporarily lowered cell density and thus lowered pressure (Fig.33 E/F). If there was no additional nutrient limitation of growth as for example in 2D (refer to section 3.5), cytolysis largely destroyed (Fig.33 C/D) the typical layered proliferation pattern (section 3.5.1) of growing cell populations.

Furthermore, the constant cell renewal introduced oscillations to the growth kinetics. Nevertheless, the mean kinetics of population size and radius growth remained the same compared to the corresponding simulations without cytolysis (Fig.31). Moreover, we found no further changes of any of the previously described biomechanical influences of the tumor host tissue on the morphologies and growth dynamics of tumor cell populations. We therefore consider the results presented in previous sections to be robust and especially not depending on cell proliferation to be confined to the border or surface of a multicellular population.

### 3.6.9. Quantitative analysis of dendritic morphologies

In order to systematically quantify the observed morphological changes we measured the fractal dimension of the embedded tumor cell clone. The fractal dimension is a measure for the irregularity of a complex object [Dubuc et al., 1989]. The fractal dimension or, more formally, the Minkowski-Boulingand or box-counting dimension $df$ is given by:

$$df = \lim_{\varepsilon \to 0} \left( \frac{\log N(\varepsilon)}{\log \varepsilon^{-1}} \right) \tag{24}$$

whereby the analyzed structure is overlayed with a grid of element width $\varepsilon$ and $N(\varepsilon)$ designates the total number of grid elements that that structure [Schroeder, 1992].

The radii of our three-dimensional tumor cell populations were too small to establish a robust measure of *df* and therefore we limited the analysis in this section to embedded tumor monolayers. In the following, we used the box-counting method as proposed in [Dubuc et al., 1989] and [Feng et al., 1996] to obtain *df*.

In two dimensions, we expected $N(t) \sim L^2$, which we approximately found for compact populations (Fig.31A, $df = 1.98$). For populations with a more dendritic border we expected $N(t) \sim L^{df}$ with $df < 2$. In agreement with this assumption, we found $df = 1.73$ (Fig.27E) for tumor cell populations growing into a host tissue of reduced motility ($D_T = 0.05 D_0$). Furthermore, we found $df = 1.70$ for populations growing into host tissue composed of smaller cells ($l_T = 10 \mu m$) of increased selective adhesivity ($\zeta_T = 5\zeta_m$) (Fig.30D). The Minkowski-Boulingand dimension further decreased to $df = 1.66$ if we additionally lowered the motility of the embedding cells (Fig.30E).

We further analyzed the morphologies observed in our model simulations by counting the number of dendritic fingers of a growing tumor cell clone in different constant distances from its center of mass. In order to ensure that all morphological features had been fully established, the counting algorithm was applied only to populations whose growth already had been saturated.

We counted the number of dendritic branches by measuring the cell density $d(\varphi,R)$ around a circle of radius $R$ that had its center at the center of mass of the population and $0 \le \varphi < 2\pi$. For cell populations with a dendritic morphology $d(\varphi,R)$ was a complex oscillatory function. We calculated the number of dendritic fingers $B(R)$ and their average width $\alpha(R)$ for different radii (Fig.34) by analyzing the oscillations of $d(\varphi,R)$. We observed both, $B(R)$ and $\alpha(R)$ for a broad range of radii $R$. However, in order to obtain robust results we ignored very small radii at which the morphologies of the populations had not been properly established and large radii near saturation size for which the branching was influenced by the outer environment (Fig.30).

Interestingly, we found the number of dendritic fingers (averaged over 5 realizations) to increase linearly with $R$ (Fig.34) and their width to be constant. This observation was confirmed by the average number of branches $\beta(R)$ within a given segment along a specific radius $R$ which was found to be also approximately constant (Fig.34 inset). For the most dendritic population (Fig.30E) we found an average width of the dendritic fingers of $\alpha(R) = 97.6$ µm, while for less branched populations we found $\alpha(R) = 242.1$ µm (Fig.27D) and $\alpha(R) = 376.4$ µm (Fig.27C).

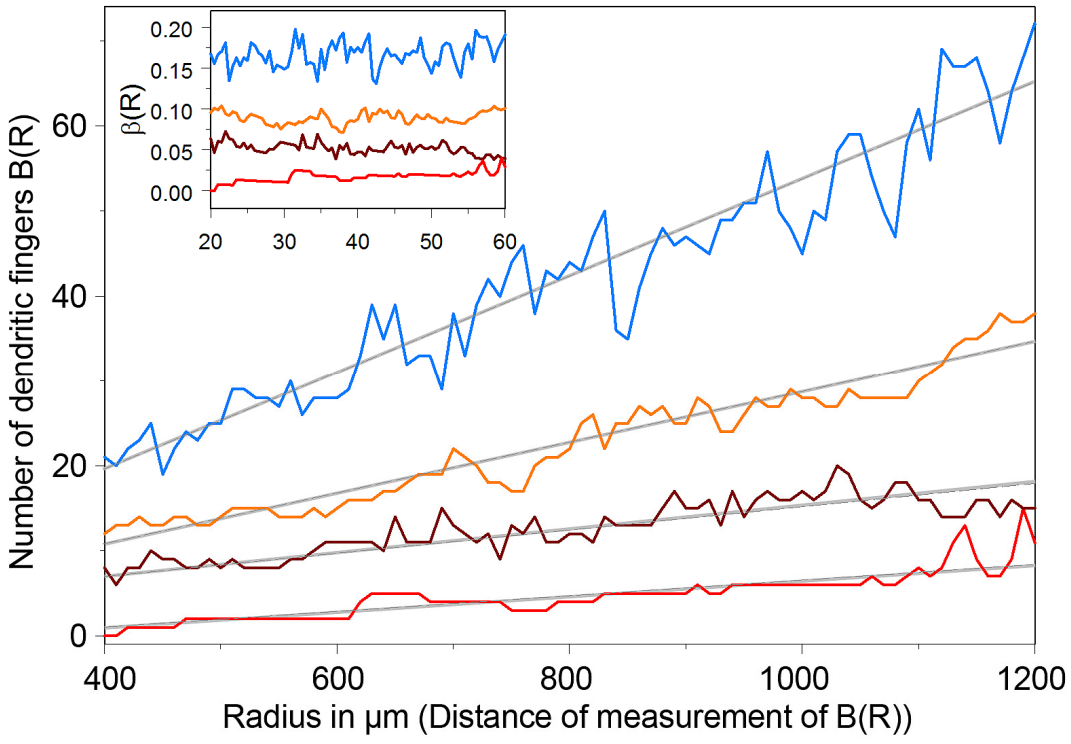


**Fig. 34: Quantitative analysis of dendritic morphologies.**
Number of dendritic fingers at a specific distance $R$ from the center of mass of the tumor cell population. Red line: Population C in Fig.30, Dark red line: Population B in Fig.30, Orange line: Population D in Fig.30, Blue line: Population E in Fig.30, Inset: Average number $\beta(R)$ of dendritic fingers for a given length on a circular segment.

## 3.6.10. Comparison to experimental data

In order to validate our results, we compared our model simulations with experimental data by [Helmlinger et al., 1997] and [Galle et al., 2006]. Both grew multicellular tumor spheroids (LS174T and WiDr cell lines) in an inert matrix (agarose gels). In this experimental setting the growing cell population had to displace the agarose gel in order to further expand. Thereby, the agarose gel was increasingly compressed by the growing cell clone and thus exerted an increasing mechanical stress to the expanding population. [Helmlinger et al., 1997] demonstrated that such solid stress inhibits tumor growth and leads to a saturation of growth. However, if the stress was alleviated by enzymatic digestion of the agarose, the tumor spheroids were found to resume growth after 2-4 days. [Helmlinger et al., 1997] repeated this experiment with BA-HAN-1, rhabdomyosarcoma and MCaIV tumor spheroids and found the results to be robust for different host species or tissue of origin.

The model for tumor cell populations growing into an embedding tissue elaborated in this section represents a natural extension of the experimental setting described by [Helmlinger et al., 1997]. The explicit modeling of the tumor microenvironment using individual objects (granular particles or type B cells) allowed us to study the biomechanical influences of the embedding tissue more realistically in comparison to its experimental approximation by an agarose gel with rather homogenous properties. We consider this increase in detail an important step towards the modeling of *in vivo* systems.

We mimicked the different concentrations of agarose studied by [Helmlinger et al., 1997] and [Galle et al., 2006] by varying the initial density $\rho_\Gamma$ in the host tissue thereby modulating the mechanical stress exerted on the growing cell population. As shown in Fig.31 for two-dimensional tumor cell populations, a variation of $\rho_\Gamma$ changed both, the expansion velocity and the saturation size of the growing cell clones. Interestingly, in a three-dimensional setting we were able to obtain a good agreement (Fig.35) with the experimental results of both [Helmlinger et al., 1997] and [Galle et al., 2006] only by varying $\rho_\Gamma$. Considering the variety of complex biophysical influences of the tumor host tissue on growing cell populations discussed in the preceding sections, however, this indicates that the common experimental models using agarose may not be sufficient to study all important aspects of these influences. Especially the wide variety of influences of the host tissue on tumor morphology can evidently not be captured by agarose-based models.

Additionally, we were able to mimic the experimentally observed resume of growth in case the embedding tissue was removed [Helmlinger et al., 1997]. In our model, we represented the enzymatic digestion of agarose by removing all objects of the host tissue (granular particles or type B cells). Thereafter, due to the alleviation of pressure which previously had been exerted by the embedding tissue, cells that until then had remained in $G_0$ (quiescence) successively reentered the cell-cycle. After 2-3

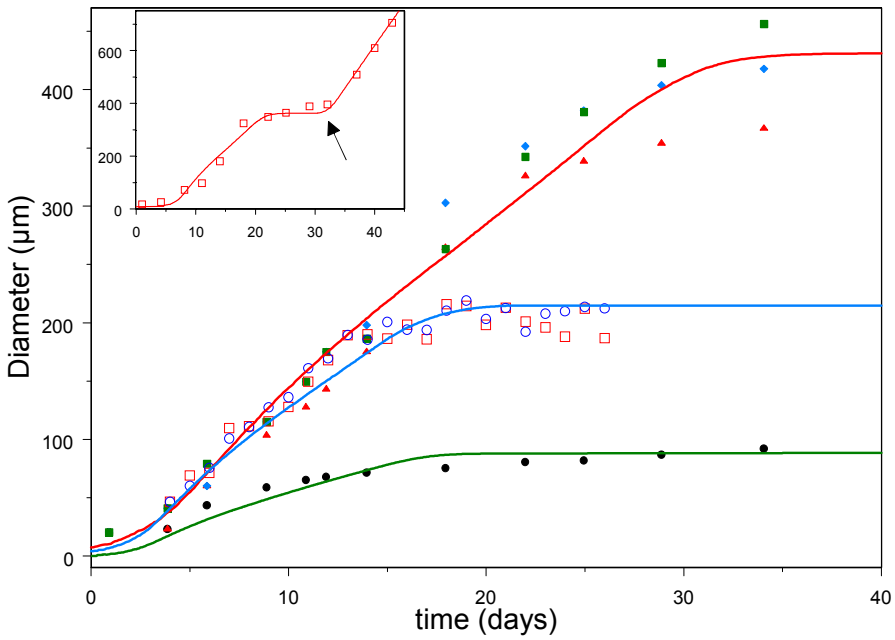


**Fig. 35: Comparison with experimental data in 3D.**

*Filled symbols*: Experiments by [Helmlinger et al., 1997]. Black circles: LS174T spheroids, 1.0% agarose gel, Red triangles: 0.8% agarose gel, Blue diamonds: 0.5% agarose gel, Green squares: 0.3% agarose gel. *Empty symbols*: Experimental data by [Galle et al., 2006]. Red squares: WiDr spheroids, 5.0% agarose gel, Blue circles: 2.5% agarose gel. *Lines*: Model simulations. Red line: Simulation modeling LS174T spheroids in agarose gel of low concentration ($\rho_\Gamma = 207 \cdot 10^3$ cells/mm³), Green line: High agarose concentration ($\rho_\Gamma = 611 \cdot 10^3$ cells/mm³), Blue line: Simulation modeling growth of WiDr spheroids ($\rho_\Gamma = 225 \cdot 10^3$ cells/mm³). *Symbols in inset*: Experimental data on growth alleviation by [Helmlinger et al., 1997] 0.7% agarose gel, *Line in inset*: Model simulation of $\rho_\Gamma = 215 \cdot 10^3$ cells/mm³ and removal of complete host tissue at $t$ = 30d (black arrow).

days a proliferating rim at the surface of the once embedded population had reestablished and led to further growth. The expansion velocity again crossed over to a linear regime and even slightly increased in comparison to the initial growth velocity before saturation. We believe this to be caused by the complete alleviation of mechanical stress due to the removal of all cells of the embedding tissue. Again, these findings were in very good agreement (Fig.35 inset) with experimental data obtained by [Helmlinger et al., 1997].

## 3.7. Discussion and Summary

In the third chapter of this work we established an agent-based biophysical model for the growth of multicellular populations that approximates cells by isotropic, homogeneous elastic adhesive objects. We elaborated the detailed modeling of structural properties of the cells for example concerning their cytoskeleton or cell-cell interactions and complemented them with more dynamic properties of the modeled cells for example regarding cell migration, growth and division. In principle all model parameters can be experimentally determined.

On this basis we studied the growth of multicellular populations thereby successively increasing the degree of realism in our model. We started by modeling two-dimensional monolayer cultures and compared our model to experimental data obtained by [Bru et al., 2003]. We proposed a biomechanical form of contact inhibition of cellular growth that largely explained the experimentally observed growth kinetics and population morphologies. Thereby we reached a remarkable agreement of model and experiment regarding many aspects of monolayer growth.

Subsequently, we crossed over to the third dimension by studying substrate detachment whereby normally two-dimensional monolayers due to the failure of certain control mechanisms expand perpendicular to the monolayer plane. A failure of growth control mechanisms is known to play an important role in the development of cancer [Hanahan & Weinberg, 2000].

Furthermore, we studied the growth of three-dimensional avascular tumor spheroids and additionally included nutrient diffusion and consumption into our model. We could show that the previously proposed biomechanical form of contact inhibition also determines the growth kinetics of tumor spheroids and that the nutrient concentration mainly controls the size of the necrotic core.

In the last section of this chapter we further increased the degree of realism of our model by simulating the growth of multicellular populations embedded in a granular medium of cell-like behavior or in a tissue of other cells. We studied the biophysical impact of this environment on growth dynamics and population morphology of tumor cell clones by systematically varying the motility, density, elasticity, adhesivity and size of the embedding objects. We modeled two- and three-dimensional cell populations and observed Saffman-Taylor-like instabilities leading to fractal interfaces and an increased ability of tumor cells to invade harsh environments if the motility of the embedding cells was small. Furthermore, we observed larger wavelength fluctuations as a consequence of decreased density, increased elasticity, strong adhesion or increased object size of the embedding tissue. We predicted inhibition of growth for specific tissue properties and achieved a good agreement with experimental data by [Helmlinger et al., 1997] and [Galle et al., 2006].

In general, the comparison with experimental results is especially helpful to identify in how far cells may be controlled by simple, mainly physically motivated influences and at which point "intelligent" regulation mechanisms that have emerged on the

time scale of evolution control the properties of a cell. For example, we found that the fraction of apoptotic cells in the interior of a cell population was significantly reduced if cells that became quiescent as a response to mechanical stress actively down-regulated their elasticity. Such active regulation of the physical properties of the cells may also explain the decrease of apoptosis at increased stress observed by [Helmlinger et al., 1997] which without active regulation could not be explained by our model. Nevertheless, despite we currently did not yet consider active regulation and angiogenesis that are known to take place *in vivo*, we were able to mimic experimental data *in vitro* for example by [Helmlinger et al., 1997] and [Galle et al., 2006] very precisely. Therefore, we believe our model for tumor spheroids growing into embedding tissue to be an important step in the direction of the *in vivo* situation.
However, in order to establish a model for a specific *in vivo* situation that would exhibit a tremendously increased predictive strength, one cannot solely relate to published data. We believe that a very close coupling of experimental data including three dimensional *in vivo* imaging techniques and modeling is required to iteratively advance the model also by refining the experimental techniques and stimulating new informative experiments. In the next chapter of this thesis we elaborate an example that follows this strategy by investigating the fascinating process of liver regeneration.

# 4. Modeling the regenerating liver lobule

## 4.1. Introduction

### 4.1.1. The liver

The liver is the largest solid organ of the human body [Chisari et al., 2001]. It is located in the upper left quadrant of the abdominal cavity (Fig.36A) and consists of two main (left and right) and two accessory (quadrate and caudate) lobes (Fig.36B,C). Alternatively, the liver can be subdivided into sectors and segments with afferent and efferent blood supply and biliary channels. This functional description of liver anatomy was first described by Claude Couinaud [Couinaud, 1954] [Sutherland & Harris, 2002]. The sectors of the liver are considered independent as there is no collateral circulation between them [Burt et al., 2006]. Segments are numbered clockwise from II to VIII and the caudate lobe represents segment I. This specific partitioning corresponds to the many functions of the liver of which until today over 500 different have been identified. The most prominent functions are processing of digested food from the intestine and converting it into energy, plasma protein synthesis and the production of bile, cholesterol and hormones [Elias & Sherrick, 1969]. The liver also plays a vital role in fighting infections by mobilizing macrophages which in the liver are known as Kupffer cells. It contains over 50% of all macrophages in the human body. Furthermore, the liver stores glycogen, iron, vitamins and other essential chemicals and thereby regulates their concentrations in the blood [Kuntz & Kuntz, 2008]. One of the most important functions of the liver, however, is the detoxification of blood. The blood from the intestine contains high levels of bacteria, bacterial endotoxins, antigen-antibody complexes and other toxic substances [Chisari et al., 2001]. A healthy liver almost completely filters these harmful organisms and substances by specialized metabolization and secretion processes. A complete failure of this detoxification functions could be lethal within 24 hours.

On a smaller length scale, the liver is organized in repetitive functional units called liver lobules (Fig.36D,E). These lobules mainly consist of hepatocytes (liver parenchymal cells), endothelial (sinusoidal) cells, Kupffer cells, stellate (Ito) cells, oval cells and bile duct cells [Fausto & Campbell, 2003] [Burt et al., 2006]. The most common cells in the liver are hepatocytes which account for approximately 80 - 90 % of the liver mass [Cunningham & Horn, 2003] [Taub, 2004].

In humans after the age of five years most hepatocytes are arranged in one-cell-thick columns, commonly designated as hepatic plates or muralium simplex (green in Fig.36D,E) [Elias & Sherrick, 1969]. This specific columnar architecture maximizes contact between blood and hepatocytes [Chisari et al., 2001].

The liver is provided with a dual blood supply: branches of both, the hepatic artery (bringing highly oxygenated blood) and portal vein (transporting blood to the liver from the intestine) guide blood to the periportal regions of the liver lobules. From there it flows through microvessels along the hepatocyte columns that are lined by

fenestrated endothelial cells usually named sinusoidal cells (yellow in Fig.36D) and drains into the central vein. These microvessels are called sinusoids. Furthermore, the lobules contain bile ductules that carry bile away to larger bile ducts [Michalopoulos & DeFrances, 1997] (Fig.36D,E).

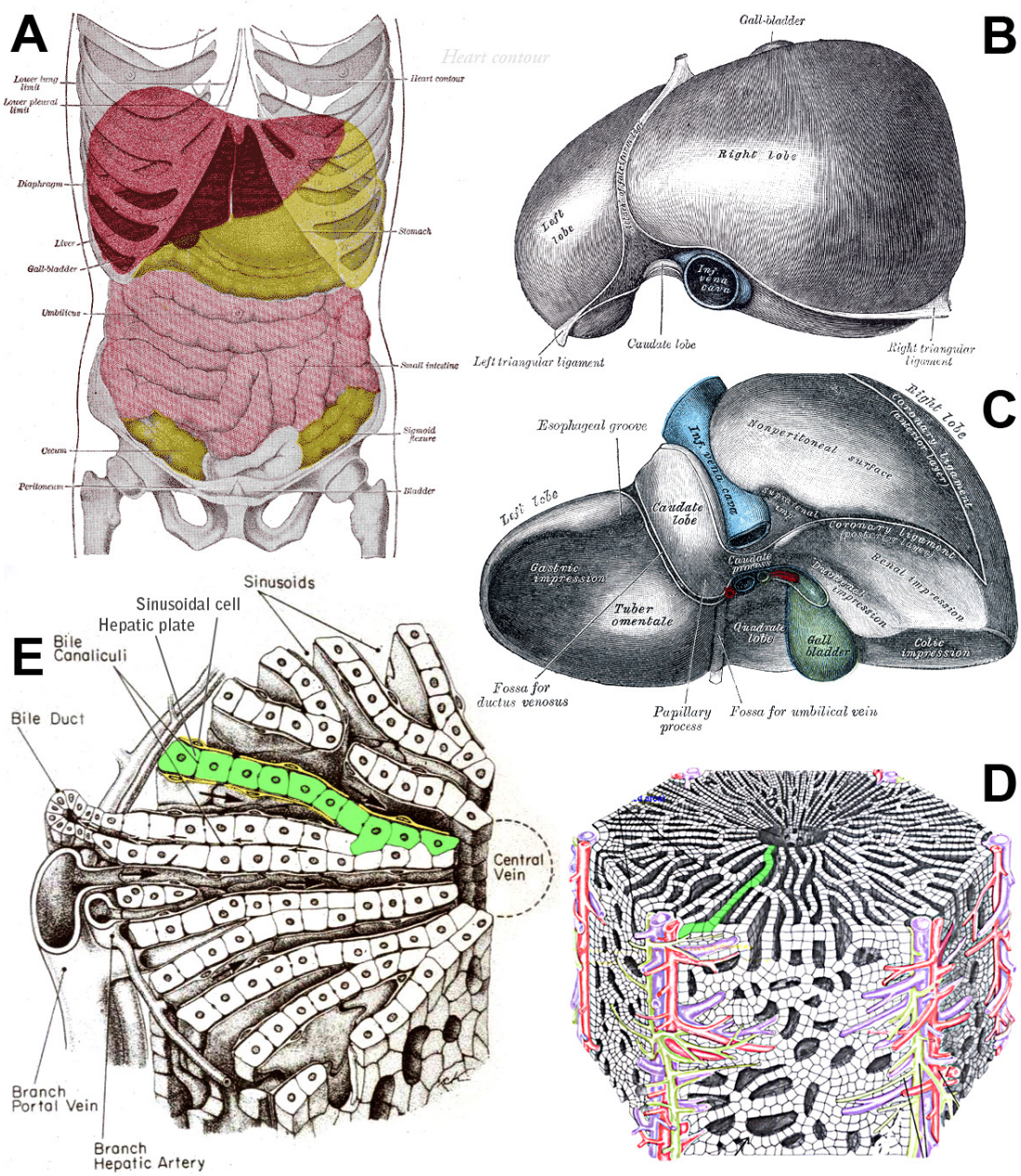


**Fig. 36: Liver anatomy and the liver lobule.**

A: Anterior (front) view of the localization of the liver (dark red) in the human abdominal cavity. B: Superior (top) view of the liver. C: Inferior (bottom) view. A-C from [Gray, 1998]. D,E: Schematic illustration of a liver lobule (from: [www, 10]).

### 4.1.2. Liver regeneration after intoxication with $CCl_4$

The liver has the fascinating capability to regenerate up to 80% of its mass and restore its functionality after intoxication, infection, injury or surgical resection. This unique property of the liver has likely been known for over two thousand years. The myth of Prometheus indicates that, for example, the ancient Greeks knew about liver regeneration. In the Greek mythology Prometheus is a Titan who stole the fire from Zeus and gave it to the mortals. As a consequence, Zeus punished Prometheus by having him chained to a rock while an eagle ate his liver every day only to have it regenerate in the night and to be eaten again the next day [Hesiod, 700 BCE] [Frazer, 1983] (Fig.) . Prometheus first appeared in the poem *Theogony* (Greek: *Θεογονια* ) that is attributed to the Greek poet Hesiod who lived in the eighth century before the Common Era.

**Fig. 37: Liver regeneration in Greek mythology.** A kylix (drinking cup) from Sparta dated 550 BCE showing figures from Greek mythology. Left: Atlas, a Titan that holds the world on his shoulders, Right: Prometheus, whose liver is being eaten by an eagle.

Liver regeneration presumably has evolved to protect animals from the consequences of liver loss caused by food toxins [Michalopoulos & DeFrances, 1997] [Fausto, 2000] [Michalopoulos & DeFrances, 2005] [Michalopoulos, 2007]. Since the first description of major liver resection in [Keen, 1899] the understanding of hepatic anatomy and operative techniques have improved considerably [Helling, 2006]. Today, the mechanisms of liver regeneration are increasingly studied on a functional, cellular and molecular level [Pahlavan et al., 2006]. Many insights are gained by experiments studying liver regeneration after partial hepatectomy (HPx) and intoxication in animals and *in vitro* cell cultures [Michalopoulos & DeFrances, 1997] [Sato et al., 1999] [Blindenbacher et al., 2003]. A typical way to experimentally induce a loss of hepatic tissue *in vivo* is by administration of hepatic toxins. Carbon-Tetrachloride ($CCl_4$) is often used for that purpose [Lafdil et al., 2006] [Nussler et al., 2006] [Hengstler et al., 2005] [von Mach et al., 2004]. $CCl_4$ causes hepatocyte necrosis primarily in the peri-central areas of the liver lobules, because only peri-central cells express CYP2E1 that metabolically activates $CCl_4$ [Gómez et al., 2006].

In contrast to other tissues, such as the bone marrow or skin, regeneration in the liver does not depend on a small group of progenitor or stem cells [Michalopoulos & DeFrances, 1997] [Michalopoulos & DeFrances, 2005] [Michalopoulos, 2007]. In general, regeneration is carried out by proliferation of the remaining mature hepatocytes. Additionally, the other hepatic cell types, namely biliary epithelial cells, fenestrated endothelial cells, Kupffer and Ito cells also proliferate contribute to the regeneration of the lost hepatic tissue. However, liver regeneration after toxic insult is not only a matter of cell proliferation but also of the capacity of the new cells to organize themselves in the characteristic three-dimensional columnar architecture that is found in healthy liver lobules (muralium simplex) as described in the previous section. In order to guarantee liver function this architecture has to ensure that the blood can freely flow from the portal vein through the sinusoids into the central vein within each liver lobule, and that the arrangement of the new liver cells facilitates maximum exchange between the blood and the hepatocytes (Fig.36D,E).
Recent research on liver regeneration has focused on molecular pathways and mechanisms involved [Michalopoulos, 2007] [Juskeviciute et al., 2008]. In contrast, considerably less is known about how liver cells coordinately behave to restore the described functional lobule architecture and thus many of the fundamental mechanisms underlying the complex process of liver regeneration remain to be elucidated.

### 4.1.3. Systems biology of the liver

Contemporary hepatology roots in the clinical descriptions of the ancients that inspired the classical works of the French and German schools of the 19th century [Chisari et al., 2001]. The influence of Rudolph Vichow [Virchow, 1858] and those who followed dominated the studies of the liver until the 1950s when biochemistry increasingly elucidated the structure and regulation of hepatic function.
In the last decades, amazing advances in cellular and molecular biology, immunology, chemistry, biophysics, mathematical biology and computer science have greatly facilitated our understanding of liver biology and pathobiology and have led hepatology to exciting discoveries.
Many of the questions that still remain are of pronounced multidisciplinary nature and thus require interdisciplinary collaborations to be answered. A systems biology approach (refer to section 1.1) that strives for a larger, system-level perspective [Kitano, 2002b], also by combining knowledge from different scientific disciplines, seems to be ideally suited to gain insights into the complex processes that determine liver regeneration.
In the following chapter 4 of this work we combined recent advances in biology, physics and computer science to iteratively set up the first single-cell-based three-dimensional model of liver regeneration. We used this model to study liver lobules after intoxication with $CCl_4$ and were able to show how a systems biology approach

can lead to novel insights and a deeper understanding of the complex process of liver regeneration.

In order to reach this goal, we adapted the agent-based model used in the previous chapter to the liver domain. As a first step, we set up a two-dimensional model of a schematic liver lobule to introduce and study the basic mechanisms of liver regeneration in a simple and very controllable 2D environment (section 4.2). In the next section 4.3, we extended this preparatory work and set up a more detailed three-dimensional model to obtain more exact and verifiable results. We closely coupled this model to experimental data obtained by bright field and confocal laser scanning microscopy. Furthermore, we showed how data from both micrographic techniques can be made accessible to spatial modeling by image processing, reconstruction and analysis techniques (section 4.3.2). We then iteratively improved the model by comparison with experiments that were directly stimulated by our model predictions. In summary, the described combination of image processing, quantitative image analysis, modeling and experiments (all in 3D) represents an exemplary interdisciplinary systems biology procedure that enabled us to elucidate a yet unknown mechanism that we believe is essential for successful liver regeneration.

## 4.2. Modeling liver regeneration in 2D

### 4.2.1. Model extensions

Single-cell-based models are particularly suited to represent the spatio-temporal multicellular organization processes within the complex architecture of a liver lobule since they permit to directly relate to spatial structures that vary on the length scale of individual cells [Drasdo, 2000] [Drasdo & Löffler, 2001] [Meineke et al., 2001] [Drasdo & Hoehme, 2005] [Drasdo et al., 2007]. In order to adapt the model elaborated in the previous chapter to the liver domain and create a simple two-dimensional representation of a single lobule, we had to implement only minor changes and additions to consider the specific situation in the liver. In the next sections we describe these new aspects that involve lobule architecture (section 4.2.1.1.), hepatocyte polarity (section 4.2.1.2.) and the dynamics of the intoxication and regeneration process (section 4.2.1.3.).

#### 4.2.1.1. Lobule architecture

A healthy liver typically consists of approximately $10^3$ (mouse) – $10^6$ (human) liver lobules (section 4.1.1, Fig.36D,E). Several concepts for the histological description of these repetitive functional units exist. Kiernan described the "classical hepatic lobule" with portal tracts in its periphery and a central vein in its center [Kiernan, 1833] while Mall proposed the "portal lobule" by focusing on the portal tract [Mall, 1906]. Based on vascular injection studies Rappaport and co-workers introduced the concept of the "liver acinus" that still described the liver as composed of segments of several hepatic lobules but had as its central axis a terminal branch of the portal vein, hepatic artery, and bile duct [Rappaport et al., 1954]. Based on detailed angioarchitectural studies, Matsumoto and co-workers refined the concept of Kiernan and implied that the periportal tracts of the lobules form a three-dimensional continuity, while in their central area discrete branches establish [Matsumoto et al., 1979] [Matsumoto & Kawakami, 1982]. Later, this description of lobule histology was validated by several histological studies [Lamers et al., 1989a] [Lamers et al., 1989b].

Since after intoxication with $CCl_4$ similar processes occur in all affected liver lobules, we modeled only a single lobule according to the concept described in [Matsumoto & Kawakami, 1982]. Accordingly, we assumed a hexagonal lobule shape with a central vein in the center of the hexagon and three portal triads at three of its edges (Fig.38C).

Despite liver lobules are composed of a number different cell types, in the two-dimensional model elaborated in this section, we only considered hepatocytes. Nevertheless, hepatocytes are the main constituents of a typical liver lobule and account for approximately 80 - 90 % of the liver mass [Cunningham & Horn, 2003] [Taub, 2004].

As described in the last section, lobules are pervaded by a complex network of small blood vessels that connect the portal tract with the central (centrilobular) vein. These sinusoids are composed of a discontinuous layer of fenestrated endothelial cells.

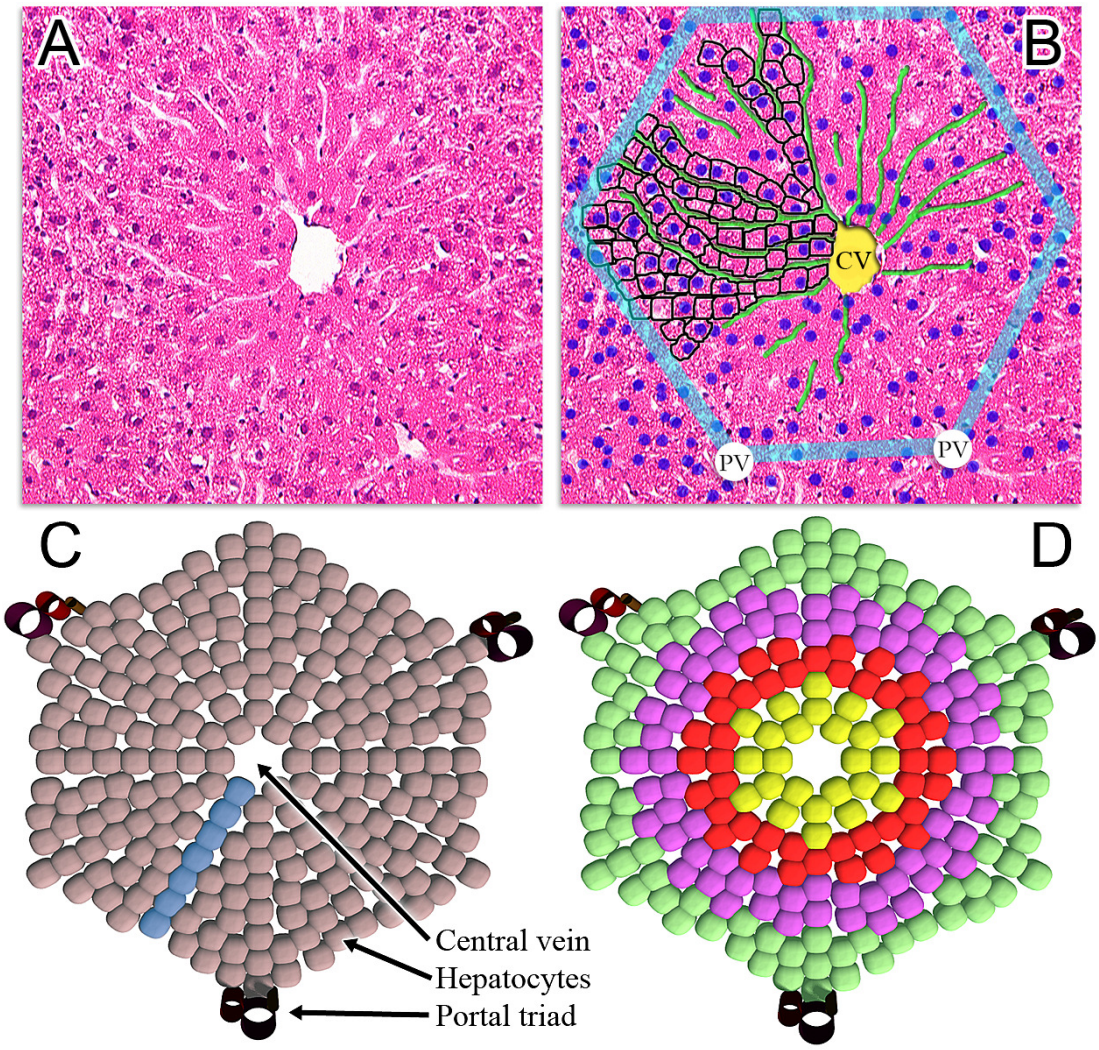


**Fig. 38: Reconstruction of a schematic liver lobule.**

A: Bright field micrograph of a Hematoxilin-Eosin stained liver section. B: Schematic lobule in which important functional elements are highlighted. The blue dots denote hepatocyte nuclei. CV(PV) denotes the position of the central (portal) vein. A selection of clearly visible sinusoids is highlighted in green. In general, they are radially oriented towards the central vein. Sinusoids coming from the PV merge and thereby approximately maintain sinusoid density. The position of the lobule border is marked by cyan straight bars indicating the approximately hexagonal shape of the lobule. Despite the fact that hepatic plates are difficult to follow in 2D, the location of the cell nuclei visible in a particular slice confirms that a cell-column between two adjacent sinusoids is typically one-cell thick. C: Schematic liver lobule in a computer simulation. Cells accentuated in blue color illustrate the typical arrangement of the hepatocytes in hepatic plates D: We subdivided the lobule into three zones, a central zone (red) close to the cells are assumed to die as a consequence of intoxication by $CCl_4$ (yellow), a mid-zone (violet) and a peri-portal zone (green) to directly compare the proliferation pattern to the experimental observations by [Gebhardt & Burger, 1987] shown in Fig. 40.

Oxygenated blood originating from the hepatic artery and deoxygenated, nutrient-laden blood from the portal vein pours into the sinusoids and mixes as it flows from the portal tracts to the central vein. In contrast to the three-dimensional model later introduced in section 4.3, in this section we did not explicitly consider sinusoids and only modeled larger blood vessels. Biomechanical interactions among hepatocytes and between hepatocytes and veins were modeled utilizing the same elastic models (extended Hertz- and JKR-model) that were used for cell-cell interactions in chapter 3 of this thesis.

As described before, hepatocytes and endothelial cells that line the sinusoids together form a specific architecture, where the hepatocytes are arranged in hepatic columns (Fig.36D,E, Fig.38) [Elias & Sherrick, 1969] to maximize contact between blood and hepatocytes [Chisari et al., 2001]. We mimicked this specific columnar architecture (Fig.36D,E, Fig.38) by initially arranging the model cells in columns concentrically radiating from the central vein (blue in Fig.38C).

In this section, the characterization of a typical, average liver lobule (Fig.38) was preliminarily performed by determination of (i) the mean number of hepatocytes between the central vein and the portal tract, (ii) the mean size of the hepatocytes and (iii) the mean number of hepatocyte columns in the inner, midzonal and peripheral ring of the lobule using bright field micrographs of liver cross-sections (Fig.38A/B). This resulted in key features of a typical liver lobule (Tab.2) that were used to set up a schematic model lobule in 2D (Fig.38C) which served as initial state for all model simulations in this section. In addition to the estimation of the model parameters from liver cross-sections, we parameterized our model by measurable quantities from published experimental data (for a comprehensive summary of all parameters refer to Appendix 5).

We are aware that several details of this schematic lobule deviate from genuine liver lobules. Besides sinusoids were not considered, for instance the diameter of the hepatocytes is known to vary and hepatocyte columns generally are not arranged in straight but in more irregular and three-dimensional chains.

**Table 2: Key parameters of the schematic liver lobule in 2D.**

| Parameter | Value | Description |
|---|---|---|
| $R_L$ | 9 cells | Average number of hepatocytes between the central vein and the portal tract |
| $R_C$ | 25 µm | Average size of the hepatocytes |
| $NC_{pv}$ | 22 columns | Mean number of hepatocyte columns in the inner ring of the lobule (also see Fig.36D) |
| $NC_{mz}$ | 36 columns | Mean number of hepatocyte columns in the midzonal ring of the lobule |
| $NC_{pp}$ | 45 columns | Mean number of hepatocyte columns in the peripheral ring of the lobule |

However, note that the described 2D model represented only the first step towards a realistic 3D model (section 4.3). But we will show that already this minimalistic approach in 2D was able point in the direction of several key factors of successful liver regeneration.

4.2.1.2. Hepatocyte polarity

In close relation to their numerous metabolic functions, hepatocytes are known to have specialized membrane domains that, for example, are responsible for sinusoidal transport or bile canalicular secretion [Depreter et al., 2002]. The existence of these functionally diverse membrane domains is termed hepatocyte polarity. In hepatocytes, these domains are typically classified in (1) apical or bile canalicular and (2) basolateral domains [Chisari et al., 2001]. Apical domains are morphologically characterized by the existence of microvilli and junctional complexes while basolateral domains are typically in contact to the blood [Bartles et al., 1985] [Maurice et al., 1994]. Experiments with hepatocyte-sinusoidal cell co-cultures suggested that hepatocyte polarity also influences selective cell-cell adhesion [Hoehme et al., 2009].
In the 2D model, we phenotypically represented hepatocyte polarity by introducing a specific type of hepatocyte adhesion that depended on the location of the membrane domains that in turn was determined by the orientation $\psi$ of the hepatocytes. We studied two cases: For (A) isotropic (non-polar) hepatocytes we assumed the interaction forces between adjacent hepatocytes to only depend on the distance but not on the orientation of the cells (Fig.39A). This situation corresponds to the model elaborated in section 3.2. For (B) polar hepatocytes, however, we assumed that cell adhesion molecules were placed only in certain membrane domains of the hepatocyte

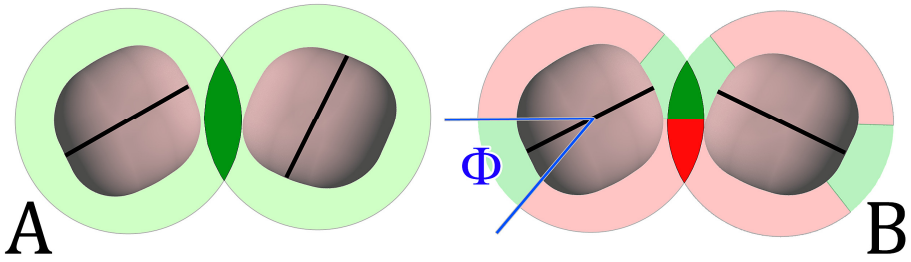


**Fig. 39: Hepatocyte polarity.**
The distribution of adhesion molecules on the surface of the hepatocytes is denoted by light green color (light red = no adhesion molecules). Dark green color illustrates the part adhesive region that contributes to cell-cell interactions between the two exemplarily shown cells (dark red = no adhesive interaction in this region). Straight lines indicate the orientation of the cells. In case (A) of an isotropic distribution of adhesion molecules, the strength of cell-cell adhesion is independent of cell orientation. In case (B) of an anisotropic distribution of adhesion molecules, however, cell-cell adhesion depends on the relative orientation of the cells. Here, hepatocytes are considered to be polar, whereby the size of the light green region in (B) determines the degree of polarity (in our simulations $\phi = 15^{\circ}$).

surface (Fig.39B) [Drasdo et al., 2007]. The interaction force $\underline{F}_{ij}^{pol}$ between adjacent polar cells was then proportional to the overlap area of the membrane regions that were covered with adhesion receptors:

$$\underline{F}_{ij}^{pol} = \frac{A_{ij}^{adh}}{A_{ij}} \underline{F}_{ij} \tag{25}$$

where $A_{ij}^{adh}$ denotes the overlap area of the adhesive membrane regions, $A_{ij}$ the total contact area and $\underline{F}_{ij}$ the interaction force if cells were isotropic (case A). Note that the strength of adhesion was maximal if the adhesive regions completely overlapped. The size of the adhesive surface area further depended on the angle $\Phi$ that determined the proportions of apical and basolateral membrane regions (blue color in Fig.39).

In case (B) where we considered polar hepatocytes we permitted cell orientation to change which effectively corresponds to an active relocation of the membrane domains. For simplicity we modeled this by energy minimization which can be shown to be an alternative to forced-based single-cell dynamics [Drasdo et al., 2007]. For this purpose each cell was rotated within a time period $\Delta t_{rot}$ by an angle $\theta$ ($|\theta| \ll 2\pi$). The probability $P_{Rot}$ that this orientation change in 2D was accepted depended on the resulting energy change $\Delta V$ and was calculated by $P_{Rot} = \min(1, e^{-\Delta V / F_T})$, whereby $\Delta V = V$(after rotation) – $V$(before rotation) and $F_T$ was a reference energy [Drasdo & Hoehme, 2005]. Furthermore, $V$ was linked to the force $\underline{F}_{ij}$ by $V = \sum_{ij, i \neq `j} V_{ij}$ and $\underline{F}_{ij} = -\frac{\partial V_{ij}}{\partial d_{ij}}$ where the sum was formed over all pairs of cells $i$ and $j$ and $d_{ij}$ was the distance between cells $i$ and $j$. This definition ensured that orientation changes that led to a decrease of the configuration energy were always accepted while those which led to an energy increase were only accepted with probability $e^{-\Delta V / F_T}$. For isotropic cells (case A) we did not consider orientation changes since they did not modify the total energy stored in the multicellular configuration.

### 4.2.1.3. Hepatocyte migration and lobule veins

We modeled the complex dynamics of hepatocyte migration as a friction-dominated over-damped motion with a stochastic contribution by Langevin-type equations of motion for each cell as described in section 3.2 [Drasdo & Hoehme, 2005] [Drasdo et al., 2007] [Hoehme et al., 2007]. Additionally, we considered interactions of hepatocytes with the central and portal veins of the lobule. The elastic properties of these relatively large blood vessels were modeled analogously to cell-cell

interactions using the extended Hertz model. Thereby for isotropic cells (case A), the velocity of cell *i* was determined by:

$$\zeta \underline{v}_i(t) = \sum_j \left( \varsigma_{ij}^C (\underline{v}_j(t) - \underline{v}_i(t)) + \underline{F}_{ij}^C \right) + \sqrt{2(\varsigma_i^C)^2 D^C} \cdot \underline{\eta}_i(t) + \sum_z \underline{F}_{iz}^{CV} + \sum_m \underline{F}_{im}^{PV} \quad (26)$$

where $\underline{v}_i(t)$ denotes the velocity of hepatocyte *i*, $\varsigma_{ij}^C$ the friction between hepatocytes *i* and *j*, $\underline{F}^X$ summarizes the repulsive and adhesive forces between hepatocytes *i* and *j* (X=C), between hepatocyte *i* and central vein *z* (X=CV) and between hepatocyte *i* and portal vein *m* (X=PV). Typically, *m*=3 and *z*=1. $\varsigma_i^C$ denotes an effective friction between hepatocyte *i* and its surrounding extra-cellular matrix and $\underline{\eta}_i(t)$ was modeling an uncorrelated noise term.

In case we considered polar hepatocytes (case B), the velocity of hepatocyte *i* was determined by:

$$\zeta \underline{v}_i(t) = \sum_j \left( \varsigma_{ij}^C (\underline{v}_j(t) - \underline{v}_i(t)) + \underline{F}_{ij}^C(\psi_{ij}) \right) + \sqrt{2(\varsigma_i^C)^2 D^C} \cdot \underline{\eta}_i(t) + \sum_z \underline{F}_{iz}^{CV}(\psi_i) + \sum_m \underline{F}_{im}^{PV}(\psi_i) \quad (27)$$

whereby in contrast to Eqn.26 forces explicitly depended on the orientation $\psi_{ij}$ of hepatocyte *i* and *j*.

#### 4.2.1.3. Intoxication and regeneration process

In a healthy liver almost all hepatocytes remain quiescent (in $G_0$ resting state) and only approximately one cell per thousand undergoes proliferation at any given time [Diehl & Rai, 1996] [Court et al., 2002]. $CCl_4$ administration disturbs this situation and induces cell death in a ring of 2-5 cell layers adjacent to the central vein [Gebhardt & Burger, 1987]. Cell death peripheral of this inner ring was rare and thus was not considered in the model.

Experiments [Gebhardt & Burger, 1987] [Hoehme et al., 2007] show that after $CCl_4$ induced liver damage hepatocytes start to divide in large numbers. In order to analyze this hepatocyte proliferation, we determined the fraction of BrdU positive nuclei in the periportal (pp), midzonal (mz) and perivenous (pv) zone of the lobule (Fig.38D) during different time periods after intoxication (for details refer to section 4.2.2.). The specific design of this analysis was chosen in correspondence with the experimental schedule in [Gebhardt & Burger, 1987]. As shown in Fig.40, initially the highest fraction of BrdU positive hepatocytes was observed perivenous. Later

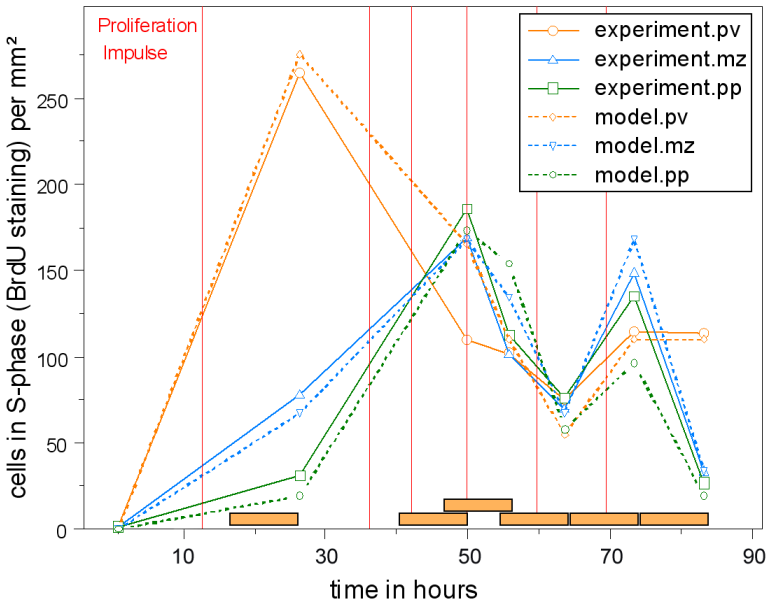


**Fig. 40: Hepatocyte proliferation in experiment and model.**
Number of BrdU-labeled cells per $mm^2$ as published in [Hoehme et al., 2007].

proliferation also increased in the midzonal and periportal zone, which was accompanied by decreased BrdU incorporation in perivenous hepatocytes. This suggests that an intoxication by $CCl_4$ leads to a wave of proliferation that starts in the surviving hepatocytes adjacent to the necrotic lesion and continues to the midzonal and peripheral cells. Therefore, the probability for a particular hepatocyte to divide at a certain point in time seems to depend on its location within the lobule.

We directly integrated these experimental findings into our model by actively stimulating hepatocyte proliferation (red vertical lines in Fig.40) such that the experimental situation was closely mimicked (Fig.40). We assumed that hepatocytes, after receiving a stimulus, enter proliferation phase and thereafter on the average need 10 hours to enter S-phase. Furthermore, we assumed a length of the S-phase of 8 hours and an average intrinsic cell cycle time of $\tau$ = 24h as determined by [Vintermyr & Døskeland, 1987]. In all other aspects, hepatocyte growth was modeled as described in section 3.2.2.

We considered two alternative mechanisms of cell orientation after division. We either assumed (1) that after (or during) cell division cells orient themselves towards the central vein or (2) in a purely random direction. In this section we termed case (1) “directed cell orientation” (DCO) which ensured that cells tended to arrange themselves in the experimentally observed typically concentric hepatic columns. By dropping this assumption in case (2) we studied the consequence of a failure of DCO. We termed this case “random cell orientation” (RCO).

## 4.2.2. Experimental procedures

### 4.2.2.1. Administration of $CCl_4$ and BrdU and preparation of livers

Male Sprague Dawley rats (200-300 g; Charles River) were fed ad libidum with standard diet (Alma 1003, Botzenhart, Kempten, Germany). Liver damage was induced by intraperitoneal $CCl_4$ administration at three subsequent days (day 0: 750 µl/kg; day 1: 750 µl/kg; day 2: 500 µl/kg). $CCl_4$ was dissolved in an equal volume of corn oil. This particular schedule had been chosen, because it guaranteed cell death of all hepatocytes within two to four cell layers from the central vein [Gebhardt & Burger, 1987]. In contrast, an only single injection of $CCl_4$ killed only a fraction of hepatocytes within this region which would render conditions for modeling more difficult. Controls (n=3) received injections of corn oil. In order to study regeneration after $CCl_4$ induced liver damage, hepatocyte proliferation was quantified after administration of 5-bromodeoxyuridine (BrdU). BrdU was administered to cover periods of 10 h. For this purpose five intraperitoneal injections of 80 µg BrdU/g body weight dissolved in physiological saline were given at intervals of 2 h. Six 10 h BrdU exposure periods were analyzed, namely 16-26, 40-50, 70-80, 78-88, 88-98 and 98-108 h after the first injection of $CCl_4$. Three rats were studied for each period.
Preparation of the livers was performed immediately after the 10 h BrdU exposure periods. For this purpose rats were anaesthetized by intraperitoneal injections of phenobarbital (2 ml/kg of a 30 mg/ml stock solution). The livers were perfused by the portal vein with physiological saline for 5 min, followed by perfusion with 30 ml icecold 3.5% paraformaldehyde in PBS. Afterwards, the fixed liver was removed, incubated in 3.5 % paraformaldehyde for 30 min and embedded in paraffin in order to cut 3 µm thick slices. A typical slice representing a liver lobule is shown in Fig.38A, in Fig.38B the characteristic structures within a liver lobule are illustrated.
Hepatocytes from male Sprague Dawley were isolated as described [Reder-Hilz et al., 2004] [Carmo et al., 2004] [Osterod et al., 2001] [Osterod et al., 2002].

### 4.2.2.2. Immunostaining of BrdU and glutamine synthetase

For immunostaining of BrdU paraffin slices were deparaffinized by warming the slices to 45°C followed by a short heating to 65°C in order to liquefy the paraffin.
Subsequently, the slices were washed for 10 min in xylene and hydrated in an ethanol gradient. Endogenous peroxidase was blocked by incubation with 0.5 % $H_2O_2$ in methanol for 30 min. After washing in distilled water, slices were incubated in 1N HCl for 7 min at 60°C followed by washing in ice-cold distilled water. Subsequently, the slices were washed in PBS, pH 7.4, incubated with goat serum (diluted 1:10 in PBS, pH 7.4) for 30 min, washed in a solution of 0.5% Tween 20 in PBS (pH 7.4) for 30 min, incubated with the first antibody (monoclonal mouse anti-BrdU, 1:30; DAKO) for 2 h at room temperature, followed by washing in PBS and incubation with the secondary antibody (sheep anti-mouse IgG, peroxidase coupled;

1:300 in PBS; Boehringer, Mannheim) as indicated by the manufacturer. Slices were washed in Tris buffer (100 mM; pH 7.6) and stained with a solution of 50 mg diaminobenzidine, 200 mg aminotriazole in 100 ml 100 mM Tris, pH 7.6, to which 33 µl 30% $H_2O_2$ were added immediately before use. As soon as a brown stain occurred (usually 4-8 min) slices were washed in PBS, pH 7.4. A similar procedure was applied for immunostaining of glutamine synthetase using a rabbit anti-rat glutamine synthetase antibody. After washing in PBS, pH 7.2 with 1.1 mM $MgCl_2$, incubation with the secondary antibody (donkey anti-rabbit; galactosidase coupled; 1:40 in PBS, pH 7.2 with 1.1 mM $MgCl_2$, Amersham) was performed for 2h at room temperature.
Subsequently, slices were washed in PBS, pH 7.2 with 1.1 mM $MgCl_2$, stained with a 5-bromo-4-chloro-3-indolyl-β-D-galactopyrazoside solution at 37°C for 30 min as described [Bondi et al., 1982]. Afterwards, slices were washed in PBS, pH 7.4, dehydrated in an ethanol gradient and mounted in Eukitt. For evaluation, photos of liver lobules were taken and subdivided into periportal, midzonal and perivenous regions using a procedure described by [Lamers et al., 1989a]. This technique is based on lines connecting the central vein and respective periportal fields. These lines are subdivided into three equal sections (33 and 66% marks) and interconnected at the 33 and 66% marks. In each region the fraction of BrdU positive nuclei and the number of BrdU positive nuclei per $mm^2$ was determined. At least 5000 hepatocytes were evaluated per rat. Mean values and standard deviations of the rats from each treatment group were calculated.

## 4.2.3. Results

### 4.2.3.1. Simulating liver regeneration in 2D

Based on the schematic two-dimensional liver lobule and the corresponding model adaptions discussed in section 4.2.1., we were now able to simulate the regeneration of a model lobule after $CCl_4$ intoxication (Fig.41). Initially, the model parameters were chosen to reflect the *in vivo* situation as closely as possible such that computer simulations and experimental observations were in good agreement (Fig.40). Therefore, in the following the model shown in Fig.41 is referred to as "reference model".

In the computer simulations discussed in this section, the behavior of the hepatocytes within the regenerating liver lobule was mainly controlled by five model parameters:

**(1) Probability of cell division** (denoted by $P_{CD}$) at a defined position within the lobule at a given time. In the reference model, this probability was determined by the above described *in vivo* experiments by [Gebhardt & Burger, 1987] whose results were directly integrated into our model (Fig.40). Accordingly, $P_{CD}$ was calculated by the number of proliferating cells per mm² within each zone of the lobule divided by the total number of cells per mm²

**(2) "Directed cell orientation" (DCO).**

Hepatocytes are typically arranged in columns. We modeled this behavior in 2D by assuming that hepatocytes (initially and after cell division) were oriented towards the central vein. In the reference model (Fig.41) we assumed directed cell orientation (DCO). Alternatively, we studied the case where hepatocyte orientation after division was random (RCO).

**(3) Cell cycle duration.**

In the reference model, according to *in vitro* studies the duration of an average cell cycle was assumed to be 24 hours [Vintermyr & Døskeland, 1987].

**(4) Cell micromotility.** This parameter controlled the velocity of rearrangements necessary for a cell to adapt to changes in its local environment for example due to cell divisions. Furthermore, isolated cells are known to migrate randomly as it has been experimentally observed for hepatocytes [Hengstler, 2008] and other cell lines [Schienbein et al., 1994].

**(5) Cell polarity.** Cells within multicellular configurations tend to maximize their cell-cell contacts since this minimizes the total configuration energy. For isotropic cells this minimum energy configuration is hexagonal [Galle et al., 2003] (Fig.42A), while for polar cells the minimum free energy configuration favors columns [Drasdo, 2000] (Fig.42B).

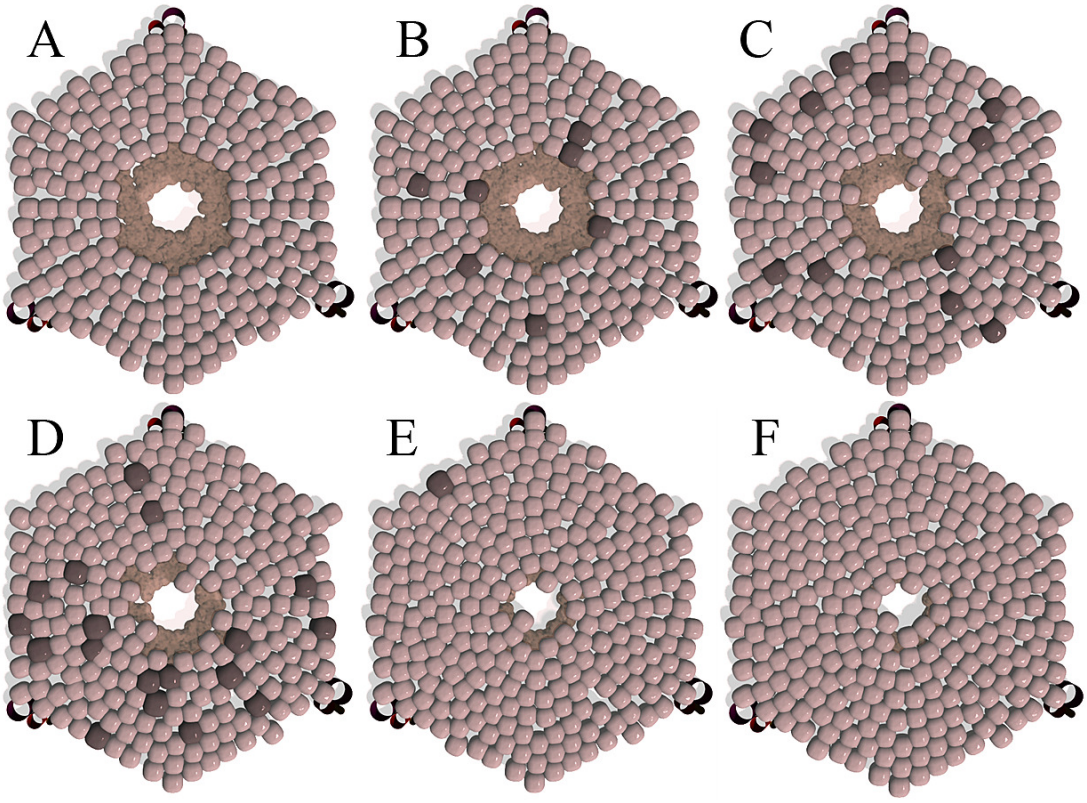


**Fig. 41: Typical 2D model simulation** of liver regeneration after $CCl_4$ intoxication in a schematic liver lobule at A: t=0, B: 1, C: 2, D: 3, E: 4 or F: 7 days. A: After intoxication, an inner ring of hepatocytes dies indicated by brown color. B: This is followed by proliferation (dark brown cells), first close to the central vein, then gradually spreading towards the periportal zone (C-E). F: After seven days the microarchitecture characterized by columns of hepatocytes was almost completely restored (also refer to Supporting video 20).

The reference model simulation mimics a typical experimental regeneration scenario after $CCl_4$ intoxication in an otherwise healthy liver (Fig.41). Initially, an inner ring of hepatocytes dies due to toxic damage and leaves debris, indicated by brown color in Fig.41. Cell death is followed by a wave of proliferation that starts in the surviving hepatocytes next to the inner ring of dead cells and continues to the peripheral hepatocytes. This wave of proliferation initially leads to an increased degree of disorder, but finally the characteristic columnar microarchitecture within the lobule was largely restored within a 7 day process.

4.2.3.2. Variation of key model parameters

In the previous section, model parameters were chosen to reflect the *in vivo* situation in a healthy liver as closely as possible to set up a reference model (Fig.41). In a next step we systematically modified five major parameters in the two-dimensional model in order to study their influence on the regeneration process.

The model allowed predictions of three endpoints:

(i) **The cell mass** in the lobule during regeneration which was approximated by the cellcount and compared to the reference model.
(ii) **The size of the necrotic lesion** in the lobule center. After $CCl_4$ administration cell death around the central vein led to a hepatocyte free area (necrotic lesion) that was closed with a specific velocity and to a certain degree (corresponding to the size of the remaining lesion). The model allowed predictions of the area of the necrotic lesion in a time dependent manner.
(iii) **The microarchitecture** of the liver lobule. The model predicted whether the normal microarchitecture characterized by columns of hepatocytes was maintained or destroyed after the cell count had reached its saturation value.

Reduction of the probability $P_{CD}$ to enter the proliferation cycle (model parameter 1) by 50% resulted in a 15% reduction of the liver lobule mass compared to the reference simulation while a doubling of this probability led to an increase of lobule mass by 30% (Fig.45C). For higher $P_{CD}$ the microarchitecture of the lobule tended towards hexagonal structures. In contrast, a smaller $P_{CD}$ supported maintenance of the columnar structure found in healthy liver, although closure of the central lesion was impaired (Fig.45D).
The influence of directed cell orientation (DCO, model parameter 2) is illustrated in Fig.44 and Supporting videos 20-25, where the situation for DCO was compared to random cell orientation (RCO) for different micromotilities. For RCO, the speed of recovery of the cell count within the lobule after $CCl_4$ intoxication was the same as for DCO (Fig.45A). However, as soon as proliferation took place the characteristic columnar microarchitecture of the hepatocytes was destroyed by cell divisions in random directions which led to a high degree of disorder (Fig.44B,D,F; Supporting videos 23-25). This was accompanied by a slower closure of the central necrotic lesion (Fig.45B). Therefore, we found the orientation of the hepatocytes towards the central vein (DCO) to be of utmost importance for the restoration of the microarchitecture of the lobule.

Modification of the cell cycle duration (model parameter 3) mainly influenced the regeneration speed. Shorter cell cycle duration led to a faster closure of the central necrotic lesion (Fig.45D). However, a decrease in cell cycle duration also increased

the tendency of the hepatocytes to form pathological hexagonal patterns as the hepatocytes had less time to relax disturbances by more frequent cell divisions.
Cell micromotility (model parameter 4) directly affected the speed at which hepatocytes were able to rearrange and migrate to their final location (Fig.44, Supporting videos 20-25). As shown in Fig.44 and Fig.45B, a higher micromotility permitted a faster adjustment to changes in the local cell environment and therefore led to faster closure of central necrotic lesion. This also influenced the microarchitecture of the lobule. On the one hand, if micromotility was too low, the capability of the hepatocytes to find local configurations of low energy, which in case of polar hepatocytes tended to be columnar arrangements, was limited. On the other hand, if the micromotility was too high, the disorder generated by the stochastic movement of the hepatocytes outweighed its positive effects and simultaneously impaired the lobule microarchitecture. Furthermore, after intoxication we found the hepatocytes to preferentially migrate into the direction of the central vein. This active movement was mainly triggered by cell-cell interaction forces.

**Table 3: Influence of main model parameters on different aspects of liver regeneration.**

We compare the influence of the listed parameter variations to the reference model (Fig.41) that reflects the *in vivo* situation in a healthy animal as closely as possible. "+" means that this change has a positive effect on the corresponding, whereas "o" means that there is no effect and "-" indicates a negative effect.

| Model parameter | Change | Regeneration of liver mass | Velocity of closure of the necrotic lesion | Quality (completion) of closure of the necrotic lesion | Restoration of liver microarchitecture |
|---|---|---|---|---|---|
| **1. Probability of cell division ($P^{CD}$)** | Increased | + | + | + | - |
| | decreased | - | - | - | + |
| **2. Directed cell orientation** | enabled | o | + | + | + |
| | disabled (RCO) | o | - | - | - |
| **3. Cell cycle duration** | shorter | o | + | + | - |
| | longer | o | - | - | + |
| **4. Cell micromotility** | increased | o | + | + | - |
| | decreased | o | - | - | - |
| **5. Hepatocyte polarity** | enabled | o | o | o | + |
| | disabled | o | o | o | - |

Hepatocyte polarity (model parameter 5) had only minor influence on the dynamics of the regeneration of the cell mass or the central necrotic lesion but was found to be required to maintain a columnar architecture within the lobule especially on a longer time scale. As shown in Fig.42 and Fig.43 on a larger time scale, isotropic cells tended to arrange into pathological hexagonal patterns, whereas polar hepatocytes in the same situation were able to maintain a columnar arrangement.
The complex influence of each of the five major model parameters on the different aspects of liver lobule regeneration is summarized in Tab.3.

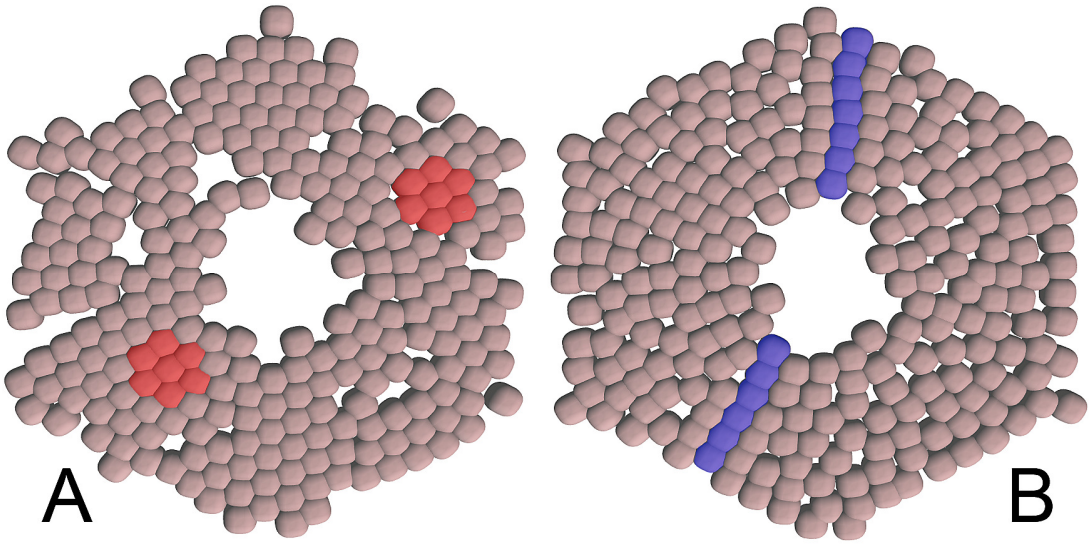


**Fig. 42: Long time behavior of the cell pattern.**
A: For long times (here: 20 days), isotropic cells tended to locally arrange into hexagonal patterns (accentuated in red). This was a consequence of isotropic cell–cell interactions since in two dimensions a cell with six interaction partners had the lowest energy and therefore formed the most stable patterns. However, hexagonal order is experimentally observed only in pathological cases (see Fig.43). B: Polar hepatocytes, in contrast, after 20 days tended to locally maintain columnar patterns (accentuated in blue).

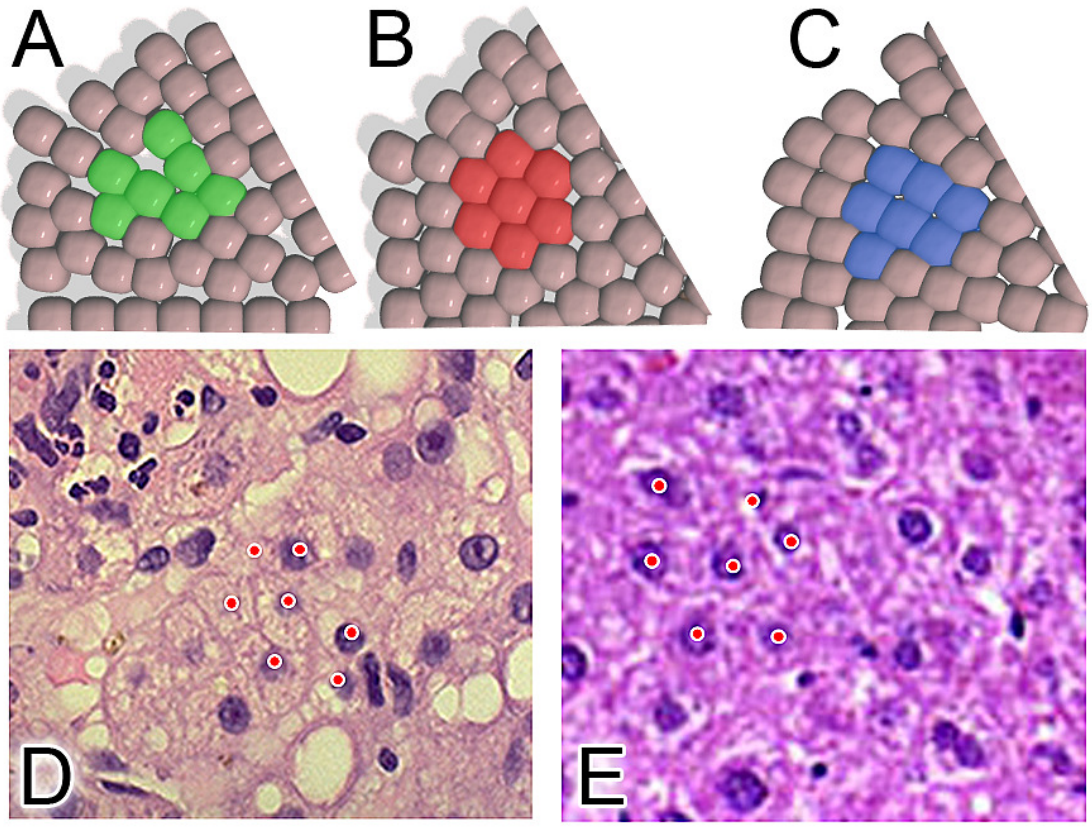


**Fig. 43: Columnar vs. hexagonal hepatocyte arrangement.**
In healthy livers, hepatocytes are arranged in columns. After regeneration, models with 1) increased cell division, 2) RCO, 3) significantly increased or decreased micromotility and 4) isotropic cell-cell adhesion, however, tended to a pathological hexagonal hepatocyte arrangement. A columnar microarchitecture as in healthy livers can only be found after liver regeneration if certain mechanisms were included in the model. A-C show the typical localization of seven model hepatocytes that initially were arranged in columns (green cells in A) but depending on model parameters after regeneration have adopted a pathological, hexagonal (red cells in B, mechanisms 1 + 4) or normal, columnar arrangement (blue cells in C, DCO and polarity). Hexagonal hepatocyte arrangements were also experimentally observed in pathological conditions of the liver, such as D: in cirrhotic nodules (from: [www, 08]) or E: liver adenomas (from: [www, 09])

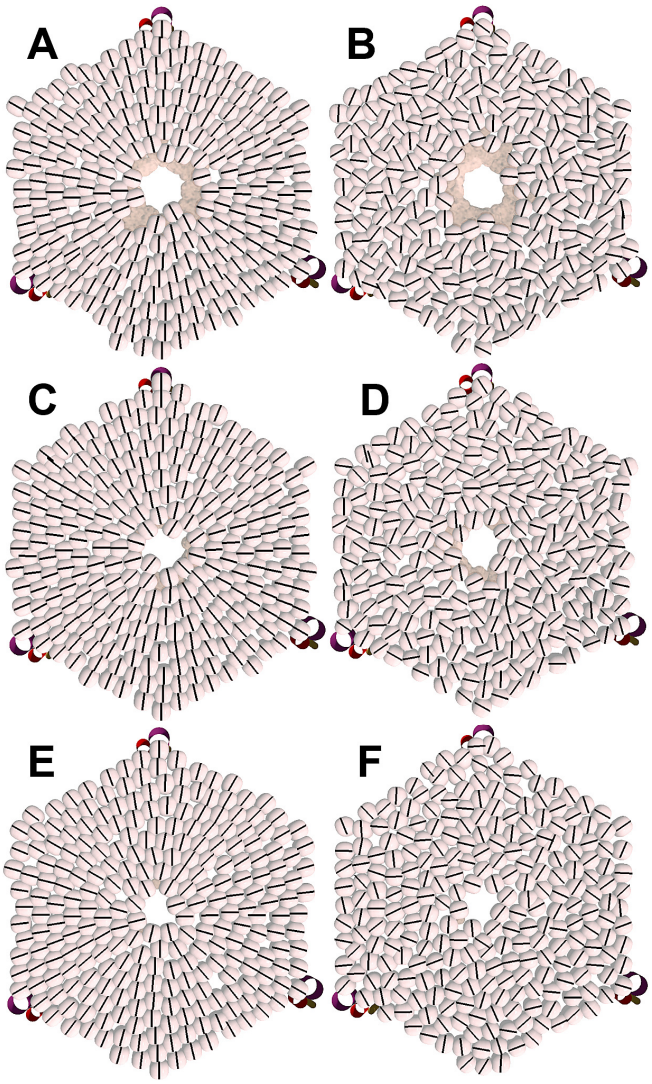


**Fig. 44: Illustration of the influence of DCO** (model parameter 2) **and cell micromotility** (model parameter 4) **on the regeneration process.** The latter was characterized by the effective friction coefficients which were obtained by dividing the coefficients $\zeta \approx 0.1$kg/s used in our reference simulation (C) by a=0.2 in (A,B) and a=5 in (E,F). An increase in the value of parameter "a" corresponded to a decrease in the effective friction coefficient and consequently to an increase in cell motility. In (A,C,E; left column) cell division was oriented towards the central vein (DCO). In (B,D,F; right column) it was random (RCO). The black lines denote cell orientation (compare to Fig. 39). Generally, DCO resulted in a global orientation of cell columns towards the central vein (A,C,E). Otherwise, the normal microarchitecture of the liver lobule was lost (B,D,F). The degree of global orientation towards the central vein was found to be approximately independent of cell micromotility. For all parameter choices the temporal proliferation pattern was in excellent agreement with the experimental observations in [Gebhardt & Burger, 1987]. In none of the simulations cell orientation changes were permitted. In computer simulations where we permitted cell reorientation (not shown), we found the orientation order in A, C, E to be destroyed while the cell positions remained unaffected. Despite cell migration, for DCO the cell orientation towards the central vein was maintained. However, dislocations occurred that led to locally hexagonal pattern as explained in the text.

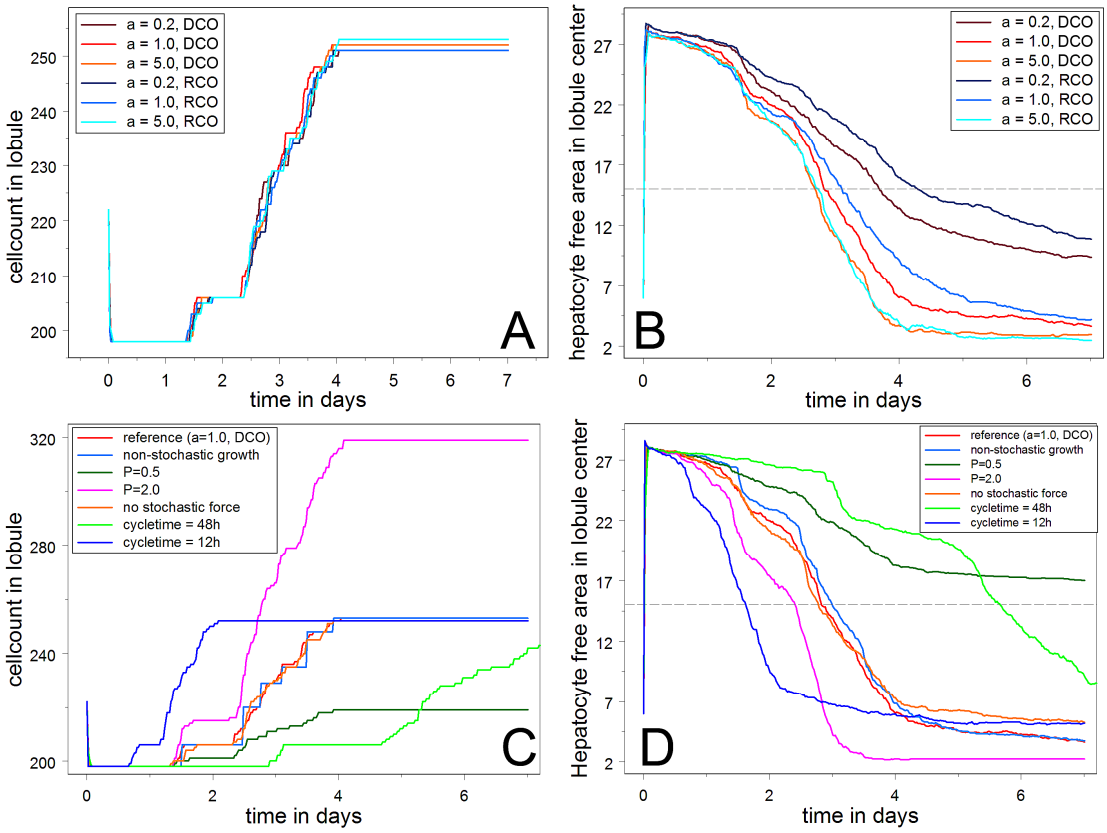


**Fig. 45: Regeneration dynamics in the model**

A: The temporal development of the cell count in a liver lobule during regeneration was found to be insensitive to changes of cell orientation (DCO/RCO) and cell migration. B: The velocity and quality of the regeneration of the initial necrotic lesion was found to increase continuously with increasing ability of the cells to optimize their cell orientation (model parameter 2) and for faster cell migration (model parameter 4). C/D: With increasing $P_{CD}$ (model parameter 1) the velocity and quality of the regeneration also increased (dark green and magenta lines). Stochastic influences in cell movement were found to have no measurable influence (red and orange lines). A decreased cycle time (model parameter 3), however, led to an increased regeneration speed and quality (light green and dark blue lines).

## 4.2.4. Discussion

In this section, we established a spatio-temporal computational model of the liver lobule regenerating after $CCl_4$ intoxication in 2D. Behavior of the cells in our model was mainly controlled by five model parameters, namely (1) probability of cell division, (2) directed cell orientation (DCO), (3) cell cycle duration, (4) cell micromotility and (5) polar cell-cell adhesion. One of the advantages of this minimal model was the possibility to systematically modify these model parameters and predict their influence on specific aspects of the regeneration process in a simplified and thus controllable environment (Tab.3). Due to the two-dimensional setting, the results of the corresponding computer simulations were easy to observe and could directly be compared to experiments.

Within physiologically relevant parameter ranges, we found DCO to be crucial for maintenance of the columnar microarchitecture in the liver lobule. In our model DCO defined the ability of two daughter cells to orient themselves in the direction of the central vein. Elimination of DCO (for example by replacement with RCO) did not influence the regeneration of the lost cell mass but severely impaired the restoration of the liver microarchitecture and led to pathological, hexagonal cell structures. Furthermore, the regeneration of the central necrotic lesion was delayed.
However, although DCO was able to largely ensure a columnar microarchitecture during the regeneration within 7 days, long time simulations showed that after 20 days the columnar pattern had transferred into a locally hexagonal pattern (Fig.42A). This pathological arrangement represents a low state of energy allowing the cells to maximize cell-cell contacts [Galle et al., 2003] whereas healthy columnar structures represent a higher state of cell-cell adhesion energy. Since general multicomponent systems (here a component is a cell) tend to lower their energy, the model predicts that additional stabilizing factors must be active in healthy livers maintaining the columnar structure on a longer time scale.
We found hepatocyte polarity to be a candidate for such stabilizing factor. Elimination of hepatocyte polarity caused an increase in the number of hexagonal structures while its presence in interplay with DCO maintained a columnar structure in the lobule even on a longer time scale (Fig.42B, Fig.43). Elimination of both, hepatocyte polarity and DCO led to a complete loss of columnar architecture and caused severe hexagonal structures (Fig.43B). Similarly but to a lower degree, also increased probability of proliferation (model parameter 1) promoted formation of hexagonal structures. Interestingly, these kinds of structures had been experimentally observed in several pathological states of the liver, such as cirrhotic nodules (Fig.43D) and adenoma (Fig.43E) [Nussler et al., 2006]. In both pathological conditions the probability of cell division (model parameter 1) is known to be increased, which supports our model predictions. Whether these liver diseases are associated with alterations of other model parameters remains to be elucidated.
The model further predicted an increased micromotility to have a positive effect on the velocity and completeness of the regeneration of the necrotic lesion whereas a decreased micromotility impeded regeneration.
Most recent research on liver regeneration has concentrated on regeneration networks controlling hepatocyte proliferation. Relevant growth factors include HGF, IL-6, TGFα, VEGF, FGF1, FGF2, Angiopoietins 1 and 2, PDGF, HB-EGF, Jagged, Delta and stem cell factor [Michalopoulos & DeFrances, 2005]. In addition, neurotransmitters of the sympathetic nervous system have been shown to induce effects on many liver cell types, including hepatocytes. It can be expected that these parameters influence model parameter 1 (probability of cell division).
In contrast, only little is known about the mechanisms controlling model parameter 2 (DCO). However, our model predicts DCO to be crucial for the restoration of the microarchitecture of the liver lobule. Furthermore, it is well-known that an intact microarchitecture is a precondition for optimal liver function [Burt et al., 2006]. The

lobule architecture has to ensure a free blood flow from the portal vessels through the sinusoids into the central vein. Each obstruction of the sinusoids will hinder blood flow and is likely to compromise exchange between blood and the hepatocytes.

In an *in vivo* situation, at least three factors can be expected to support the columnar microarchitecture within the lobules:

(i) Fenestrated endothelial cells (sinusoidal lining cells) may biomechanically or biochemically guide the hepatocytes. After partial hepatectomy and as a consequence of hepatocyte proliferation, the formation of cell clusters containing 10-14 hepatocytes had been observed [Martinez-Hernandez & Amenta, 1995]. These clusters were devoid of sinusoids. Four days after hepatectomy, however, processes from Ito cell infiltrated into the hepatocyte clusters. This infiltration was followed by fenestrated endothelial cells, and in this manner the normal columnar microarchitecture was restored [Martinez-Hernandez & Amenta, 1995].

(ii) Chemical gradients between the periportal tract and the central vein may lead to local concentration differences by which hepatocytes may sense the direction of the central vein. In a typical liver lobule, the oxygen concentration, for example, decreases from the portal field towards the central vein [Burt et al., 2006].

(iii) As predicted by the two-dimensional model, hepatocyte membrane polarity is likely to support the columnar microarchitecture [Chisari et al., 2001].

The minimal two-dimensional model presented in this section did not yet include these complex biomechanical or biochemical interactions of hepatocytes with non-parenchymal and sinusoidal cells. We also did not yet consider the portal blood flow which is known to affect liver regeneration [Nobuoka et al., 2006] [Fan et al., 2002]. Nevertheless, already the minimal two-dimensional model was able to predict three key factors with significant relevance for a successful liver regeneration in our model: (1) directed hepatocyte orientation, (2) hepatocyte polarity and (3) micromotility.

Many of the aspects that were missing in the 2D model, however, will be included into a more elaborated three-dimensional model in the next section. This advanced model will also be much more tightly coupled to experimental data which will allow us to shed further light on the complex mechanisms involved in liver regeneration.

## 4.3. Modeling liver regeneration in 3D

### 4.3.1. Introduction: Liver systems biology

The minimal two-dimensional model introduced in the previous section already pointed in the direction of several important aspects that are likely to influence liver regeneration. The model simulations especially predicted the specific columnar microarchitecture of the lobules to be a major factor for a successful liver regeneration. However, as discussed in section 4.2.4, a more detailed model is required to better capture the complex mechanisms of liver regeneration *in vivo*. Besides hepatocytes, such extended model should consider the blood vessels system within the lobules (veins and sinusoids) which is known to have a pronounced three-dimensional structure [Matsumoto & Kawakami, 1982] and further biochemical factors that are likely to influence liver regeneration.

Only little is known about how cells coordinately behave to restore the columnar microarchitecture during liver regeneration. Research in this field is hampered by a lack of techniques that allow quantification of tissue architecture and its development. In order to bridge this gap and shed light on the underlying processes and mechanisms we have established a procedure based on confocal laser scans, image processing and image analysis that allows three-dimensional tissue reconstruction as a foundation for quantitative computational modeling.

Our procedure uses three parameter types: (Lobule) architectural parameters to quantify the static liver lobules, (regeneration) process parameters to quantify the regeneration process and modeling parameters to characterize the computational model. We utilize the architectural parameters to set up the initial state of a detailed computational model of liver lobule regeneration after toxic damage. For determination of the process parameters, we complemented conventional techniques such as BrdU incorporation with new techniques of processing and analysis of the experimentally obtained 3D confocal images to extract quantitative information that otherwise would be inaccessible, such as the spatio-temporal proliferation pattern of hepatocytes in 3D and the contact area between hepatocytes and sinusoidal cells during the regeneration process. We identified possible mechanisms underlying the observed regeneration process by analyzing a wide range of model variants within plausible physiological model parameter ranges followed by a quantitative comparison of the simulation results with the experimental observations using the same process parameters for both, experiments and simulations. Finally, we utilized the computational model to guide further experiments by predicting the most informative experiments to select the correct out of several possible mechanisms underlying regeneration. Using this strategy we identified a novel mechanism, which we named hepatocyte-sinusoid alignment (HSA), an alignment of daughter cells after hepatocyte division along the closest sinusoid. Model simulations and experiments demonstrated that HSA is a key mechanism necessary for the regeneration of the functional architecture of the liver lobule that cannot be replaced by alternative

mechanisms. Quantitative spatio-temporal computational modeling of tissue organization represents a generic way to merge information from different sources to synergistically obtain new quantitative and qualitative insights into tissue organization processes. We believe our procedure is widely applicable in the systems biology of tissues.

### 4.3.2. Image processing: From microscopy to model

In order to establish a quantitative three-dimensional model of the regenerating liver we first reconstructed and quantitatively described the architecture of liver lobules based on experimental data (section 4.3.2.1). We used volumetric data sets obtained by confocal laser scanning microscopy to reconstruct the full three-dimensional structure of the sinusoidal blood vessel network by a sequence of image processing, restoration (section 4.3.2.2) and analysis (section 4.3.2.3) steps. The same confocal laser scans have been used to determine and analyze the position of hepatocyte nuclei (section 4.3.2.4). We subsequently used these reconstructions to obtain information on the tissue microarchitecture (section 4.3.2.5) that until today is not experimentally accessible.

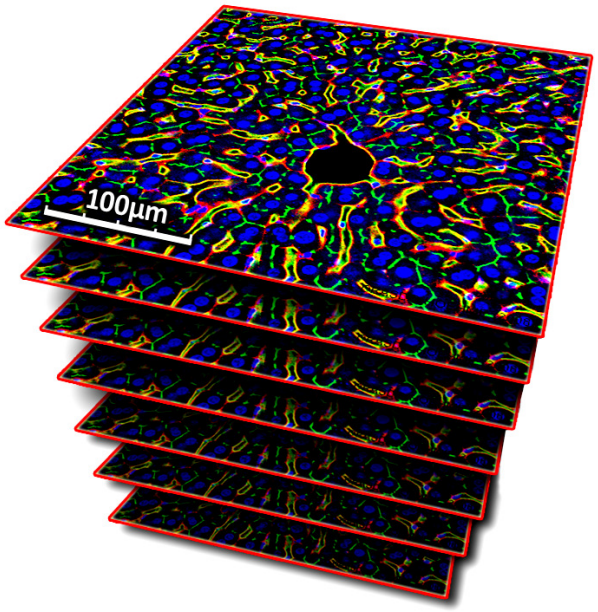


**Fig. 46: Volumetric experimental data.**
Spatially consecutive images obtained by confocal laser scanning microscopy.

All results were validated using transgenic mice (section 4.3.2.6). Furthermore, we used bright field microscopy to further elucidate the dynamics of the destruction and regeneration processes (section 4.3.2.7). Based on this combination of 2D and 3D images, we obtained statistical distributions for the architectural and process parameters. In order to capture variations among different liver lobules we studied 56 lobules (26 confocal laser scans and 30 bright field micrographs) from different mice. From the obtained parameter distributions we generated a representative liver lobule (section 4.3.2.8) as initial configuration for our model simulations. Alternatively, we used a single confocal data set to parameterize a concrete (section 4.3.2.9) lobule.

4.3.2.1. Experimental data

In order to reconstruct and analyze liver lobules in 3D we obtained volumetric data sets using a confocal laser scanning microscope (Olympus, Germany, FV1000). A key advantage of confocal microscopy is its capability to produce in-focus images of thick specimens. This process termed optical sectioning allows three-dimensional reconstructions of topologically complex features. Approximately 150 µm thick vibratome slices of mouse liver tissue had been immunostained using simultaneously antibodies directed against ICAM and DPPIV (for details see section 4.3.4). Nuclei were visualized by DAPI (for a collection of typical data sets see Supporting Fig.2). Each data set consisted of 50-120 spatially consecutive images (layers) of effectively 0.5 µm offset (Fig.46) each revealing a depth of 1 µm per layer. Each layer was 512 x 512 pixels in size, typically represented 318 x 318 µm and included 3 color channels (RGB) that corresponded to the local intensity of fluorescent light emitted by the costained specimen. This intensity $I(\chi)$ was available in normalized form ($0 \leq I(\chi) \leq 1$) and covered 256 different levels corresponding to an 8 bit resolution per channel. The software Cellsys (chapter 2) was used to integrate this partly overlapping image information into a single volume data set for each specimen. For a typical scanning depth of 100 µm such volume data set consisted of approximately 25 million voxels (volume elements) each possessing a particular intensity of $I(\chi)$ (for 2D images $\chi = (x, y)$, for 3D volumetric data $\chi = (x, y, z)$).

Images and volume data sets obtained by bright field or confocal laser scanning microscopy often exhibit significant deficiencies considering their suitability for direct automated analysis. Various difficult to predict factors as the adjustment of the microscope, thickness of the pictured slice or efficiency of the staining often lead to extensive fluctuations of contrast, brightness and color saturation that, together with sensor inherent noise, complicate the automated analysis of such images. Therefore often image enhancement algorithms must be applied in order to prepare microscopic images or volume data for image analysis.

In general, the process of image enhancement seeks to improve the visual appearance of pictured structures such that they become better suited for analysis by a human or a machine [Pratt, 2007]. In this work our first priority was suitability for machine processing. Until today, there exists no unifying theory of image enhancement due to the lack of a generally accepted standard of image quality which could serve as criterion [Pratt, 2007]. Nevertheless, as the sole purpose of all image and volume processing algorithms in this thesis was to prepare experimental images for automated analysis, we used the fitness for this purpose as a criterion.

Most image enhancement algorithms fall into two categories: (1) spatial domain algorithms and (2) frequency domain algorithms. While spatial domain algorithms directly manipulate pixels of an image plane or voxels of a volume, frequency domain algorithms modify the Fourier transform of an image or volume [Gonzalez & Woods, 2007]. All image enhancement algorithms used in this work operate in the

spatial domain. In general spatial domain techniques are denoted by the expression:

$$g(\chi) = T\left(f(\chi)\right) \tag{28}$$

where $f(\chi)$ is the input image or volume, $g(\chi)$ is the output image or volume and $T$ is an operator on $f$ that is often defined over a neighborhood of $\chi$.

Many spatial domain image enhancement techniques involve image histogram processing [Gonzalez & Woods, 2007]. The normalized histogram of an image with intensity levels $I$ is (for each color channel) a discrete function:

$$H(I_k) = n_k / n \tag{29}$$

where $I_k$ is the $k^{th}$ intensity level and typically $0 \le k \le 255$. $n_k$ is the number of image elements (pixels or voxels) with intensity level $I_k$ and $n$ is the total number image elements.

A common deficiency of microscopic images is poor contrast that results from a reduced image intensity level range [Pratt, 2007]. Additionally, the images are often locally or globally too bright or dark. However, these deficiencies can be automatically improved by a technique called histogram equalization (HE) or histogram linearization. Thereby the transformed output image is given by the equation:

$$HE(\chi) = \sum_{j=0}^{I(\chi)} H\left(I_j\right). \tag{30}$$

$HE(\chi)$ maps each image element with an intensity level $I(\chi)$ to the corresponding image element with intensity level $HE(\chi)$ in the output image. This transformation leads to images whose intensity levels cover the entire intensity range and thereby in general are of improved contrast and brightness (Fig.47). Note that all information for this transformation can be extracted directly from the input image and thereby requires no further parameterization. Fig.47A-C shows typical microscopic images obtained by a bright field micrograph that exhibited deficiencies of contrast and brightness. Fig.47D-F shows the corresponding images after application of the histogram equalization technique whereby these problems had been resolved. The processed images were then accessible for analysis (section 4.3.2.7).

However, since histogram equalization is based on the histogram of the entire input image, it is not able to selectively improve contrast in regions of the image that exhibit poor contrast while preserving regions with already good contrast. For this purpose, a more advanced technique was developed by [Tom & Wolfe, 1982]. The method is called adaptive histogram equalization (AHE) and utilizes only the

histograms $H(I_k, \Psi^{AHE})$ of local contextual regions $\Psi^{AHE}$ of the image. Thereby, improved contrast can be obtained in all regions of the image. Several improved variants have been presented by [Pizer et al., 1987], [Stark & Fitzgerald, 1996], [Gillespy, 1998], [Kim et al., 2001] and [Wang & Tao, 2006]. These improved algorithms produce superior results for many applications. However, adaptive histogram equalization remains a computationally demanding algorithm whose major problem is the amplification of noise in image regions of low intensity gradients [Acharya & Ray, 2005].

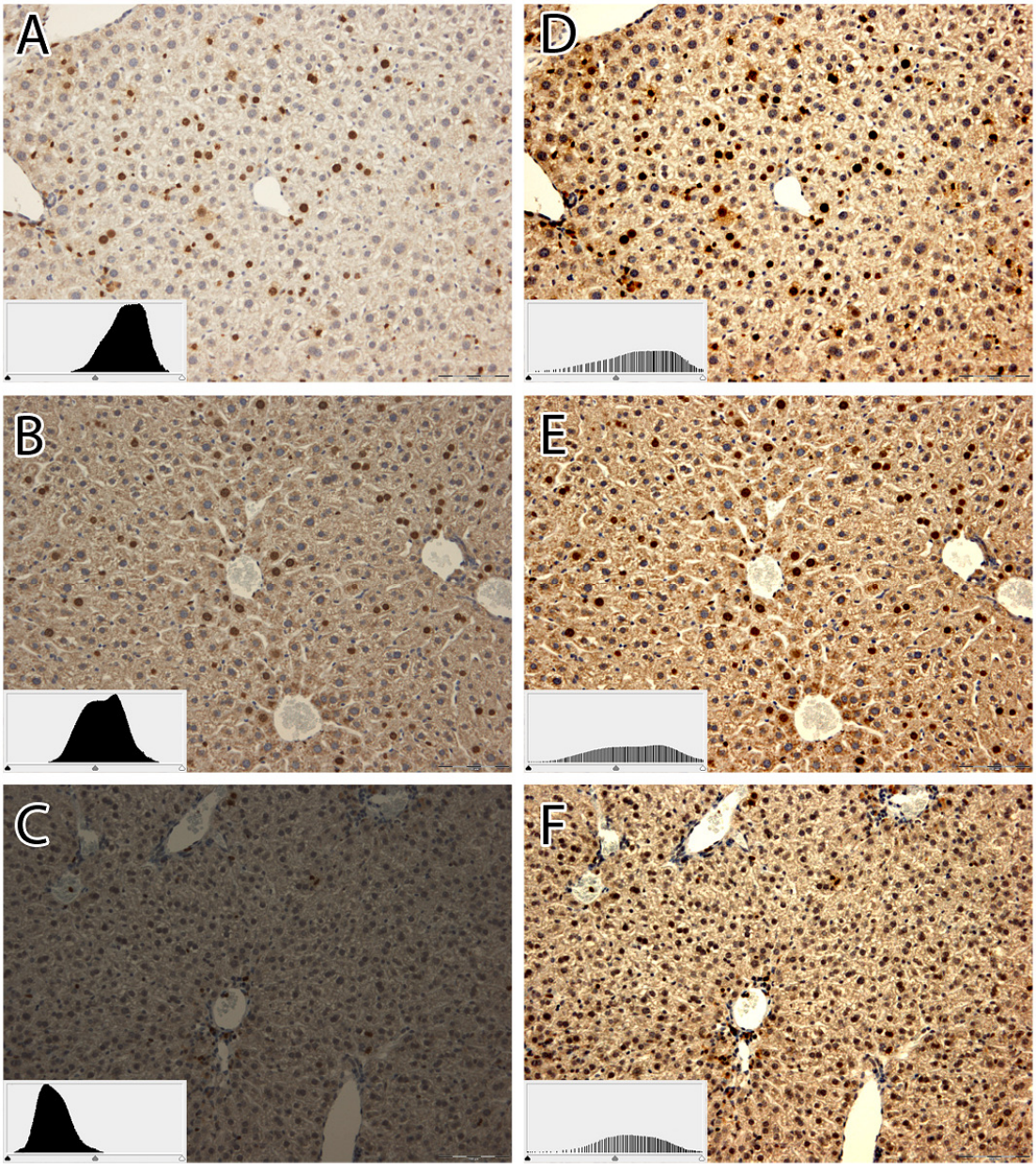


**Fig. 47: Histogram equalization in 2D**

A-C show typical bright field micrographs of low contrast and varying brightness. D-F show the corresponding images after histogram equalization.

4.3.2.2. Sinusoidal network reconstruction

In the experimental data sets obtained by the confocal laser scanning microscope the intensity of the red color channel corresponded to antibodies directed against ICAM while the green color channel yielded information on antibodies directed against DPPIV staining. DPPIV staining visualized preferentially the bile canalicular interface between hepatocytes, whereas ICAM was expressed on the sinusoidal cells and not on the hepatocytes. Brightness and contrast of these images were relatively low. Additionally, the intensity of the immunostaining in some cases varied considerably within the volume due to inhomogeneous penetration of the antibodies (Fig.48A). This complicated the interpretation of the experimental data and required more complex image enhancement transformations in order to prepare the data sets for analysis.

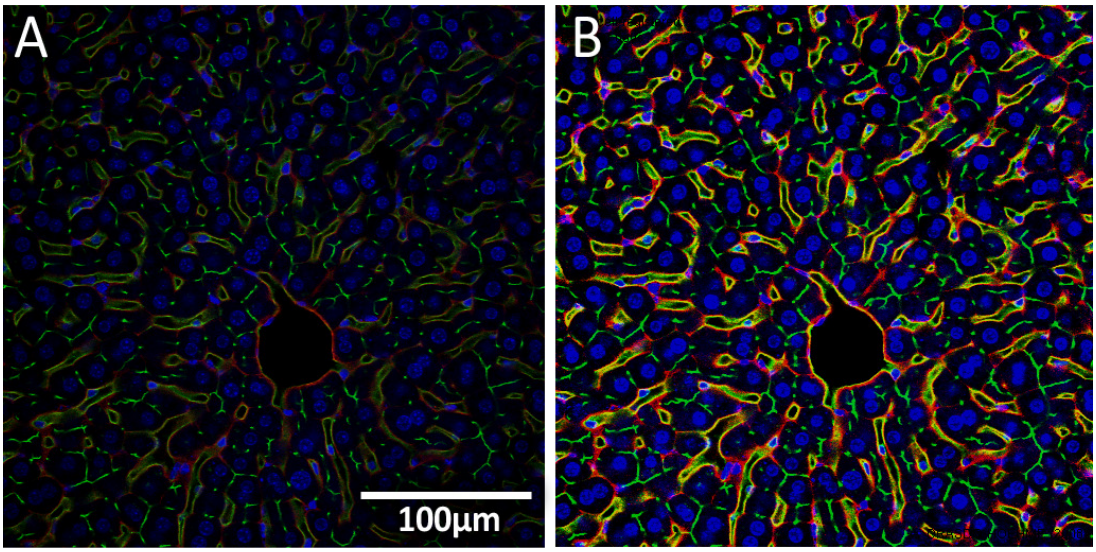


**Fig. 48: Enhancement of confocal data.** A: Typical image layer before image processing steps. Note the low brightness at the borders of the image and the overall poor contrast. B: The same image after AHE exhibiting increased contrast and equalized brightness.

We used an adaptive histogram equalization (AHE) technique as proposed in [Pizer et al., 1987] to compensate the described deficiencies. Histogram modification was applied to each voxel at position $\chi=(x,y,z)$ within the data set based on the averaged histogram of all voxels within a local spherical neighborhood $\Psi^{AHE}$ with a radius of 64 voxels. The AHE transformation significantly increased contrast and equalized brightness within the volume (Fig.48B). However, the amplitude of impulse noise inherent in confocal micrographs (e.g. due to sensor noise) was also increased. The amplification of noise is a well-known problem of histogram equalization algorithms [Acharya & Ray, 2005]. Nevertheless, in our situation the problem could be solved, because noise related voxels could easily be identified in later processing steps.
In the following we focus on the combined information obtained from ICAM (red) and DPPIV (green) immunostaining which yielded the most robust information on

the vessel network architecture within liver lobules. Due to additive color superposition this local combination of stainings is shown in Fig.48B in yellow color. On this basis, we now applied a sequence of morphology-based volume processing operators to reconstruct the lobule architecture and enhance the signal-noise ratio to prepare segmentation of the vessel network.

We used two elementary operators that can be characterized as generalized erosion and dilatation volume transformations. For each voxel of intensity I(χ) ($0 \le I(\chi) \le 1$) at position $\chi$ we determined the fraction $\Phi\left(\chi,\alpha,\Psi^{GED}\right)$ of voxels within a spherical neighborhood $\Psi^{GED}$ that exceed an intensity threshold $\alpha$. $\Psi^{GED}$ contains all voxels within a radius $R\left(\Psi^{GED}\right)$ that was chosen in the range of the average sinusoid diameter. On this basis we defined generalized erosion (GE) and dilatation (GD) operators as:

$$\text{GE: If } \Phi\left(\chi,\alpha,\Psi^{GED}\right) \le \alpha_{GE} : I(\chi)=0, \text{ else } I(\chi)=1, \tag{31}$$

$$\text{GD: If } \Phi\left(\chi,\alpha,\Psi^{GED}\right) \ge \alpha_{GD} : I(\chi)=1, \text{ else } I(\chi)=0, \tag{32}$$

where $\alpha_{GE}$ and $\alpha_{GD}$ are iteration-dependent thresholds.

An initial application of the GE operator ($\alpha = 0.5, R\left(\Psi^{GED}\right) = 2$, for a comprehensive summary of all parameter ranges see Appendix 5) removed most of the impulse noise in our data sets (Fig.49C) and resulted in a binarized volume ($I(\chi) = \{0,1\}$). Subsequently, we used the concatenation of GD and GE operators which together may be characterized as a generalized closing operator on the one hand to further reduce noise and on the other hand to reconstruct vascular structures by filling minor holes and bridging small discontinuities. By continuously applying the same number of both elementary operators we ensure to maintain fundamental structure dimensions within their original sizes.

Subsequently, we used an additional morphological operator (CC) for a further, more powerful restoration of vessel discontinuities and to close remaining cavities within already restored structures (e.g. the lumina of the sinusoids). Here, for each voxel at position χ we determined the fraction $\Theta\left(\chi,\alpha,R^{CC}\right)$ of vectors of length $R^{CC}$ that originate in χ, go off in arbitrary direction and have at least one intersection with a voxel whose intensity exceeds the threshold $\alpha$.

$$\text{CC: If } \Theta\left(\chi,\alpha,R^{CC}\right) \ge \alpha_{CC} : I(\chi)=1, \text{ else } I(\chi)=0 \tag{33}$$

with $\alpha_{CC}$ being an iteration-dependent threshold. Typically, we chose $\alpha_{CC} = 0.9$ and $R^{CC}$ along known vascular structure sizes to preserve the original vessel architecture.

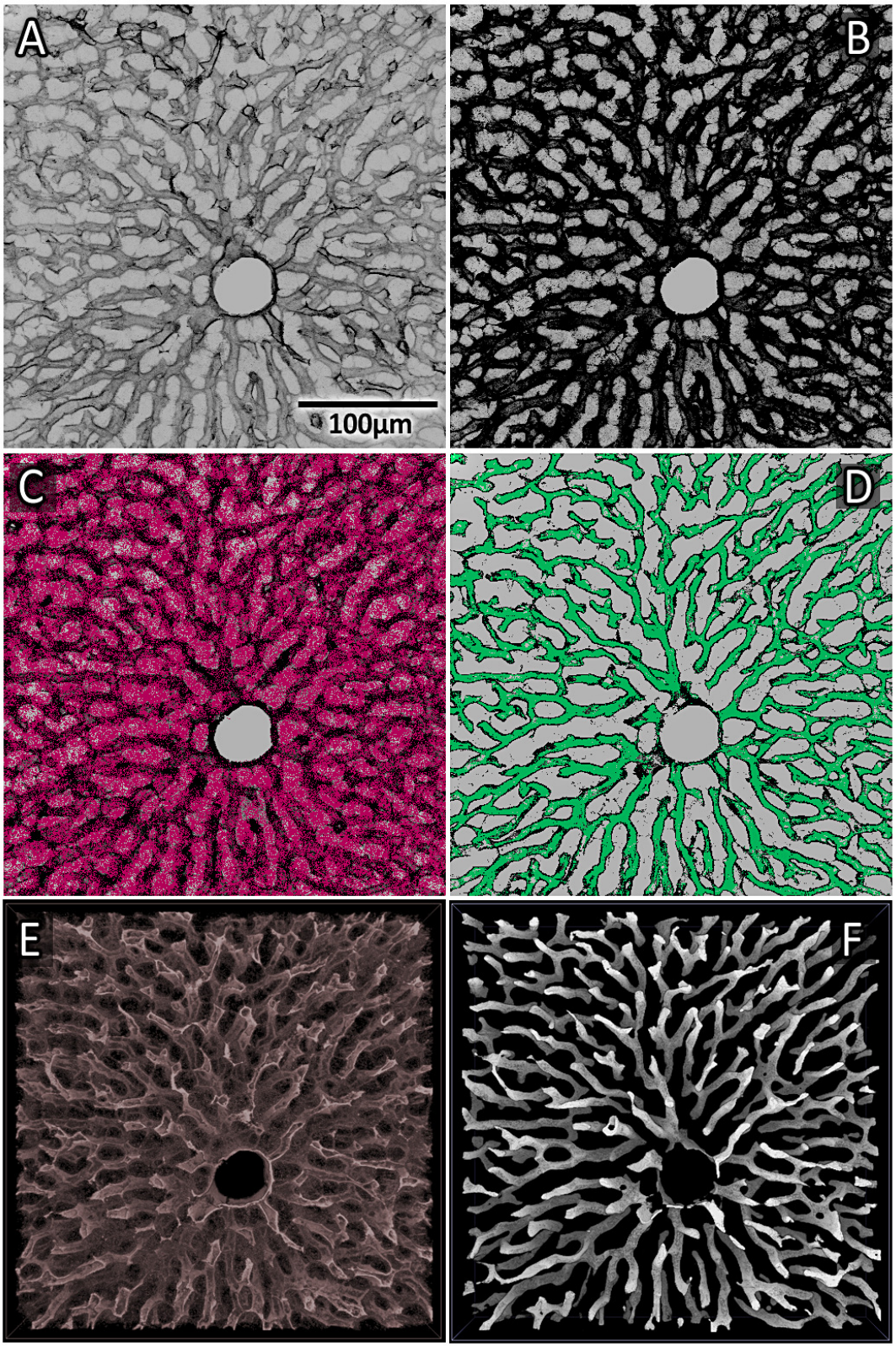


**Fig. 49: Vascular network enhancement.** A-D: Images show a maximum intensity projection. A: Before adaptive histogram equalization (AHE), B: After AHE, C: After initial GE-Operator (red voxels are removed), D: After CC-Operator (green voxels are added), E: Volume data before enhancements (equivalent to A), F: Volume data after enhancement. (See Supporting video 26)

In order to efficiently implement the CC operator, we approximated $\Theta(\chi,\alpha,R^{CC})$ utilizing 20 random sample vectors in uniformly distributed directions.
Furthermore, we discretized these vectors using the Bresenham algorithm [Bresenham, 1996]. We found that the iterative application of the CC operator very effectively closed internal cavities in the reconstructed vascular network while preserving the outer vessel surface (Fig.49D). In order to finalize the volume enhancement process, we cropped the volume data set by discarding outer layers with no voxels exceeding the intensity threshold $\alpha$. We also removed all remaining very small ($\leq 0.001\%$ of the volume) isolated 6-connected sub-structures (Von Neumann neighborhood) that are assumed not to contribute to the lobule vessel network. Both steps considerably decreased the computational complexity of later volume analysis steps.

4.3.2.3. Analysis of lobule vessel network

On the basis of the enhanced volume data set we next conducted a volume analysis to gather quantitative information on the blood vessel network within the lobules.
In a first step we determined the position of the central vein. The detection algorithm relies on the fact that neither the cytoplasm of the cells nor the lumina of vessels within the lobule are stained by any of the used markers. Therefore voxels associated to the cytoplasm or the lumina tend to have low intensity values in all color channels. Especially the central veins could easily be identified as relatively large tubes free of ICAM as well as DPPIV staining. We determined the position of the central vein in each layer by analyzing spatially averaged intensities (refer to Fig.50A) using a circular kernel whose radius $R^{AVG}$ considerably exceeds the sinusoid vessel radius and the mean sinusoid-nuclei distance (typically $R^{AVG} = 25$ voxels). The central vein was then assumed to be localized at the center of mass of the largest 4-connected assembly of voxels with averaged intensities below a threshold $\alpha_{AVG}$. The lumen of the central vein is lined with endothelial cells stained by ICAM. This information was used to further refine the shape of the central vein to increase the precision of its reconstruction. We then used the obtained information on the position, orientation, radius and shape of the central vein to parameterize the central vein in our model liver lobule (sections 4.3.2.8 and 4.3.2.9).
In a second step we constructed an undirected graph to extract a simple, robust representation of the sinusoids within the lobule in order to quantify the corresponding vessel network. Algorithmically, the construction of this “sinusoids graph” is closely related to the construction of the topological volume skeleton that can be calculated by a medial axis transform [Gonzalez & Woods, 2007]. The topological volume skeleton is defined as the locus of the centers of all maximal inscribed hyper-spheres of radius $R^{G}$. An inscribed hyper-sphere is maximal if it cannot be completely embedded in any other inscribed hyper-sphere. Next, we

constructed the sinusoids graph by iteratively determining the positions of its nodes and edges by analyzing the foreground voxels ($I(\chi)=1$) of the enhanced volume data set from section 4.3.2.2. Additionally, we associated a radius to each (spherical) node that later was used for extracting quantitative information on the sinusoidal network (refer to Fig.50B). (1): In a preparatory step, we calculated the radius $R^G(\chi_i)$ of the maximal inscribed hyper-sphere (in our three-dimensional case: a sphere) for all voxels i (at position $\chi_i$) within the volume. At this point, we considered all voxels to be unprocessed. (2): We started the construction of the sinusoids graph with voxel j of maximal $R^G(\chi_j)$. In case multiple $R^G(\chi_j)$ were equal, we randomly selected one from those. At position $\chi_j$ we now added the first node k of the sinusoids graph and stored its radius $R^G(\chi_j)$. Furthermore, we considered all voxels overlapped by node k associated to this node and therefore processed. (3): We now continued the construction of the sinusoids graph by adding node m at position $\chi_n$ of the voxel n with maximal $R^G(\chi_n)$ that is located on the surface of node k. Again all voxels that are overlapped by node m with radius $R^G(\chi_n)$ were considered processed. We also added an undirected edge between the nodes k and m.
The process of adding the next node on the surface of the last (step 3) was iterated until no unprocessed voxels remained on the surface of the last node. This corresponds to a depth-first-search. (4): If any voxels remained unprocessed, we repeated the construction from step 2. Each of these iterations added a new part of

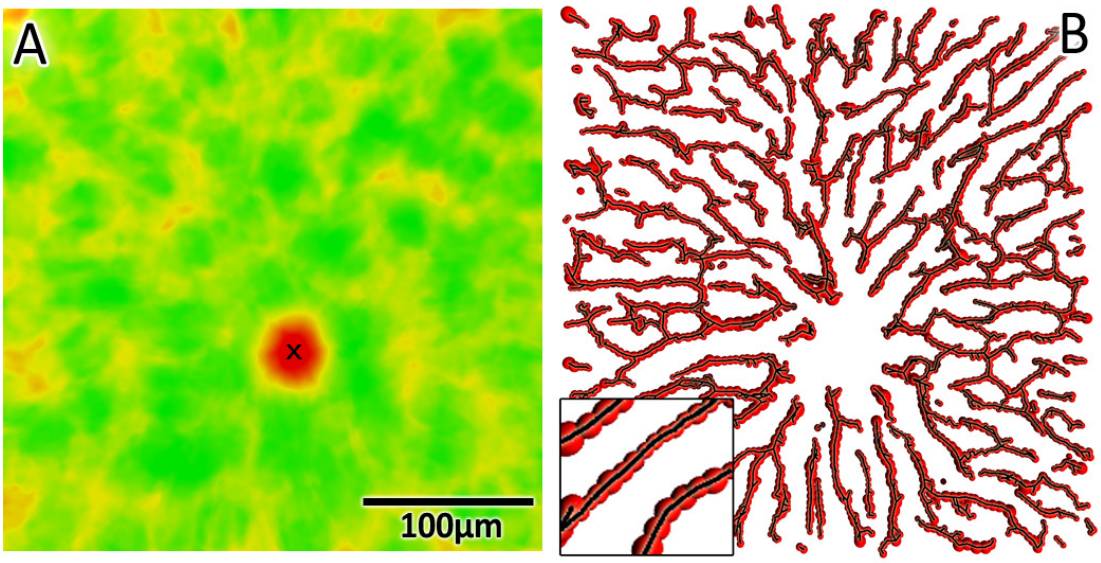


**Fig. 50: Vascular network analysis.** A: Multi-channel intensity average ($R^{AVG} = 25$ voxels) of the reference volume (Fig.48). Red indicates low and green indicates high averaged intensity. The black cross marks the detected position of the central vein. B: Sinusoids graph. Black lines show edges and red spheres show nodes and associated radii. Lower left corner: magnification of nodes in sinusoid graph.

the sinusoids graph that was not connected to any existing parts. Therefore the resulting graph could be considered both undirected and unconnected. When no unprocessed voxels remained, the construction algorithm terminated.
We used the resulting graph to extract quantitative information for example on the sinusoid radii including their average value and distribution within the lobule. Furthermore, we calculated the mean minimal distance between two neighboring sinusoid vessels to determine the density of the network and analyze branching properties (see Table 4 for a list of all obtained parameters). By averaging the results of volume enhancement and analysis over many liver lobules (see Supporting Fig.2 and Supporting Fig.3 for an overview of typical data sets) we obtained statistically robust quantitative values that laid the foundation for the parameterization of the model lobule that served as a starting point for our computer simulations (section 4.3.2.8). The results of the volume analysis were also used without averaging to set up a model for a specific, concrete liver lobule (section 4.3.2.9).

#### 4.3.2.4. Quantification of hepatocyte characteristics

Besides the analysis of the vascular network, we also used the same volume data sets to obtain quantitative information on the hepatocytes within the lobule. The blue color channel yielded intensity values that originated in a DAPI-staining which labels cell nuclei of both hepatocytes and non-parenchymal cells by forming fluorescent complexes with double-stranded DNA. However, especially the blue color channel in our confocal laser scanning micrographs suffered from high noise levels (Fig.51A).
In general, confocal laser scanning micrographs are subject to noise from a number of sources including inherent sensor noise or channel transmission errors [Pratt, 2007]. In addition to continuous noise that has a flat power spectral density and in analogy to white light is also termed white noise, we consider noise in our images to be dominated by impulse noise that leads to intensity spikes of random location, amplitude and spectral content.
Most traditional noise cleaning algorithms [Graham, 1962] [Rosenfeld et al., 1969] [Nathan, 1970] and especially linear noise filtering techniques perform well on images with continuous noise. However, they incline towards too strong smoothing for images with impulse noise. Median filtering is a nonlinear signal processing algorithm originally developed by [Tukey, 1971] that commonly is considered a cornerstone of current image processing. It is widely used for smoothing and removal of image noise distortions [Baxes, 1994] [Haralick & Shapiro, 1992] [Yin et al., 1996] as it preserves edges more effectively than a linear smoothing filters (Fig.51C). Recently, [Weiss, 2006] presented a fast logarithmic-time ($O(\log R_k)$ with $R_k$ the radius of the filter kernel) variant of median filtering scalable to any kernel radius and image bit-depth. This fundamental advancement eliminated the (until then) major disadvantage of median filtering, namely its relatively high computational cost.
In order to prepare our confocal laser scanning micrographs for analysis, we complemented the volume enhancement steps as described in section 4.3.2.2. with

median filtering. We used adaptive histogram equalization as proposed in [Pizer et al., 1987] to equalize brightness and enhance contrast (Fig.51A) and applied a sequence of GE and GD operators that already removed parts of the impulse noise (Fig.51B). In contrast to the filigree structures of the sinusoidal blood vessel network, hepatocyte nuclei were typically compact spherical structures whose staining with DAPI in general led to large intensity gradients (Fig.51A). Therefore, we additionally applied a non-linear 3x3 median filter that almost eliminated the remaining image noise (Fig.51C).

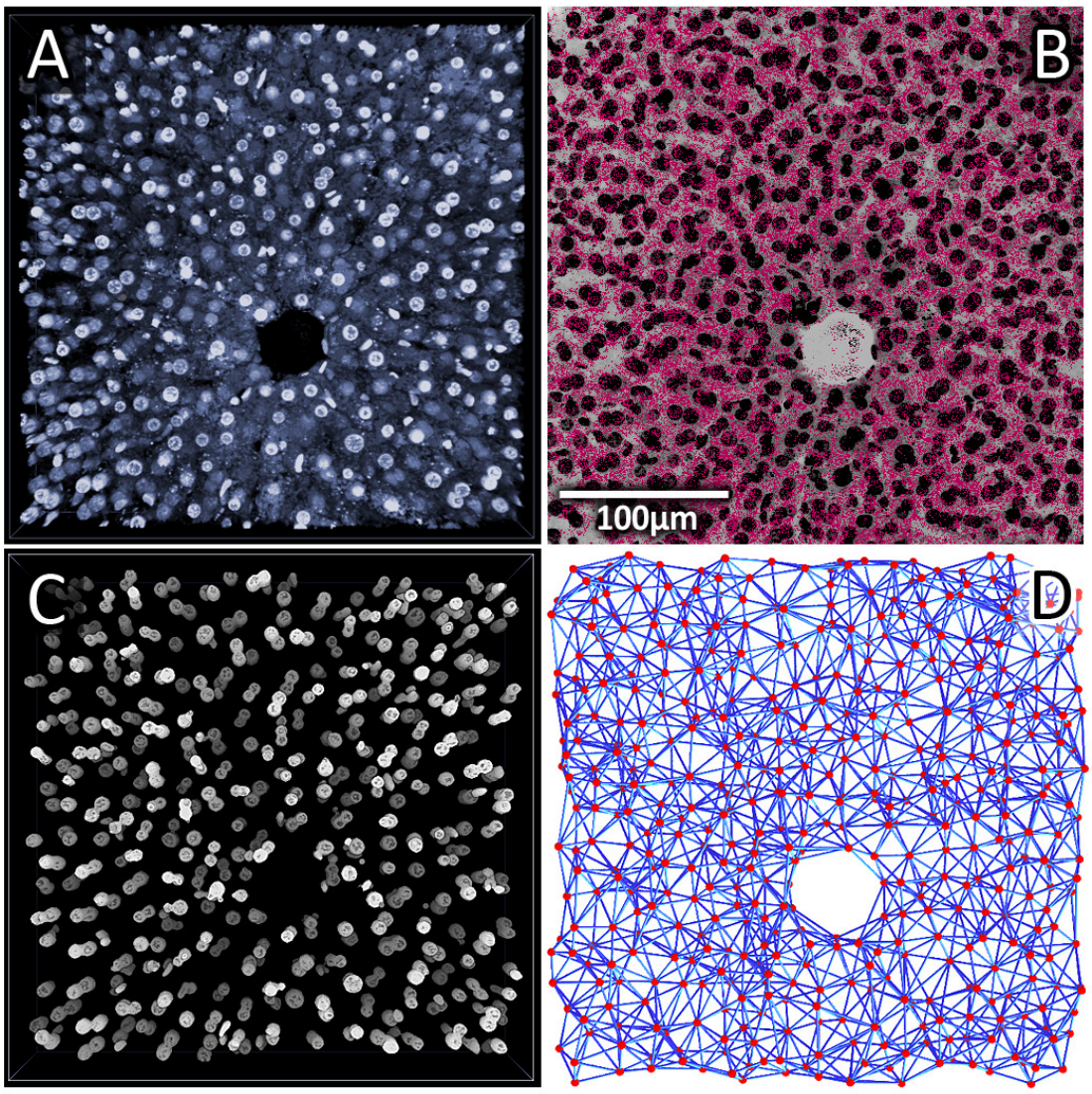


**Fig. 51: Hepatocytes enhancement and analysis.**
A: Volume data sets (blue channel) after adaptive histogram equalization (AHE) (high brightness=high intensity). B: Noise reduction by GE operator (red voxels are removed). C: Volume data set after enhancement and classification of hepatocyte nuclei. D: Delaunay triangulation. Vertices (red dots) are given by the center of mass of hepatocyte nuclei.

The resulting volume was then binarized ( $I(\chi)=\{0,1\}$ ) using an intensity threshold $\alpha_{HEP}$ (typically $\alpha_{HEP}=0.8$) to reduce the computational complexity of later analysis steps. All foreground voxels ( $I(\chi)=1$ ) within the volume data set were partitioned into isolated, 6-connected subsets. We used a morphological classification inspecting diameter, volume and shape of each subset to differentiate between hepatocyte nuclei, nuclei of non-parenchymal cells and artifacts. Typically, hepatocytes have one or two nuclei of approximately spherical shape. In our experiments, we found an average diameter of 9.3 µm for hepatocyte nuclei (Fig.52A). The diameter of non-parenchymal cell nuclei is known to be significantly smaller. We found an average diameter of 5.6 µm (Fig.52A).

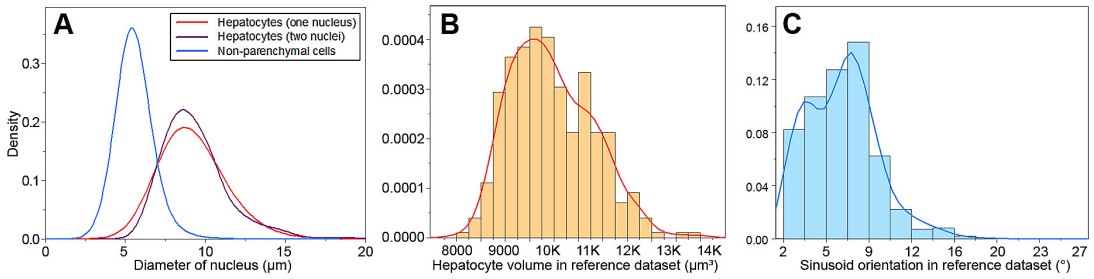


**Fig. 52: Statistical analysis of lobule properties.**
A: Distribution of nucleus diameters of hepatocytes and non-parenchymal cells. B: Distribution of hepatocyte volume (µm³) in reference dataset. C: Distribution of sinusoid orientation (in comparison to a perfect alignment in the direction of the central vein).

In the following, we focused our analysis on voxel subsets classified as hepatocyte nuclei (Fig.51C). By calculating the center of mass for each subset, we obtained a set of points P. On the one hand, P was used to directly study hepatocyte positions. On the other hand, however, a number of more complex analyses were conducted based on a refined Voronoi decomposition of metric three-dimensional space [Aurenhammer & Klein, 2000] that was constructed using P. Fig.51D shows P (red points) and the corresponding Delaunay triangulation [Okabe et al., 2000] for our reference volume data set. The Delaunay triangulation is the dual structure of the Voronoi diagram and for example allows the simple determination of cell-cell neighborhoods. Traditional Voronoi decomposition associates each point in space to its nearest base point. We refined this approach using additional information from the analysis of the vascular network to associate parts of the volume to sinusoidal vessels or the central vein instead of Voronoi cells representing hepatocytes. We then used this refined Voronoi decomposition to analyze hepatocyte characteristics. For example, we found an average hepatocyte diameter of 23.3 µm (see Table 4 for a list of all obtained parameters).

4.3.2.5. Quantification of tissue microarchitecture

In order to quantify the tissue microarchitecture of the liver lobules we analyzed the surface contact area of each hepatocyte to other hepatocytes and adjacent sinusoids. The segmentation of the sinusoids (section 4.3.2.2) and the hepatocyte nuclei (section 4.3.2.4) laid the foundation for the calculation of a refined Voronoi space decomposition as described in the previous section that we utilized to calculate these contact areas. We used the positions P of the hepatocyte nuclei as base points for the construction of the Voronoi diagram and additionally confined the extension of the Voronoi cells by 1) a maximal radius that was chosen along typical hepatocyte cell sizes and 2) the sinusoids (Fig.53). Thereby each point in the volumetric data set was associated to either a specific hepatocyte (defined by the nuclei that served as its base point) or a sinusoid. Only a small fraction of the volume (< 5%) remained unassociated which was caused for example by the lumina of large vessels (Fig.53). By comparison with the original experimental data we found the fraction of the volume data set associated to each hepatocyte by this technique to be a good approximation for the shape of this hepatocyte. We next used this shape approximation to calculate the fraction of the surface of each hepatocyte that was in contact to 1) neighboring hepatocytes, 2) adjacent sinusoids or 3) unassociated space. The average fraction of the hepatocyte surface that was in contact with sinusoids $\tilde{A}^{C}_{Sinu}$ seemed to be a robust measure for liver lobule function and thus was used as process parameter in our model. We found a rapid decline of $\tilde{A}^{C}_{Sinu}$ during the first two

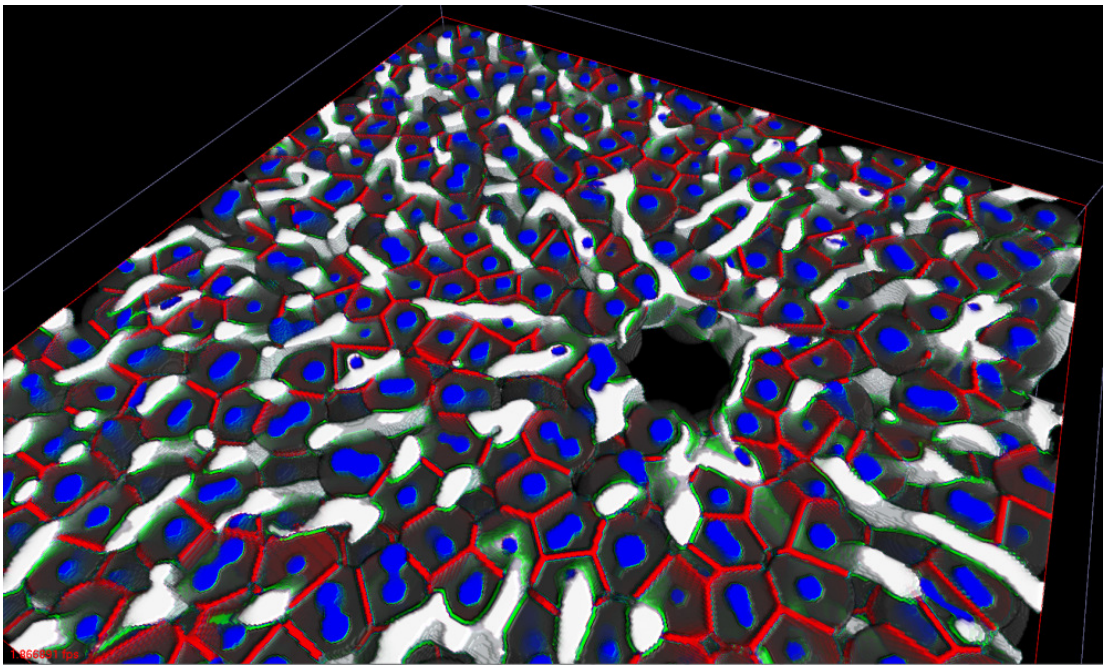

**Fig. 53: Quantification of tissue microarchitecture**.
Refined Voronoi space decomposition. White = vascular network, blue = hepatocyte nuclei, red = hepatocyte-hepatocyte surface contacts, green = hepatocyte-sinusoid surface contacts.

days after administration of $CCl_4$. During the regeneration process, however, $\tilde{A}^{C}_{Sinu}$ recovered to its original value after 16 days (Fig.62C). In liver disease, such as hepatocellular cancer, we found a significantly (unpaired t-test: p=0.0015) decreased $\tilde{A}^{C}_{Sinu}$ that is likely to contribute to compromised liver function in liver tumors of mice (Fig.55).

4.3.2.6. Validation by different staining procedures

So far all described reconstructions were based on confocal laser scans of mouse liver tissue immunostained by antibodies directed against ICAM and DPPIV. Although the technical quality of theses stainings was excellent it can never be completely excluded that the antibodies lead to unspecific staining patterns that may compromise the quality of reconstructed tissue. In order to validate the so far obtained data we performed the same reconstructions described in sections 4.3.2.1 – 4.3.2.5 using mouse liver tissue in which the relevant structures were stained by completely different techniques: (1) hepatocytes were visualized by transgenic expression of enhanced green fluorescent protein (EGFP) under control of a modified albumin promoter (alfp/Cre), (2) sinusoidal cells were visualized by antibodies directed against CD31 (for experimental details see section 4.3.4, for typical examples refer to Supporting Fig.3).
Most algorithms used to reconstruct the lobule architecture were identical to the techniques used during the analysis of the confocal data sets stained with ICAM/DPPIV. Nevertheless, after an initial adaptive histogram equalization filtering

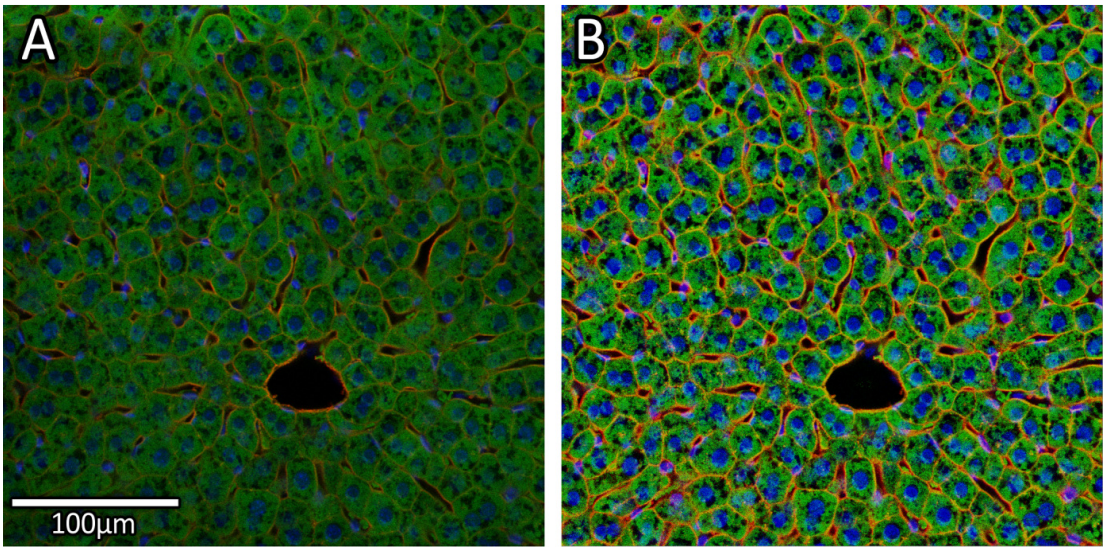


**Fig. 54: Alternative CD31 / EGFP / DAPI staining.**
A: Typical image layer before image processing steps. Note the fluctuating brightness of the image and the relatively poor contrast. B: The same image after adaptive histogram equalization exhibiting increased contrast and equalized brightness.

of the EGFP/CD31 data sets (Fig.54), we segmented the sinusoidal network by a technique similar to the one used in section 4.3.2.3 to reconstruct the central vein by averaging intensity values (Fig.50A). In this case, however, the algorithm relied on the fact that the lumina of the sinusoidal vessels within the lobule were not stained by any of the used markers (EGFP, CD31, DAPI) and therefore voxels associated to these lumina tended to have low intensity values in all color channels. In order to apply this method to reconstruct the sinusoids we used a circular kernel whose radius $R^{AVG}$ that was chosen in the range of the average sinusoid diameter and thus was considerably smaller than the one used in section 4.3.2.3. The sinusoids could then be identified as tubes free of EGFP as well as CD31 staining. This basic segmentation of the sinusoids was subsequently used as starting point for the reconstruction of the sinusoidal network by application of the morphological operators described in section 4.3.2.2. Importantly, the same results were obtained using this strategy compared to the data obtained with ICAM/DPPIV co-staining as described in sections 4.3.2.1 – 4.3.2.5.

#### 4.3.2.7. Quantification of destruction and regeneration process

In the previous sections we obtained quantitative parameters that described the static architecture of a liver lobule in 3D regarding its vascular network and parenchymal cells. However, to model the process of lobule regeneration after intoxication with $CCl_4$, further experimental data on the dynamics of this process was required. Parameters describing the destruction and regeneration process were named: “process parameters”. To describe the centrilobular cell death and subsequent hepatocyte proliferation induced by $CCl_4$ administration to mice, we additionally analyzed paraffin slices from livers prepared between 12 hours and 14 days after administration of $CCl_4$. Mice received BrdU injections to cover a period of 6 hours before the livers were prepared (section 4.3.4). BrdU is incorporated into newly synthesized DNA of replicating cells (during the S-phase of the cell cycle) and thus is commonly used to detect proliferating cells. Incorporated BrdU was visualized by immunostaining, which resulted in brown staining of nuclei that had incorporated BrdU.

We analyzed 30 images (see Supporting Fig.4 for typical examples) taken on 8 different time points (0, 1, 2, 3, 4, 8 and 16 days after intoxication with $CCl_4$) of 3 different mice per time period. For each image we obtained the number and positions of hepatocytes and non-parenchymal cells and differentiated their proliferation status using the BrdU staining.

We assumed lobules to have a hexagonal shape and studied variations from the corresponding regular hexagon. We found the mean variation of edge lengths from a regular hexagon to be approximately 20% with no systematic tendencies. By calculating the area of the lobules, we were able to obtain robust and normalized ($A_{ref}$ = 0.21 mm²) cell density measures for proliferating and non-proliferating cells (Fig.57A, Fig.57D).

Furthermore, we calculated the area of the pericentral necrotic lesion caused by the intoxication with $CCl_4$ that could clearly be distinguished from the surviving hepatocytes (Fig.57). The necrotic area was maximal 1-2 days after $CCl_4$ administration (Fig.57B) when the average hepatocyte density within the lobule was minimal (Fig.57A). We obtained its precise extension and area using a "seeded region growing segmentation" algorithm based on intensity values [Shapiro & Stockman, 2001] typically using a threshold intensity of $\alpha_{NEC}$= 0.85. The results of this segmentation are illustrated in Fig.56 by the green striped areas.

By combining the information on cell positions and the extension of the necrotic area, we were able to analyze the minimal Euclidean distance of each cell to the central necrosis (illustrated in Fig.56A). Additionally, we associated each cell to a layer that refers to the pericentral necrosis using refined 2D Voronoi space decomposition, whereby the hepatocyte layer next to the central dead cell area was considered cell layer 1, hepatocytes in contact with cell layer 1 formed cell layer 2, etc. (illustrated in the right half of Fig.56B). Compared to Euclidean distances such layer association had proved to be a more robust measurement for the distance of a cell to the central necrosis that also exhibits better scaling properties for variable cell and lobule sizes. Therefore, the technique of cell layer association had been applied to describe the distribution of BrdU positive hepatocytes over the liver lobule (Fig.57D).

BrdU incorporation into hepatocytes peaked 2-3 days after $CCl_4$ administration. Furthermore, the distribution of proliferating hepatocytes over the lobule was not homogeneous and preferentially occurred in the hepatocyte layers next to the dead cell area (Fig.57D). The spatio-temporal BrdU-incorporation pattern was later used as an input parameter to determine proliferation in our computational model.

The pericentral hepatocyte marker glutamine synthetase as evidenced by mRNA expression, immunostaining and enzyme activity analysis showed a transient decrease (Supporting Fig.5-7). This demonstrates that the dynamics of destruction and regeneration of the pericentral hepatocytes is in agreement with previously reported

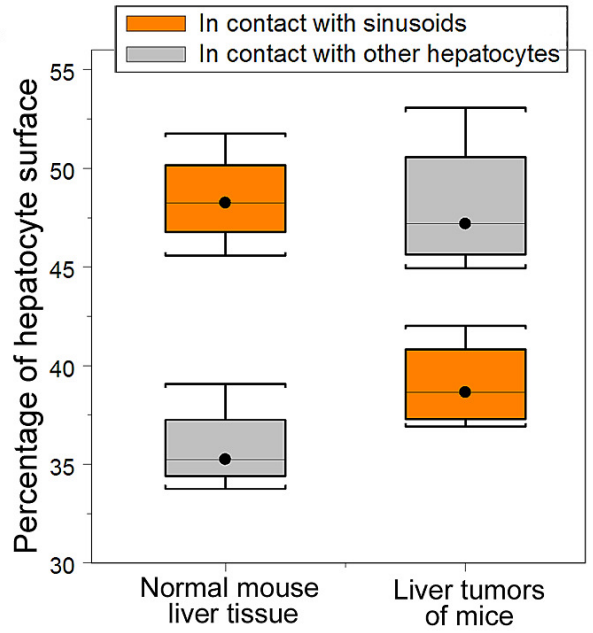


**Fig. 55: Hepatocyte surface contact analysis.** Fraction of surface area of hepatocytes in contact with sinusoids (orange) and other hepatocytes (grey) in normal liver tissue and liver carcinomas obtained by method described in 4.2.3.5.

observations [Hoehme et al., 2007] [Michalopoulos, 2007] [Michalopoulos & DeFrances, 2005] [Michalopoulos & DeFrances, 1997]. The number of macrophages was observed to increase in the necrotic zone which was accompanied by increased RNA of CD68 (Supporting Fig.8). This may explain the rapid disappearance of the dead cell mass. A transient decrease of ATP content

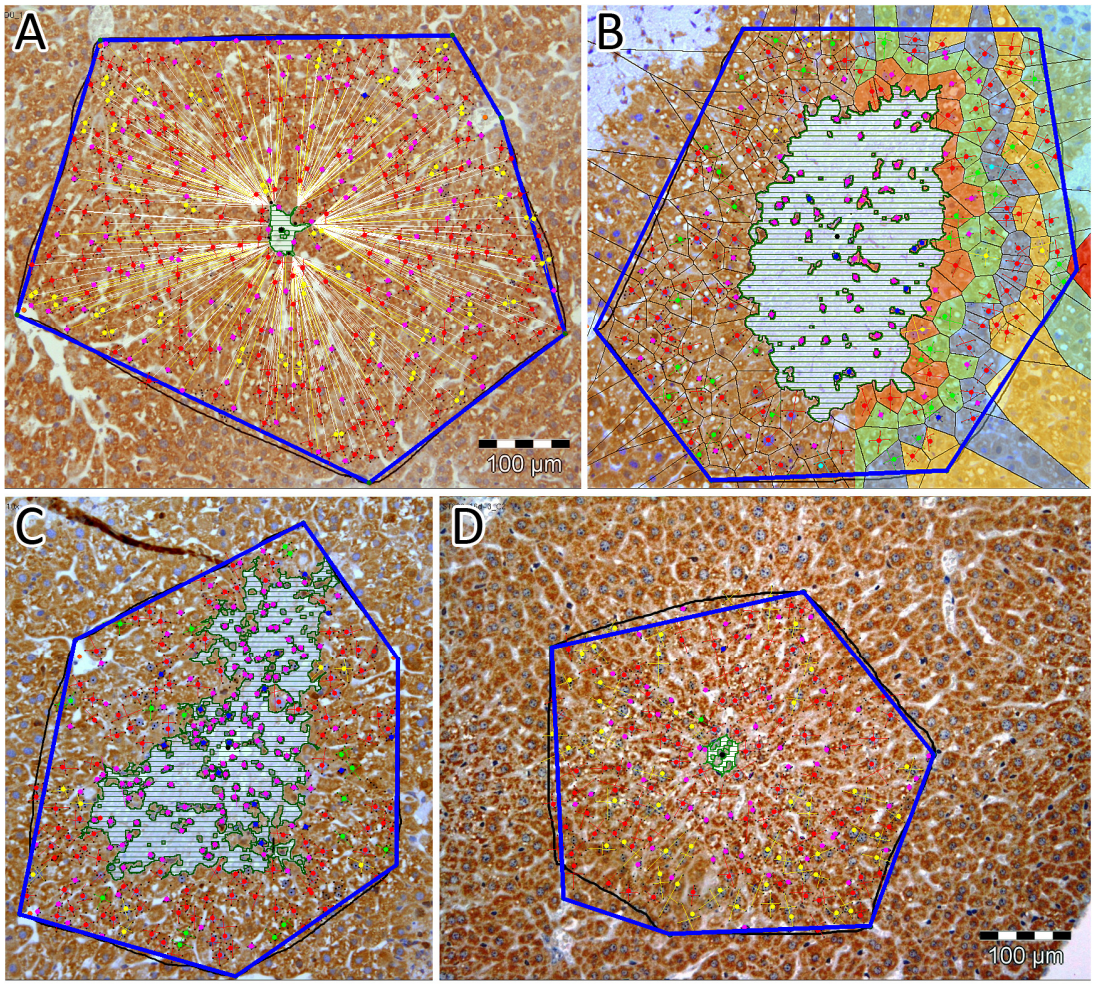


**Fig. 56: Analysis of lobule regeneration dynamics**. Images show representative paraffin slices of liver tissue of mice at different time periods after administration of $CCl_4$ illustrating the emergence and regeneration of the central dead cell area. BrdU positive nuclei had been visualized by immunostaining. Blue lines denote the approximate lobule borders. Colored dots mark cell positions (green=BrdU positive hepatocyte with one nucleus, red=BrdU negative hepatocyte with one nucleus, cyan=BrdU positive hepatocyte with two nuclei, yellow=BrdU negative hepatocyte with two nuclei, blue=BrdU positive non-parenchymal cell, magenta=BrdU negative non-parenchymal cell). The green striped area shows the extension of the central necrotic lesion. / A: Controls (without $CCl_4$). Lines denote minimal Euclidean distances of cells to the necrotic area, B: 2 days after $CCl_4$ administration. The area of the central necrotic lesion is maximal. The right half illustrates the association of cells to layers using refined Voronoi space decomposition (red=cell in direct contact with necrosis, green=layer 2, etc.), C: 4 days after $CCl_4$ administration. Regeneration progresses. D: 8 days after $CCl_4$ administration, the regeneration is complete.

(Supporting Fig.9) as well as albumin, CYP3A11 and BSEP RNA expression, factors responsible for differentiated liver functions, a transient increase of AFP and ubiquitin RNA expression (Supporting Fig.5) and also the macroscopical appearance of the analyzed livers was in agreement with a destruction and regeneration process. Within 8 days the central necrotic area was closed (Fig.57B) and the liver mass restored (Fig.57A). As soon as the central dead cell areas had been regenerated it became difficult to histologically identify the central veins. This was achieved by glutamine synthetase immunostaining of neighboring slices (Fig.57E/F). It is important to note that the structure of the sinusoidal network remained almost unaffected by $CCl_4$ (Fig.4F).

In order to quantify the liver lobule microarchitecture, we measured the hepatocyte-sinusoid and the hepatocyte-hepatocyte contact areas. We validated this measure by comparing healthy liver and liver carcinoma (Fig.55). We found that in normal liver 35.8±2.3% (mean ± standard deviation) of the hepatocyte surface is in contact with other hepatocytes and 48.5±2.5% with sinusoids. In liver carcinomas the respective contact areas are 48.1±3.6% (hepatocytes) and 39.1±2.3% (sinusoids) illustrating the significant (unpaired t-test: p=0.0015) decrease in hepatocyte-sinusoid contact and a corresponding increase of hepatocyte-hepatocyte-contact in liver tumors. Since both measures are complementary we below only consider the hepatocyte-sinusoid contact area at which the exchange of metabolites between blood and hepatocytes

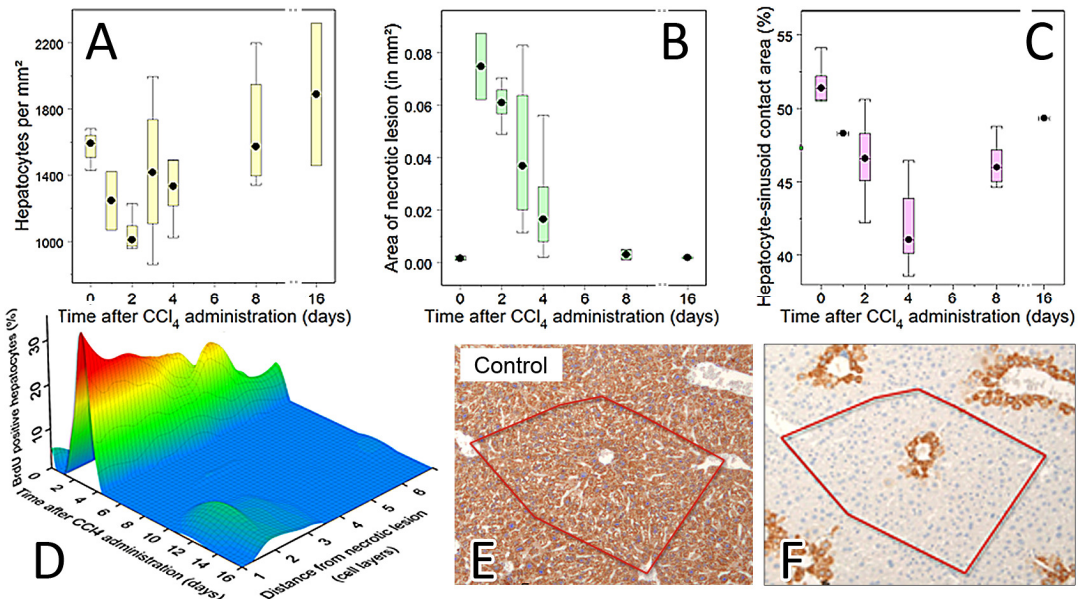


**Fig. 57: Process parameters for quantification of the regeneration process.**
Three mice were analyzed 0, 1, 2, 3, 4, 8 and 16 days after administration of $CCl_4$. At least two liver lobules were analyzed per mouse. A: Hepatocyte density which reflects the lobule mass, B: Area of central necrosis with time, C: Hepatocyte-sinusoid contact area, D: Distribution of BrdU-positive cells in liver lobule. E: Red hand drawn lines in E and F show the approximate extension of the liver lobule. F: Central veins were identified by immunostaining for glutamine synthetase (GS).

**Table 4: Lobule parameters obtained by volume analysis.**
The plausibility of all parameters was verified using unprocessed experimental images. Parameter values were obtained by analysis of 26 different lobules.

| Parameter | Source | Value ± Standard deviation |
|---|---|---|
| **Lobule** | | |
| Confocal scanning depth | Confocal data | 95 ± 57 µm |
| Lobule height in model | - | 250 ± 0 µm |
| Lobule area (2D slice) | Bright field microscopy | 0.21 ± 0.05 mm² |
| Lobule radius in model (2D slice) | $R = \sqrt{2A/3\sqrt{3}}$ A… lobule area (regular hexagon) | 284.3 ± 56.9 µm (12.2 ± 2.4 hepatocytes) |
| Lobule volume in model | - | $52.5 \cdot 10^{-3} \pm 12.5 \cdot 10^{-3}\, mm^3$ |
| Area of necrotic lesion before regeneration | Image analysis | 0.073 ± 0.011 mm² |
| Radius of necrotic lesion before regeneration | $R_{nec} = \sqrt{A_{nec}\pi^{-1}}$ (circular necrotic lesion) | 149 ± 22 µm (6.4 ± 1.0 hepatocytes) |
| **Sinusoids** | | |
| Radius of sinusoid vessels | Volume analysis | 4.75 ± 2.25 µm |
| Orthogonal minimal vessel distance | Volume analysis | 16.45 ± 4.22 µm |
| Non-branched segment length | Volume analysis | 43.1 ± 18.9 µm |
| Mean branching angles | Volume analysis | 32.5° ± 11.2° |
| Vessel volume in lobule | Volume analysis | 7.4 ± 1.1% |
| **Hepatocytes** | | |
| Hepatocyte volume | Volume analysis | $1.2653 \cdot 10^{-5} \pm 3.915 \cdot 10^{-6}$ mm³ |
| Hepatocyte size | Volume analysis | 23.3 ± 3.1 µm |
| Hepatocyte density | Image analysis | 1889 ± 341 cells/mm² |
| Next neighbor distance | Volume analysis | 21.6 ± 13.1 µm |
| Diameter of hepatocyte nucleus | Image analysis | 9.3 ± 4.4 µm |
| **Central vein** | | |
| Length in Volume | Volume analysis | 107 ± 69 µm |
| Radius | Volume analysis | 41.2 ± 32.1 µm |
| Inclination to viewing plane | Volume analysis | 6.6° ± 4.1° |

occurs. Also during the regeneration process after intoxication with $CCl_4$, the hepatocyte-sinusoid contact transiently decreases with a minimum at day 2 and subsequently recovers until day 16 (Fig.57C).

#### 4.3.2.8. Construction of a representative initial model state

The previous analyses (sections 4.3.2.1 – 4.3.2.5) provided robust information on all major architectural parameters (see Table 4) of liver lobules in 3D. On that basis we set up a representative model liver lobule that served as starting position for our model simulations.

The general shape of this representative lobule is an 8-faced polyhedron defined by a 6-edged polygonal base and a parallel 6-edged polygonal top. The distance between base and top determines the height of the model lobule. The analyzed volume data sets typically covered a lobule height of 50-100 µm which corresponds to 2-4 hepatocyte layers. In the model lobule we extrapolated this information using a lobule height of 250 $\mu m$ which corresponds to approximately 10 hepatocyte layers. The base and top 6-sided polygons only moderately differ from regular hexagons. These minor variations of the lobule shape are in agreement with our findings from 2D bright field micrographs (see section 4.3.2.7). Within this polyhedral environment, we first constructed a model vascular network (Fig.58A) whose properties correspond to the parameters obtained from confocal volume data sets (see section 4.3.2.2 and 4.3.2.3). Position and orientation of the central vein in the model are defined by the line connecting the centers of the top and base hexagon of the polyhedral environment. The radius of the model central vein corresponds to experimentally obtained values (section 4.3.2.3).

Starting at the surface of the model central vein we now iteratively added model sinusoids as concentric segments (Fig.52C) using a distribution of segment length, segment radius and branching properties that corresponds to the experimentally obtained properties of the vascular network (section 4.3.2.3). In the periportal area the so far approximately concentric model sinusoids gradually change their orientation towards the model portal veins that are located at three edges of the lobule polyhedron as illustrated in Fig.58A. The sinusoids graph extracted from concrete confocal volume data sets often is unconnected mainly due to the technical limitation of confocal laser scanning microscopy to a depth of approximately 150 µm. However, we assume the sinusoidal blood vessel network in the lobule to be connected and therefore the described construction algorithm was designed to generate a connected model vascular network. This connectivity is of significant advantage for the modeling of biomechanical interactions with hepatocytes or when modeling blood flow through the model vascular network. We further imposed a direction to the model sinusoidal network according to the direction of physiological blood flow from the portal veins to the central vein.

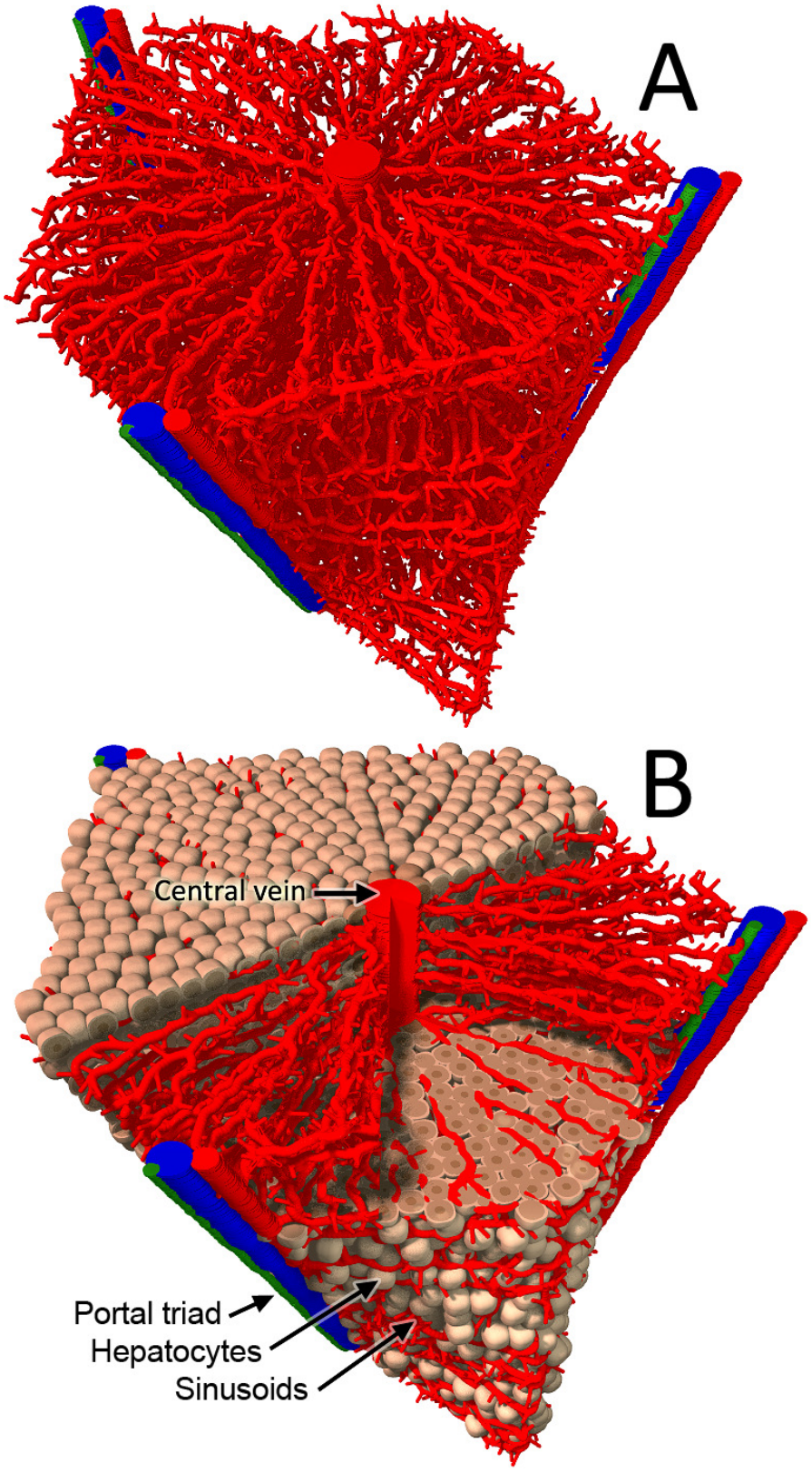


**Fig. 58: Initial model state in 3D.**
A: Vascular network in the model. The outer vessel triad includes a bile duct (green), a portal artery (red) and a portal vein (blue). B: Initial model state including hepatocytes (ochre) and vessels (red). Parts of the lobule are not shown.

Nevertheless, despite these differences between the sinusoids graph and the vascular network in the model, both are equivalent regarding all major architectural parameters (see Table 4). In the second phase of the construction of the model lobule we added hepatocytes to the existing vessel network. Currently we only include parenchymal liver cells into our model. However, hepatocytes are known to account for approximately 80 - 90 % of the liver mass [Cunningham & Horn, 2003] [Taub, 2004]. Analyzing confocal laser scans of mouse liver tissue we observed that hepatocytes have a relatively narrow size distribution (see Table 4) that also is roughly constant over time and independent from their position between the pericentral area and the periportal field. Based on these observations, all model hepatocytes are assumed to have the same size (23.3 μm). Statistical analysis of the experimental data showed no spatial correlation between the positions of hepatocytes within the confocal volume data sets. Therefore we iteratively added model cells at uniformly distributed random positions within the model lobule only considering constraints imposed by the already existing hepatocytes and the model vessel network. New model hepatocytes were added until cell density in the model lobule (the polyhedral environment) reached the experimentally observed value (1889 cells/mm²).

In the last phase, the constructed assembly of model cells and sinusoids was allowed to biomechanically relax until cell-cell and cell-sinusoid forces had been equilibrated (Fig.58B, also see Supporting videos 33-35). However, only minor spatial changes occurred during this relaxation process and the resulting model configuration still complied with all experimental parameters. Interestingly, during this relaxation the hepatocytes tended to align along sinusoidal vessels thereby organizing themselves (at least partly) in columnar structures that were also observed in experiments. However, we found this inherent organization process induced by the concentrically oriented sinusoids to be relatively weak and to have only minor influence during regeneration.

For the representative initial configuration of the 3D lobule model (Fig.58) the hepatocyte-sinusoid contact area was 51.0±1.2% of the hepatocyte surface which was close to the experimental value of 48.5±2.5%. Note that this parameter cannot be directly tuned as it is fully determined by the architectural parameters

4.3.2.9. Construction of a concrete initial model state

The information obtained on the vascular network, the central vein and the hepatocytes within the lobule can also be used to set up an initial model state that represents a specific liver lobule. Preconditions are high quality confocal laser scans that include an entire lobule (Fig.59A). Such concrete model state is less representative in comparison with a model state that was constructed using averaged information from many lobules (section 4.3.2.8). However, specimen-specific model states (Fig.59B, also see Supporting videos 36-38) allowed us to verify our simulation results by excluding artifacts that may have been introduced by averaging. Furthermore, a concrete initial model state allows simulations that can make predictions for a specific tissue specimen which lays the foundation for patient-specific modeling.

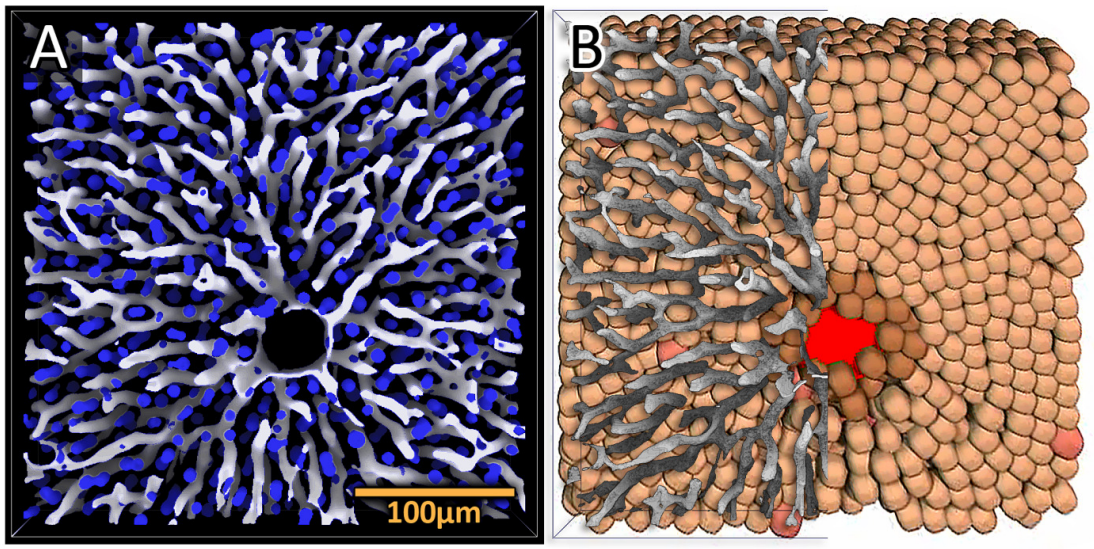


**Fig. 59: Modeling a concrete liver lobule**.
A: Fully processed volume data set. White=sinusoids, blue=hepatocyte nuclei.
B: Corresponding concrete initial model state. Grey overlapping over the left half of the model state shows the corresponding vascular network (A).

## 4.3.3. Model extensions

### 4.3.3.1. Hepatocyte migration and sinusoids

We extended the model elaborated in section 4.2. by introducing a detailed blood vessel network that included not only central and portal veins but also the microvessels (sinusoids) connecting them [Hoehme et al., 2009]. In this setting, we again simulate cell migration as a friction-dominated over-damped motion with a stochastic contribution by a stochastic equation of motion for each cell [Drasdo, 2005] [Drasdo et al., 2007] [Hoehme et al., 2007].

For isotropic cells, the velocity of cell *i* is determined by:

$$\begin{aligned}\zeta \underline{v}_i(t) = \sum_j \left(\gamma_{ij}^C (\underline{v}_j(t) - \underline{v}_i(t)) + \underline{F}_{ij}^C\right) + \sqrt{2\gamma_i^2 D^C} \cdot \underline{\eta}_i(t) + \\ \sum_z \underline{F}_{iz}^{CV} + \sum_m \underline{F}_{im}^{PV} + \sum_k \left(\gamma_{ik}^S (\underline{\omega}_k(t) - \underline{v}_i(t)) + \underline{F}_{ik}^S\right)\end{aligned} \tag{34}$$

where $\underline{v}_i(t)$ is the velocity of hepatocyte *i*, $\gamma_{ij}^X$ denotes the friction between hepatocytes *i* and *j* (X=C) or between hepatocyte *i* and sinusoid *j* (X=S) and $\gamma_i$ denotes an effective friction between hepatocyte *i* and the extracellular matrix. $\underline{F}_{ij}^X$ denotes the JKR or extended Hertz - force between hepatocytes *i* and *j* (X=C), between hepatocyte *i* and sinusoid *j* (X=S), between hepatocyte *i* and central vein *j* (X=CV) or hepatocyte *i* and portal vein *j* (X=PV) . $\underline{\omega}_k(t)$ denotes the velocity of sinusoid *k*. $\underline{\eta}_i(t)$ is an uncorrelated noise term with amplitude:

$$\left\langle \eta_{in}(t)\eta_{jm}(t')\right\rangle = \delta_{ij}\delta_{mn}\delta(t-t') \tag{35}$$

whereby *i* and ,*j* denote different cells, and *n*,*m* ϵ (x, y, z) denote the coordinates.

In case we consider anisotropic, polar hepatocytes and an active directed migration, the velocity of cell *i* is determined by:

$$\begin{aligned}\zeta \underline{v}_i(t) = \sum_j \left(\gamma_{ij}^C (\underline{v}_j(t) - \underline{v}_i(t)) + \underline{F}_{ij}^C(\psi_{ij})\right) + \sqrt{2\gamma_i^2 D^C} \cdot \underline{\eta}_i(t) + \\ \sum_z \underline{F}_{iz}^{CV}(\psi_i) + \sum_m \underline{F}_{im}^{PV}(\psi_i) \sum_k \left(\gamma_{ik}^S (\underline{v}_k(t) - \underline{\omega}_k(t)) + \underline{F}_{ik}^S(\psi_i)\right) + \underline{F}_i^{Active}\end{aligned} \tag{36}$$

whereby in contrast to Eqn.34 forces depend on the orientation $\psi_{ij}$ of hepatocyte *i* and *j* or the angle $\psi_i$ of the hepatocyte *i* to veins and sinusoids, respectively. $\underline{F}_i^{Active}$ denotes a force that results from active cell migration for example in direction of a

mechanical or chemical gradient. For a chemical gradient, $\underline{F}_i^{Active} = \chi \nabla c$. For a mechanical gradient,

$$\underline{F}_i^{Active} = \left(1 - \Theta\left[\underline{\nabla}\hat{p}_i \cdot \Delta\underline{r}_i\right]\right)\underline{\sqrt{2\gamma_i^2 D^C}\eta}_i(t) \tag{37}$$

with $\Delta\underline{r}_i = \underline{r}_i' - \underline{r}_i$. Here, Θ(x) = 1 if x≥0 and zero otherwise is the Heaviside step function and

$$\hat{p}_i = \sum_j \left( \frac{\underline{F}_{ij}^{C,\zeta_m=0}}{A_{ij}} \frac{\underline{r}_i - \underline{r}_j}{\left|\underline{r}_i - \underline{r}_j\right|} \right) + \sum_k \left( \frac{\underline{F}_{ik}^{S,\zeta_m=0}}{A_{ij}} \frac{\underline{r}_i - \underline{r}_k}{\left|\underline{r}_i - \underline{r}_k\right|} \right) \tag{38}$$

is a measure for stress of cell *i* by adhesion or external forces. It is zero only if the cell is isolated. We implemented this by shifting a cell by a distance of $d \in [0, qR]$ into a random direction. We then calculated the difference $\Delta p(t+\Delta t) = p_i(t+\Delta t) - p_i(t)$ using Eqn.38 and added a corresponding force contribution to the equation of motion (Eqn.36) as indicated if this difference was not larger than zero ($\Delta p_i(t+\Delta t) \leq 0$). If it was larger than zero then we tried another shift; at most $N_s$ different shifts were tested. If for none of the shifts $\Delta p_i(t+\Delta t) \leq 0$, then we did not add any force contribution to Eqn.36. We have tested the algorithm with $q \in [0.3, 2]$ and $N_s \in [50, 500]$ and found that the results do not depend critically on the values of $q$ or $N_s$ within these ranges. In the simulations described in the following sections we have chosen $q = 0.6$ and $N_s = 200$. We assumed for simplicity that:

$$\underline{F}_{ij}^X(\psi_{ij}) = \frac{A_{ij}^{adh}(\psi_{ij})}{A_{ij}} \underline{F}_{ij}^X \qquad - \tag{39}$$

where $A_{ij}^{adh}(\psi_{ij})$ is the area of the overlapping regions that are able to form adhesive bond within the contact area $A_{ij}$ of interacting hepatocytes and sinusoids and $\underline{F}_{ij}^X$ is the interaction force in case of isotropic hepatocytes. For a complete list of all model parameters see Appendix 5.

4.3.3.2. Hepatocyte reorientation in 3D

Extending the concept introduced in section 4.2, for polar cells we permitted cell orientation changes in three dimensions. For simplicity we modeled these by energy minimization (the Metropolis algorithm) instead of numerically integrating equations for the torques. Energy minimization provides an alternative to a forced-based single-cell dynamics [Drasdo et al., 2007]. Within each time interval Δt for each cell a rotation trial around three space-fixed axes by angles $\delta\beta_i$ with i=1, 2, 3, $\delta\beta_i \in [0, \delta\beta_{max})$, with $\delta\beta_{max} \ll \pi/2$ was performed, using the algorithm of Barker and Watts as

explained in [Drasdo et al., 2007]. The probability $P_{Rot}$ that the rotation trial is accepted was calculated by $P_{Rot} = \min(1, e^{-\Delta V/F_T})$ where $\Delta V = V(t+\Delta t) - V(t)$. $V(t+\Delta t) = \sum_{i<j}^{N} V_{ij}(t+\Delta t)$ is the total potential energy after the orientation change, $V(t)$ the total potential energy before the orientation change. $F_T$ is a reference energy [Drasdo & Hoehme, 2005]. Energy and force are linked by Eqn.15. The Metropolis algorithm ensures that orientation changes that lead to a decrease of the energy of the multicellular configuration are always accepted while those which lead to an energy increase are only accepted with probability $e^{-\Delta V/F_T}$.
For isotropic cells we do not consider orientation changes since they do not change the total energy of the multicellular configuration.

4.3.3.3. Sinusoid and vein model

The sinusoidal network and the central and portal veins of the liver lobule are modeled as semi-flexible chains of spheres of radius $R_{Sinu}$ that are connected by springs. In all models the velocity $\underline{\omega}_i(t)$ of model sinusoid *i* is determined by:

$$\zeta \underline{\omega}_i(t) = \sum_k \left( \gamma_{ik}^S (\underline{\omega}_k(t) - \underline{\omega}_i(t)) + \underline{F}_{ik}^S \right) + \underline{F}_i^{Spring} + \sum_m \underline{F}_{im}^C + \sum_m \left( \gamma_{im}^S (\underline{v}_m(t) - \omega_m(t)) + \underline{F}_{im}^S(\psi_{im}) \right) \quad (40)$$

where $\gamma_{ik}^S$ denotes the friction between sinusoid *i* interacting hepatocytes *k*, $\underline{F}_i^{Spring}$ are spring forces that arise from the chain connections and $\underline{F}_{im}^C$ summarizes the repulsive and adhesive forces between sinusoid *i* and interacting hepatocytes *m*.

4.3.3.4. Further model extensions

Moreover, we considered a possible influence of morphogenes either transported with the blood into the liver lobules or secreted by the necrotic cells close to the central vein. For the diffusion, secretion and dissociation of the morphogenes, a reaction-diffusion equation as elaborated in section 3.5.1 was used.

We considered two starting configurations: (i) a representative liver lobule that has been generated by averaging over the architectural parameters of 26 liver lobules (section 4.3.2.8) and (ii) a concrete liver lobule that has been reconstructed from a specific confocal data set to avoid possible artifacts that may arise from averaging (section 4.3.2.9).

## 4.3.4. Experiments

### 4.3.4.1. Mice and administration of substances.

Male C57BL/6N mice, 11-14 weeks old (Charles River, Sulzfeld, Germany) were used for the regeneration experiments. The mice were fed ad libidum with Ssniff R/M-H, 10 mm standard diet (Ssniff, Soest, Germany) and all experiments were approved by the local authorities. 1.6 g $CCl_4$/kg body weight was administered in corn oil using a stock solution of 0.4 g/ml. Three mice were analyzed at each of the time periods given in the results section. Mice received injections of 80mg BrdU/kg body weight (in 0.9% NaCl solution) 6, 4, and 2h before preparation of the livers, respectively. To generate the Tie-2-tTA transgenic reporter mice a construct containing the Tie-2 promoter and enhancer governing the expression of tTA was injected into the pronucleus of fertilized mouse eggs. The tetO-Cre and the EGFP-reporter mice, where EGFP expression is activated by Cre-mediated excision of a STOP-cassette, have been described previously [Saam & Gordon, 1999], [Constien et al., 2001]. The Tie-2 tTA transgene was established and exposed to doxycycline as described in [Deutsch et al., 2008]. For validation of the reconstructed liver lobules we used Alfp-Cre transgenic mice [Kellendonk et al., 2000] and mated them to the above mentioned EGFP-reporter mice where hepatocytes were EGFP marked. Fig.60 illustrates the experimental design used to study daughter cell orientation as elaborated in section 4.3.5.3.

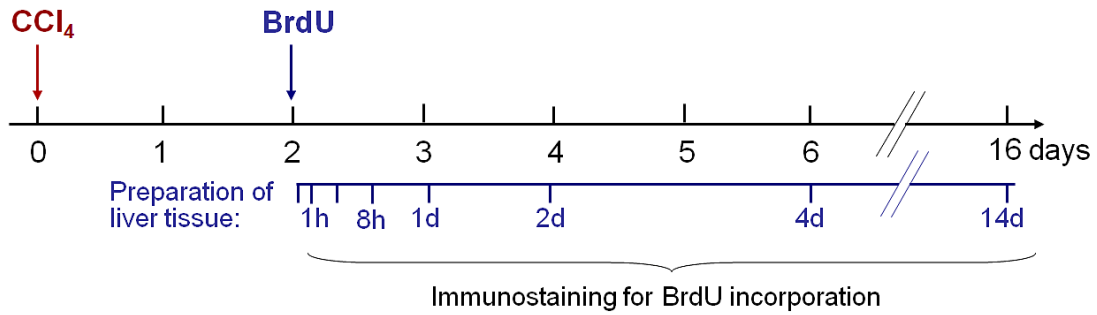


**Fig. 60: Experimental design for the analysis of daughter cell orientation**. Mice received 1.6 g/kg $CCl_4$ followed by injection of BrdU two days later, when proliferation is maximal. Subsequently, liver tissue was prepared at different time intervals after BrdU injection and immunostained for BrdU positive nuclei. Three mice were analyzed per time interval.

### 4.3.4.2 Excision and fixation of liver tissue

After the specified period of time the mice were sacrificed. To avoid any degradation of RNA the abdominal cavity was immediately opened and the whole liver was carefully excised without damaging the liver capsule. Then the tissue was separated into three different parts. One part of about $5mm^3$ in size was frozen in liquid nitrogen and then stored at -80°C for later RNA isolation. The two larger parts of about $1cm^3$ in size were used for immunohistochemical analysis. For the preparation

of vibratome slices one of them was collected in 4% paraformaldehyde (Sigma, Munich, Germany) and penetrated for 48h at room temperature and then stored in PBS at 4°C until further use. The latter part of the liver was embedded into paraffin. For this purpose it was transferred to paraffin embedding cassettes (Carl-Roth, Karlsruhe, Germany) and stored in 4% paraformaldehyde for 48h at 4°C.

4.3.4.2. Immunostaining of the cytoskeleton using vibratome slices

Using a vibratome (Leica, Wetzlar, Germany) slices of 50-150µm thickness were prepared prior to the immunostaining and collected in phosphate buffered saline (PBS; 2.7mM KCl, 1.5mM $KH_2PO_4$, 140mM NaCl and 6.4mM $Na_2HPO_4.12H_2O$). All following steps were performed on a flat shaker at a frequency of 150 table movements per minute (IKA, Staufen, Germany). To block unspecific binding sites for the used antibodies the slices were incubated for 3h at room temperature with 3% bovine serum albumin (BSA; Serva, Heidelberg, Germany) / 1% Tween®20 (Sigma, Munich, Germany).
Rhodamin labeled phalloidin (Biotrend, Cologne, Germany; 1:100 dilution) was used to stain the cytoskeleton. Primary antibodies were directed against either CD31 (BD, Heidelberg, Germany; raised in rat, 1:50 dilution), ICAM (Proteintech Group, Manchester, UK; raised in rabbit, 1:100 dilution), dipeptidyl peptidase IV (DPP IV; BD, Heidelberg, Germany; raised in goat, 1:25 dilution), 5-bromo-2-deoxyuridine (BrdU; Serotec, Düsseldorf, Germany; raised in rat, 1:25 dilution), b-actin (Sigma, München, Germany, raised in mouse; 1:25 dilution) or glutamine synthetase (BD Transduction Laboratories, Heidelberg, Germany; raised in mouse, 1:1000 dilution). Cy2-, Cy3- and Cy5-labelled secondary antibodies (Dianova, Hamburg, Germany) or the avidin-biotin-complex-method (ABC) with diaminobenzidine (DAB; Dako, Glostrup, Denmark) were applied to visualize the primary antibodies.
Incubation with the different primary antibodies using the listed dilutions was performed over night at 4°C on a shaker with the above specified parameters. All antibodies were diluted in a solution of 0.3% BSA / 0.1% Tween®20 in PBS. The incubation period was followed by three subsequent washing steps in PBS at room temperature for 10min each. All secondary antibodies labeled with fluorescent dyes were applied in a 1:100 dilution and incubated with the slices over night at 4°C on a shaker to visualize bound primary antibodies. In the case of multi-labeling the second antigen was stained after finishing the first one. If not specified differently, antigens of CD31 and ICAM were stained using Cy3-labelled secondary antibodies, whereas b-actin was visualized using Cy2-labelled secondary antibodies. In case of DPP IV, Cy5-labelled secondary antibodies were applied. The procedure of incubation was exactly the same as for the first antigen. Following these stainings the slices were incubated with 4',6-diamidino-2-phenylindole (DAPI, Invitrogen, Karlsruhe, Germany) at a concentration of 2.35µg/mL for 2h at room temperature to identify the nuclei. After three washing steps using PBS the vibratome slices were transferred to a water filled Petri dish and mounted on SuperfrostPlus slides (Menzel,

Braunschweig, Germany) using aqueous Mowiol mounting media and stored in the dark at 4°C until further analysis.

4.3.4.3. Immunostaining of BrdU using paraffin slices

Formalin-fixed liver tissue was washed in PBS for 48h, dehydrated through an ethanol gradient (four times 5min in 70%, 90% and 95% ethanol, respectively, followed by three times in 100% ethanol). Subsequently, tissue specimens were incubated four times in xylene (Carl-Roth, Karlsruhe, Germany) and incubated over night in xylene/paraffin (1:1) at 60°C. Afterwards, tissue specimens were incubated twice in 60°C paraffin for 3h, followed by embedding in paraffin. Slices of 5µm were prepared using a microtome (Microm, Walldorf, Germany) mounted onto SuperfrostPlus slides, and heated for 20min at 60°C. Sections were then deparaffinized by five times washing in Rotihistol (Carl-Roth, Karlsruhe, Germany) for 5min each, followed by hydration through a descending ethanol gradient (100%, 95%, 90%, and 70% ethanol for 5min each) and 5min in PBS. During the next step the sections were boiled twice in a microwave oven for 7min in 0.01M citrate buffer (Carl-Roth, Karlsruhe, Germany; pH 6.0). Endogenous peroxidase was blocked by 30min incubation in a solution of 7.5% $H_2O_2$ in methanol at room temperature. All further incubations were performed in a humidified chamber. Unspecific binding sites were blocked by 3% BSA / 0.1% Tween®20 / PBS using 100µL per section. Subsequently, endogenous biotin and avidin were blocked using a commercially available kit (Avidin-/Biotin-Blocking-Kit, Vector Lab., Burlingame, USA) according to the manufacturer's instructions. Leaving out a washing step the blocking solution was dripped off carefully and the primary antibodies (rat-anti-BrdU, Serotec, Düsseldorf, Germany; 1:25 diluted) were incubated on the tissue section for 1h at room temperature. Before proceeding with the next incubation step the slides were washed three times 5min in PBS. Biotinylated secondary antibodies (Dianova, Hamburg, Germany; raised in goat, 1:250 diluted) were chosen to detect the primary antibodies. After 1h incubation at room temperature the slices were washed again for three times 5min in PBS. Streptavidin-horseradish-peroxidase (Dianova, Hamburg, Germany; 1:500 diluted) was incubated on the tissue sections for 1h at room temperature. After three times 5min washing in PBS the slices were incubated for 5min at room temperature with DAB (Dako, Glostrup, Denmark) freshly prepared according to the manufacturer's instructions. Following this the slides were rinsed for 10min under tap-water and then counter stained using Mayer's hemalum (Merck, Darmstadt, Germany) for 90s. Again the slides were rinsed for 10min under tap-water and then dehydrated using the graded ethanol series (70%, 90%, 95%, and 100% for 90s each) and four times 90s of Rotihistol. Using Entellan (Merck, Darmstadt, Germany) the slides were mounted and stored in the dark at room temperature until further analysis.

#### 4.3.4.4. Confocal microscopy

All slices were screened shortly after the staining procedure using appropriate microscopes. As for the vibratome slices stained with fluorescent dyes a confocal microscope (Olympus FV-1000) was used. Excitation and emission wavelengths were used as specified by the manufacturer. The colors were mapped as following: Cy2 – green, Cy3 – red, Cy5 - green, DAPI – blue. In case, Cy3 and Cy5 were detected in one slice the mapping was as following: Cy3 – red, Cy5 – green, DAPI – blue. In all cases the different dyes could be detected very specifically with no cross-talk between the channels.
For reconstruction of whole liver sections, z-scans using stained vibratome slices were performed. Firstly the range of possible scans was determined. Laser parameters such as intensity, amplification and threshold of the signal were adjusted over the whole liver section to assure constant capturing of images regardless of the scan depth. Acquired image stacks were then processed using Imaris software.

#### 4.3.4.5. Bright field microscopy

Screening of DAB-stained slices was done using a conventional bright field microscope (Olympus BX41). Images were acquired and organized using cell^M software (Olympus).

#### 4.3.4.6. Induction of mouse liver tumors

Mouse liver tumors were available to us from a previously conducted experiment [Marx-Stoelting et al., 2008]. Tumors were induced in 6 weeks old male C3H/HeJ mice by single intraperitoneal injection of N-nitrosodiethylamine (90µg/kg body wt.) followed by continuous exposure of mice to phenobarbital (0.05% in diet). Following sacrifice of mice isolated tumors were immediately frozen in liquid nitrogen and stored until at -70° until analysis.

## 4.3.5. Results

### 4.3.5.1. Simulating liver regeneration in 3D

We started our analyses with the model that was elaborated in chapter 3 of this thesis to quantitatively mimic the growth dynamics and morphologies of growing cell populations [Drasdo & Hoehme, 2005] [Drasdo et al., 2007] [Hoehme & Drasdo, 2009a]. In the following, we call this initial approach "model 1". In model 1 we assumed random orientation of cell division, no morphogen that influences the direction of cell movement and an unspecific homogeneous isotropic adhesion of hepatocytes to other hepatocytes and to the sinusoids (Fig.61A, Supporting video 33). Despite this model was in good correspondence with the experimental findings regarding the average hepatocyte density (Fig.62A) it could not explain the experimentally observed dynamics of the regeneration process, because closure of the central necrotic lesion was too slow (Fig.62B). Furthermore, the hepatocyte-sinusoid contact area did not correspond to the experimental data (Fig.62C). We verified this finding by simulations over the wide range of physiologically valid parameters modifying hepatocyte micromotility, hepatocyte-hepatocyte and hepatocyte-sinusoid adhesion, hepatocyte-hepatocyte and hepatocyte-matrix friction

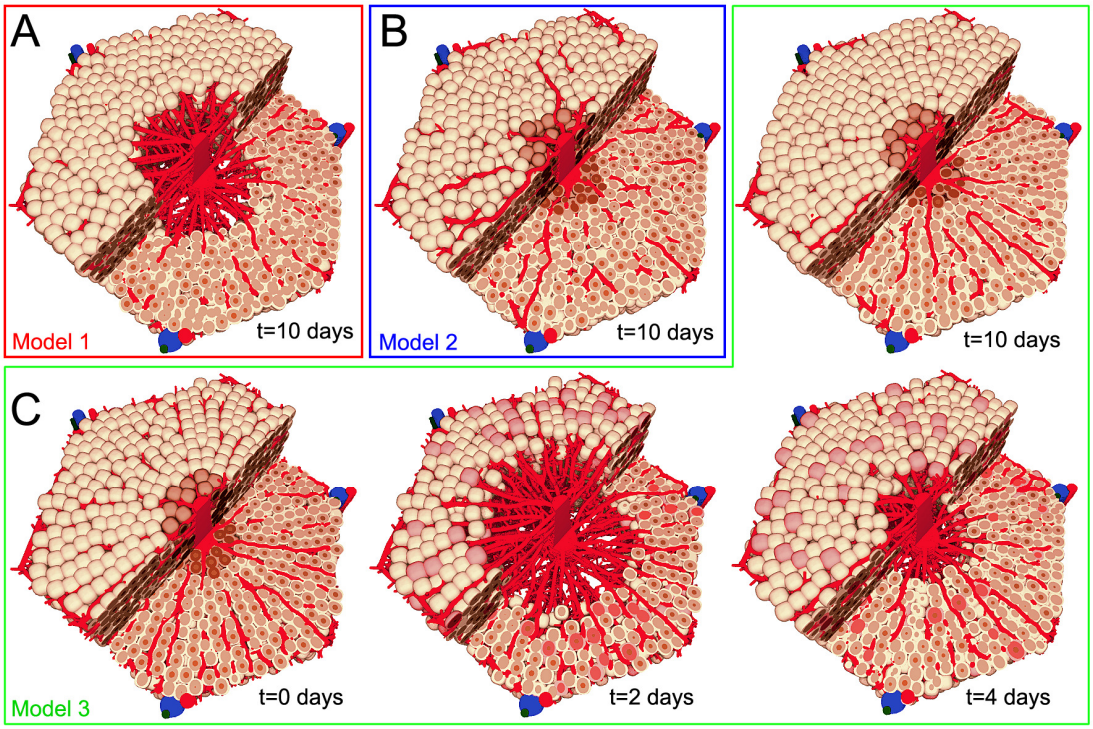


**Fig. 61: Regeneration in the model starting with a representative liver lobule.**
A-C partly show cross sections (compare to Fig.58B) of model simulations; A: Result of simulation with model 1 after 10 days. B: Result of simulation with model 2 after 10 days C: Illustration of the regeneration process (after t=0,2,4 and 10 days) with model 3 (also see Supporting videos 33-35).

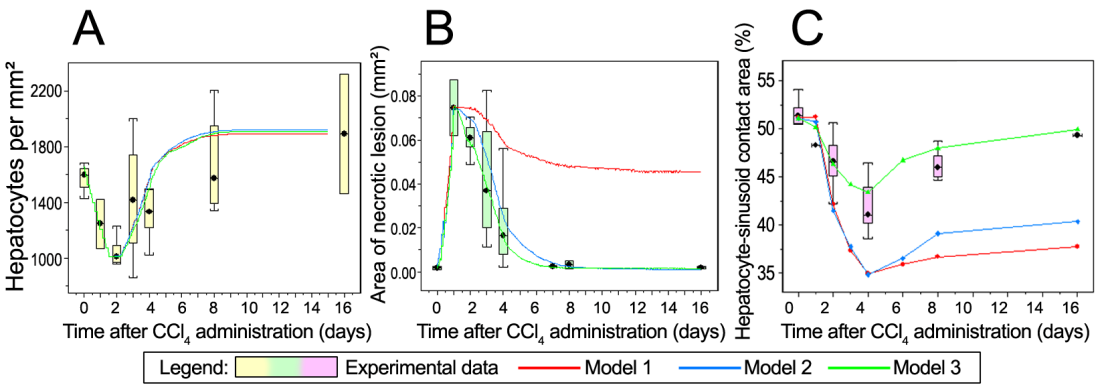


**Fig. 62: Quantitative comparison of experimental data and model.**
A: Average hepatocyte density. B: Area of central necrosis. C: Hepatocyte sinusoid contact area. Lines denote model simulations whereas the box plots represent experimental data.

and changed the biophysical properties of hepatocytes and sinusoids. For example, strongly increased micromotility resulted in detachment of hepatocytes migrating individually into the necrotic lesion (Supporting Fig.10). However, a detachment of single cells from the regeneration front was not observed in our experiments. Therefore, the maximum micromotility must be considered to arise from forces that do not exceed that of hepatocyte-hepatocyte adhesion. We concluded that without a mechanism that directs hepatocyte migration into the necrotic zone without leading to detachment of single hepatocytes the lesion cannot be closed at the necessary speed. We tested morphogen and mechanical force gradients to direct migration of the hepatocytes towards the necrotic area. We additionally introduced polar hepatocytes as described in section 4.2.1.2 and modified cell-cell adhesion in the model such that adjacent polar hepatocytes only form adhesive bonds at their apical sides. This reduced adhesion with the sinusoids and thereby increased cell migration speed. The best data fit was obtained with a model (model 2) that integrated polar hepatocytes with a micromotility that was biased into the direction of the necrotic area and thereby directed cell migration. Model 2 (Fig.61B, Supporting video 34) was in agreement with the experimental observations regarding hepatocyte density (Fig.62A) and successfully mimicked the regeneration dynamics (Fig.62B). A bias in the micromotility may be caused by a local mechanical- or a morphogen gradient as long as both affect only 2-5 cell layers at the edge of the necrotic lesion. We found that if all hepatocytes in a lobule would be affected the lobule architecture would be distorted. We modeled the influence of gradients caused by cytokine secretion of dead or dying hepatocytes from the central necrotic region or cytokine transport with the blood. However, none of those model variations was able to successfully restore the lobule microarchitecture (Fig.62C). After 16 days the representative model 2 showed a hepatocyte-sinusoid contact area of only 37.1±1.1% which is significantly lower compared to the experimental situation (48.5%±2.5%).

4.3.5.2. Hepatocyte-sinusoid alignment

Since neither model 1 nor model 2 were able to fully explain the experimentally observed data we included a further mechanism into our model that we named hepatocyte-sinusoid alignment (HSA). HSA means that daughter hepatocytes after cell division align themselves along the closest sinusoid, such that the line connecting the centers of the two daughter cells is parallel to the local orientation of the closest sinusoid. This mechanism could be seen as a refinement of the "directed cell orientation" proposed in section 4.2 based on experimental observations. The first experimental evidence that sinusoids may serve as an aid to orientation of regenerating hepatocytes came from our tie2-reporter mice. Sinusoidal cells survive after administration of $CCl_4$ even in the central region of the lobule where almost all hepatocytes die. However, since sinusoidal cells are very thin they may easily be overlooked in the central dead cell mass when paraffin slices are prepared and stained by conventional techniques (Supporting Fig.11). We first noticed their presence in the central dead cell mass using tie2-reporter mice carrying three constructs, whereby the transactivator protein tTA was formed under control of the tie2 promoter, tTA causes expression of Cre recombinase after binding to the responsive element of the second construct and Cre recombinase catalyzes the loxP site-specific recombination of DNA leading to removal of the STOP cassette in the third construct. (Fig.63A).

Consequently, cells with tie2 promoter activity and their progeny were EGFP marked. Livers of untreated tie2-reporter mice expressed EGFP only in endothelial cells of veins and other vessels, whereas the sinusoidal cells remained unmarked (Fig.63B). A completely different picture was obtained after administration of $CCl_4$ to tie2-reporter mice. A relatively high fraction of sinusoidal cells especially in the dead cell area started to express EGFP (Fig.63C,D). This result was confirmed by qRT-PCR analysis, where an intermittent increase of tTA RNA and a permanent increase of EGFP RNA expression were observed after injection of $CCl_4$ (Supporting Fig.12). This result shows that the sinusoidal cells in the dead hepatocyte area survive, but may be stressed and begin to show tie2 promoter activity, which is known to be involved in vessel remodeling [Saharinen et al., 2008]. In order to visualize the state of the sinusoidal network we immunostained sinusoidal cells with ICAM antibodies and reconstructed the network in healthy livers and two days after $CCl_4$ administration. Although the sinusoidal network showed some degree of destruction, the basic network structure remained intact (Fig.63E,F). Analysis of the numbers of hepatocytes and sinusoidal cells showed that the majority of sinusoidal cells survived even in the central area where almost all hepatocytes were killed by $CCl_4$ (Supporting Fig.13). This prompted us to study the hypothesis that sinusoidal cells may play a role during the regeneration process and to include the HSA mechanism into our model.

We found the resulting model 3 (Fig.61C, Supporting video 35) to be in excellent agreement with all experimental observations including hepatocyte density (Fig.62A)

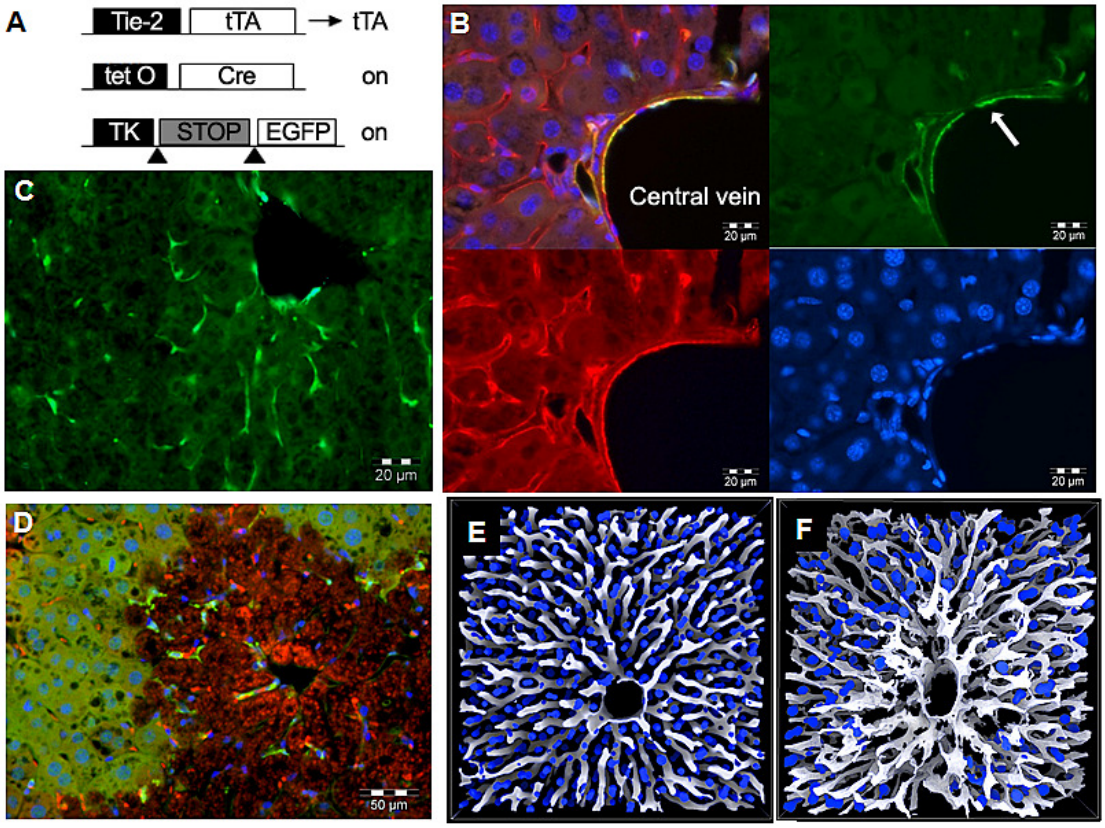


**Fig. 63: Sinusoidal cells survive in the central dead cell area** of the liver lobule after $CCl_4$ poisoning and activate the tie-2 promoter. A. Constructs of the triple transgenic tie2-reporter mice. B. Liver tissue of an untreated tie2-reporter mouse. Green fluorescence (EGFP) indicates tie2 promoter activity that is positive in the endothelial cells of a vein (white arrow in upper right image). Sinusoidal cells are visualized by CD31 immunostaining (light red in the lower left image) and nuclei by DAPI (blue in the lower right image). The merged picture (upper left image) demonstrates that endothelial cells of the vein but not the sinusoidal cells express EGFP (yellow). C and D. Two days after $CCl_4$ administration some of the sinusoidal cells start to express EGFP. C. EGFP green fluorescence. D. Green, red and blue merged fluorescence. The central dead cell area is characterized by loss of nuclei and increased red background fluorescence. A substantial fraction of the sinusoidal cells within the central dead hepatocyte area survives and starts to express EGFP as a reporter of tie2-promoter activity. E: 3D-reconstructed lobule before and (F) after $CCl_4$ administration. While the hepatocytes (blue) die, the sinusoids (grey) remain largely intact.

and regeneration dynamics (Fig.62B). Furthermore, the lobule architecture was restored as after 16 days and the hepatocyte-sinusoid contact area was 50.4% which corresponds to the experimental situation (48.5%±2.5%) (Fig.62F). Fig.61C illustrates a typical computer simulation with model 3 (see also Supporting video 35). In summary, our regeneration of the liver architecture. From a sensitivity analysis our model predicts that the alignment of daughter cells along the closest sinusoid must occur within at most about two hours after cell division.

4.3.5.3. Experimental validation of hepatocyte-sinusoid alignment

In a next step we experimentally tested the prediction of the computational model by determining the degree of alignment of hepatocytes after cell division along sinusoids. For this purpose we reconstructed the three-dimensional sinusoidal network as well as resting hepatocytes (BrdU negative) and hepatocytes after cell division (BrdU positive) from confocal laser scans (Fig.64). BrdU positive nuclei were visualized by green fluorescence whereas the cell borders appeared red due to phalloidine staining. We applied an experimental design, where BrdU was injected 48h after $CCl_4$ administration, when hepatocyte proliferation was close to its maximum. Livers were prepared at time intervals between 8 hours and 14 days after BrdU injection (experimental design: Fig.60). Two-dimensional analysis of paraffin slices suggested that daughter cells are well aligned in the direction of the sinusoid (Fig.64A-C). However, in two-dimensional analyses the result may be compromised by the choice of the cutting plane. Therefore, we reconstructed and analyzed the full three-dimensional structure of the lobules (as described in section 4.3.2) and identified all pairs of BrdU-positive neighboring hepatocytes.
Adjacent hepatocytes whose nuclei incorporated BrdU can either have emerged from the same mother cell by cell division or because or can have entered the S-phase by chance almost simultaneously. For peaks of proliferation activity (t = 2–3 days), we determined a chance of 20-30% for the latter case by studying the spatial pattern of the proliferating cells in our computer simulations. We neglected cases where more than two adjacent nuclei incorporated BrdU because it was rare (< 5 %). Hence, about 20-30% misaligned cells would still not contradict our model prediction of proliferating cells alignment along the closest sinusoid. If adjacent BrdU positive hepatocytes are daughter cells, the line connecting the centers of mass of their nuclei defines a vector $\vec{c}$ that could be used to describe their orientation. This orientation was then compared to the orientation $\vec{s}$ of the most adjacent sinusoid that could easily be extracted from the sinusoids graphs. The angle $\alpha$ that we use as a measure for the alignment of hepatocytes and sinusoids was then calculated using the scalar product for vectors by:

$$\cos(\alpha) = \frac{\vec{c} \cdot \vec{s}}{|\vec{c}| \cdot |\vec{s}|} \tag{41}$$

where $\vec{c}$ and $\vec{s}$ are vectors. The closer this angle is to zero the better is the alignment. 8 hours after BrdU injection (the earliest analyzed time period) the majority of daughter cells showed a good alignment to the neighboring sinusoid (Fig.64; Supporting Fig.14). The simulation result with model 3 showed an excellent agreement with the experimentally observed angle distribution while in models 1 and 2 the orientation angle was uniformly distributed in [0,π/2] (Fig.64E).

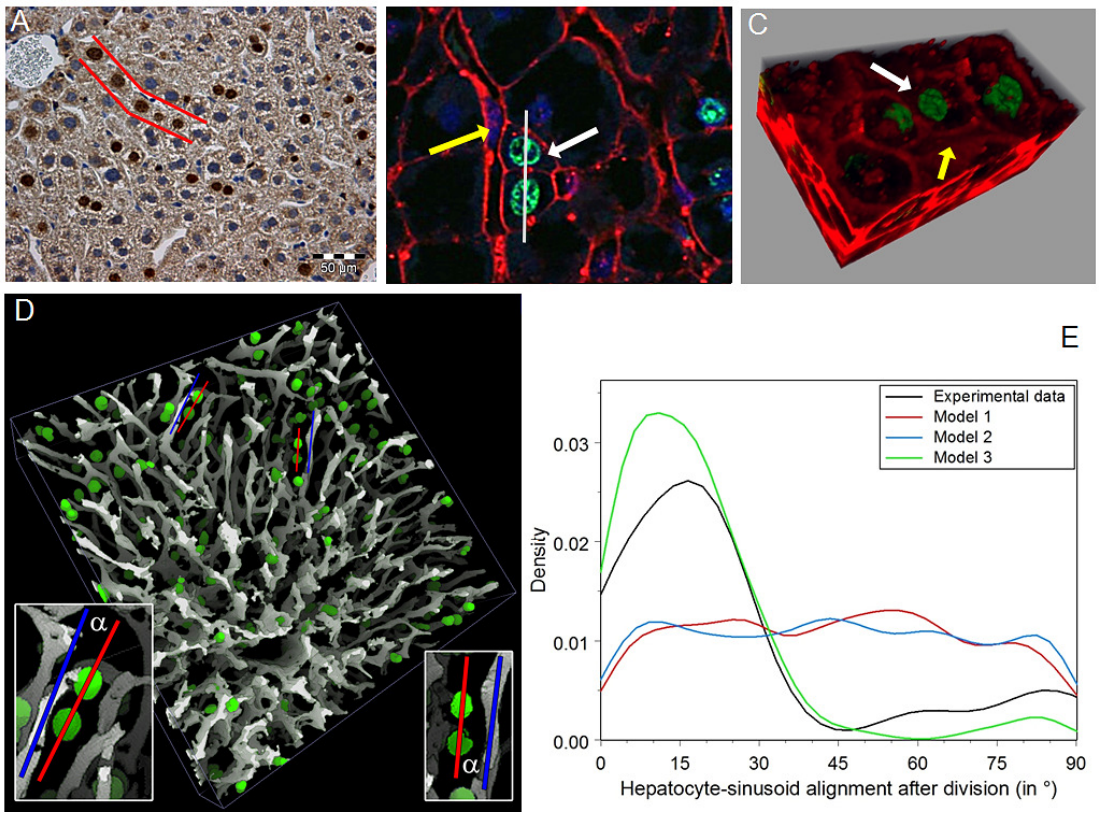


**Fig. 64: Experimental validation of HSA.**

A: Immunohistochemistry staining in bright field microscopy; BrdU-positive nuclei in dark brown. B: Confocal microscopy image. green: BrdU positive cells, blue: non-proliferating hepatocytes, red: lectin (cell boundaries; sinusoids). Notice the pair of BrdU-positive cells indicated by the white arrow is oriented in parallel to the neighboring sinusoid indicated by a yellow arrow. C: Three dimensional reconstruction of two daughter cells that are oriented in the direction of the neighboring sinusoid D: 3D distribution of BrdU-positive cells and sinusoids. The inset shows the connecting line of daughter hepatocytes (red) and their orientation (angle α) with regard to the closest sinusoid (blue line). E: density-distribution for angle α in experiments and models 1-3.

## 4.3.6. Discussion

Development, architecture and function of tissues depend on interactions between cells that can vary in time and space [Hui & Bhatia, 2007]. Such interactions occur primarily by direct contact or secretion of soluble factors. In particular, liver function and dysfunction depend on its microarchitecture. Blood flows through the sinusoids thereby getting into contact with hepatocytes before it outflows into the central vein (Fig.36D,E and Fig.58B). The quantitative analysis of the liver lobule microarchitecture suggests that during evolution an optimal sinusoidal architecture has formed to guarantee an efficient exchange between blood and hepatocytes. Liver function is compromised if the hepatocyte-sinusoid contact area decreases. Obviously, the two most abundant cell types of the liver, hepatocytes and sinusoidal cells are crucial for maintenance of liver microarchitecture. However, analysis of hepatocyte-sinusoid interactions and their influence on liver microarchitecture is experimentally challenging. Conventional techniques were insufficient in describing three-dimensional spatio-temporal processes, so no techniques were available that allowed for quantification of liver microarchitecture. Therefore, we established a process chain that utilizes the synergies from experiment, image analysis and direct spatio-temporal modeling. As starting point we reconstructed liver lobules from confocal laser scans such that the position of all individual hepatocytes and sinusoidal cells as well as all further relevant information on lobule architecture were correctly captured. We introduced architectural parameters to quantify lobule mass and structure. The architectural parameters served to define the initial state of our computational model. In order to quantify the regeneration process after $CCl_4$ induced necrosis of hepatocytes close to the central vein and to permit a quantitative comparison with the simulation results of our model, we introduced process parameters.

These parameters were experimentally determined in regenerating mouse liver covering a period of 0 - 16 days after intoxication with $CCl_4$ and included (1) a measure for the spatio-temporal pattern of cell proliferation, (2) a measure for the liver lobule mass, (3) a measure for the area of the necrotic lesion, and (4) a measure to describe liver lobule microarchitecture, namely, the hepatocyte-sinusoid contact area reflecting liver function. By model simulations we have demonstrated that if any of these parameters would have not been taken into account we would have failed to correctly identify the key mechanisms involved in liver regeneration after $CCl_4$ intoxication. Parameter 1 served as an input parameter and – together with our abstract but still realistic description of a cell - ensured that the lobule mass was restored (parameter 2). However, if cell migration is completely dictated by physical interaction forces, the cells accumulate in the periportal zone and the lesion is not closed (Fig.61A, Supporting video 33). Only if hepatocytes actively migrate towards the necrotic zone, it is closed (parameter 3). Several lines of evidence suggest that dead or dying hepatocytes indeed cause surviving hepatocytes to migrate in their direction: (I) Time lapse videos of cultivated mouse hepatocytes demonstrate that

vital hepatocytes are attracted by dead hepatocytes (Supporting video 27 and 28), (II) filopodia extend several micrometers ahead of the hepatocytes at the edge of the dead cell area (Supporting Fig.10), (III) some hepatocytes show stress fiber formation as evidenced by phalloidine staining similar to hepatocytes *in vitro* showing a high scattering activity (Supporting Fig.15). We also included the known polarity of hepatocytes into the model that implicates a reduced adhesion between hepatocytes and sinusoids that leads to reduced hepatocyte-sinusoid friction. However, none of the mechanisms ensured that the hepatocytes aligned properly. They locally formed double- instead of single-cell thick columns by pushing apart adjacent sinusoids thereby increasing the hepatocyte-hepatocyte contact area at the expense of the hepatocyte-sinusoid contact area (Fig.61B, Supporting video 34).

Only when we introduced a new mechanism, the alignment of daughter hepatocytes in the direction of the closest sinusoid - a so far unrecognized process which we named hepatocyte-sinusoid alignment (HSA) – then the simulated tissue architecture was in agreement with the experimentally obtained data. Importantly, by a model parameter sensitivity analysis within all model variants we could show that HSA could not be substituted by including any other likely mechanisms into the model. Therefore, the model unambiguously predicted that HSA must take place and that complete regeneration is not possible without HSA. In order to experimentally validate the model prediction of HSA, we three-dimensionally reconstructed and analyzed the orientation of daughter hepatocytes in relation to the sinusoids. The results of this analysis (Fig.64E) confirmed the model prediction.

As previously already recognized, sinusoidal cells are central to triggering hepatocyte proliferation [LeCouter et al., 2003], [Maher, 1993], [Ping et al., 2006], [Michalopoulos & DeFrances, 2005], [Malik et al., 2002]. An important mechanism is that intoxication by $CCl_4$ causes a more than 5-fold increase of HGF in sinusoidal cells leading to increased proliferation of hepatocytes [Maher, 1993]. Besides HGF also IL-6 and TNF-alpha are secreted by sinusoidal cells contributing to the proliferative stimulus [Malik et al., 2002], whereas the same cells also secrete the mito-inhibitor TGF-beta1, which after a spectacular phase of hepatocyte proliferation terminates liver regeneration [Michalopoulos & DeFrances, 1997]. Because of the influence of sinusoidal cells on hepatocyte proliferation, we wondered whether cytokines secreted by sinusoidal cells might also explain HSA. Some explorative experiments indeed led to results supporting this hypothesis. When we co-cultured hepatocytes and sinusoidal cells under the time-lapse microscope, we observed that hepatocytes are attracted by sinusoidal cells and tend to maximize the hepatocyte-sinusoidal contact area (Supporting video 29-32; Supporting Fig.16). This is plausible, because HGF does not only induce proliferation but also serves as a chemoattractant for hepatocytes [Michalopoulos & DeFrances, 1997], [Michalopoulos & DeFrances, 2005] and thus may provide a mechanism that contributes to the proposed HSA. In this case, the hepatocyte alignment along the sinusoid should not occur during but subsequent to cell division. In order to test this hypothesis we performed pilot experiments and studied the orientation of mitotic

spindles by tubulin staining in 2D slices using the same liver samples that have been applied for analysis of daughter cell orientation. In contrast to the above described BrdU positive daughter cells, the mitotic spindles were not systematically aligned in the direction of the sinusoids (Supporting Fig.17). This data suggests that the orientation of the mitotic spindles of hepatocytes may be random but the daughter cells realign themselves in the direction of the closest sinusoid within a short period of time. The analysis of mitotic spindle orientation in 3D turned out to be challenging and is currently under investigation. However, we mimicked the mechanism in computer simulations by replacing the alignment of dividing cells along the closest sinusoid in model 3 by the following two sub-mechanisms: (1) cell division in random direction corresponding to a random orientation of the mitotic spindle and (2) attraction of hepatocyte cells by a short range morphogen that was secreted from the sinusoids. We found that morphogen-induced attraction of hepatocytes by sinusoids could explain HSA if one additionally assumes the re-establishment of hepatocyte polarity after cell division. Without that re-establishment, hepatocytes formed columns with at least two cell layers between the sinusoids induced by local energy minima.

In conclusion, we have shown that HSA represents a so far unrecognized essential mechanism to restore liver microarchitecture. It will be interesting to further investigate the role of HSA in liver diseases such as cirrhosis and hepatocellular carcinoma where microarchitecture is compromised.

# 5. Summary

In the presented thesis we elaborated a general agent based model for multicellular populations. We used this model to shed light on the processes that determine the growth of avascular tumor spheroids and studied the key mechanisms of liver regeneration.

In order to make such analyses possible, we developed a comprehensive software tool that allowed us to effectively simulate, visualize and analyze the constructed computational model. We started with a minimal model for two-dimensional monolayers which are a common experimental technique for *in vitro* cell cultures. We successively advanced our model in order to reflect an *in vivo* situation more closely for example by simulating complex three-dimensional tumor spheroids embedded in granular medium and host tissue.

We proposed a biomechanical form of contact inhibition that was able to explain the experimentally observed linear growth of the diameter in monolayer cultures [Bru et al., 1998] [Bru et al., 2003] and their specific proliferation pattern where cells mainly proliferate at the monolayer border. Furthermore, our model could mimic the growth dynamics of monolayer cultures very precisely.

Subsequently, we considered three-dimensional cell aggregates by studying substrate detachment whereby normally two-dimensional monolayers due to the failure of certain control mechanisms expand perpendicular to the monolayer plane. Failure of growth control mechanisms is known to play an important role in the development of cancer [Hanahan & Weinberg, 2000]. By additionally introducing nutrient diffusion and consumption, we established a further extended model for three-dimensional tumor spheroids which are a common experimental model in therapeutically oriented cancer research. Surprisingly, we found that the proposed biomechanical form of contact inhibition also explains the growth of these tumor spheroids. Thereby, our model suggests in agreement with experimental data [Freyer & Sutherland, 1985] [Freyer & Sutherland, 1986] that the nutrient concentration in the environment of a growing tumor, which is widely believed to control its growth, only determines the size of its necrotic core. Moreover, also in this three-dimensional situation our model precisely mimicked the growth dynamics and proliferation pattern of tumor spheroids *in vitro* where the necrotic core is enclosed by an intermediate layer of quiescent cells and an outer layer of proliferating cells [Kunz-Schughart, 1999].

We further advanced our model for the growth of three dimensional cell populations even closer towards *in vivo* tumors by including aspects from the surrounding tissue. We showed that the biomechanical properties of an embedding tissue have a major impact on the growth dynamics and morphology of growing cell populations by systematically varying the biophysical properties of the embedding tissue. Our model predicts Saffman-Taylor-like instabilities leading to fractal interfaces and an increased ability of cells to invade harsh environments if the motility of the embedding cells is small. We additionally observed large wavelength instabilities as a consequence of decreased density, increased elasticity, strong adhesion or

increased cell size of the embedding tissue or granular medium. Interestingly, we found a nearly complete inhibition of tumor growth for specific properties of the embedding tissue which, if experimentally validated, could have direct therapeutical implications.

Furthermore, we achieved a remarkable agreement with experimental data on tumor growth dynamics by [Helmlinger et al., 1997] and [Galle et al., 2006]. However, the large variety of complex influences predicted by our model strongly indicates that the widespread experimental technique of embedding growing tumor spheroids in agarose gels [Helmlinger et al., 1997] [Galle et al., 2006] [Cheng et al., 2009] may not be sufficient to realistically capture all the biomechanical effects of an embedding tissue. Effects due to the granularity of the surrounding tissue, for example, are missing in experiments like those performed in [Helmlinger et al., 1997].

In contrast to chapter three where we mainly compared our model to published *in vitro* data, in chapter four we investigated a particular *in vivo* situation and studied the fascinating process of liver regeneration after intoxication with $CCl_4$, a prototypical substance for drugs inducing pericentral liver damage.

We established a procedure to use three-dimensional confocal laser scans to reconstruct *in vivo* tissues by image processing and image analysis. We then combined this very detailed and quantitative information with a further advanced version of our repeatedly experimentally validated model. We started with a minimal two-dimensional model for the regenerating liver lobule that nevertheless led to first impressions of the specific impact of the various factors that influence liver regeneration. On that basis we extended our model and created the first three-dimensional agent-based model of the regenerating liver lobule.

By capturing a 16 day regeneration process, our model underlined the importance of the complex columnar microarchitecture within the liver lobules, which is formed by hepatocytes and sinusoids. This microarchitecture ensures optimal exchange of metabolites between blood and hepatocytes. The model unambiguously predicted a so far unrecognized mechanism, the alignment of daughter hepatocytes along the orientation of the closest sinusoid, which we named hepatocyte-sinusoid alignment (HSA), as essential for liver regeneration. Only if HSA was included into the model the simulated tissue architecture was in agreement with the experimentally obtained data and no other likely mechanism could replace it. In order to experimentally validate the model prediction of HSA, we analyzed the orientation of daughter hepatocytes in relation to the sinusoids in three-dimensions. The results of this analysis clearly confirmed the model prediction and thus verified HSA as a yet unknown key mechanism of liver regeneration.

During this analysis we introduced novel techniques that made currently experimentally not accessible information available by image processing and analysis of volumetric datasets obtained by confocal laser scanning microscopy. In addition to the three-dimensional analysis of HSA, we used a similar approach to obtain further currently not experimentally available information on the average

contact area between hepatocytes and sinusoids. Surprisingly, we found this parameter to allow for an automatic differentiation between normal liver tissue and hepatocellular carcinoma. The further pursuit of this finding will be interesting.

In summary, in this thesis we present an interdisciplinary approach to combine microscopic imaging, image processing and analysis and computational modeling - all in three dimensions. The integration of methods and results from different scientific fields like cell biology, physics and computer science enabled us to obtain new insights in cancer research and hepatology.
We therefore consider the presented interdisciplinary approach and the corresponding procedures exemplary and widely applicable in the systems biology of tissues in general.

# 6. Outlook

In the last chapter of this thesis, we give a brief outlook to a selection of current and future research directions that ground on the results presented in this work. Because most of these studies are neither finished nor published, we only sketch out the basic ideas and do not go into detail. The following should merely illustrate some of the perspectives opened up by this work.

In general, the computational complexity of our model largely depends on the mimicked situation. As a result the duration of the corresponding computer simulations spans a wide range from a few minutes to several months in extreme cases. For example, a 14-days simulation of a single regenerating liver lobule in 3D takes about 2 hours computation time on a recent workstation utilizing only a single processor core. Therefore in this particular example, a 100 fold increase of computational complexity of the model simulations seems feasible (200 hours ~ 8 days). This underlines that our model can still be considered very extensible in both granularity directions. On the one hand, on a cellular scale intracellular evolution (section 6.1) and regulation (section 6.2) can readily be implemented. Both extensions would lead to further intercellular heterogeneity. On the other hand, on a multicellular scale we started to extend our liver model towards larger system sizes and incorporated multiple interacting liver lobules (section 6.3) which brings us closer to the simulation of the whole liver and opens up the possibility to study for example partial hepatectomy or diseases like hepatocellular carcinoma that cannot be modeled within a single liver lobule.

## 6.1. Somatic evolution

In traditional evolutionary biology and ecology evolution commonly designates the adaption of a species of genetically varying individuals driven by natural selection and genetic drift. Germ line mutation and recombination across generations lead to differences in survival and reproduction fitness. Natural selection of the fittest individuals is mainly driven by abiotic factors, competitors, predators and parasites [Crespi & Summers, 2005]. In general evolutionary changes proceed across very long periods of time typically hundreds of thousands of years. However, in the presence of significant gene flow microevolution of populations can still occur rapidly [Sparkman et al., 2009] [Hendry & Kinnison, 1999] [Bell et al., 2004].
In the last decades molecular biology has started studying evolutionary processes on a cellular rather than on population scale. For example, carcinogenesis has been recognized as evolutionary process involving selection among cancer cells [Greaves, 2000]. In contrast to the evolution of populations, the evolution of cancer cells arises from variations in cellular replication, apoptosis and senescence. Phenotypic changes origin in somatic mutation, epigenetic alteration and genetic instability. Main selective pressures are intercellular competition for resources as space, nutrient, waste disposal or immune system responses [Crespi & Summers, 2005]. Somatic

cellular evolution in carcinogenesis proceeds – in comparison to the evolution of populations - on a much shorter time scale of years or even months. This commonly results in rapid adaption of cancerous cells towards persistent survival and unrestrained growth with potentially lethal consequences for the host individual.
During carcinogenesis most types of cancer acquire a number of nested genetic mutations that are believed to be essential for the transformation of normal to malignant cells. Hanahan and Weinberg outline six “hallmarks of cancer” that are:

(1) Self-sufficiency in growth signals (SG)
(2) Insensitivity to anti-growth signals (IA)
(3) Evasion of apoptosis (EA)
(4) Unlimited replicative potential (LR)
(5) Sustained angiogenesis (SA) and
(6) Tissue invasion and metastasis (TI)

[Hanahan & Weinberg, 2000]. The accumulation of these hallmark mutations is known to be an evolutionary and developmental process involving selection, stabilization of gene expression and even heterochronic dedifferentiation [da Costa, 2001]. Whether a cell subclone of varying genotype prevails, depends on its ability to outcompete other cells in its local environment in survival capability and growth velocity. In this thesis, however, model cells were assumed to be genetically homogeneous. Microevolutionary selection among cancer cells has therefore not yet been considered. However, clonal heterogeneity is believed to be an important characteristic and key advantage of tumors surviving in harsh environments for example due to chemotherapeutic treatment or nutrient shortage [Hoehme & Drasdo, 2009a]. Aspects of evolution have already been studied, for example for growing cell populations [Anderson et al., 2006], in early development [Hogeweg, 2000], and for cell migration [Drasdo & Kruspe, 2005]. Some models assumed direct effects on the parameters of the cells [Anderson et al., 2006] [Drasdo et al., 2007], others include

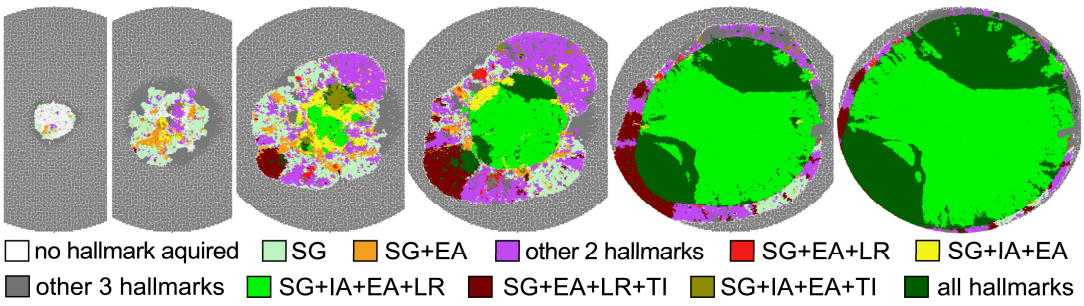


**Fig. 65: Accumulation of hallmark mutations** leading intercellular heterogeneity. Ultimately, invasively growing cell clones (green) dominate the cell population. Abbreviations: SG: self-sufficiency in growth signals, IA: insensitivity to anti-growth signals, EA: evasion of apoptosis, LR: unlimited replicative potential, SA: sustained angiogenesis and TI: tissue invasion and metastasis

regulatory networks and couple the state of these networks either to the parameters or the behavior of the cells [Hogeweg, 2000] [Drasdo & Kruspe, 2005].
However, agent-based models are particularly well suited to integrate microevolutionary changes on the level of an individual agent (cell). For example, Fig.65 shows a model cell population in a homeostatic, stable condition (Fig.65, left image) in which single cells randomly acquire hallmark mutations as described by [Hanahan & Weinberg, 2000]. Mutations in individual cells then lead to the development of cell-clones of increased fitness that outgrow the other cells. Within these fitter clones more hallmark mutations can accumulate which ultimately leads to a rapidly accelerated and invasive growth (Fig.65,right image; Supporting Video 39).
Furthermore, we started to study phenotypic changes in cell behavior or properties that were caused by genetic heterogeneity. We study morphological changes on a multicellular scale and predict variations in tumor growth kinetics caused by these changes. For example, Fig.66 shows two monolayers growing in embedding tissue as elaborated in section 3.6 only here cells were assumed to have heterogeneous properties. This kind of analysis can predict what phenotypic changes on the level of a single cell may lead to fitter cell clones that are able to outcompete other cells. In a next step we thereby can predict the impact of such changes on multicellular level. From a therapeutical point of view, this information can be utilized to study what changes on cellular level may favor or prevent certain, potentially harmful phenotypes on multicellular level from forming. Such analysis could even show how to trigger their regression and thus could be used to optimize cancer treatment.

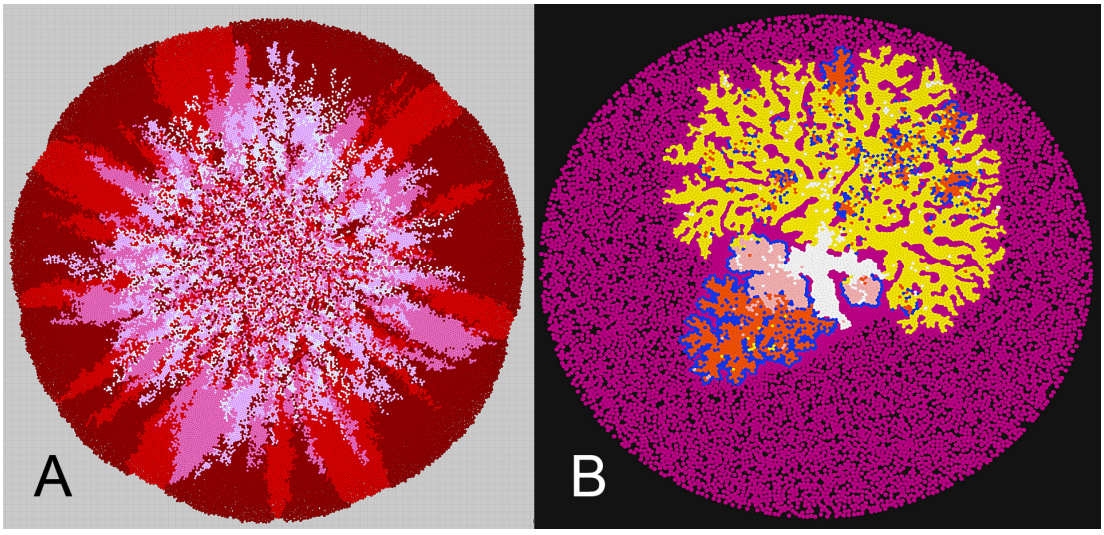


**Fig. 66: Analysis of the impact of phenotypical changes of cell properties and behavior** on the morphology of multicellular populations. A: The capability of cells to migrate has a large impact on their fitness. Clones of higher migration velocity (darker red) show an increased fitness and outgrow cell clones of lower migration velocity (brighter red). B: Reduced cell-cell adhesion (predominantly yellow cell clone) leads to more invasive growth patterns compared to cells of increased cell-cell adhesion (rose color) (also see Supporting video 40 ). The embedding tissue is shown in dark magenta.

## 6.2. Active intracellular regulation

In case of a significant limitation of nutrient and oxygen supply, cells are known to actively adapt their behavior to survive such disfavorable conditions. *In vivo*, cells for example secrete angiogenesis factors that trigger endothelial cells of the neighboring blood vessels to divide, form sprouts towards and eventually penetrate the growing tumor to nourish it [Hanahan & Folkman, 1996] [Bergers & Benjamin, 2003]. Oxidative stress by extreme hypoxia, for example, can lead to changes in protein synthesis [Sutherland et al., 1986]. In that reference the authors observed that many of these changes can also be triggered by glucose deprivation. It is widely accepted that tumor cells switch to anaerobic glycolysis which permits the cells to generate ATP even under hypoxia.

For example, we study how cell populations can survive critically low nutrient concentrations if single cells adapt individually to the disfavorable conditions by actively regulating their properties or behavior [Hoehme & Drasdo, 2009a]. We believe that it is crucial to understand the possible variability of phenotypes of cells and cell populations in order to permit predictions for an *in vivo* situation. Fig.67 exemplarily illustrates the survival of a cell population under disfavorable conditions by active regulation of cell micromotility. In this case, active regulation on a cellular level has a strong impact on the morphology of the multicellular population which shifts from a compact spherical shape towards a dendritic morphology (Fig.67).

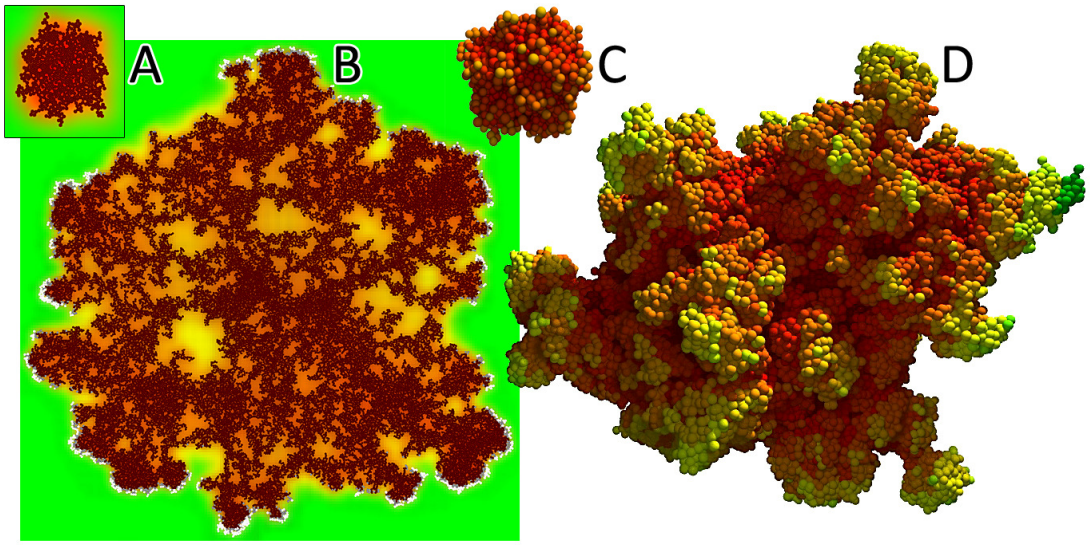


**Fig. 67: The effect of active regulation of the micromotility** in two (A,B) and three (C,D) dimensions. In case the micromotility is independent of the local glucose concentration, the cell populations saturate at the size shown in (A/C) for two/three dimensions. In case the micromotility increases with the local glucose concentration, however, finger-like morphologies with hollow regions inside the cluster form (B,D). The coloring of the substrate in (A,B) and the cells in (C,D) indicates nutrient concentration (green=high, red=low). Also see Supporting Video 41.

Active regulation has also been observed in the transition from an in-situ tumor, which is well separated from its surrounding tissue, to an invasive cancer. For example, cells down-regulate cell-cell adhesion, and eventually detach and invade the surrounding tissue [Weinberg, 2007]. The down-regulation of cell-cell contacts is triggered or at least accompanied by a down-regulation of E-cadherin/$\beta$-catenin complexes in the cell membrane followed by a the release of free $\beta$-catenin into the cytosol which, if its degradation by a proteosome apparatus involved in the Wnt-pathway is not fast enough, enters the cell nucleolus and triggers the processing of Tcf-related gene cascades eventually leading to an increase of cell migration [Ramis-Conde et al., 2008].
In general, active regulation can be successively included into our models either phenomenologically by variation of cell parameters depending on certain conditions (e.g. the local nutrient concentration) [Hoehme & Drasdo, 2009a] or by explicit modeling of intracellular pathways [Ramis-Conde et al., 2009].

## 6.3. Further model improvement

We started to further improve the lattice-free agent-based model used in this work. For example, the use of spheres to represent the shape of model cells is computationally very efficient but in certain scenarios, e.g. for active cell shape changes, may not be a very realistic approximation.
Furthermore, the forces resulting from the contact models described in section 3.2.3. for certain configurations, e.g. in the interior of a growing tumor, may not prevent an unphysical compression of cells. This is often in direct violation of the chosen material parameters. In these cases, the volume that is available to each cell may be

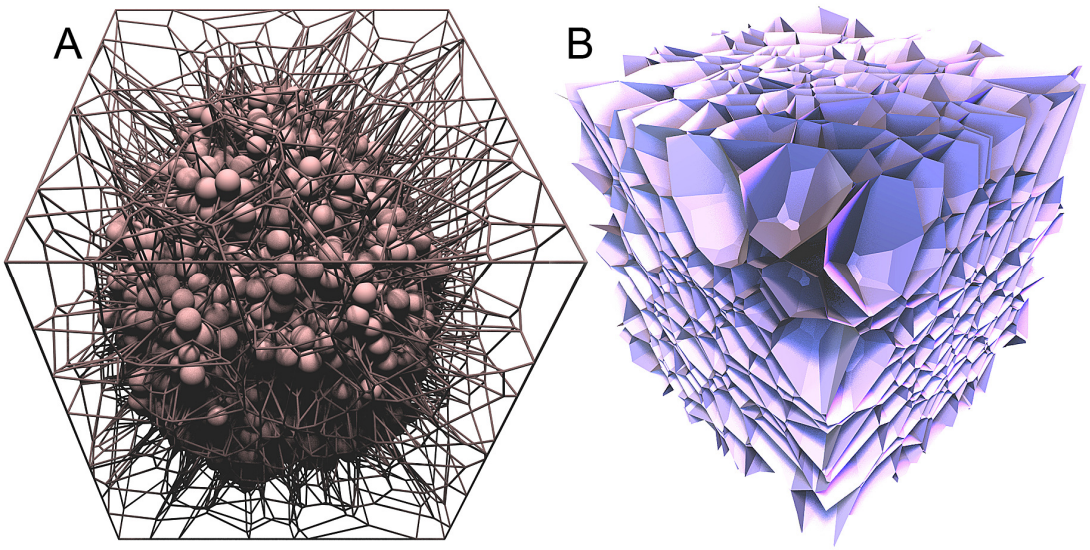


**Fig. 68: Improvement of cell shape.**
A: Illustration of a Voronoi space decomposition in 3D based on a spherical cell population (rose) and B: the resulting and in many cases more accurate cell boundaries.

significantly smaller than the volume of the corresponding spherical model cell. Thereby certain biomechanical aspects of the model that at least partly relate to the cell volume (e.g. the intracellular pressure) may be misrepresented. Furthermore, under such conditions the contact area between two interacting cells resulting from the extended Hertz or JKR model may be erroneous. Therefore, we started to implement an improved description of cell shape based on three-dimensional Voronoi space decomposition [Klein, 2005]. Fig.68 exemplarily illustrates such space decomposition that can be used to more accurately represent cell shape.

## 6.4. Towards whole liver modeling

A natural extension of the three-dimensional model of an individual liver lobule developed in this thesis would be a model of multiple interacting lobules (Fig.69). Despite the liver lobule is the structural and functional building block of the liver, many diseases and other aberrant states like partial hepatectomy and hepatocellular carcinoma affect the liver on the scale of multiple liver lobules.
During partial hepatectomy, for example, a part of the whole liver is resected [Michalopoulos & DeFrances, 1997] [Sato et al., 1999] [Blindenbacher et al., 2003]. In the following complex hypertrophic and hyperplasic regeneration processes the size of the remaining liver lobules increases until a nearly complete recovery of the original liver mass within days. Subsequently, liver function is restored within two to three weeks [Court et al., 2002]. However, the exact mechanism and the interplay of hepatic cells and cytokines are not fully understood. Furthermore, modeling the key mechanisms of liver regeneration after partial hepatectomy is of high clinical

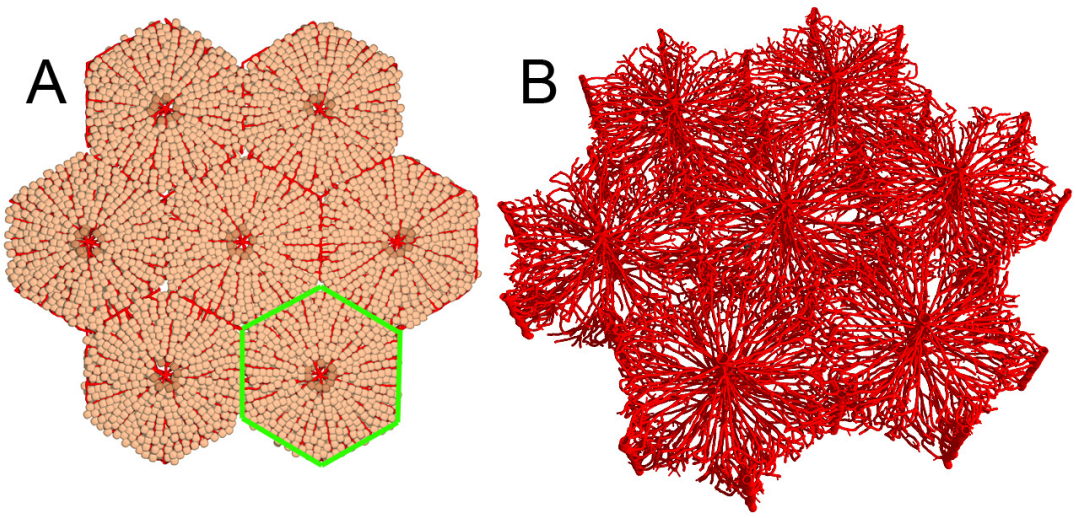


**Fig. 69: Multi-lobule model.**
A: Model integrating 7 liver lobules in 3D (green outline encompasses a single liver lobule).
B: Corresponding blood vessel network.

relevance because patients with liver metastasis often undergo liver resection. After surgery in a fraction of those patients, however, regeneration is delayed leading to severe and potentially life threatening liver insufficiency [Nagino et al., 2001].
On the foundation of our analysis of liver regeneration after intoxication that we elaborated in this thesis (chapter 4), an extended multi-lobule model could help to shed light on the important mechanisms of liver regeneration after partial hepatectomy.
Moreover, we started to use such multi-lobule model not only to optimize cancer treatment but to model hepatocellular cancer itself. Fig.70 illustrates first steps in this direction where we modeled the growth of a solitary encapsulated tumor, a special form of hepatocellular carcinoma, with a three-dimensional multi-lobule model that consisted of seven interacting liver lobules.

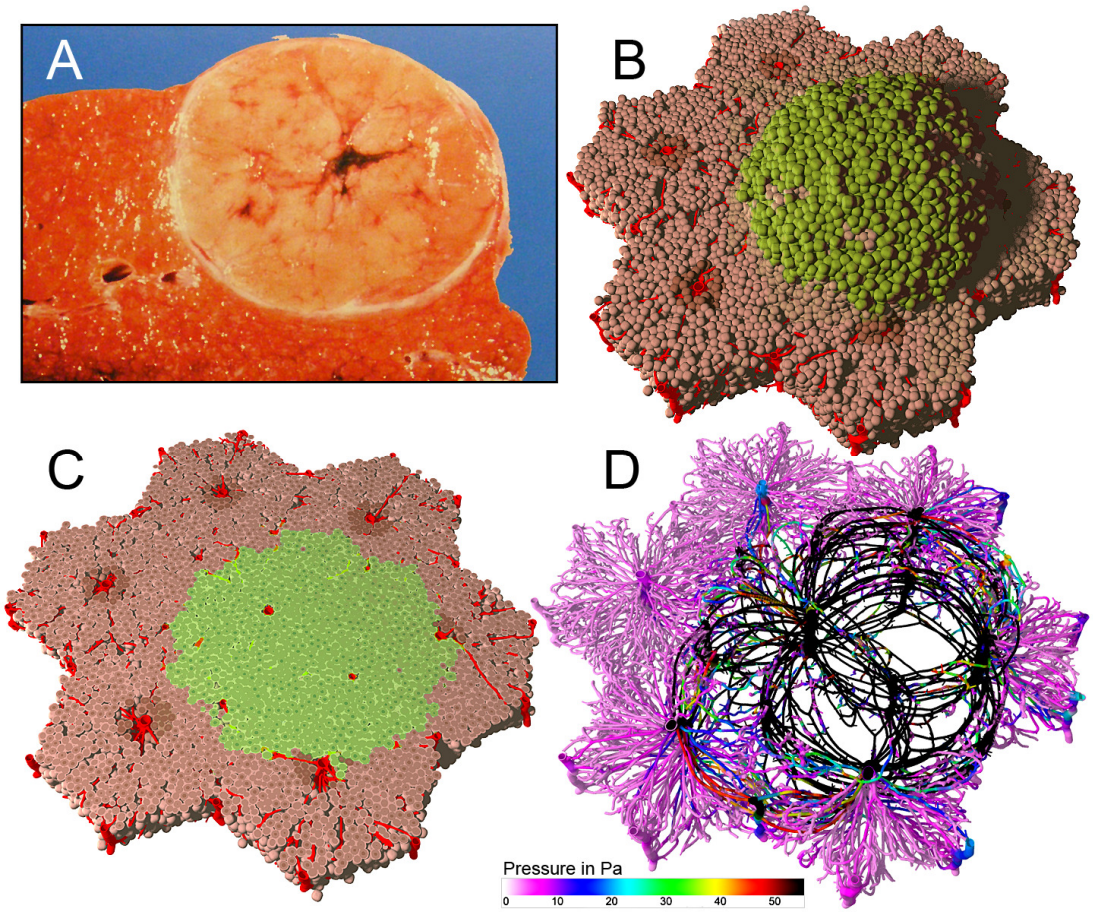


**Fig. 70: Simulation of hepatocellular carcinoma**.
A: Hepatocellular carcinoma *in vivo*. A cirrhotic liver with a solitary encapsulated tumor (Image from [Burt et al., 2006]). B: Solitary tumor (green) growing within a multi-lobule model. C: Cross section of B. D: Deformations of the blood vessel network within the liver lobules (compare to the healthy state shown in Fig.69B). Colors denote the pressure on the blood vessels (see legend). Also see Supporting Videos 42 and 43.

# Appendix 1: Supporting Figures

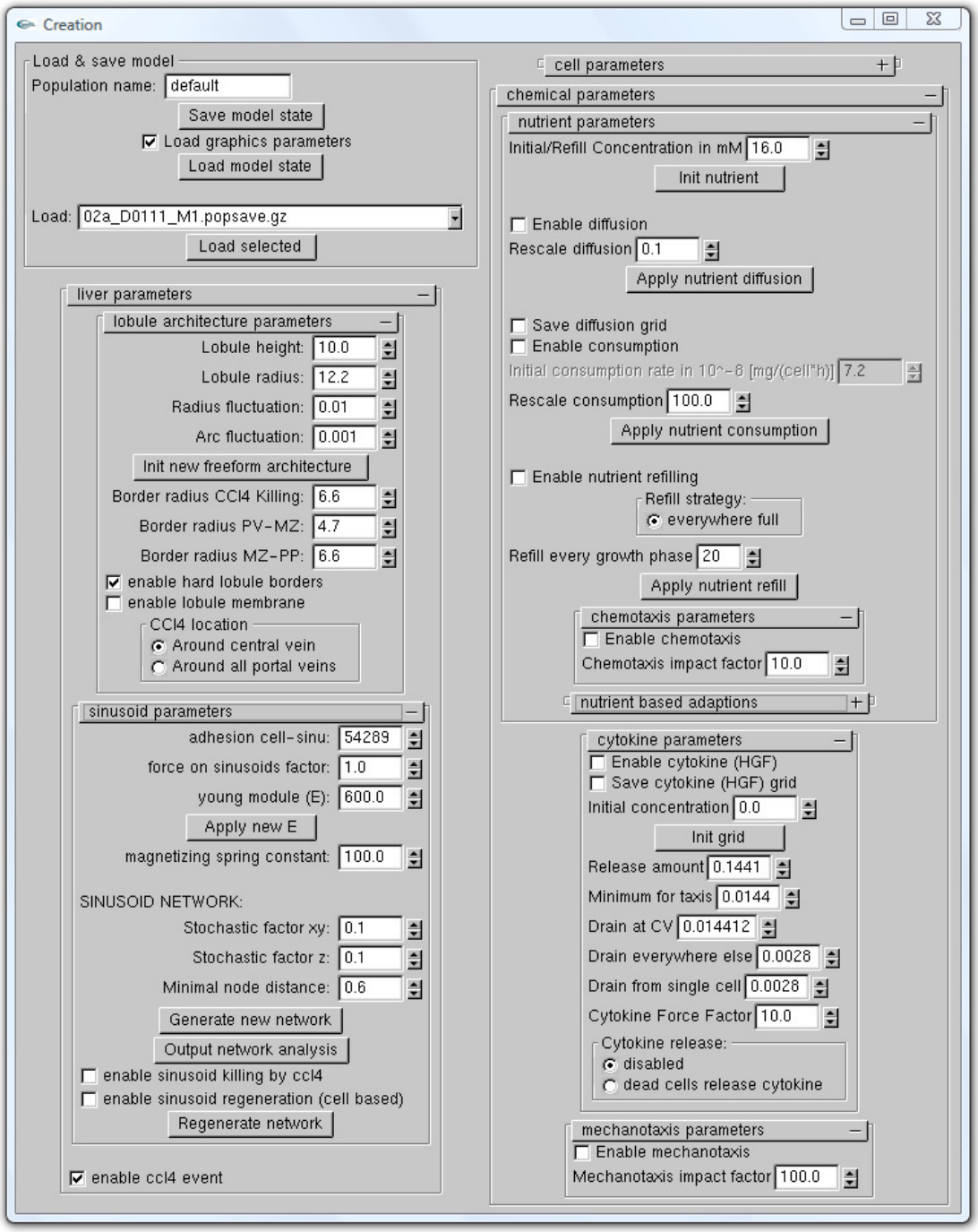


**Supporting Fig. 1: Exemplary component window** (Creation) of graphical user interface of Cellsys. For an overview see Fig.5.

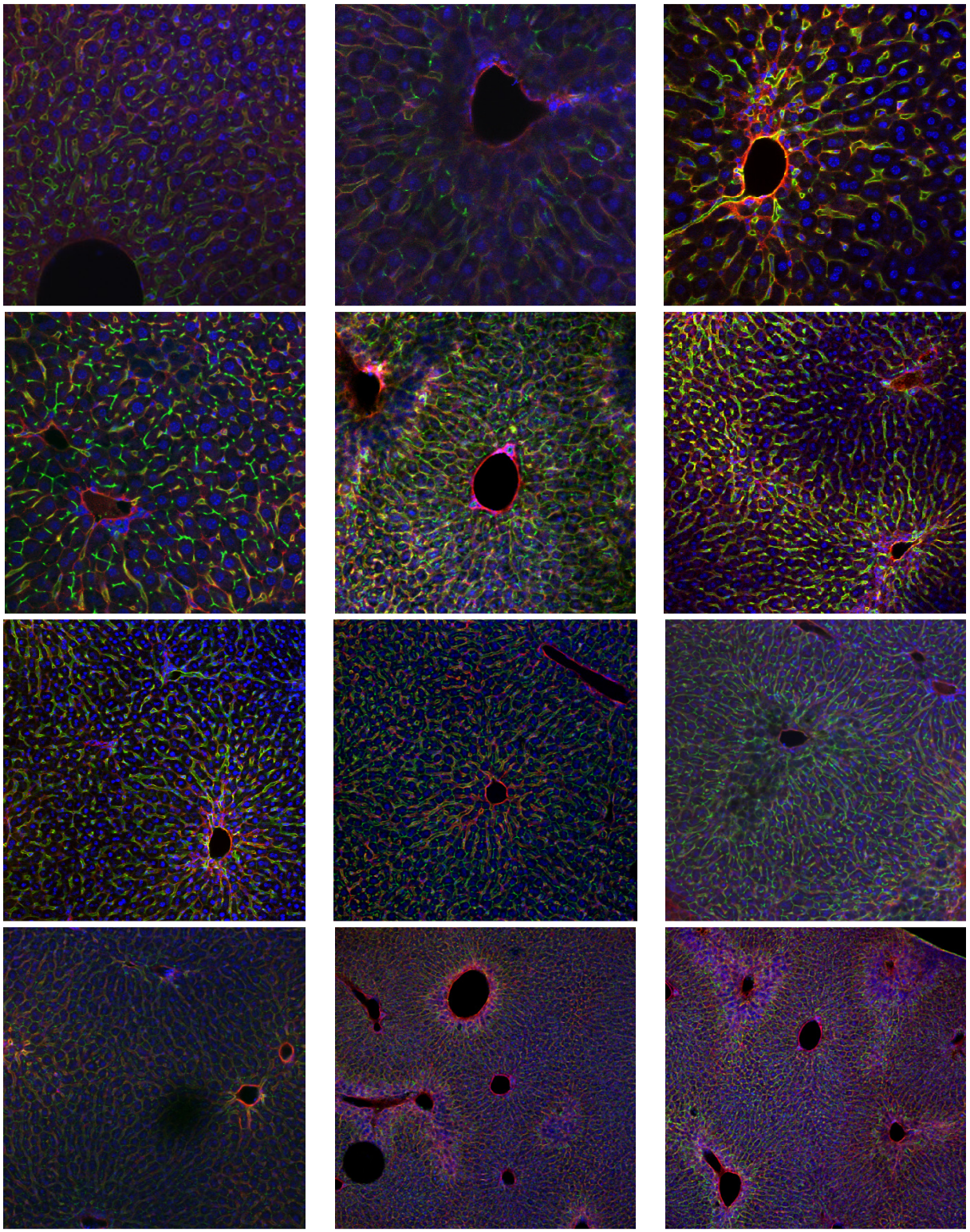

**Supporting Fig. 2: Typical confocal micrographs** (ICAM / DPPIV/ DAPI)

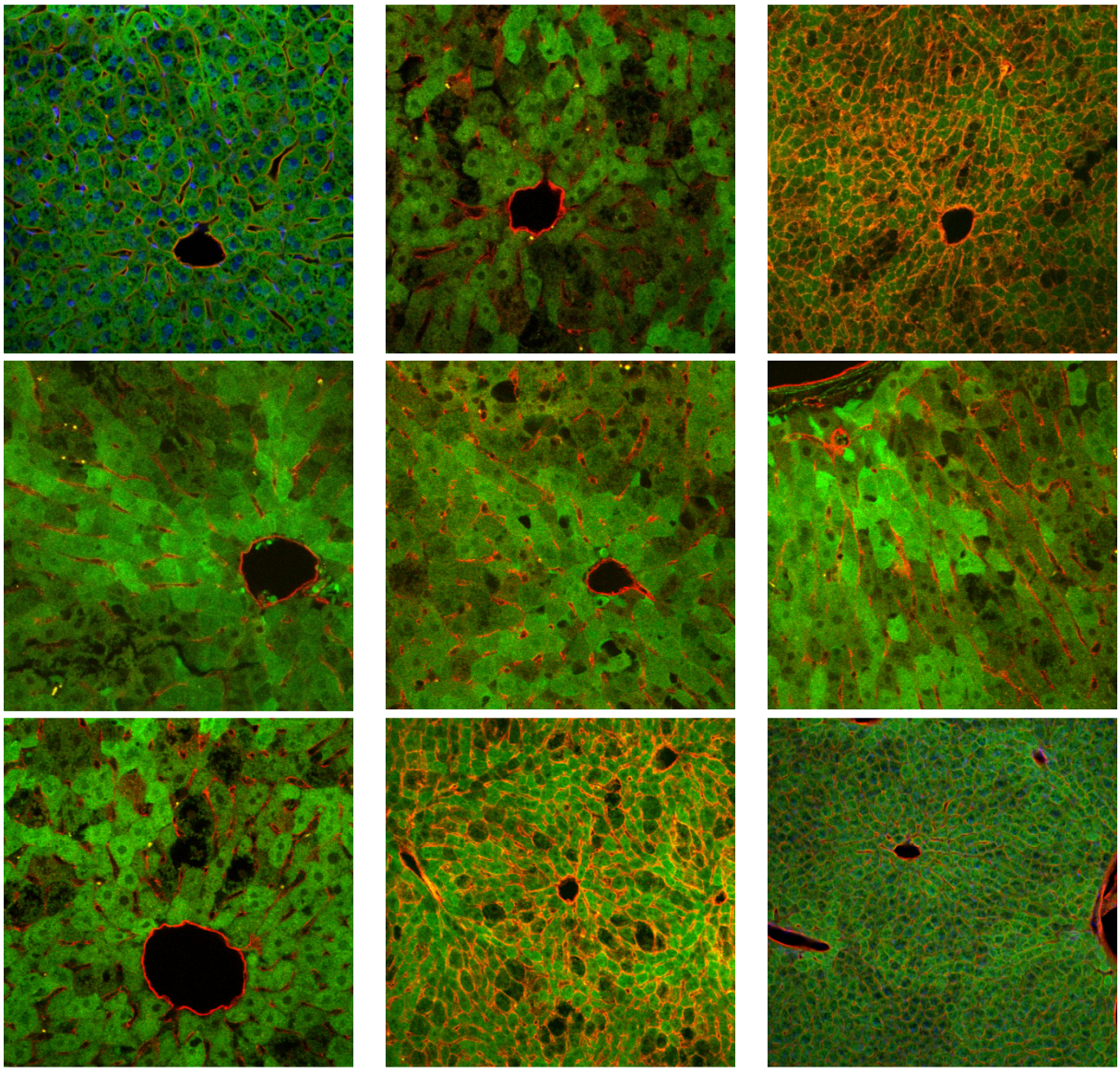

**Supporting Fig. 3: Typical confocal micrographs** (CD31 / EGFP / DAPI)

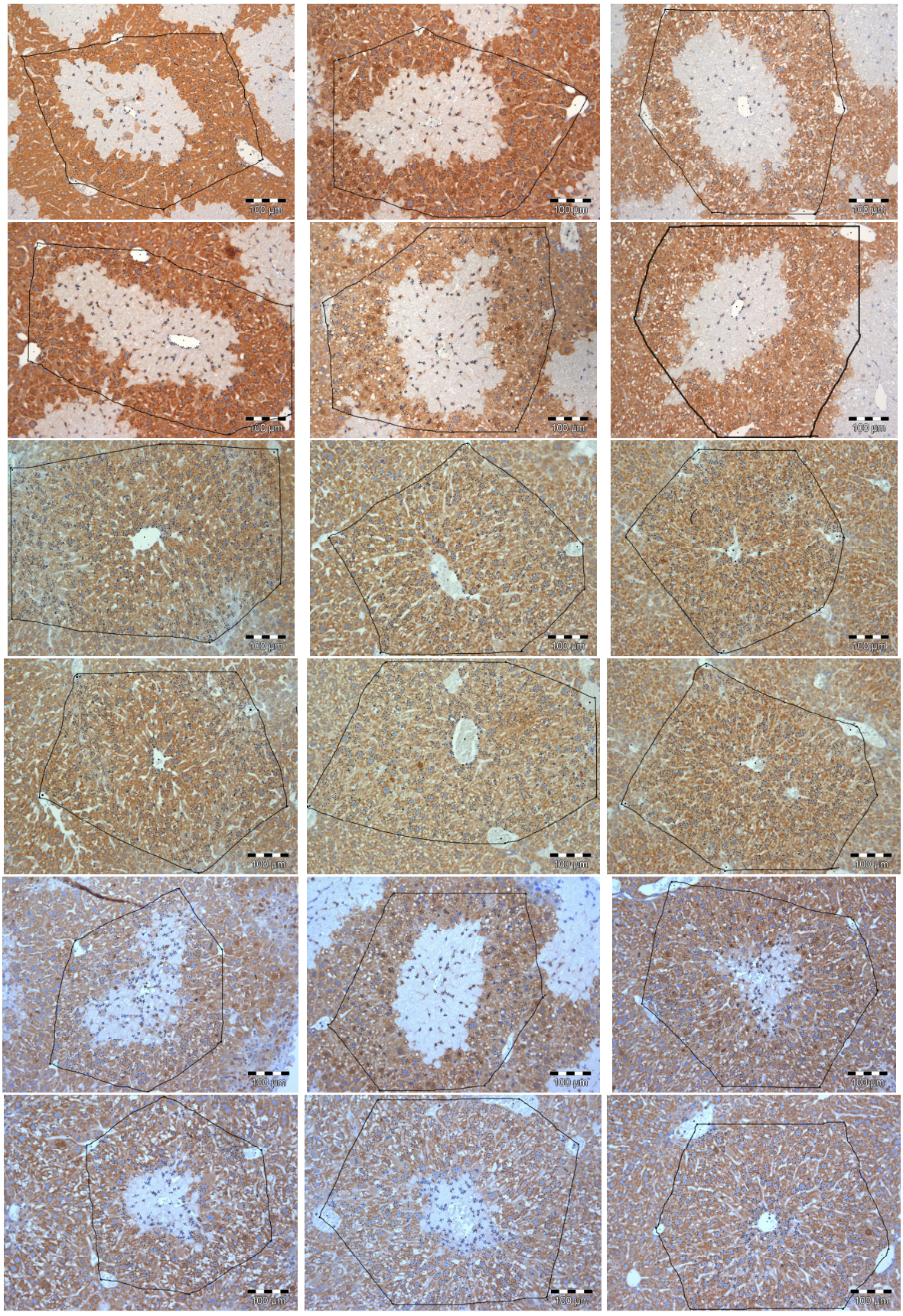


**Supporting Fig. 4: Typical bright field micrographs**

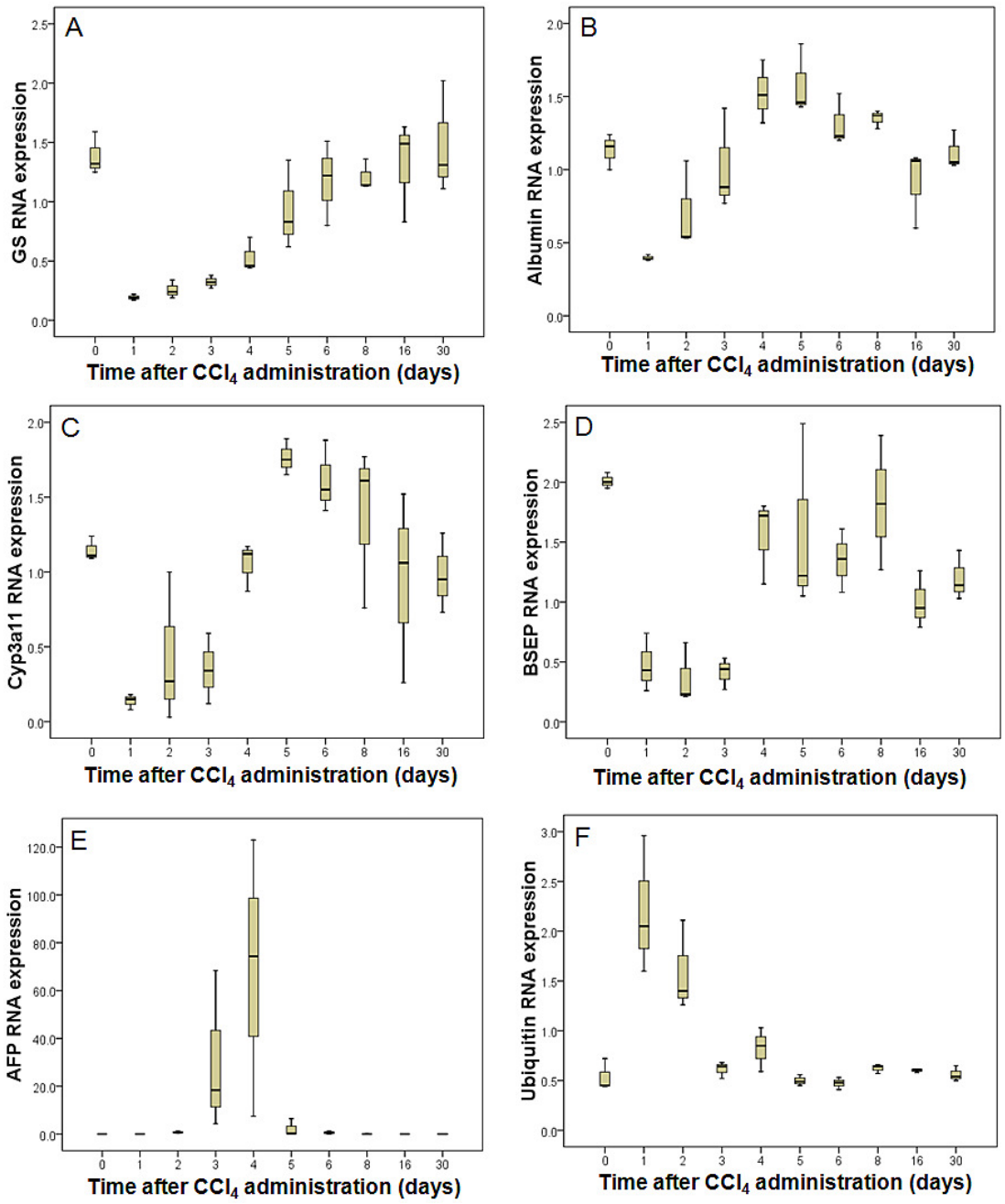


**Supporting Fig. 5: RNA expression** of genes known to be down (A-D) or upregulated (E,F) during liver regeneration. Analyses were performed at time intervals between 1 and 30 days after administration of 1.6 g/kg $CCl_4$ to mice. Glutamine synthetase (GS), albumin, cytochrome P450 3a11 (Cyp3a11) and bile salt export pump (BSEP) RNA were transiently down regulated after administration of $CCl_4$. In contrast, alpha-fetoprotein (AFP) and ubiquitin were transiently upregulated. The results suggest a process of liver damage induction and regeneration that is in agreement with previously published reports (review: [Michalopoulos & DeFrances, 1997] [Michalopoulos & DeFrances, 2005] [Michalopoulos, 2007]). Data were obtained from three mice per time period.

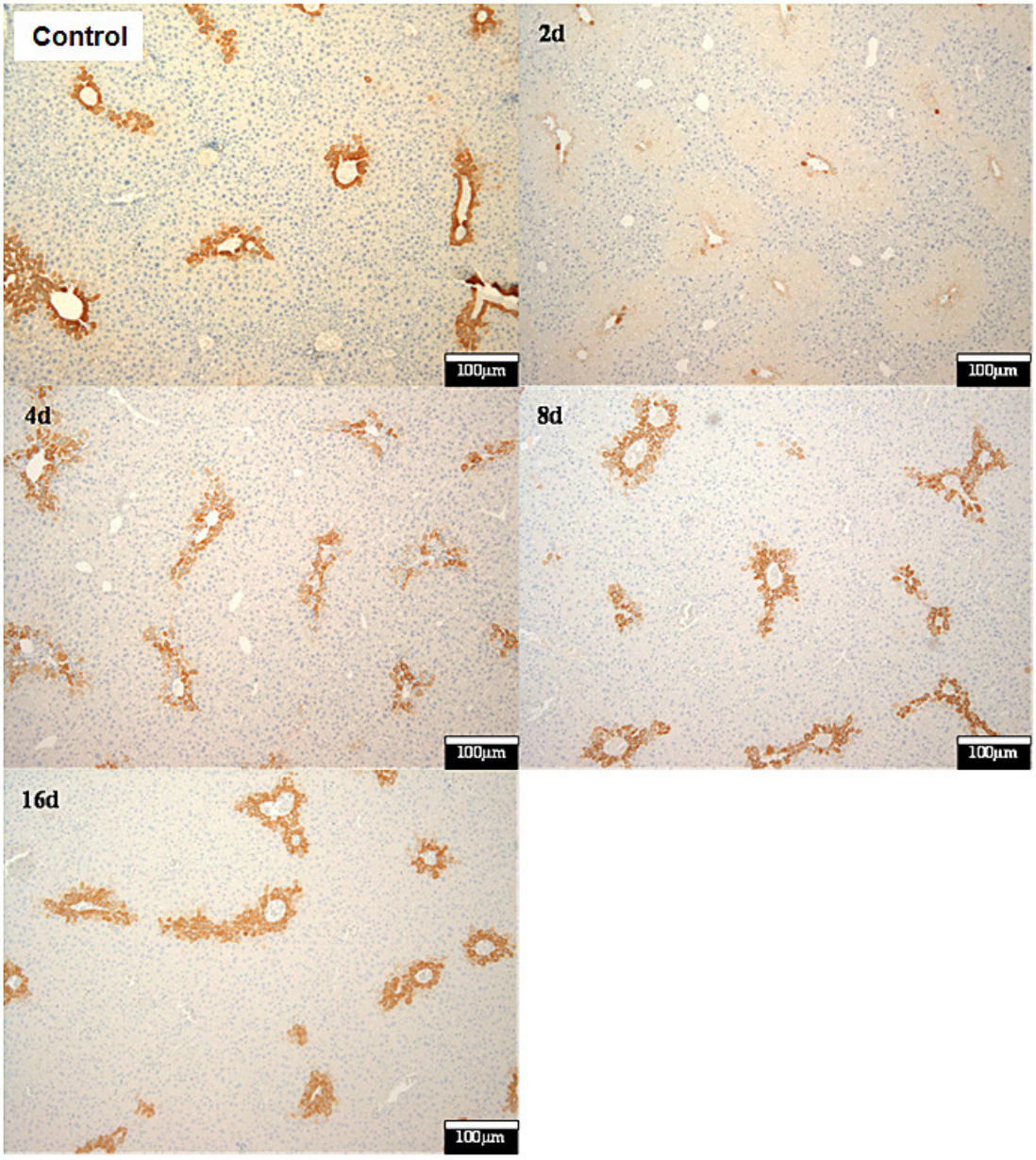


**Supporting Fig. 6: Immunostaining of glutamine synthetase (GS) of paraffin slices** from liver tissue of mice before as well as 2, 4, 8, and 16 days after administration of $CCl_4$. The data illustrate a transient decrease in GS protein levels at 2 and 4 days after administration of $CCl_4$, whereas after 8 and 16 days GS expression is similar to that of controls.

| Time after $CCl_4$-administration [d] | GS-activity [mU/mg protein] |
|---|---|
| 0 | 249 ± 11.1 |
| 1 | 245 ± 16.7 |
| 2 | 205 ± 85.2 |
| 3 | 51 ± 8.8 |
| 4 | 11 ± 1.9 |
| 5 | 26 ± 3.8 |
| 6 | 94 ± 13.6 |
| 8 | 138 ± 19.6 |
| 16 | 269 ± 20.9 |

**Supporting Fig. 7: Glutamine synthetase activity** of liver tissue from mice at time intervals of 1 to 16 days after administration of 1.6 g/kg $CCl_4$. Similar to the data for RNA expression (Supporting Fig.5) and immunostaining (Supporting Fig.6) a transient decrease was also observed for activity of GS. Data are mean values and standard deviations obtained from three mice per time interval. We observed in independent experiments that GS immunostaining (Supporting Fig.6) and GS activity after CCl4 intoxication (Supporting Fig.7) did not correlate perfectly. Immunostaining shows a decrease already 2h after $CCl_4$ administration whereas a decrease in activity is not observed before day 3. On the other hand recovery of the activity took longer than restoration of immunoreactivity. We did not study the reason of the observed discrepancy, because the documentation of a destruction and recovery process seemed sufficient for the purpose of the present study.

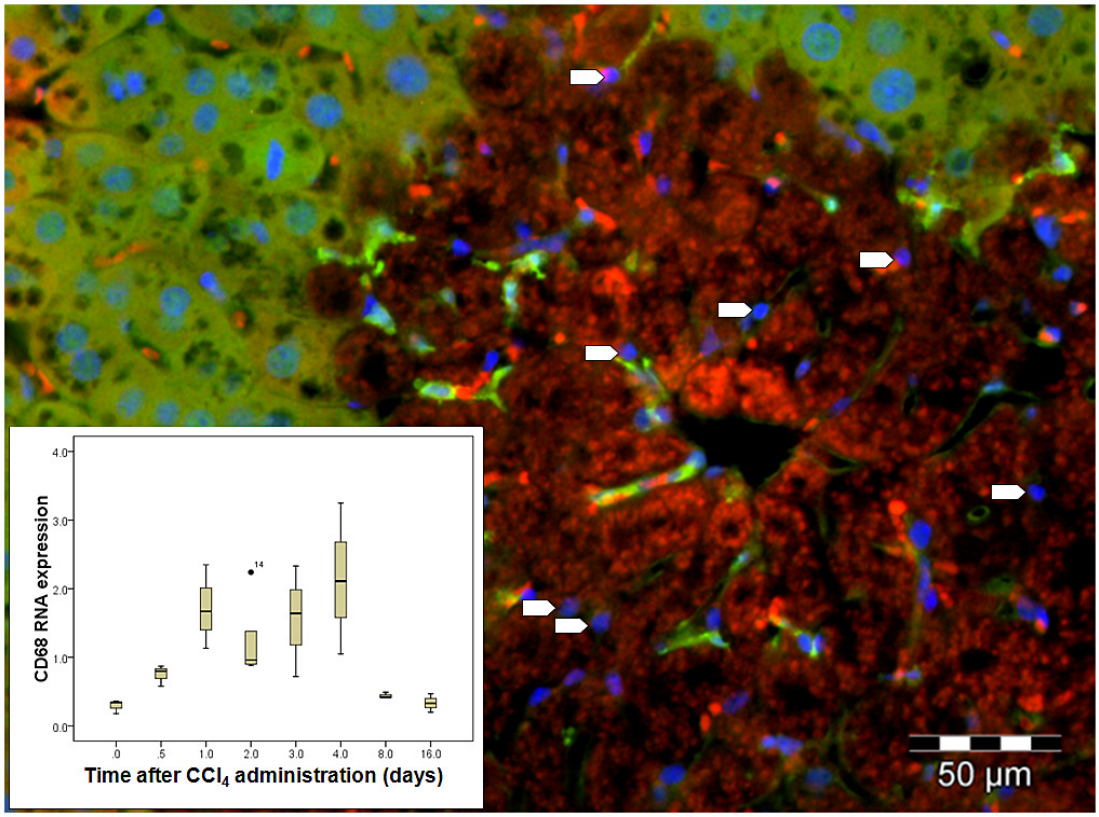


**Supporting Fig. 8: Time dependent increase of CD68 RNA expression** in liver tissue after administration of 1.6 g/kg $CCl_4$. Data were obtained from three mice per time period. The immunostained liver slice shows a central necrosis after $CCl_4$ intoxication. White arrows indicate the nuclei of some infiltrated macrophages.

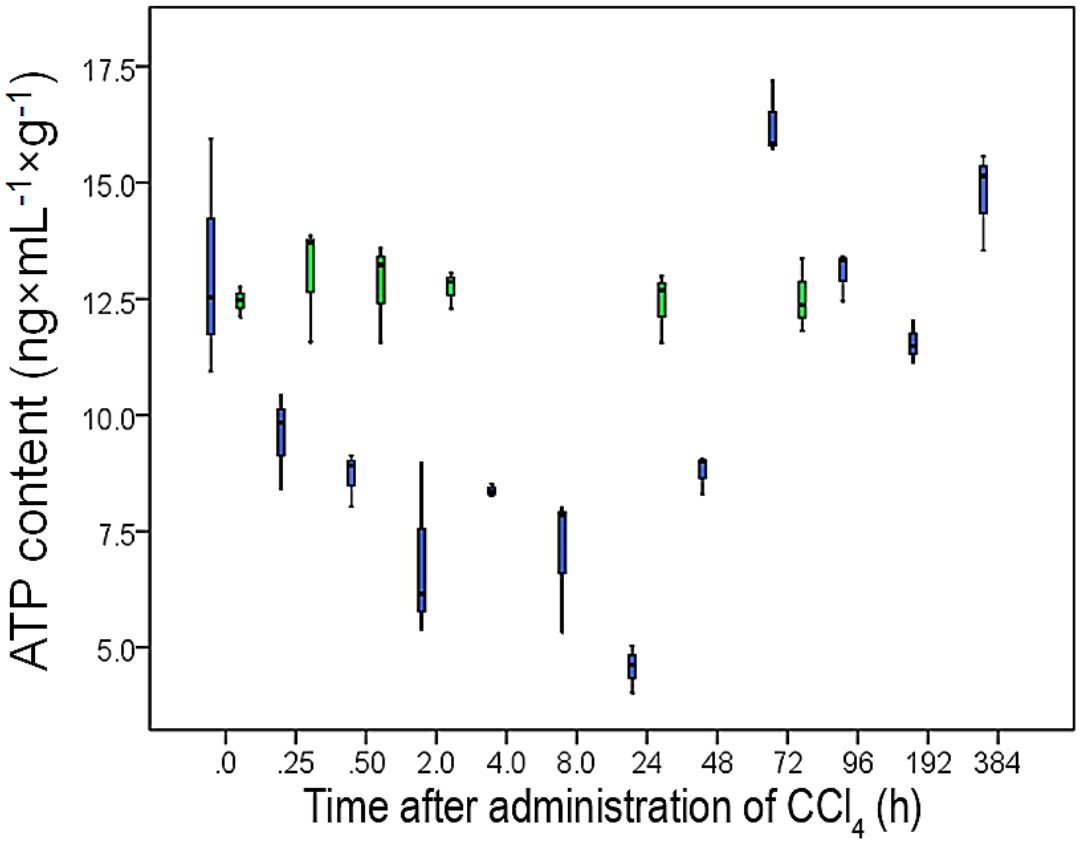


**Supporting Fig. 9: Administration of $CCl_4$ causes a rapid decrease in ATP content** in mouse liver tissue (blue boxes). Control mice (green boxes) received the solvent only (100 µl corn oil, i.p.) which did not cause a decrease in ATP content. Data were obtained from three mice per time period. The present figure gives supplemental information to Fig.62B where the time course of the dead cell area in the center of the liver lobule is shown. According to Fig.62B the dead cell area peaks 24h after administration of $CCl_4$. However, "dead cell area" as shown in Fig. 62B is defined as a cell mass, where no nuclei are visible. It should be considered that first signs of toxicity, such a decrease in ATP content are visible much earlier compared to the degradation of nuclei. The models presented in this article do not focus on molecular details of the destruction process but present a situation where destruction of the pericentral region of the liver lobule by $CCl_4$ is complete after 24h.

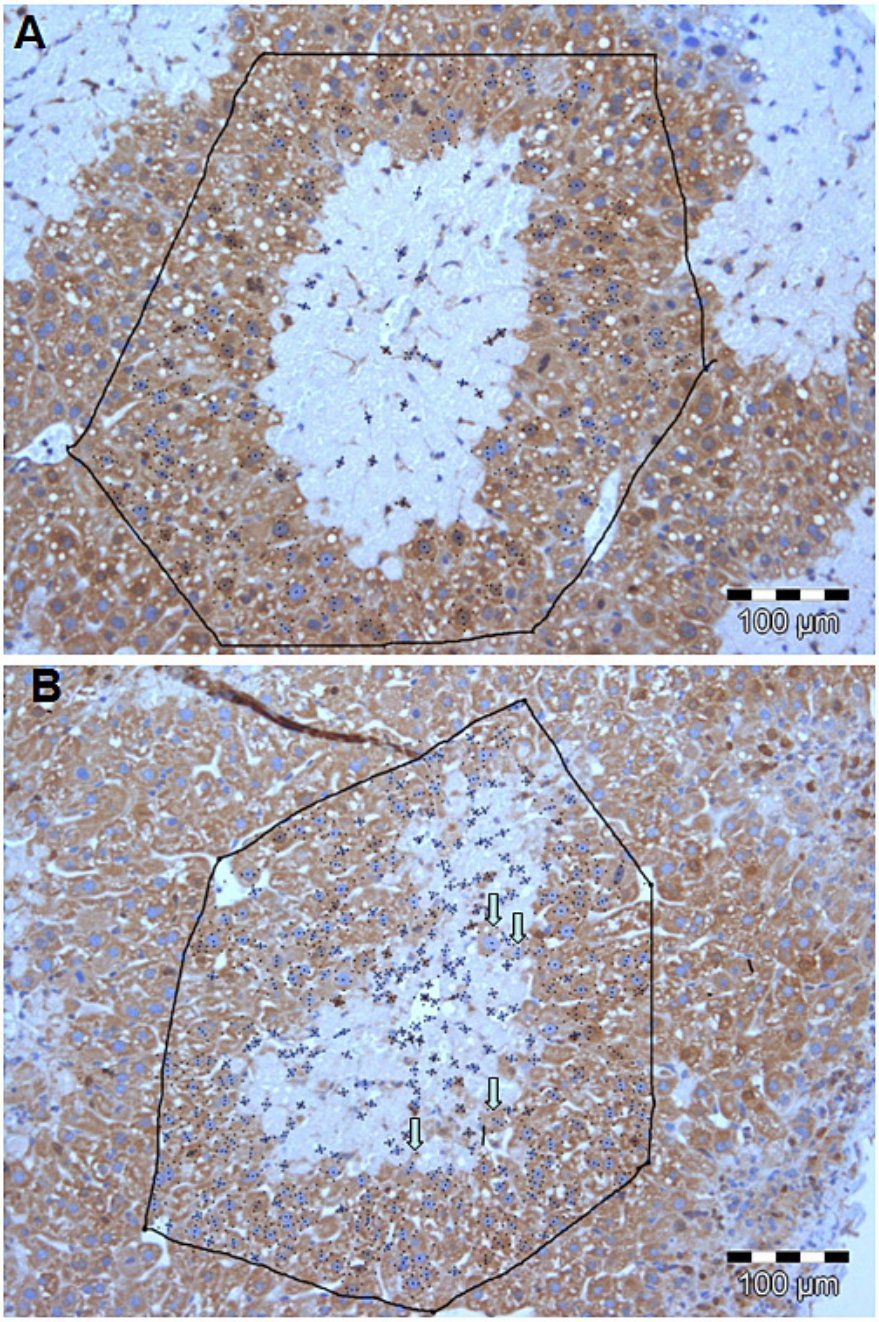


**Supporting Fig. 10: Evidence that hepatocytes migrate into the central dead cell area** caused by $CCl_4$ administration. A. Liver lobule 2 days after $CCl_4$ administration. At this stage the border between the surviving hepatocytes and the dead cell area appears relatively smooth. B. Four days after $CCl_4$ administration some hepatocytes extend into the dead cell area and form filopodia (arrows).

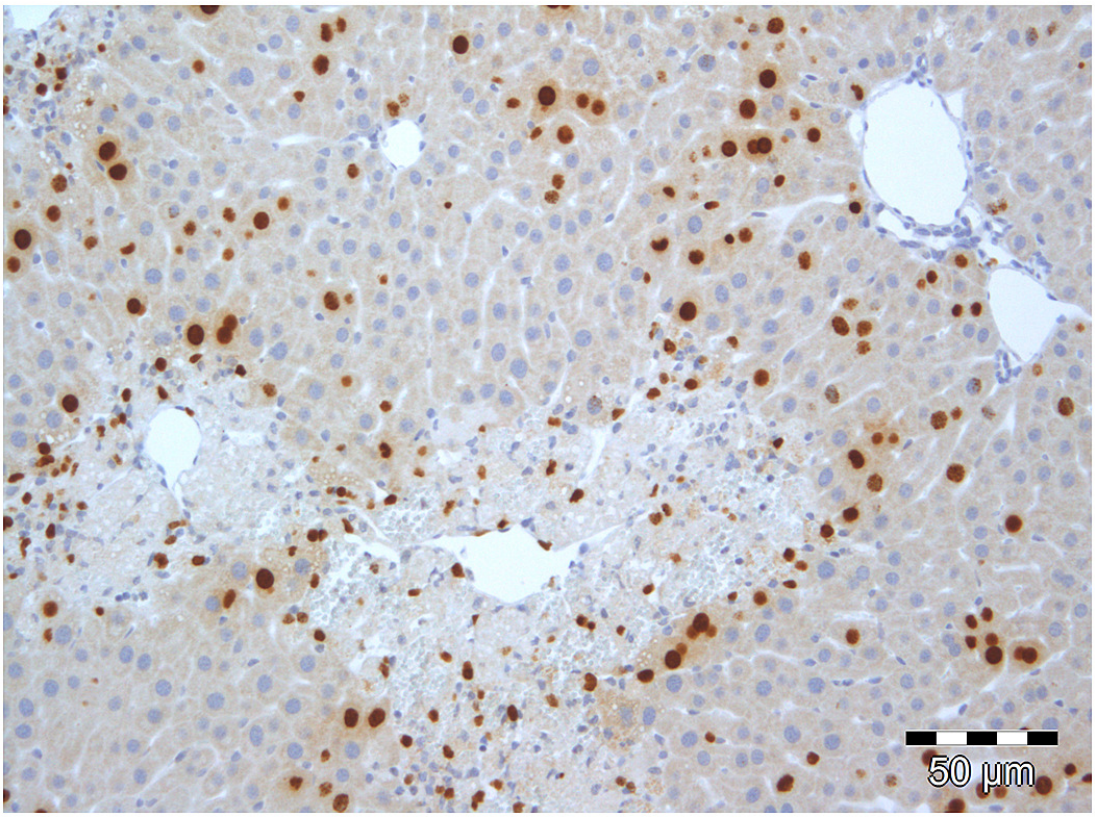


**Supporting Fig. 11: Mouse liver tissue 48 h after i.p. administration of 1.6 g/kg $CCl_4$.** Paraffin slices have been immunostained for BrdU. The picture shows two central veins surrounded by dead cell masses. Using this or similar conventional staining techniques for paraffin slices it is difficult to realize that the basic structure of the sinusoidal network is intact, even in the central necrotic area where almost all hepatocytes are dead.

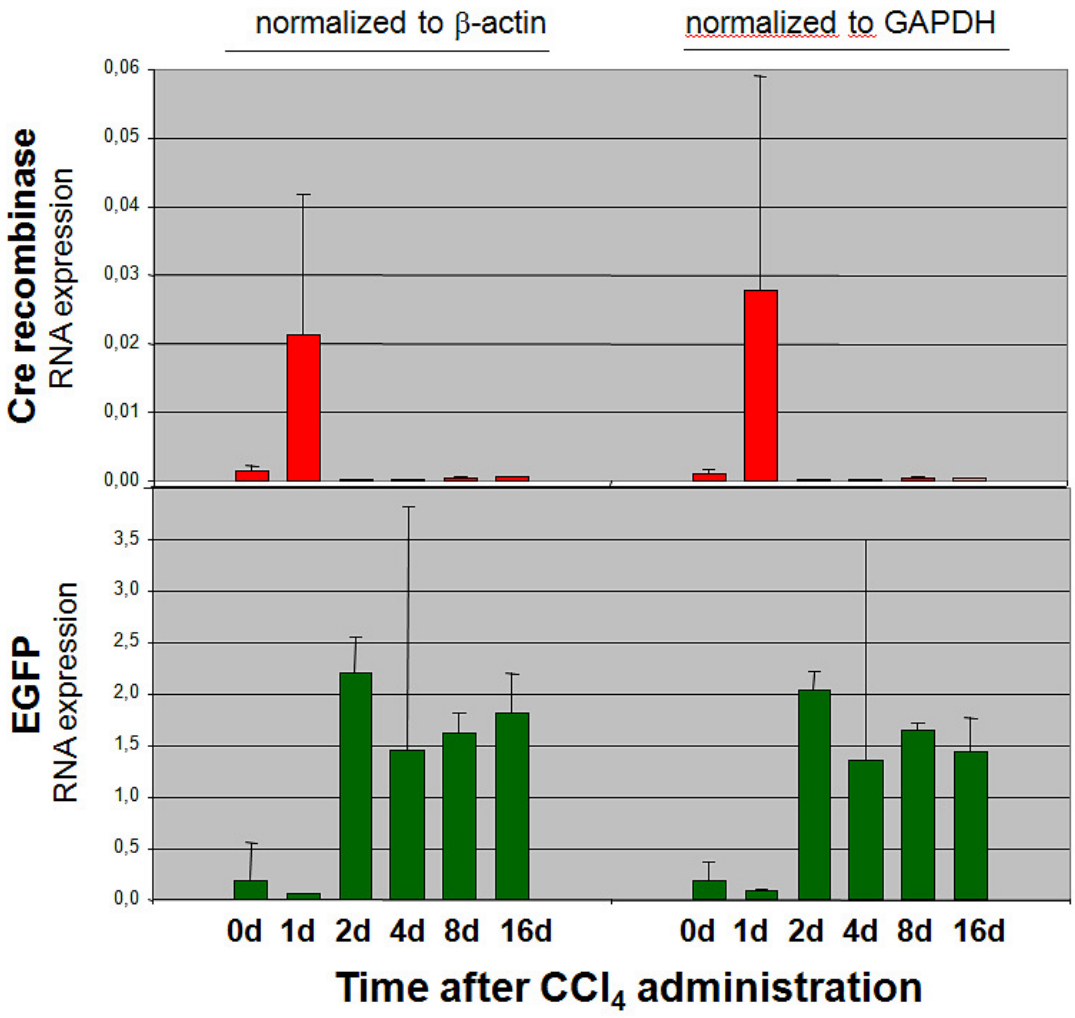


**Supporting Fig. 12: Administration of 1.6 g/kg $CCl_4$ induces tie2 promoter activity** in tie2/Cre/EGFP triple transgenic mice as evidenced by a transient increase in Cre recombinase and a permanent increase in EGFP RNA expression. Data are mean values and standard deviations from three mice per time period.

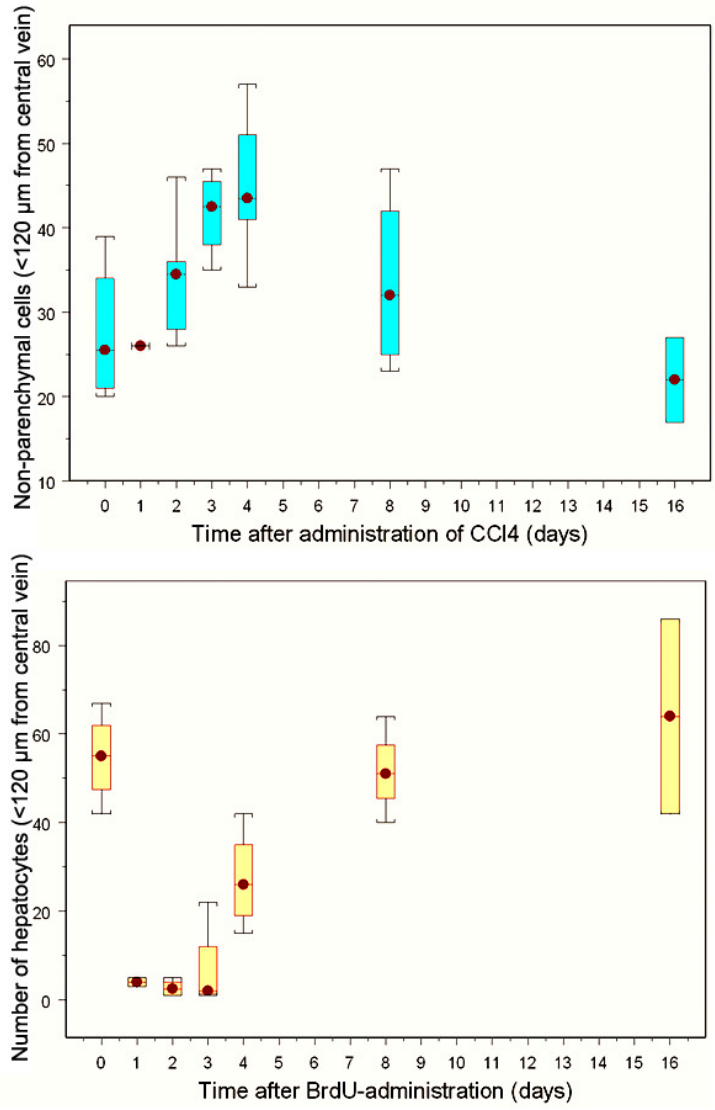


**Supporting Fig. 13: Administration of 1.6 g/kg $CCl_4$ reduces the number of hepatocytes in a pericentral area of the liver lobule**. In contrast, the number of sinusoidal cells is not reduced in this area. Data were obtained from three mice per time period.

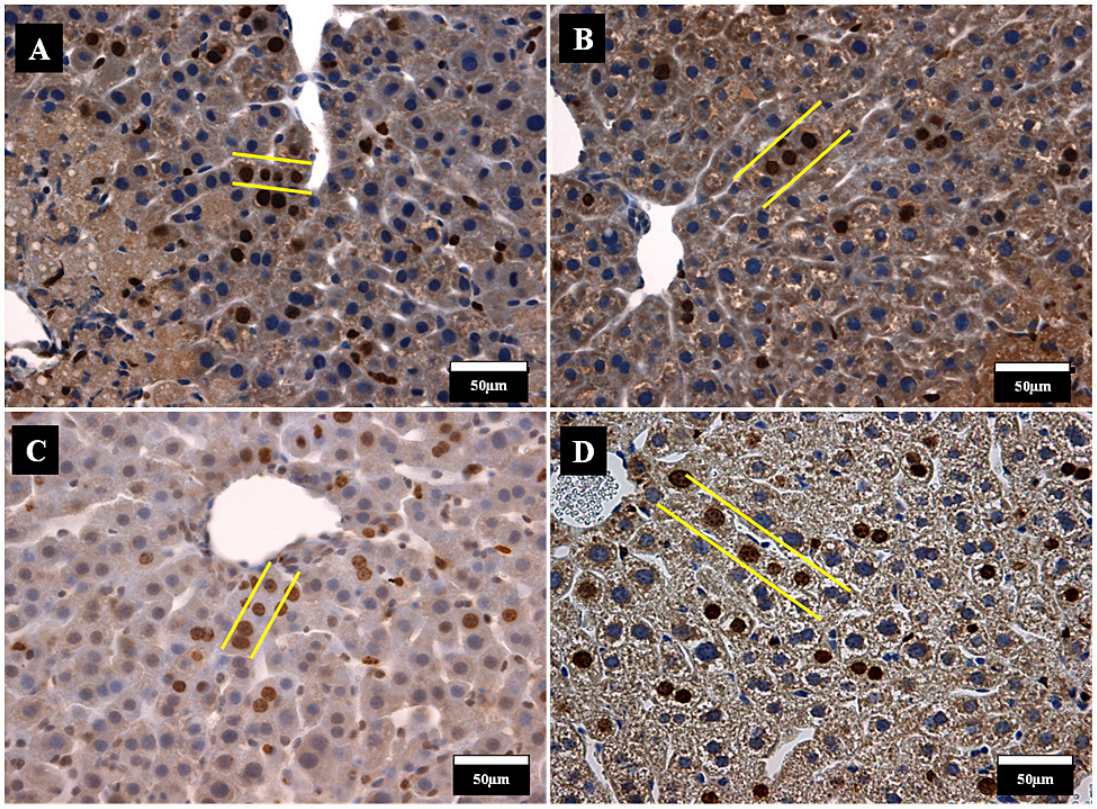


**Supporting Fig. 14: BrdU positive cells are well aligned in the direction of the sinusoids.** Mice received i.p. injections of 1.6 g/kg $CCl_4$ and BrdU was administered two days later, when hepatocyte proliferation is maximal. The yellow lines indicate the orientation of the sinusoids. However, the complex three-dimensional orientation of the sinusoids complicates a purely two-dimensional analysis. Therefore, we established a three dimensional type of reconstruction as shown in Fig. 64D. Using this technique we identified 17 pairs of BrdU-positive cells from which 14 showed an excellent alignment while three pairs of BrdU-positive cells were misaligned. However, BrdU-positive cells may either be neighbors since they emerged from the same mother cell by cell division or since they entered the cell cycle simultaneously by chance. Using our computational model we determined that about 30% of the BrdU-positive cell pairs are expected to be neighbors by chance which is able to explain the three pairs of misaligned cells.

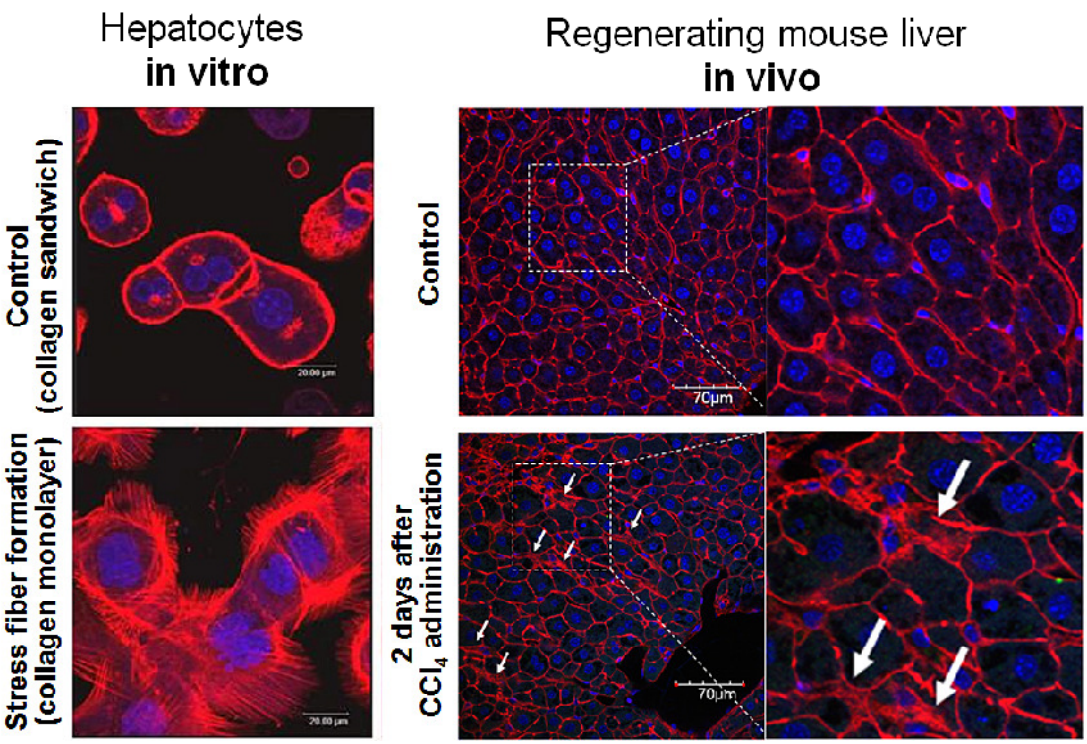


**Supporting Fig. 15: Stress fiber formation.**

Some hepatocytes in regenerating livers after $CCl_4$ administration show stress fiber formation (arrows) as evidenced by phalloidine staining. This is similar to hepatocytes *in vitro* cultivated on collagen monolayers (72h; [Godoy et al., 2009]) where hepatocytes start to show a similar formation of stress fibers. It is known from *in vitro* experiments that formation of stress fibers indicates an increased migration (scattering) activity. In both examples stress fiber formation has been visualized by staining of the actin cytoskeleton.

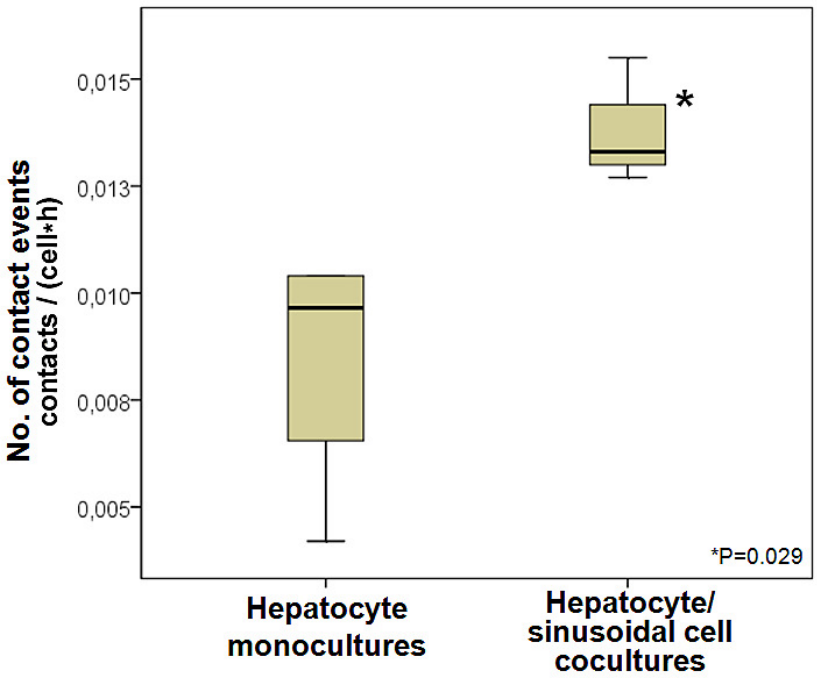


**Supporting Fig. 16: Hepatocytes are attracted more by sinusoidal cells than by other hepatocytes.**

In order to study the degree by which cells attract each other we studied time lapse videos of subconfluent hepatocytes (hepatocyte monocultures) and of subconfluent hepatocyte/sinusoidal cell cocultures for 48h. Representative examples are shown in Supporting videos 29-32. As a measure for cell-cell attraction we counted the number of "contact events" where cells actively touch each other without forming permanent cell-cell contacts. Significantly more cell-cell contact events were observed between hepatocytes and sinusoidal cells than between hepatocytes in monocultures cultivated under similar conditions (Mann-Whitney test, P=0.029). The difference cannot be caused by differences in motility, because hepatocytes show a higher motility than sinusoidal cells. Together with the time lapse videos of hepatocyte/sinusoidal cell cocultures (Supporting videos 29-32) the data show that hepatocytes are attracted by sinusoidal cells and try to maximize the contact area with the latter.

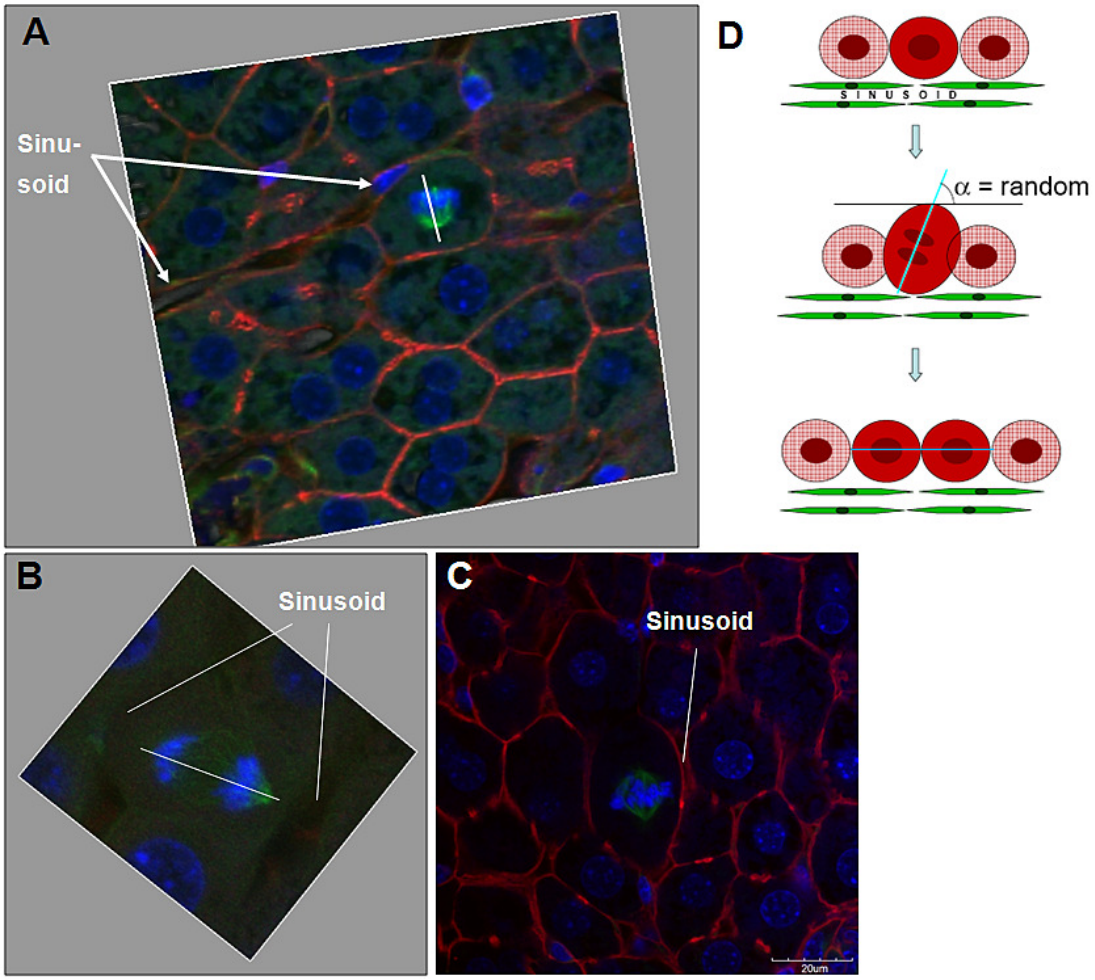


**Supporting Fig. 17: Orientation of mitotic spindles in relation to the sinusoids.** A. and B. show mitotic spindles that are not aligned in the direction of the neighboring sinusoids. C. Example of a well aligned mitotic spindle. However, in this preliminary two-dimensional study the majority of analyzed mitotic spindles were not aligned in the direction of the sinusoid as shown in A. and B. The same liver samples already shown in Fig.64 were used for the analyses of mitotic spindles. Mice received 1.6 mg/kg $CCl_4$, 48h later BrdU was injected and the livers were prepared 8h after BrdU injection. D. Probable mechanism of hepatocyte-sinusoid alignment (HSA) Initially, the orientation of the mitotic spindle is random. However, after cell division the daughter cells rapidly realign themselves in the direction of the sinusoid. Nevertheless, a validation of these preliminary results in 3D is still pending.

# Appendix 2: Supporting Videos

All Supporting Videos are available on DVD and online at *www.hoehme.com/phd/videos*

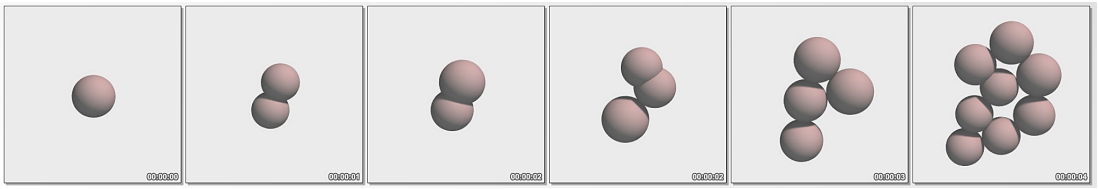

**Supporting Video 1:** Illustration of cell division in the model (algorithm variant B).

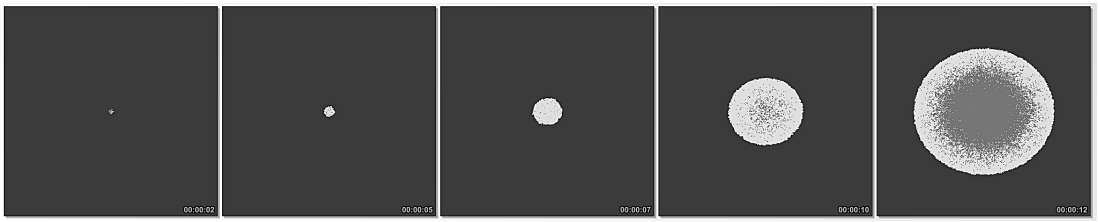

**Supporting Video 2:** Illustration of two-dimensional monolayer growth and the time development of cell states (white = proliferating, grey = quiescent).

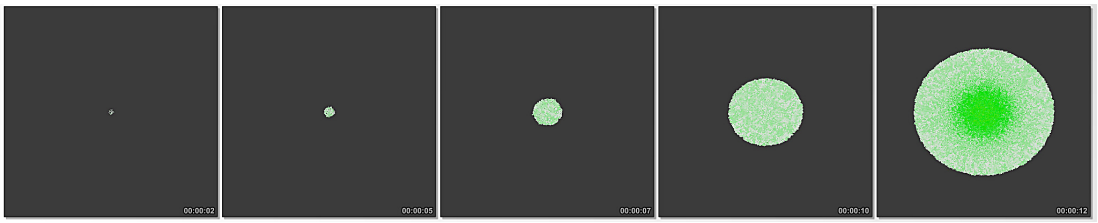

**Supporting Video 3:** Illustration of monolayer growth and cell division activity (coloring according to Supporting Video 5).

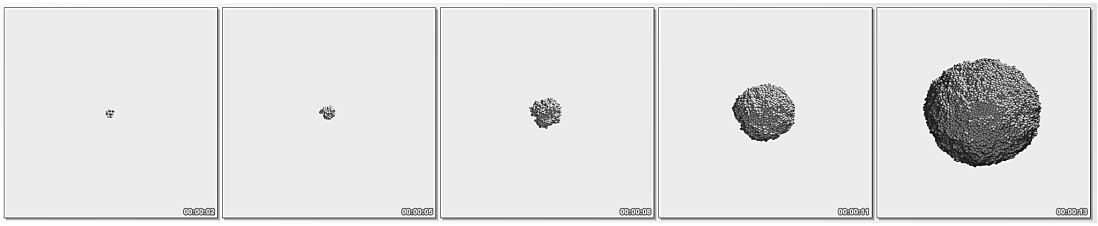

**Supporting Video 4:** Illustration of three-dimensional tumor spheroid growth from N=1 to N= $5 \cdot 10^5$ cells.

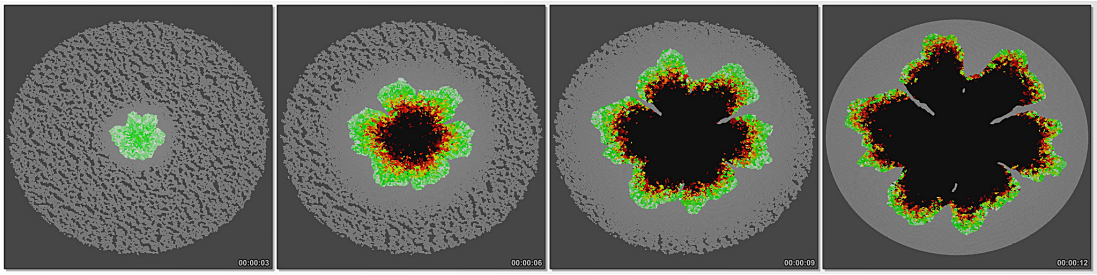

**Supporting Video 5:** Illustration of two-dimensional multicellular growth embedded in tissue (grey). Cells of white color have divided within the average cell cycle time, whereas green cells have not divided for two times the average cell cycle time (yellow = 4 times, red = 6 times, black = more than 10 times) ($D_T = D_0$ ). Also see Fig.26.

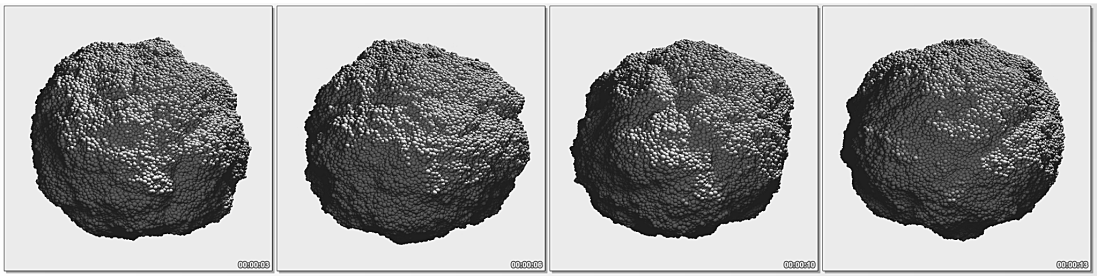

**Supporting Video 6:** Three-dimensional tumor spheroid growing into an embedding tissue (not shown) of reference motility ($D_T = D_0$). Note, the relatively smooth surface of the tumor. The corresponding image is shown in Fig.27A.

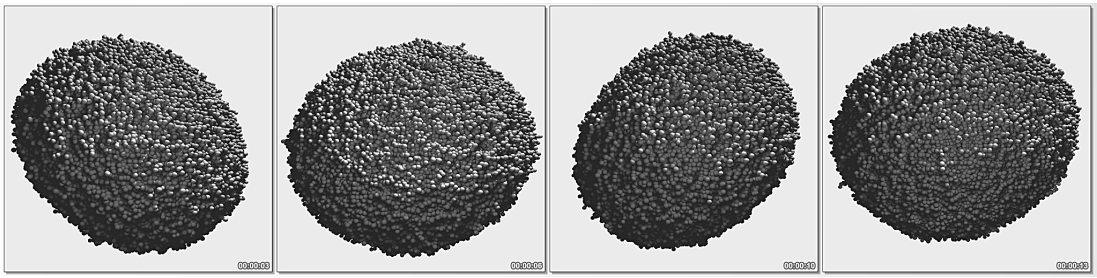

**Supporting Video 7:** Three-dimensional tumor spheroid growing into an embedding tissue (not shown) of decreased motility ($D_T = 0.05D_0$). Note, the very rough, dendritic surface of the tumor (also see Supporting Video 8). Refer to Fig.27B.

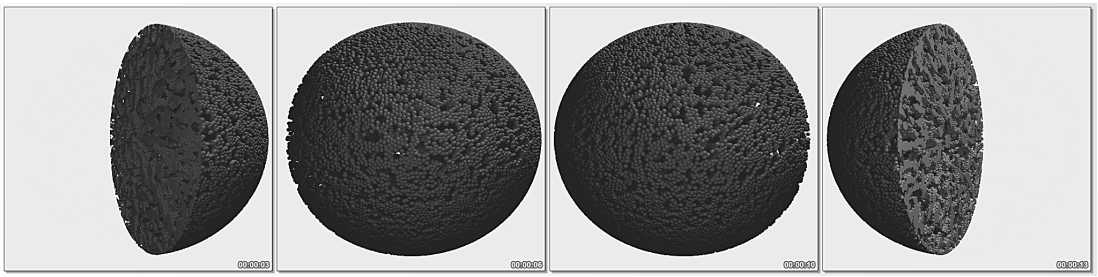

**Supporting Video 8:** Embedding tissue of tumor shown in Supporting Video 7. The embedding tissue (the embedded tumor is not shown) clearly reveals the dendritic structure of the tumor.

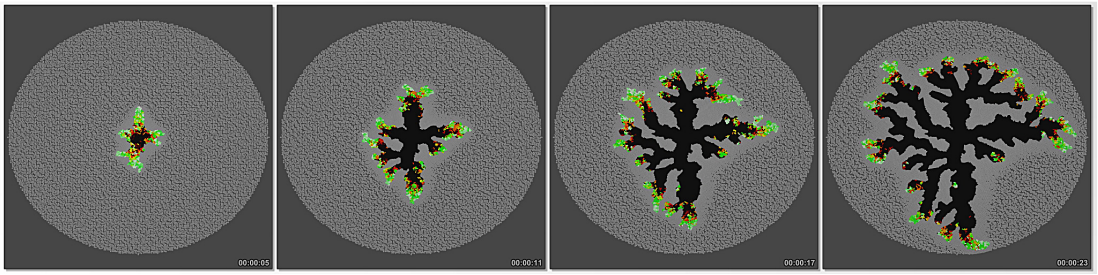

**Supporting Video 9:** Dendritic monolayer embedded in tissue of lowered motility ($D_T = 0.05D_0$). Cell coloring corresponds to the description in the caption of Supporting Video 5. Refer to Fig.27E.

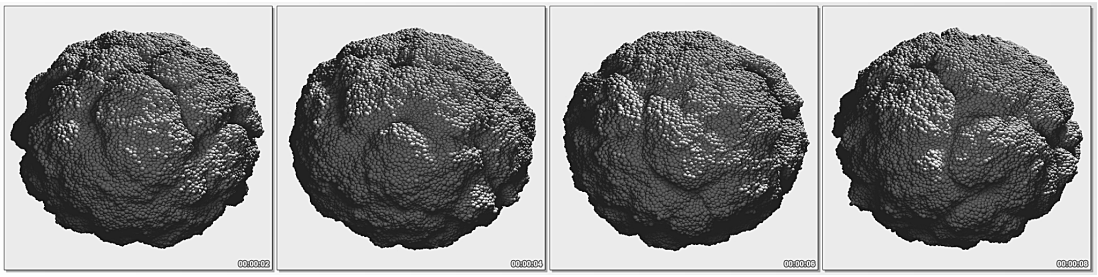

**Supporting Video 10:** Tumor growing into host tissue (not shown here) of decreased density ($\rho_T = 0.8\ \rho_0$). Refer to Fig.28F

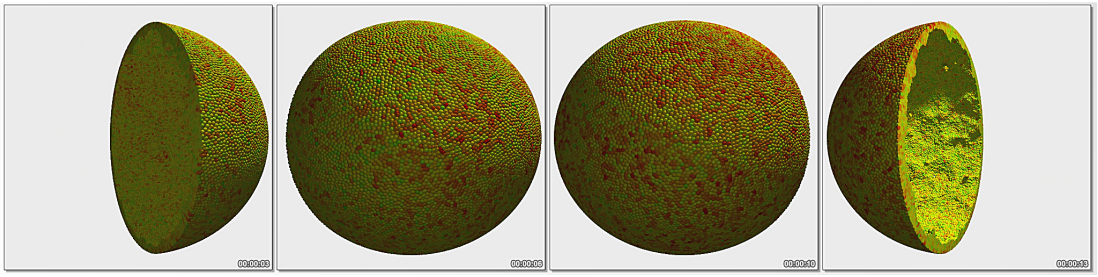

**Supporting Video 11:** Host tissue of tumor (not shown here) from Supporting Video 10. Refer to Fig.28F.

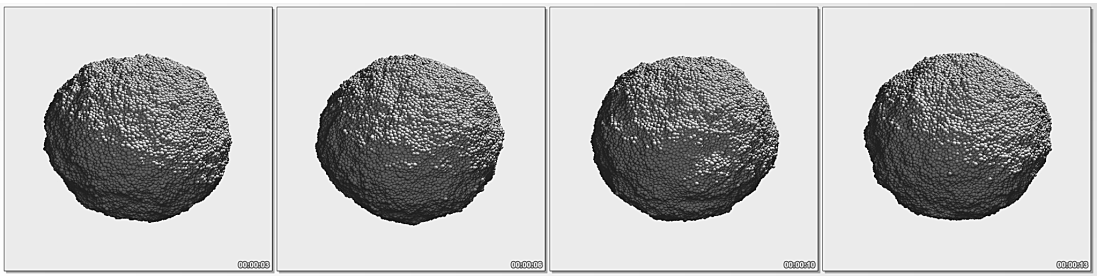

**Supporting Video 12:** Tumor growing into host tissue (not shown here) of decreased density ($\rho_T$ = 1.2 $\rho_0$). Refer to Fig.28G

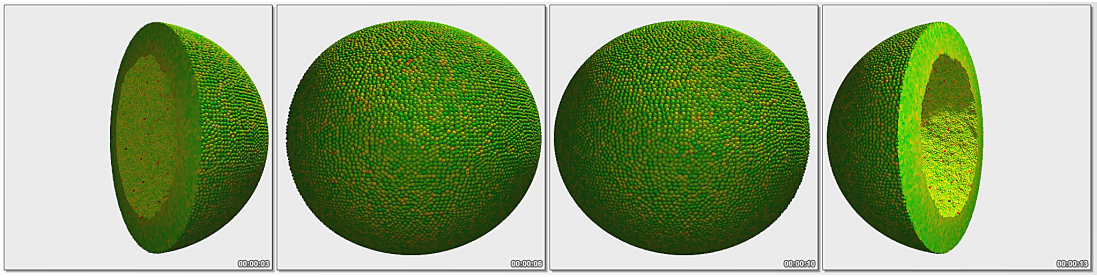

**Supporting Video 13:** Host tissue of tumor (not shown here) from Supporting Video 12. Refer to Fig.28G.

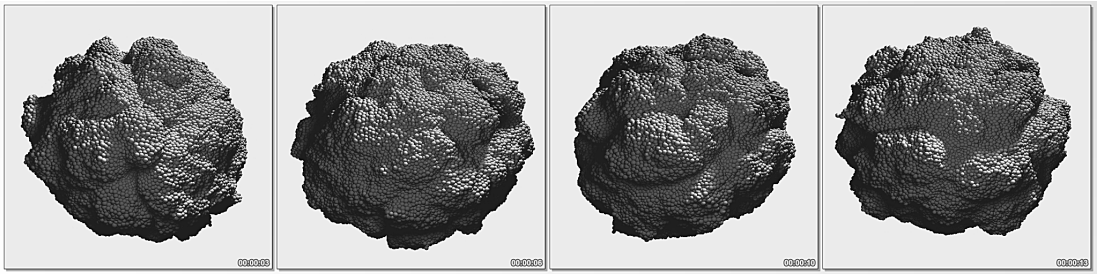

**Supporting Video 14:** Three-dimensional tumor spheroid growing into embedding tissue (not shown here) of increased elasticity ($E_T$=300 Pa). Note, the large wavelength surface fluctuations. Refer to Fig.29A.

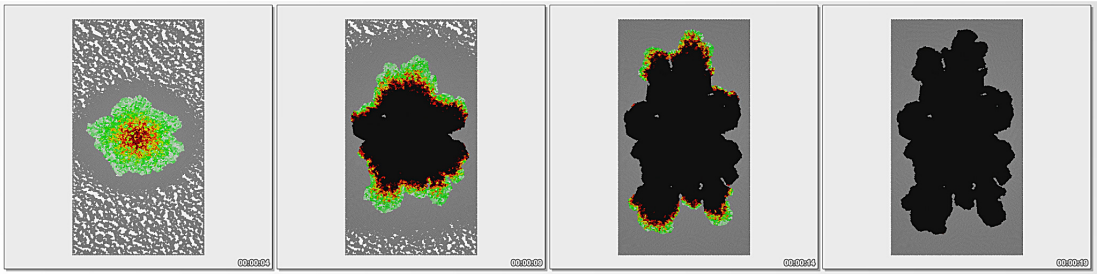

**Supporting Video 15:** Monolayer growing in an anisotropic environment (grey). Cell coloring corresponds to the description in the caption of Supporting Video 5. Also refer to Fig.32A.

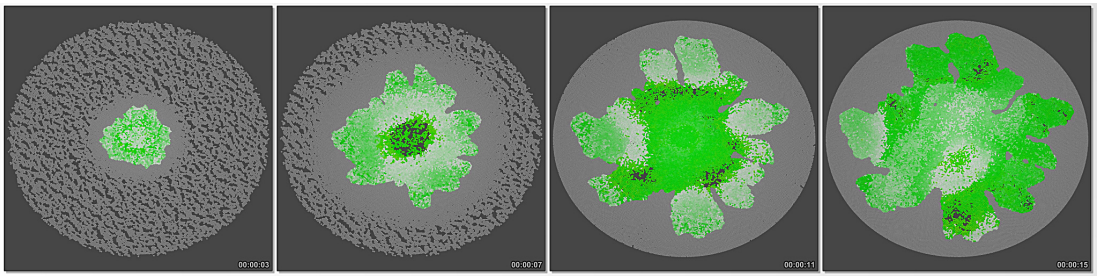

**Supporting Video 16:** Tumor cell population growing into host tissue (grey). In this simulation cytolysis was activated ( $\Delta t_{cl}$ =12h) and we used the reference host tissue motility ($D_T = D_0$). Cell coloring corresponds to the description in the caption of Supporting Video 5. Refer to Fig.33B.

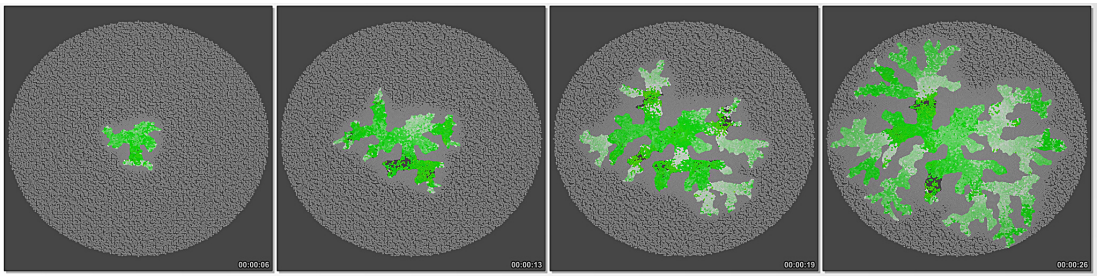

**Supporting Video 17:** Tumor cell population growing into host tissue (grey). In this simulation cytolysis was activated ( $\Delta t_{cl}$ =12h) and we used a decreased reference host tissue motility ($D_T = 0.05 D_0$). Cell coloring corresponds to the description in the caption of Supporting Video 5. Refer to Fig.33A.

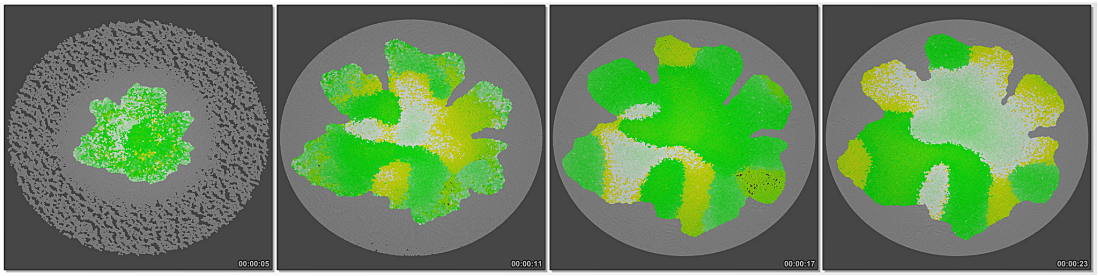

**Supporting Video 18:** Tumor cell population growing into host tissue (grey). In this simulation cytolysis was activated ( $\Delta t_{cl}$ =4d) and we used the reference host tissue motility ($D_T = D_0$). Cell coloring corresponds to the description in the caption of Supporting Video 5.

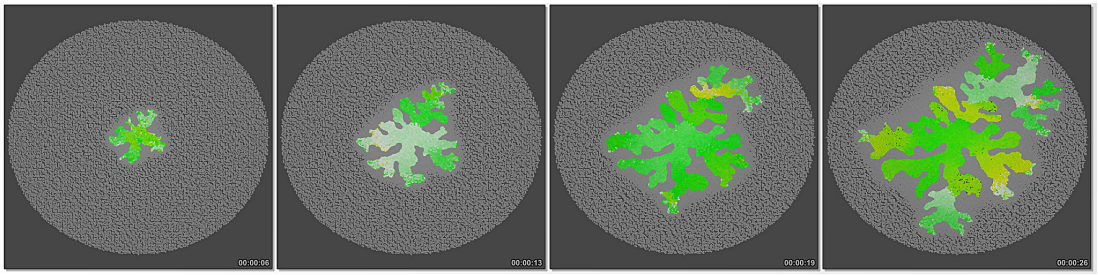

**Supporting Video 19:** Tumor cell population growing into host tissue (grey). In this simulation cytolysis was activated ( $\Delta t_{cl}$ =4d) and we used a decreased host tissue motility ($D_T = 0.05 D_0$). Cell coloring corresponds to the description in the caption of Supporting Video 5.

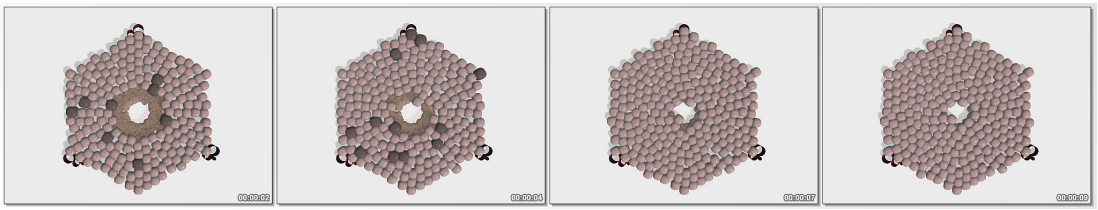

**Supporting Video 20:** Typical 2D model simulation of liver regeneration after $CCl_4$ intoxication in a schematic liver lobule. Here we used DCO and the reference hepatocyte micromotility (a=1). This simulation is designated as "reference simulation" in the text (Fig.44C).

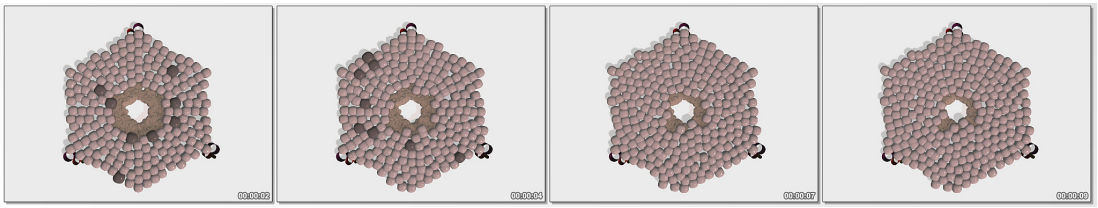

**Supporting Video 21:** Model simulation of liver regeneration after $CCl_4$ intoxication in 2D in a schematic liver lobule. Here we used DCO and a decreased hepatocyte micromotility (a=0.2). Refer to Fig.44A.

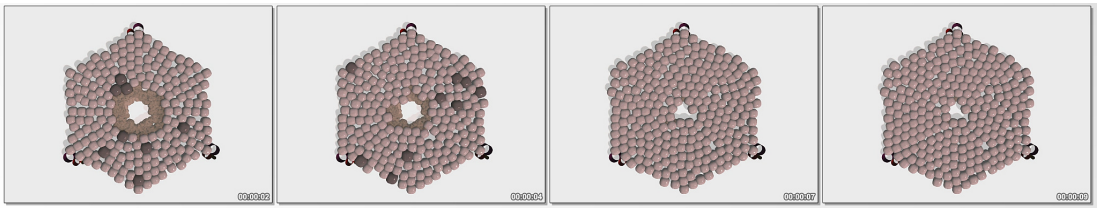

**Supporting Video 22:** Model simulation of liver regeneration after $CCl_4$ intoxication in 2D in a schematic liver lobule. Here we used DCO and an increased hepatocyte micromotility (a=5). Refer to Fig.44E

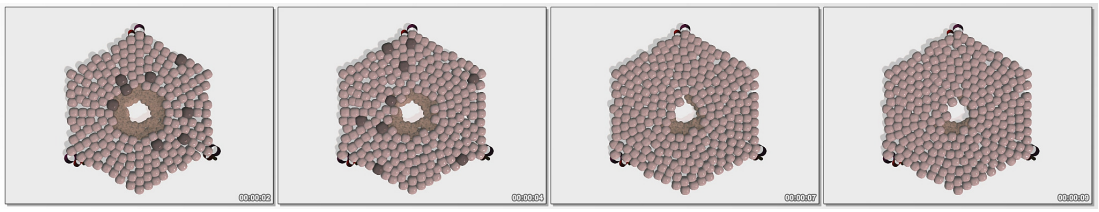

**Supporting Video 23:** Model simulation of liver regeneration after $CCl_4$ intoxication in 2D in a schematic liver lobule. Here we used RCO and the reference hepatocyte micromotility (a=1). Refer to Fig.44D.

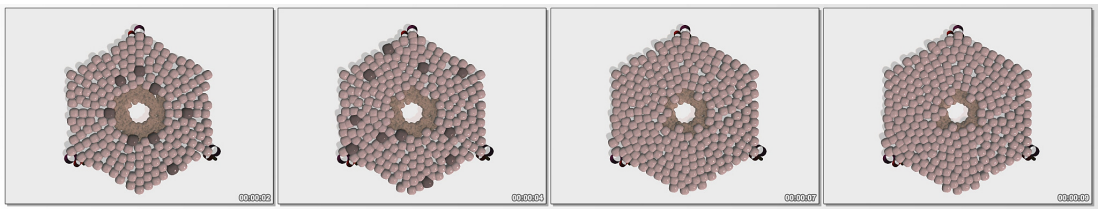

**Supporting Video 24:** Model simulation of liver regeneration after $CCl_4$ intoxication in 2D in a schematic liver lobule. Here we used RCO and a decreased hepatocyte micromotility (a=0.2). Refer to Fig.44B.

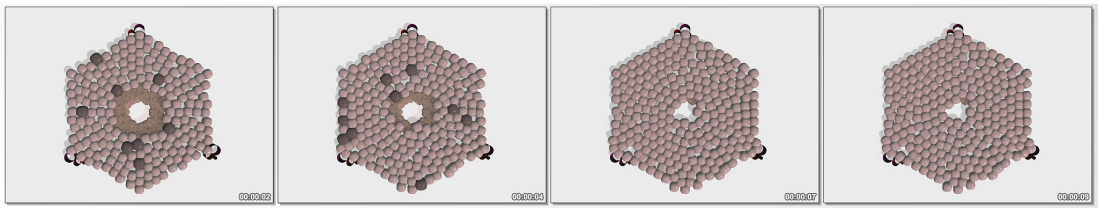

**Supporting Video 25:** Model simulation of liver regeneration after $CCl_4$ intoxication in 2D in a schematic liver lobule. Here we used RCO and an increased hepatocyte micromotility (a=5). Refer to Fig.44F.

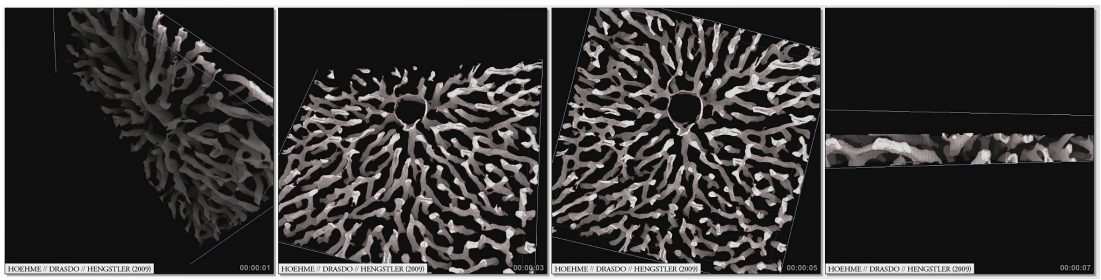

**Supporting Video 26:** Visualisation of volume data after reconstruction of sinusoidal blood vessel network (white) after enhancement. Refer to Fig.49F.

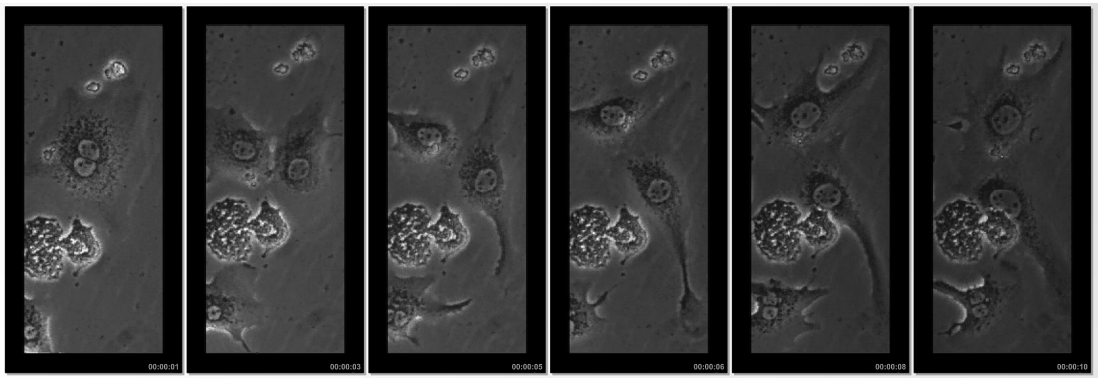

**Supporting Video 27:** Time lapse video showing an actively scattering hepatocyte that is attracted by a dead hepatocyte. Hepatocyte isolation and cultivation was performed as described by [Brulport et al., 2007] and [Klingmüller et al., 2006].

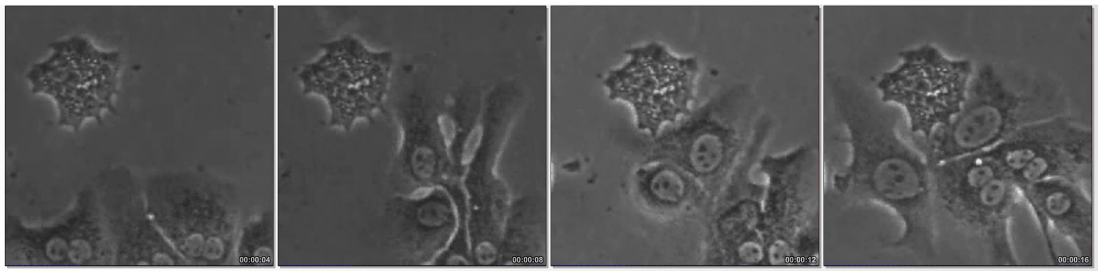

Supporting Video 28: Another variation of Supporting video 27.

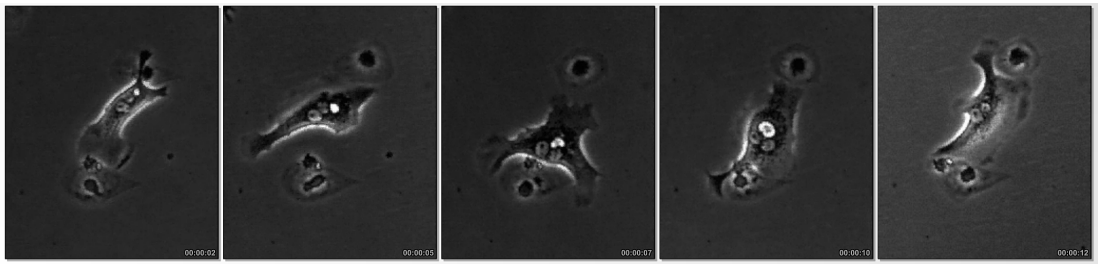

**Supporting Video 29:** Time lapse video showing hepatocyte-sinusoidal cell co-cultures. Hepatocytes show a much higher scattering activity compared to the co-cultured sinusoidal cells. One hepatocyte is attracted by two co-cultured sinusoids, one in the upper and one in the lower part of the image. The hepatocyte scatters between the two sinusoidal cells and tries to stay in contact with both of them.

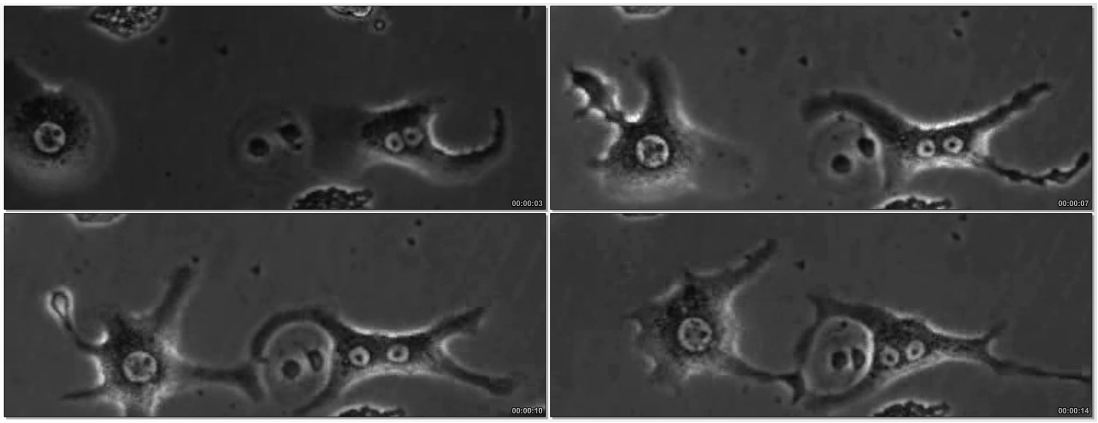

**Supporting Video 30:** Time lapse video showing hepatocyte-sinusoidal cell co-cultures. In the first part of the video one hepatocyte approaches a sinusoidal cell (in central position) from the right hand side and aims at maximizing the contact area with the sinusoidal cell. Next, a second hepatocyte approaches from the left hand side and also contacts the sinusoidal cell. Supporting videos 29 and 30 illustrate that sinusoidal cells attract the hepatocytes and that hepatocytes maximize their contact area with sinusoidal cells.

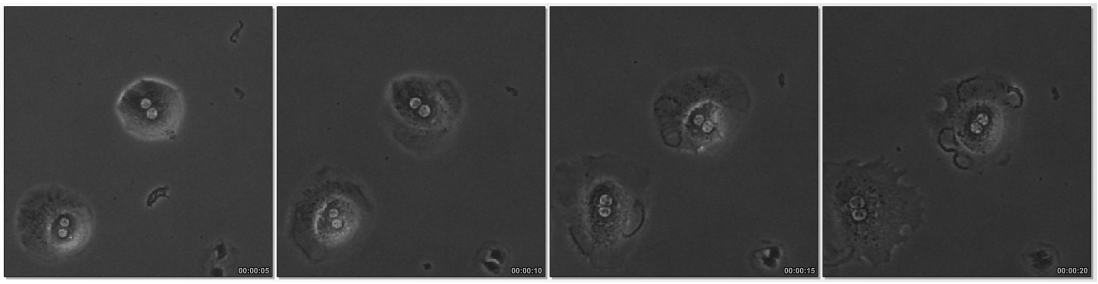

**Supporting Video 31:** Time lapse video showing hepatocyte monoculture. In contrast to sinusoidal cells hepatocytes do not attract each other.

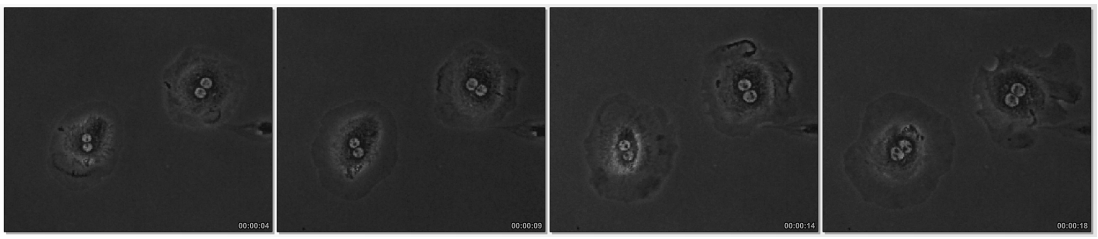

**Supporting Video 32:** Time lapse video showing hepatocyte monoculture. In contrast to sinusoidal cells hepatocytes do not attract each other (variation).

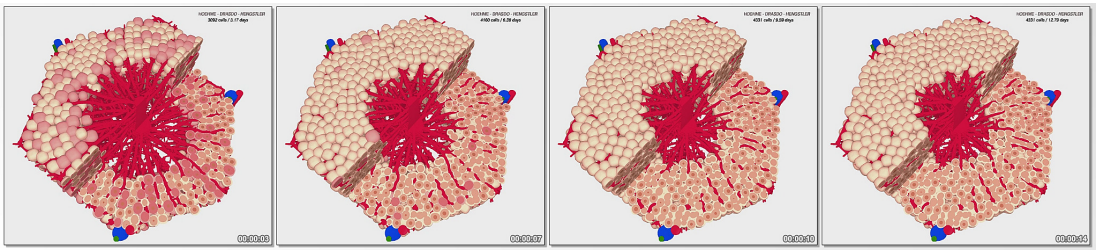

**Supporting Video 33:** Simulation of liver regeneration in a representative (averaged) lobule in 3D. Video shows the time development of model variant 1 (see section 4.3) during 16 days. The model simulation partly shows cross-sections. Refer to Fig.61A.

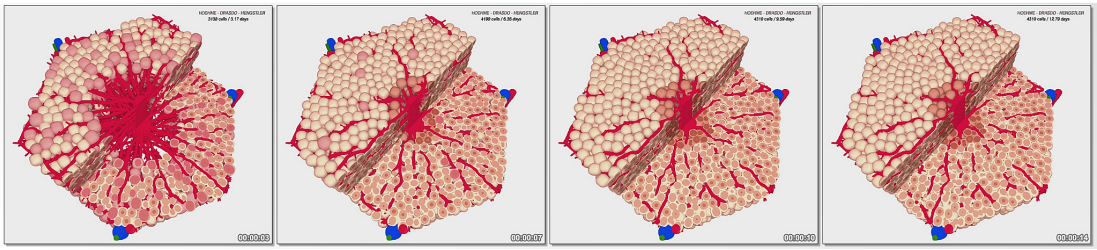

**Supporting Video 34:** Simulation of liver regeneration in a representative (averaged) lobule in 3D. Video shows the time development of model variant 2 (see section 4.3) during 16 days. The model simulation partly shows cross-sections. Refer to Fig.61B.

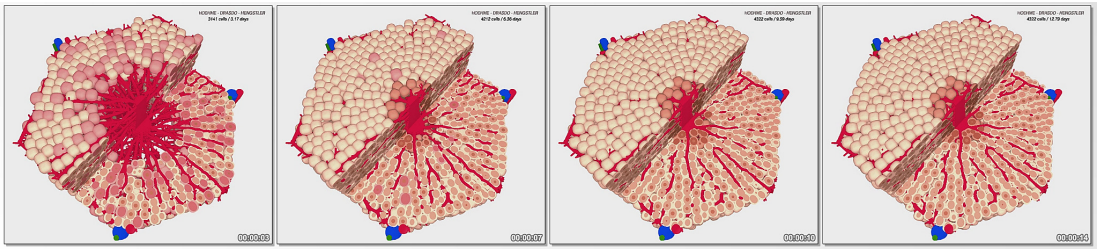

**Supporting Video 35:** Simulation of liver regeneration in a representative (averaged) lobule in 3D. Video shows the time development of model variant 3 (see section 4.3) during 16 days. The model simulation partly shows cross-sections. Refer to Fig.61C.

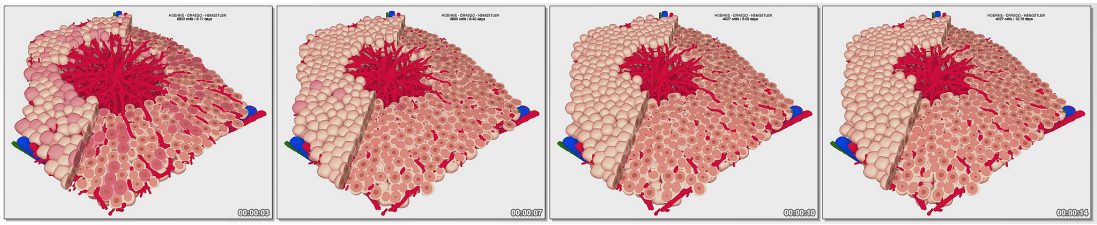

**Supporting Video 36:** Simulation of liver regeneration in a concrete lobule extracted from a single confocal dataset in 3D. Video shows the time development of model variant 1 (see section 4.3) during 16 days. The model simulation partly shows cross-sections.

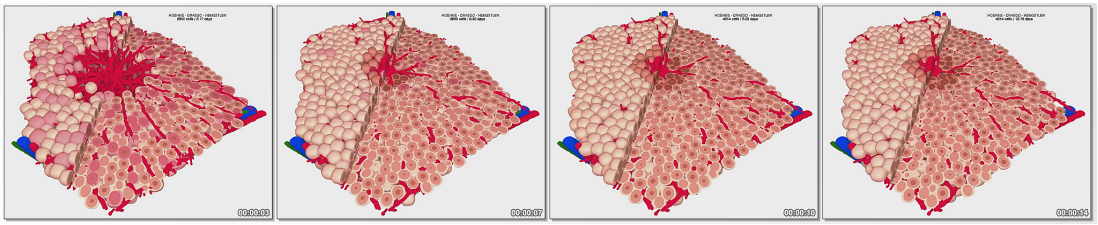

**Supporting Video 37:** Simulation of liver regeneration in a concrete lobule extracted from a single confocal dataset in 3D. Video shows the time development of model variant 2 (see section 4.3) during 16 days. The model simulation partly shows cross-sections.

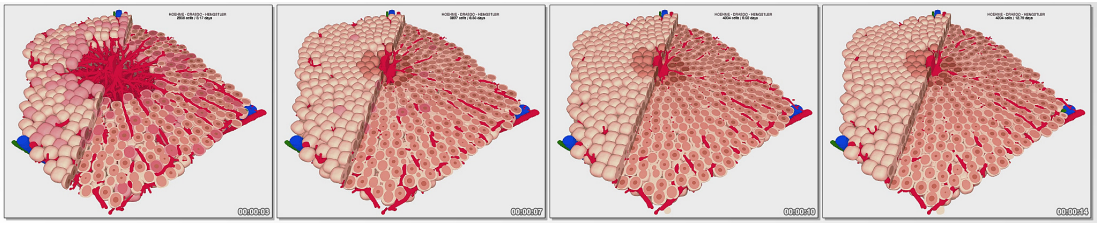

**Supporting Video 38:** Simulation of liver regeneration in a concrete lobule extracted from a single confocal dataset in 3D. Video shows the time development of model variant 3 (see section 4.3) during 16 days. The model simulation partly shows cross-sections.

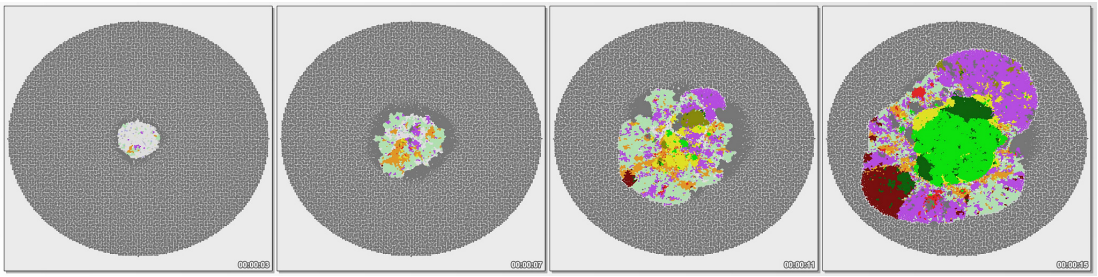

**Supporting Video 39:** Accumulation of hallmark mutations leading intercellular heterogeneity. Ultimately, invasively growing cell clones (green) dominate the cell population. Refer to Fig.65 in chapter 6.1 for further explanations.

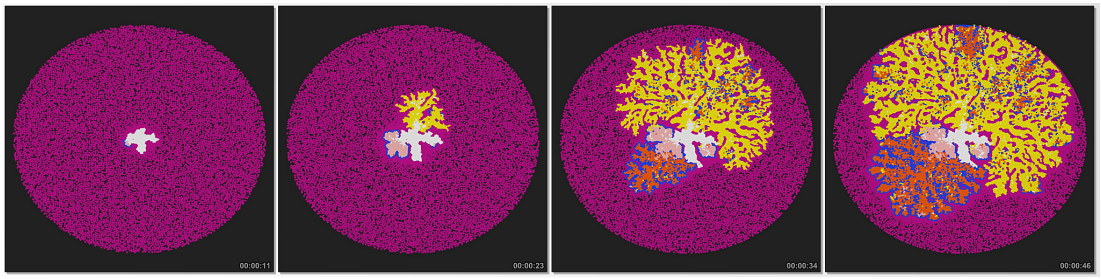

**Supporting Video 40:** Reduced cell-cell adhesion (predominantly yellow cell clone) leads to more invasive growth patterns compared to cells of increased cell-cell adhesion (rose color) The embedding tissue is shown in dark magenta. Refer to Fig.66B and chapter 6.1 for further explanations.

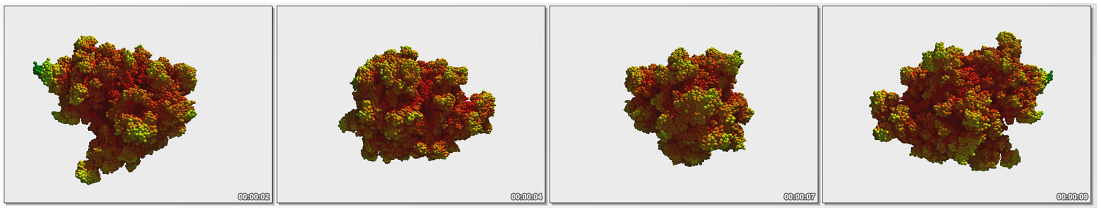

**Supporting Video 41:** The effect of active regulation of the micromotility which in this population had been increased to survive nutrient shortage. The video shows a tumor population in 3D. Colors denote nutrient concentration (green = high, red = low concentration). For details refer to section 6.2.

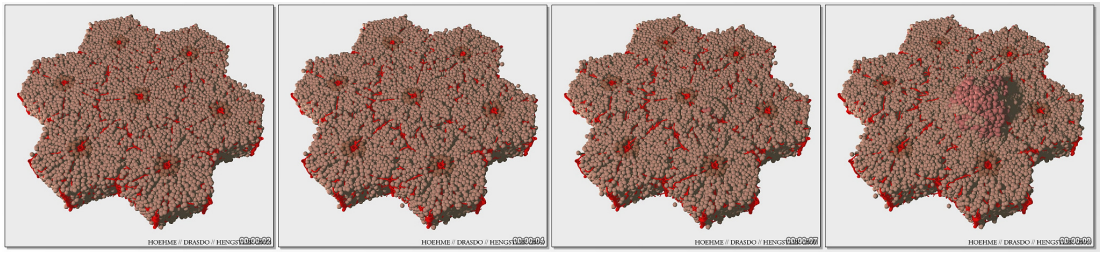

**Supporting Video 42:** Solitary tumor (rose) growing within a multi-lobule model. For details see section 6.4 and Fig.70.

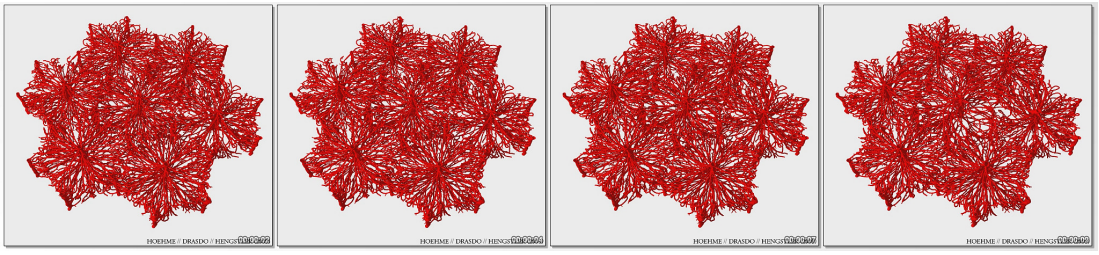

**Supporting Video 43:** Same simulation as in Supporting Video 42 but only the blood vessels are shown (no hepatocytes). The video reveals the dramatic effects of a solitary tumor on the blood vessels within the lobule. For details see section 6.4 and Fig.70.

# Appendix 3: Glossary

**Abstract class** — A class that is not able to have instances. An abstract class typically serves as a generalized blueprint for its instantiated subclasses.

**Apoptosis** — One of the two major types of cell death (compare to Necrosis). Also termed "programmed cell death". Cells that undergo apoptosis commit suicide in a physiologically regulated process as a consequence of internal or external signals.

**C6 rat astrocyte glioma cells** — Animal neuroglial cell line of neuroepithelial origin [Bru et al., 1998].

**Class** — A descriptor or blueprint for a collection of objects (or subclasses) whose behavior and structure is logically similar. Typically objects are instantiated from a class.

**Concrete class** — A class that is allowed to have instances (objects).

**Crossover size (point)** — Defined as the diameter (time) at which the tumor growth dynamics crosses over from one growth regime to another. Within this thesis, we usually refer to the transition between the exponential and the surface-growth regime

**EMT6/Ro cells** — Murine cell line [Freyer & Sutherland, 1986].

**Encapsulation** — A basic principle in the object oriented software development paradigm, whereby the internal details of a class or object are hidden from the view of other classes or objects. Thereby, an encapsulated object can often be maintained or modified without affecting other parts of the system.

**Hepatocyte** — Hepatocytes are the parenchymal cells of the liver and account for approximately 80 - 90% of the liver mass [Taub, 2004]. In healthy lobules, hepatocytes are arranged in a special columnar microarchitecture.

**Hertz model** — Classical contact model that describes the interaction of homogeneous, elastic, and isotropic bodies [Landau, 1975]. We extended the Hertz model by a term that takes into account cell-cell adhesion.

**Inheritance** The mechanism by which the relationship of generalization and specialization (class hierarchy) between classes is implemented. Due to inheritance a subclass automatically acquires the properties and behavior of its superclasses.

**Instance** A single object is often called an instance in the context of its affiliation to a particular class.

**Intrinsic cycle time** Duration of the cell cycle of an average isolated cell not affected by physical interactions with neighboring cells.

**JKR model** Johnson–Kendall–Roberts contact model that describes the interaction between homogeneous, elastic, and isotropic bodies [Johnson et al., 1971]. The JKR-model includes a hysteresis effect that becomes important e.g. in case of cell detachment processes.

**Linear velocity–force relationship** Velocity ($v$) changes proportionally to exerted force ($v \propto F$; $F$: total force). This assumes that the migration velocity of a cell as a response on an external mechanical stimulus or force is approximately proportional to the strength of the stimulus.

**Message** In the context of the object oriented paradigm, a message is a request to an object to provide a specific functionality or information. Typically, a message invokes a method of an object or the transport of information.

**Message passing** A basic principle of the object oriented paradigm that describes the way that objects interact by sending each other messages trigger methods or transport information.

**Method** The implementation of a certain functionality (typically) of an object.

**Monolayer** Monolayer cultures are a common experimental tool for two-dimensional *in vitro* cell cultures [Bru et al., 2003].

**Necrosis** One of the two major types of cell death (compare to Apoptosis). Cells may die by necrosis if they were exposed to serious physical or chemical insult.

| | |
|---|---|
| | Necrosis of cells *in vivo* is often accompanied by extensive damage to adjacent tissue. |
| **Object** | A single entity in a given application domain or software system. Within the object oriented paradigm, objects have an identity, properties (a state) and functionality (behavior). Objects are instances of a class. |
| **Sinusoid** | Sinusoids are small blood vessels in the liver that have a discontinuous (fenestrated) endothelium. |
| **Software architecture** | Describes the components of a software system and the relationships between them. |
| **Spheroid** | Short for "Multicellular Tumor Spheroid" (MCTS). Tumor cells are often able to grow and divide anchorage-independent. Therefore, they can be grown in suspension, not being attached to a substrate, where they form growing spherical aggregates termed MCTS. MCTS are a common experimental technique for three-dimensional *in vitro* cell cultures [Kunz-Schughart, 1999]. |
| **Subclass** | A (less general) class that acquires features of a more general cell higher in class hierarchy. A subclass typically adds particular characteristics of its own. |
| **Superclass** | A (more general) class that represents an abstraction of the common properties and behavior of its subclasses (lower in class hierarchy). |

# Appendix 4: List of abbreviations

| | |
|---|---|
| ABM | Agent-based model |
| AFM | Atomic force microscopy |
| AHE | Adaptive histogram equalization |
| API | Application programming interface |
| BrdU | Bromodeoxyuridine |
| $CCl_4$ | Carbon-Tetrachloride |
| CLSM | Confocal laser scanning microscopy |
| CPM | Cellular Potts Model |
| DAPI | 4',6-diamidino-2-phenylindole |

| | |
|---|---|
| DCO | Directed cell orientation |
| DNA | Deoxyribonucleic acid |
| DPPIV | Dipeptidyl Peptidase IV |
| ECM | Extracellular matrix |
| EGFP | Enhanced green fluorescent protein |
| GCC | GNU Compiler Collection |
| GD | Generalized dilatation |
| GE | Generalized erosion |
| GL | Graphics library |
| GLU | Graphics library utilities |
| GLUI | OpenGL user interface library |
| GLUT | Graphics library utility toolkit |
| GS | Glutamine synthetase |
| GUI | Graphical user interface |
| HSA | Hepatocyte-sinusoid alignment |
| HE | Histogram equalization |
| HPx | Partial hepatectomy |
| ICAM | Intercellular adhesion molecule |
| JKR | Johnson-Kendall-Roberts (model) |
| MCTS | Multicellular tumor spheroids |
| MPI | Message passing interface |
| MRI | Magnetic resonance imaging |
| MZ | Midzonal |
| NRCAM | National Resource for Cell Analysis and Modeling |
| OGL | Open Graphics Library (Open GL) |
| OMG | Object management group |
| OMP | Open Multi Processing (Open MP) |
| OOP | Object oriented paradigm |
| PIVR | Rre-integrated volume renderer |
| POV | Persistence of vision (raytracer) |
| PP | Periportal |
| PV | Perivenous |
| RCO | Random cell orientation |
| SDL | Scene description language |
| VRML | Virtual reality markup language |

# Appendix 5: Table of parameters

| Parameter | Symbol | Unit | Value | Chapter | Source |
|---|---|---|---|---|---|
| **Model cell parameters** | | | | | |
| Position of cell *i* | $\underline{x}_i$ | - | - | 3,4 | - |
| Cell size (diameter) | $l$ | µm | 10 | 3.3 | [Bru, 2006] |
| | | | 14 | 3.4-3.6 | [Freyer & Sutherland, 1985] |
| | | | 23.3 | 4 | * |
| Initial radius of a cell (after cell division) | $R_0$ | µm | $l/2$ | 3,4 | - |
| Current radius of a model cell *i* | $R_i$ | µm | $R_0$ - $1.26R_0$ | 3,4 | - |
| Change of cell radius per growth step in cell growth algorithm 2 | $\Delta R$ | µm | $\ll R_0$ | 3,4 | [Fidorra et al., 1981] |
| Current volume of a model cell *i* | $V_i$ | $\mu m^3$ | Eqn.4<br>Eqn.5 | 3,4 | - |
| Cell compartment distance | $d_i$ | µm | 0 - $2R_0$ | 3 | - |
| Change of compartment distance per growth step in cell growth algorithm 1 | $\Delta d$ | µm | $\ll R_0$ | 3 | [Fidorra et al., 1981] |
| Cell cycle time | $\tau$ | h | 18 | 3.3 | [Bru, 2006] |
| | | | 22 | 3.4-3.5 | [Freyer & Sutherland, 1986] |
| | | | 21-22 | 3.6 | [Noguchi et al., 1979] |
| | | | 24 | 4 | [Vintermyr & Døskeland, 1987] |
| Young's modulus of a cell *i* | $E_i$ | Pa | 450<br>(300-1000) | 3,4 | [Davidson et al., 1995]<br>[Lekka et al., 1999] |
| Poisson number of a cell *i* | $v_i$ | - | 0.4 | 3,4 | [Mahaffy et al., 2000]<br>[Alcaraz et al., 2003] |
| Cell diffusion constant | $D_0$ , $D_0^C$ | $\frac{cm^2}{s}$ | $20^{-12}$<br>( $20^{-12}$-$10^{-11}$) | 3,4 | [Beysens et al., 2000] |
| Cell orientation | $\psi$ | - | 0 - $2\pi$ | 4 | - |
| Size of polar adhesive region | $\phi$ | - | $\pi/12$ | 4 | [Burt et al., 2006] |
| Cell orientation change in time $\Delta t$ | $\theta(\Delta t)$ | - | $\ll \phi$ | 4 | - |

| | | | | | |
|---|---|---|---|---|---|
| **Population parameters** | | | | | |
| Population diameter | $L$ | µm | - | 3,4 | - |
| Width of the proliferating rim | $\Delta L$ | µm | - | 3 | - |
| Expansion velocity of cell population | $v$ | µm/d | - | 3 | - |
| Size of subclone arisen from cell *i* | $N_i(t)$ | cells | - | 3.3 | - |
| Average cell volume | $\bar{V}_c$ | µm³ | - | 3.5 | - |
| Box counting dimension | $df$ | - | 1 - 3 | 3 | [Dubuc et al., 1989] |
| Experimentally observed probability for proliferation at position $\chi$ at time t | $P_{CD}$ | - | 0 - 1 | 4 | [Gebhardt & Burger, 1987] |
| **Parameters of the embedding medium** | | | | | |
| Initial cell or particle density in the embedding tissue | $\rho_T$ | $\frac{cells}{mm^2}$ | 3500 - 7000 | 3.6 | [Alberts et al., 2008] |
| Young's modulus of the embedding tissue | $E_T$ | Pa | 300 - 1000 | 3.6 | [Davidson et al., 1995] [Lekka et al., 1999] |
| Diffusion constant of embedding tissue | $D_T$ | $\frac{cm^2}{s}$ | $0.05 - 1.5D_0$ | 3.6 | [Beysens et al., 2000] |
| Receptor density in interactions among tumor cells (type A) | $\zeta_{AA}$ | $m^{-2}$ | $0 - \approx 10^{15}$ | 3.6 | [Chesla et al., 1998] [Piper et al., 1998] |
| Receptor density in interactions among embedding cells (type B) or granular particles | $\zeta_{BB}$ | $m^{-2}$ | $0 - \approx 10^{15}$ | 3.6 | [Chesla et al., 1998] [Piper et al., 1998] |
| Receptor density in interactions between tumor cells and cells of type B (or granular particles) | $\zeta_{AB}$ | $m^{-2}$ | $0 - \approx 10^{15}$ | 3.6 | [Chesla et al., 1998] [Piper et al., 1998] |
| Cell size of the embedding tissue | $l_T$ | µm | 10 – 25 | 3.6 | [Alberts et al., 2008] |
| **Contact mechanics parameters** | | | | | |
| Reference energy | $F_T$ | J | $10^{-16}$ | 3,4 | [Schienbein et al., 1994] [Beysens et al., 2000] |
| Receptor density | $\varsigma_m$ | $m^{-2}$ | $\approx 10^{15}$ $(10^{14} - 10^{16})$ | 3,4 | [Chesla et al., 1998] [Piper et al., 1998] |

| | | | | | |
|---|---|---|---|---|---|
| Binding energy single bond | $W_s$ | $k_BT$ | $\approx 25$ | 3,4 | [Beysens et al., 2000] |
| Effective cell-cell friction coefficient | $\gamma$ , $\gamma^C$ | kg/s | 0.1 | 3,4 | - |
| Effective cell-sinusoid friction coefficient | $\gamma^S$ | kg/s | 0.02 - 0.2 | 4 | - |
| Potential in Hertz model | $V_{ij}^{HER}$ | - | - | 3,4 | Eqn.6 |
| Cell center distance | $d_{ij}^{HER}$ | m | - | 3,4 | - |
| Contact area between cell *i* and *j* in Hertz model | $A_{ij}^{HER}$ | $m^2$ | - | 3,4 | Eqn.9 |
| Interaction force in Hertz model | $\underline{F}_{ij}^{HER}$ | Pa | - | 3,4 | Eqn.10 |
| Potential in JKR model | $V_{ij}^{JKR}$ | - | - | 3,4 | - |
| Cell surface distance in JKR model (considers deformations) | $d_{ij}^{JKR}$ | m | - | 3,4 | - |
| Contact distance in the JKR model | $d_{con}$ | m | - | 3,4 | - |
| Interaction force in JKR model | $\underline{F}_{ij}^{JKR}$ | Pa | - | 3,4 | Eqn.15 |
| **Reaction diffusion parameters** | | | | | |
| Glucose diffusion constant | $D_{glc}$ | $\frac{cm^2}{s}$ | $10^{-6}$ | 3,4 | [Casciari et al., 1988] |
| Glucose consumption rate | $g_{glc}$ | $\frac{mg}{cell \cdot h}$ | 7.5 (7.5-21) | 3,4 | [Casciari et al., 1992] |
| Initial glucose concentration | $c_0$ | mM | 0.8 - 16.5 | 3,4 | [Freyer & Sutherland, 1986] |
| **Image and volume processing parameters** | | | | | |
| Position of a voxel in the data set | $\bar{\chi}$ | - | - | 4 | - |
| Kernel of AHE | $\Psi^{AHE}$ | voxel | $R = 64$ | 4 | - |
| Kernel of GE and GD algorithm | $\Psi^{GED}$ | voxel | $R$ = 2-6 | 4 | - |
| General intensity threshold | $\alpha$ | - | 0.5 | 4 | - |
| Threshold of GE algorithm | $\alpha_{GE}$ | - | 0.15-0.35 (Iteration-dependent) | 4 | - |

| | | | | | |
|---|---|---|---|---|---|
| Threshold of GE algorithm | $\alpha_{GD}$ | - | 0.45-0.70 (Iteration-dependent) | 4 | - |
| Length of sample vectors in CC algorithm | $R^{CC}$ | voxel | 10 | 4 | - |
| Threshold of CC algorithm | $\alpha_{CC}$ | - | 0.9 | 4 | - |
| Radius of the kernel used for the intensity averaging | $R^{AVG}$ | voxel | 25 | 4 | - |
| Threshold for intensity averaging | $\alpha_{AVG}$ | - | 0.0 – 0.2 (Iteration-dependent) | 4 | - |
| Threshold for binarization | $\alpha_{HEP}$ | - | 0.8 | 4 | - |
| Threshold intensity for seeded region growing segmentation | $\alpha_{NEC}$ | - | 0.5 | 4 | - |
| **Cell state transition parameters** | | | | | |
| Pressure exerted on model cell *i* | $P_i$ | Pa | - | 3,4 | Eq.18 |
| Pressure threshold for transition to necrosis | $p^{NECR}$ | Pa | 200-2000 | 3,4 | - |
| Pressure threshold for transition to quiescence | $P^{QUIES}$ | Pa | 100-500 | 3,4 | - |
| Deformation threshold for transition to quiescence | $\varsigma$ | - | 0.7 (0.6-0.9) | 3,4 | - |
| Inactivation threshold | $c^{NECR}$ | $\frac{mg}{mm^3}$ | $6 \cdot 10^{-6}$ | 3 | - |
| Quiescent threshold | $c^{QUIES}$ | $\frac{mg}{mm^3}$ | $2 \cdot 10^{-5}$ | 3 | - |
| Time until cytolysis | $\Delta t_{cl}$ | h | 12 - 96 | 3.6 | - |
| **Sinusoid parameters** | | | | | |
| Sinusoid vessel radius | $R_{Sinu}$ | µm | $l_{Sinu}$ / 2 | 4 | * |
| Sinusoid vessel diameter | $l_{Sinu}$ | µm | 4.75 | 4 | |

| | | | | | |
|---|---|---|---|---|---|
| Sinusoids Young's Modulus | $E_{Sinu}$ | Pa | 600 (300-1000) | 4 | - |
| Sinusoids Poisson number | $\upsilon_{Sinu}$ | - | 0.4 | 4 | - |
| * ... Quantitative analysis of volume datasets obtained by confocal laser scanning | | | | | |

# Appendix 6: List of Figures

# Appendix 7: List of Tables

# References

[Abran *et al.*, 2004] Abran, A., Bourque, P., Dupuis, R., Moore, J.W., & Tripp, L.L. 2004. *Guide to the Software Engineering Body of Knowledge - SWEBOK*. IEEE Press.

[Acharya & Ray, 2005] Acharya, T., & Ray, A. 2005. *Image Processing: Principles and Applications*. Wiley-Interscience.

[Adam & Bellomo, 1997] Adam, J.A., & Bellomo, N. 1997. *A Survey of Models for Tumor-Immune System Dynamics*. Birkhäuser, Boston.

[Adams & Cory, 2007] Adams, Jerry M, & Cory, Suzanne. 2007. Bcl-2-regulated apoptosis: mechanism and therapeutic potential. *Curr Opin Immunol*, **19**(5), 488–496.

[Aebersold *et al.*, 2009] Aebersold, Ruedi, Auffray, Charles, Baney, Erin, Barillot, Emmanuel, Brazma, Alvis, Brett, Catherine, Brunak, Søren, Butte, Atul, Califano, Andrea, Celis, Julio, Cufer, Tanja, Ferrell, James, Galas, David, Gallahan, Daniel, Gatenby, Robert, Goldbeter, Albert, Hace, Natasa, Henney, Adriano, Hood, Lee, Iyengar, Ravi, Jackson, Vicky, Kallioniemi, Ollie, Klingmüller, Ursula, Kolar, Patrik, Kolch, Walter, Kyriakopoulou, Christina, Laplace, Frank, Lehrach, Hans, Marcus, Frederick, Matrisian, Lynn, Nolan, Garry, Pelkmans, Lucas, Potti, Anil, Sander, Chris, Seljak, Marija, Singer, Dinah, Sorger, Peter, Stunnenberg, Hendrik, Superti-Furga, Giulio, Uhlen, Mathias, Vidal, Marc, Weinstein, John, Wigle, Dennis, Williams, Michael, Wolkenhauer, Olaf, Zhivotovsky, Boris, Zinovyev, Andrei, & Zupan, Blaz. 2009. Report on EU-USA workshop: how systems biology can advance cancer research. *Mol Oncol*, **3**(1), 9–17.

[Alarcon *et al.*, 2004] Alarcon, T., Byrne, H.M., & Maini, P.K. 2004. A mathematical model of the effects of hypoxia on the cell-cycle of normal and cancer cells. *J. Theor. Biol.*, **229**, 395 – 411.

[Alber, 2003] Alber, M.S., Kiskowski M.A. Glazier J.A. Jian Y. 2003. *Mathematical Systems Theory in Biology, Communication, and Finance*. Springer.

[Alber *et al.*, 2002] Alber, M.S., Kiskowski, M.A., Glazier, J.A., & Jiang, Y. 2002. *On Cellular Automaton Approaches to Modeling Biological Cells. In: Mathematical Systems Theory in Biology, Communication, and Finance*. New York: Springer.

[Alberts *et al.*, 2002] Alberts, B., Johnson, A., Lewis, J., Raff, M., Roberts, K., & Walter, P. 2002. *The Cell*. Garland Science Publ.

[Alberts *et al.*, 2008] Alberts, B., Johnson, A., P.Walter, Lewis, J., Raff, M., & Roberts, K. 2008. *Molecular Biology of the Cell*. Taylor & Francis, 5th revised edition.

[Alcaraz *et al.*, 2003] Alcaraz, J., Buscemi, L., Grabulosa, M., Trepat, X., Fabry, B., Farre, R., & Navajas, D. 2003. Microrheology of human lung epithelial cells measured by atomic force. *Biophys. J.*, **84**, 2071–2079.

[Alison & Sarraf, 1998] Alison, M., & Sarraf, C. 1998. *Understanding Cancer*. Cambridge University Press.

[Amdahl, 1967] Amdahl, Gene. 1967. Validity of the Single Processor Approach to Achieving Large-Scale Computing Capabilities. *AFIPS Conference Proceedings*, **30**, 483–485.

[Anderson, 2000] Anderson, A. 2000. Mathematical Modeling of Tumor Invasion and Metastasis. *J. Theor. Med.*, **2**, 129 – 154.

[Anderson *et al.*, 2006] Anderson, Alexander R A, Weaver, Alissa M, Cummings, Peter T, & Quaranta, Vito. 2006. Tumor morphology and phenotypic evolution driven by selective pressure from the microenvironment. *Cell*, **127**(5), 905–915.

[Anderson, 2005] Anderson, A.R.A. 2005. A hybrid mathematical model of solid tumour invasion: the importance of cell adhesion. *Math. Med. Biol*, **22**, 163–186.

[Anderson *et al.*, 2007] Anderson, A.R.A., Chaplain, M.A.J., & (editors), K.A. Rejniak. 2007. *Single-Cell-Based Models in Biology and Medicine*. Basel: Birkhäuse.

[Anton, 1999] Anton, H.C. 1999. *A New Horizon*. 6th ed. New York Wiley.

[Araujo & McElwain, 2004] Araujo, R.P., & McElwain, D.L. 2004. A history of the study of solid tumour growth: the contribution of mathematical models. *Bull. Math. Biol.*, **66**, 1039–1091.

[Armstrong, 2006] Armstrong, D.J. 2006. The quarks of object-oriented development. *Commun. ACM 49*, **2**, 123–128.

[Arthur *et al.*, 1997] Arthur, W.B., Durlauf, S.N., & Lane, D.A. (eds). 1997. *The economy as an evolving complex system II, SFI Studies in the Sciences of Complexity*. Addison Wesley: Reading, MA.

[Atherton, 1983] Atherton, Peter. 1983. A Scan-line Hidden Surface Removal Procedure for Constructive Solid Geometry. *ACM SIGGRAPH Computer Graphics*, **17**(3), 73–82.

[Aurenhammer & Klein, 2000] Aurenhammer, F., & Klein, R. 2000. *Handbook of Computational Geometry*. Amsterdam.

[Axelrod, 1997] Axelrod, Robert. 1997. *The Complexity of Cooperation: Agent-Based Models of Competition and Collaboration*. Princeton: Princeton University Press.

[Bagni *et al.*, 2002] Bagni, R., Berchi, R., & Cariello, P. 2002. A comparison of simulation models applied to epidemics. *Journal of Artificial Societies and Social Simulation*, **5**(3).

[Barthel, 2008] Barthel, E. 2008. Adhesive elastic contacts: JKR and more. *Journal of Physics D: Applied Physics*, **41**(16), 163001.

[Bartles *et al.*, 1985] Bartles, J. R., Braiterman, L.T., & Hubbard, A. L. 1985. Endogenous and exogenous domain markers of the rat hepatocyte plasma membrane. *J Cell Biol*, **100**(4), 1126–1138.

[Bates *et al.*, 2000] Bates, R.C., Edwards, N.S., & Yates, J.D. 2000. Spheroids and cell survival. *Crit. Rev. Oncol./Hematol.*, **36**, 61–74.

[Baxes, 1994] Baxes, G.A. 1994. *Digital Image Processing. Principles & Applications*. Wiley & Sons.

[Bell *et al.*, 2004] Bell, M.A., Aguirre, W.E., & Buck, N.J. 2004. Twelve years of contemporary armor evolution in a threespine stickleback population. *Evolution*, **58**, 814–824.

[Bennett *et al.*, 2005] Bennett, S., McRobb, S., & Farmer, R. 2005. *Object-oriented Systems Analysis and Design Using UML*. McGraw Hill Higher Education (3rd edition).

[Benoit *et al.*, 2000] Benoit, M., Gabriel, D., Gerisch, G., & Gaub, H.E. 2000. Discrete interactions in cell adhesion measured by single-molecule force spectroscopy. *Nature Cell Biol.*, **2**, 313–317.

[Bergers & Benjamin, 2003] Bergers, Gabriele, & Benjamin, Laura E. 2003. Tumorigenesis and the angiogenic switch. *Nat Rev Cancer*, **3**(6), 401–410.

[Beysens *et al.*, 2000] Beysens, D., Forgacs, G., & Glazier, J.A. 2000. Cell sorting is analogous to phase ordering in fluids. *Proc. Natl. Acad. Sci. USA*, **97**(17), 9467 – 9471.

[Bischofs & Schwarz, 2005] Bischofs, I.B., & Schwarz, U.S. 2005. Effect of Poisson Ratio on Cellular Structure Formation. *Phys. Rev. Lett.*, **95**, 068102–1 – 068102–4.

[Blindenbacher *et al.*, 2003] Blindenbacher, Alex, Wang, Xueya, Langer, Igor, Savino, Rocco, Terracciano, Luigi, & Heim, Markus H. 2003. Interleukin 6 is important for survival after partial hepatectomy in mice. *Hepatology*, **38**(3), 674–682.

[Bliss, 2007] Bliss, N. 2007. Addressing the Multicore Trend with Automatic Parallelization. *Lincoln Laboratory Journal*, **17**(1), 187–198.

[Block *et al.*, 2007] Block, M., Schoell, E., & Drasdo, D. 2007. Classifying the growth kinetics and surface dynamics in growing cell populations. *Phys. Rev. Lett*, **99**, 248101 – 248104.

[Blomquist *et al.*, 1993] Blomquist, E., Brunk, U., & Macieira-Coelho, A. 1993. The influence of cell co-operation, nutrients and surface area on cell division. *Cell Prolif*, **26**(1), 37–43.

[Bondi *et al.*, 1982] Bondi, A., Chieregatti, G., Eusebi, V., Fulcheri, E., & Bussolati, G. 1982. The use of beta-galactosidase as a tracer in immunocytochemistry. *Histochemistry*, **76**(2), 153–158.

[Booch, 1991] Booch, G. 1991. *Object-Oriented Design with Applications*. Redwood City California: Benjamin/Cummings.

[Boucher *et al.*, 1990] Boucher, Y., Baxter, L.T., & Jain, R.K. 1990. Interstitial pressure gradients in tissue-isolated and subcutaneous tumors: implications for therapy. *Cancer Res.*, **50**, 4478–4484.

[Boucher *et al.*, 1997] Boucher, Y., Salehi, J., Witwer, B., & Jain, R.K. 1997. Interstitial fluid pressure in intracranial tumors in patients and in rodents. *Br. J. Cancer*, **75**, 829–836.

[Bradley, 1932] Bradley, R.S. 1932. The cohesive force between solid surfaces and the surface energy of solids. *Phil. Mag.*, **13**, 853–862.

[Bredel-Geissler *et al.*, 1992] Bredel-Geissler, A., Karbach, U., Walenta, S., Vollrath, L., & Mueller-Klieser, W. 1992. Proliferation-associated oxygen consumption and morphology of tumor cells in monolayer and spheroid culture. *J Cell Physiol*, **153**(1), 44–52.

[Bresenham, 1996] Bresenham, J. 1996. Pixel-processing fundamentals. **16**(1), 74–82.

[Brown & Mcdermid, 2007] Brown, Alan, & Mcdermid, John. 2007. *The Art and Science of Software Architecture*.

[Bru, 2004] Bru, A. 2004. Private communication.

[Bru, 2006] Bru, A. 2006. Private communication.

[Bru *et al.*, 1998] Bru, A., Pastor, J. M ., Fernaud, I., Bru, I., MAelle, S., & Berenguer., C. 1998. Super-rough dynamics on tumour growth. *Phys. Rev. Lett.*, **81**, 4008–4011.

[Bru *et al.*, 2003] Bru, A., Albertos, S., Subiza, J. L., Garcia-Asensio, J. Lopez, & Bru., I. 2003. The universal dynamics of tumour growth. *Biophys. Jour.*, **85**, 2948–2961.

[Brulport *et al.*, 2007] Brulport, Marc, Schormann, Wiebke, Bauer, Alexander, Hermes, Matthias, Elsner, Carolin, Hammersen, Friedrich Jakob, Beerheide, Walter, Spitkovsky, Dimitry, Härtig, Wolfgang, Nussler, Andreas, Horn, Lars Christian, Edelmann, Jeanett, Pelz-Ackermann, Oliver, Petersen, Jörg, Kamprad, Manja, von Mach, Marc, Lupp, Amelie, Zulewski, Henryk, & Hengstler, Jan G. 2007. Fate of extrahepatic human stem and precursor cells after transplantation into mouse livers. *Hepatology*, **46**(3), 861–870.

[Burrige, 1986] Burrige, K. 1986. Substrate adhesions in normal and transformed fibroblasts: Organization and regulation of cytoskeletal, membrane and extracellular matrix components at focal contacts. *Cancer Rev.*, **4**, 18–78.

[Burt *et al.*, 2006] Burt, A.D., Portmann, B.C., & Ferrell, L.D. (eds). 2006. *MacSween's Pathology of the Liver*. Churchill Livingstone (5th edition).

[Burton, 1966] Burton, A. C. 1966. Rate of growth of solid tumours as a problem of diffusion. *Growth*, **30**(2), 157–176.

[Byrne & Drasdo, 2009] Byrne, H., & Drasdo, D. 2009. Individual-based and continuum models of growing cell populations: A comparison. *J Math Biol*, **58**(4-5), 657–87.

[Byrne & Preziosi, 2003] Byrne, H., & Preziosi, L. 2003. Modelling solid tumour growth using the theory of mixtures. *Mathem. Medicine and Biology*, **20**, 341 – 366.

[Byrne *et al.*, 2001] Byrne, H.M., King, J.R., McElwain, D.L.S., & Preziosi, L. 2001. A two-phase model of solid tumor growth. *Appl. Math. Lett.*, 1–15.

[Capretz, 2003] Capretz, L. 2003. A brief history of the object-oriented approach. *SIGSOFT Softw. Eng. Notes*, **28**(2), 6.

[Cardelli & Wegner, 1985] Cardelli, L., & Wegner, P. 1985. On Understanding Types, Data Abstraction, and Polymorphism. *ACM Computing Surveys*, **17**(4), 471–522.

[Carlsson & Yuhas, 1984] Carlsson, J., & Yuhas, J. M. 1984. Liquid-overlay culture of cellular spheroids. *Recent Results Cancer Res*, **95**, 1–23.

[Carmo *et al.*, 2004] Carmo, Helena, Hengstler, Jan G, de Boer, Douwe, Ringel, Michael, Carvalho, Félix, Fernandes, Eduarda, Remião, Fernando, dos Reys, Lesseps A, Oesch, Franz, & de Lourdes Bastos, Maria. 2004. Comparative metabolism of the designer drug 4-methylthioamphetamine by hepatocytes from

man, monkey, dog, rabbit, rat and mouse. *Naunyn Schmiedebergs Arch Pharmacol*, **369**(2), 198–205.

[Carpick *et al.*, 1999] Carpick, R.W., Ogletree, D. F., & Salmeron, M. 1999. A Gerneral Equation for Fitting Contact Area and Friction vs Load Measurements. *J. Colloid and Interface Sci*, **211**, 395–400.

[Casciari *et al.*, 1988] Casciari, J.J., Sotirchos, S.V., & Sutherland, R.M. 1988. Glucose Diffusivity in Multicellular Tumor Spheroids. *Cancer Res.*, **48**, 3905 – 3909.

[Casciari *et al.*, 1992] Casciari, J.J., Sotirchos, S.V., & Sutherland, R.M. 1992. Variations in Tumor Cell Growth Rates and Metabolism with Oxygen Concentration, Glucose Concentration, and Extracellular pH. *J. Cell. Physiol.*, **151**, 386–394.

[Castell & Gómez-Lechón, 2009] Castell, José V, & Gómez-Lechón, María José. 2009. Liver cell culture techniques. *Methods Mol Biol*, **481**, 35–46.

[Chaplain, 1996] Chaplain, M.A.J. 1996. Avascular Growth, Angiogenesis and Vascular Growth in Solid Tumours: The Mathematical Modelling of the Stages of Tumour Development. *Mathl. Comput. Modelling*, **23**(6), 47–87.

[Chapman *et al.*, 2007] Chapman, B., Jost, G., van der Pas, R., & Kuck, D.J. 2007. *Using OpenMP: Portable Shared Memory Parallel Programming.* The MIT Press.

[Chen *et al.*, 1997] Chen, C.S., Mrksich, M., Huang, S., Whitesides, G.M., & Ingber, D.E. 1997. Geometric Control of Cell Life and Death. *Science*, **276**, 1425–1428.

[Chen *et al.*, 2001] Chen, C.Y., Byrne, H.M., & King, J.R. 2001. The influence of growth-induced stress from the surrounding medium on the development of multicell spheroids. *J. Math. Biol.*, **43**, 191–220.

[Cheng *et al.*, 2009] Cheng, Gang, Tse, Janet, Jain, Rakesh K, & Munn, Lance L. 2009. Micro-environmental mechanical stress controls tumor spheroid size and morphology by suppressing proliferation and inducing apoptosis in cancer cells. *PLoS One*, **4**(2), e4632.

[Chesla *et al.*, 1998] Chesla, S.E., Selvaraj, P., & Zhu, C. 1998. Measuring two-dimensional receptor-ligand binding kinetics by micropipette. *Biophys. J.*, **75**, 1553–1557.

[Chisari *et al.*, 2001] Chisari, F.V., Fausto, N., & Schachter, D. 2001. *The Liver: Biology and Pathobiology*. Lippincott Williams & Wilkins (4th edition).

[Christini *et al.*, 2009] Christini, V., Li, X., Lowengrub, J.S., & S.M.Wise. 2009. Nonlinear simulations of solid tumor growth using a mixture model: invasion and branching. *Math. Biol.*, **58**, 723–763.

[Chu *et al.*, 2005] Chu, Yeh-Shiu, Dufour, Sylvie, Thiery, Jean Paul, Perez, Eric, & Pincet, Frederic. 2005. Johnson-Kendall-Roberts theory applied to living cells. *Phys Rev Lett*, **94**(2), 028102.

[Cickovski *et al.*, 2005] Cickovski, T.C., Huang, C., Chaturvedi, R., Glimm, T., Hentschel, H.G.E., Alber, M., Glazier, J. A., Newman, S. A., & Izaguirre, J. A. 2005. A Framework for Three-Dimensional Simulation of Morphogenesis. *IEEE/ACM TCBB*, **2**(3), 273–288.

[Claxton *et al.*, 2008] Claxton, N.S., Fellers, T.J., & Davidson, M.W. 2008. Laser scanning confocal microscopy. *Published online: www.olympusconfocal.com/theory/LSCMIntro.pdf*.

[Clendenon *et al.*, 2006] Clendenon, J.L., Byars, J.M., & Hyink, D.P. 2006. Image processing software for 3D Light Microscopy. *Nephron Exp Nephrol*, **103**(2), 50–54.

[Constien *et al.*, 2001] Constien, R., Forde, A., Liliensiek, B., Gröne, H. J., Nawroth, P., Hämmerling, G., & Arnold, B. 2001. Characterization of a novel EGFP reporter mouse to monitor Cre recombination as demonstrated by a Tie2 Cre mouse line. *Genesis*, **30**(1), 36–44.

[Cook, 1984] Cook, Robert. 1984. Distributed ray tracing. *ACM SIGGRAPH Computer Graphics*, **18**(3), 137–145.

[Couinaud, 1954] Couinaud, C. 1954. Lobes et segments hepatiques: notes sur l'architecture anatomique et chirurgicale de foie. *Presse Med.*, **62**, 709–712.

[Courant & Lewy, 1967] Courant, R.; Friedrichs, K.;, & Lewy, H. 1967. On the Partial Difference Equations of Mathematical Physics. *IBM J.*, **11**, 215–234.

[Court *et al.*, 2002] Court, F. G., Wemyss-Holden, S. A., Dennison, A. R., & Maddern, G. J. 2002. The mystery of liver regeneration. *Br J Surg*, **89**(9), 1089–1095.

[Crespi & Summers, 2005] Crespi, Bernard, & Summers, Kyle. 2005. Evolutionary biology of cancer. *Trends Ecol Evol*, **20**(10), 545–552.

[Crow, 1977] Crow, F.C. 1977. Shadow Algorithms for Computer Graphics. *Computer Graphics (SIGGRAPH '77 Proceedings)*, **11**(2), 242–248.

[Cunningham & Horn, 2003] Cunningham, C.C., & Horn, C.G. Van. 2003. Energy availability and alcohol-related liver pathology. *Alcohol Res Health*, **27**(4), 291–299.

[da Costa, 2001] da Costa, L. F. 2001. Return of de-differentiation: why cancer is a developmental disease. *Curr Opin Oncol*, **13**(1), 58–62.

[Dahl, 1968] Dahl, O.J. 1968. *SIMULA 67 common base language*. Norwegian Computing Center Publications.

[Davidson *et al.*, 1995] Davidson, L.A., Koehl, M.A.R., Keller, R., & Oster, G.F. 1995. How do sea urchins invaginate? Using bio-mechanics to distinguish between mechanisms of primary invagination. *Development*, **121**, 2005–2018.

[de Freitas *et al.*, 2006] de Freitas, P. Scandiucci, Wirz, D., Stolz, M., Göpfert, B., Friederich, N-F., & Daniels, A. U. 2006. Pulsatile dynamic stiffness of cartilage-like materials and use of agarose gels to validate mechanical methods and models. *J Biomed Mater Res B Appl Biomater*, **78**(2), 347–357.

[Depreter *et al.*, 2002] Depreter, Marianne, Walker, Tracy, Smet, Karen De, Beken, Sonja, Kerckaert, Ingrid, Rogiers, Vera, & Roels, Frank. 2002. Hepatocyte polarity and the peroxisomal compartment: a comparative study. *Histochem J*, **34**(3-4), 139–151.

[Derjaguin, 1934] Derjaguin, B. V. 1934. Untersuchungen über die Reibung und Adhäsion. *Kolloid Z.*, **69**, 155–164.

[Deutsch *et al.*, 2008] Deutsch, Urban, Schlaeger, Thorsten M, Dehouck, Bénédicte, Döring, Axinia, Tauber, Silke, Risau, Werner, & Engelhardt, Britta. 2008. Inducible endothelial cell-specific gene expression in transgenic mouse embryos and adult mice. *Exp Cell Res*, **314**(6), 1202–1216.

[Diehl & Rai, 1996] Diehl, A. M., & Rai, R. 1996. Review: regulation of liver regeneration by pro-inflammatory cytokines. *J Gastroenterol Hepatol*, **11**(5), 466–470.

[Dormann & Deutsch, 2002] Dormann, S., & Deutsch, A. 2002. Modeling of self-organized avascular tumor growth with a hybrid cellular automaton. *In Silico Biol.*, **2**, 0035.

[Drasdo *et al.*, 1995] Drasdo, Kree, & McCaskill. 1995. Monte Carlo approach to tissue-cell populations. *Phys. Rev. E*, **52**(6), 6635–6657.

[Drasdo, 2000] Drasdo, D. 2000. Buckling Instabilities in one-layered growing tissues. *Phys. Rev. Lett.*, **84**(18), 4244–4247.

[Drasdo, 2003] Drasdo, D. 2003. On selected individual-based approaches to the dynamics in multicellular systems. *Pages 169 – 203 of:* Alt, W., Chaplain, M., Griebel, M., & Lenz, J. (eds), *Multiscale Modelling and Numerical Simulations*. Birkhäuser.

[Drasdo, 2005] Drasdo, D. 2005. Coarse graining in simulated cell populations. *Adv. Complex Syst.*, **8**(2-3), 319–363.

[Drasdo & Hoehme, 2003] Drasdo, D., & Hoehme, S. 2003. Individual-based Approaches to Birth and Death in Avascular Tumors. *Math. and Comp. Modelling*, **37**, 1163 – 1175.

[Drasdo & Kruspe, 2005] Drasdo, D., & Kruspe, M. 2005. Emergence of cell migration and aggregation strategies in a simulated evolutionary process. *Adv. Complex Syst.*, **8**(2 & 3).

[Drasdo & Löffler, 2001] Drasdo, D., & Löffler, M. 2001. Individual-based models on growth and folding in one-layered tissues: Intestinal Crypts and Blastulation. *Nonl. Anal.*, **47**, 245–256.

[Drasdo *et al.*, 2007] Drasdo, D., Hoehme, S., & Block, M. 2007. On the role of physics in the growth and pattern formation of multi-cellular systems: What can we learn from individual-cell based models? *J. Stat. Phys*, **128**, 287–345.

[Drasdo & Hoehme, 2005] Drasdo, Dirk, & Hoehme, Stefan. 2005. A single-cell-based model of tumor growth in vitro: monolayers and spheroids. *Phys Biol*, **2**(3), 133–147.

[Drebin *et al.*, 1988] Drebin, R.A., Carpenter, L., & Hanrahan, P. 1988. Volume Rendering. *SIGGRAPH88 Computer Graphics*.

[Drubin & Nelson, 1996] Drubin, D.G., & Nelson, W.J. 1996. Origins of Cell Polarity. *Cell*, **84**, 335–344.

[Dubuc *et al.*, 1989] Dubuc, Quiniou, Roques-Carmes, Tricot, & Zucker. 1989. Evaluating the fractal dimension of profiles. *Phys Rev A*, **39**(3), 1500–1512.

[Eagle, 1955] Eagle, H. 1955. Nutrition needs of mammalian cells in tissue culture. *Science*, **122**(3168), 501–514.

[Eckel, 2003] Eckel, B. 2003. *Thinking in C++: Practical Programming*. Prentice Hall.

[Eden, 1961] Eden, M. 1961. A two-dimensional growth process. *Pages 223–239 of:* Neyman, J. (ed), *Proc. of the 4th. Berkeley Symposium on Mathematics and Probability*. University of California Press.

[Elias & Sherrick, 1969] Elias, H., & Sherrick, J.C. 1969. *Morphology of the liver*. New York: Academic Press.

[Emonet *et al.*, 2005] Emonet, Thierry, Macal, Charles M, North, Michael J, Wickersham, Charles E, & Cluzel, Philippe. 2005. AgentCell: a digital single-cell assay for bacterial chemotaxis. *Bioinformatics*, **21**(11), 2714–2721.

[Engel *et al.*, 2001] Engel, K., Kraus, M., & Ertl, T. 2001. High-quality pre-integrated volume rendering using hardwareaccelerated pixel shading shading. *Workshop on Graphics Hardware,*.

[Engel *et al.*, 2006] Engel, K., Hadwiger, M., Kniss, J., & Rezk-Salama, C. 2006. *Real-Time Volume Graphics*. A K Peters, Wellesley.

[Enmon *et al.*, 2001] Enmon, R. M., O'Connor, K. C., Lacks, D. J., Schwartz, D. K., & Dotson, R. S. 2001. Dynamics of spheroid self-assembly in liquid-overlay culture of DU 145 human prostate cancer cells. *Biotechnol Bioeng*, **72**(6), 579–591.

[Epstein & Axtell, 1996] Epstein, J.M., & Axtell, R. 1996. Growing Artificial Societies: Social Science from the Bottom Up. *MIT Press Cambridge, MA*.

[Epstein, 2002] Epstein, Joshua M. 2002. Modeling civil violence: an agent-based computational approach. *Proc Natl Acad Sci USA*, **99**(3), 7243–7250.

[Everitt & Kilgard, 2002] Everitt, C., & Kilgard, M.J. 2002. Practical and Robust Stenciled Shadow Volumes for Hardware-Accelerated Rendering. *NVIDIA Corporation*.

[Fan *et al.*, 2002] Fan, Ye-Dong, Praet, Marleen, Huysse, Jacques Van, Lelie, Bart, & Hemptinne, Bernard De. 2002. Effects of portal vein arterialization on liver regeneration after partial hepatectomy in the rat. *Liver Transpl*, **8**(2), 146–152.

[Fausto, 2000]Fausto, N. 2000. Liver regeneration. *J Hepatol*, **32**(1), 19–31.

[Fausto & Campbell, 2003] Fausto, Nelson, & Campbell, Jean S. 2003. The role of hepatocytes and oval cells in liver regeneration and repopulation. *Mech Dev*, **120**(1), 117–130.

[Fedoroff, 1971] Fedoroff, S. 1971. George Otto Gey. 1899-1970. *Anat Rec*, **171**(1), 127–128.

[Feinstein-Rotkopf & Arama, 2009] Feinstein-Rotkopf, Yael, & Arama, Eli. 2009. Can't live without them, can live with them: roles of caspases during vital cellular processes. *Apoptosis*.

[Fellers & Davidson, 2007] Fellers, T.J., & Davidson, M.W. 2007. *Introduction to Confocal Microscopy*. Olympus Fluoview Resource Center.

[Feng *et al.*, 1996] Feng, Jie, Lin, Wei-Chung, & Chen, Chin-Tu. 1996. Fractional box-counting approach to fractal dimension estimation. *Proceedings of the 13th International Conference on Pattern Recognition*, **2**, 854–858.

[Fidorra *et al.*, 1981] Fidorra, J., Mielke, Th., Booz, J., & Feinendegen, L.E. 1981. Cellular and Nuclear Volume of Human Cells During Cell Cycle. *Radiat. Environ. Biophys.*, **19**, 205 – 214.

[Fisher & Henzinger, 2007] Fisher, Jasmin, & Henzinger, Thomas A. 2007. Executable cell biology. *Nat Biotechnol*, **25**(11), 1239–1249.

[Folkman & Hochberg, 1973] Folkman, J., & Hochberg, M. 1973. Self-regulation of growth in three dimensions. *J. Exp. Med.*, **138**, 745–753.

[Forgacs & Newman, 2005] Forgacs, G., & Newman, S.A. 2005. *Biological Physics of the Developing Embryo*. Cambridge: Cambridge University Press.

[Frazer, 1983] Frazer, R. M. 1983. *The Poems of Hesiod*. Norman: University of Oklahoma Press.

[Freyer & Sutherland, 1985] Freyer, J.P., & Sutherland, R.M. 1985. A Reduction in the In Situ Rates of Oxygen and Glucose Consumption of Cells in EMT6 Ro Spheroids During Growth. *J. Cell. Physiol.*, **124**, 516–524.

[Freyer & Sutherland, 1986] Freyer, J.P., & Sutherland, R.M. 1986. Regulation of Growth Saturation and Development of Necrosis in EMT6 Ro Multicellular Spheroids by the Glucose and Oxygen Supply. *Cancer Res.*, **46**, 3504–3512.

[Frieboes *et al.*, 2006] Frieboes, Hermann B, Zheng, Xiaoming, Sun, Chung-Ho, Tromberg, Bruce, Gatenby, Robert, & Cristini, Vittorio. 2006. An integrated computational/experimental model of tumor invasion. *Cancer Res*, **66**(3), 1597–1604.

[Frixione, 2000] Frixione, E. 2000. Recurring views on the structure and function of the cytoskeleton: a 300-year epic. *Cell Motil Cytoskeleton*, **46**(2), 73–94.

[Galle *et al.*, 2003] Galle, J., Loeffler, M., & Drasdo, D. 2003. On the temporal-spatial organization of epithelial cell populations in-vitro. *Pages 375 – 385 of:* Capasso, V. (ed), *Mathematical Modelling and Computing in Biology and Medicine*. Marcel Dekker Inc.

[Galle *et al.*, 2005] Galle, J., Loeffler, M., & Drasdo, D. 2005. Modelling the effect of deregulated proliferation and apoptosis on the growth dynamics of epithelial cell populations in vitro. *Biophys. J.*, **88**, 62–75.

[Galle *et al.*, 2006] Galle, J., Aust, G., Schaller, G., Beyer, T., & Drasdo, D. 2006. Single-cell based mathematical models to the spatio-temporal pattern formation in multi-cellular systems. *Cytometry Teil A*, 704–710.

[Galle *et al.*, 2009] Galle, J., Hoffmann, M., & Aust, G. 2009. From single cells to tissue architecture-a bottom-up approach to modelling the spatio-temporal organisation of complex multi-cellular systems. *J Math Biol*, **58**(1-2), 261–283.

[Gartner *et al.*, 1992] Gartner, M. F., Fearns, C., Wilson, E. L., Campbell, J. A., & Dowdle, E. B. 1992. Unusual growth characteristics of human melanoma xenografts

in the nude mouse: a model for desmoplasia, dormancy and progression. *Br J Cancer*, **65**(4), 487–490.

[Gebhardt & Burger, 1987] Gebhardt, R., & Burger, H. J. 1987. Selective loss of hormonal induction of glutamate transport in primary cultures of hepatocytes from rats treated with CCl4. *J Hepatol*, **4**(3), 381–389.

[Gieni & Hendzel, 2008] Gieni, Randall S, & Hendzel, Michael J. 2008. Mechanotransduction from the ECM to the genome: are the pieces now in place? *J Cell Biochem*, **104**(6), 1964–1987.

[Gillespy, 1998] Gillespy, T. 1998. Optimized algorithm for adaptive histogram equalization. *Medical Imaging*.

[Glazier & Graner, 1993] Glazier, J., & Graner, F. 1993. Simulation of the differential adhesion driven rearrangement of biological cells. *Phys. Rev. E*, **47**(3), 2128–2154.

[Gloushankova *et al.*, 1997] Gloushankova, N.A., Alieva, N.A., Krendel, M.F., Bonder, E.M., Feder, H.H., Vasiliev, J.M., & Gelfand, I.M. 1997. Cell-cell contact changes the dynamics of lamellar activity in nontransformed epitheliocytes but not in their ras-transformed descendants. *Proc. Natl. Acad. Sci. USA*, **94**, 879–883.

[Gómez *et al.*, 2006] Gómez, Maria I Diaz, Fanelli, Silvia L, de Layño, Aurora M A Delgado, Castro, José A, & Castro, Gerardo D. 2006. Liver nuclear and microsomal CYP2E1-mediated metabolism of xenobiotics in rats chronically drinking an alcohol-containing liquid diet. *Toxicol Ind Health*, **22**(9), 367–374.

[Godoy *et al.*, 2009] Godoy, Patricio, Hengstler, Jan G, Ilkavets, Iryna, Meyer, Christoph, Bachmann, Anastasia, Müller, Alexandra, Tuschl, Gregor, Mueller, Stefan O, & Dooley, Steven. 2009. Extracellular matrix modulates sensitivity of hepatocytes to fibroblastoid dedifferentiation and transforming growth factor beta-induced apoptosis. *Hepatology*, **49**(6), 2031–2043.

[Gonzalez & Woods, 2007] Gonzalez, R.C., & Woods, R.E. 2007. *Digital Image Processing*. Prentice Hall (3rd edition).

[Gordon *et al.*, 2003] Gordon, V. D., Valentine, M. T., Gardel, M. L., Andor-Ardó, D., Dennison, S., Bogdanov, A. A., Weitz, D. A., & Deisboeck, T. S. 2003. Measuring the mechanical stress induced by an expanding multicellular tumor system: a case study. *Exp Cell Res*, **289**(1), 58–66.

[Graham, 1962] Graham, R.E. 1962. Snow Removal: A Noise Stripping Process for Picture Signals. *IRE Trans. Information Theory*, **8**(1), 129–144.

[Graner & J.Glazier, 1992] Graner, F., & J.Glazier. 1992. Simulation of Biological Cell Sorting Using a Two- Dimensional Extended Potts Model. *Phys. Rev. Lett.*, **69**(13), 2013–2016.

[Gray, 1998] Gray, H. 1998. *Gray's Anatomy: The Anatomical Basis of Medicine and Surgery*. Churchill-Livingstone.

[Greaves, 2000] Greaves, M. 2000. *Cancer: The Evolutionary Legacy*. Oxford University Press.

[Greenspan, 1976] Greenspan, H. P. 1976. On the growth and stability of cell cultures and solid tumors. *J Theor Biol*, **56**(1), 229–242.

[Griffin, 2006] Griffin, W.A. 2006. Agent-Based Modeling for the Theoretical Biologist. *Biological Theory*, **1**, 404–409.

[Guck *et al.*, 2001] Guck, J., Ananthakrishnan, R., Mahmood, H., Moon, T., Cunningham, C.C., & Käs, J. 2001. The Optical Stretcher: A Novel Laser Tool to Micromanipulate Cells. *Biophys. J.*, **81**, 767–784.

[Guiot *et al.*, 2007] Guiot, C., Delsanto, P., & Deisboeck, T. 2007. Morphological instability and cancer invasion: a 'splashing water drop' analogy. *Theoretical Biology and Medical Modelling*, **4**(4).

[Gutmann *et al.*, 1992] Gutmann, R., Leunig, M., Feyh, J., Goetz, A.E., Messmer, K., & Kastenbauer, E. 1992. Interstitial hypertension in head and neck tumors in patients: correlation with tumor size. *Cancer Res.*, **52**, 1993–1995.

[Halpern *et al.*, 1966] Halpern, B., Pejsachowicz, B., Febvre, H. L., & Barski, G. 1966. Differences in patterns of aggregation of malignant and non-malignant mammalian cells. *Nature*, **209**(5019), 157–159.

[Ham, 1965] Ham, R.G. 1965. Clonal Growth of Mammalian Cells in a Chemically Defined, Synthetic Medium. *Proc. Natl. Acad. Sci.*, **53**, 288 – 293.

[Hanahan & Folkman, 1996] Hanahan, D., & Folkman, J. 1996. Patterns and emerging mechanisms of the angiogenic switch during tumorigenesis. *Cell*, **86**(3), 353–64.

[Hanahan & Weinberg, 2000] Hanahan, D., & Weinberg, R. A. 2000. The hallmarks of cancer. *Cell*, **100**(1), 57–70.

[Haralick & Shapiro, 1992] Haralick, R.M., & Shapiro, L.G. 1992. *Computer and Robot Vision*. Addison-Wesley.

[Hartwell *et al.*, 1999] Hartwell, L. H., Hopfield, J. J., Leibler, S., & Murray, A. W. 1999. From molecular to modular cell biology. *Nature*, **402**(6761), C47–C52.

[Hayashi & Sato, 1976] Hayashi, I., & Sato, G. H. 1976. Replacement of serum by hormones permits growth of cells in a defined medium. *Nature*, **259**(5539), 132–134.

[Hedlund *et al.*, 1999] Hedlund, T. E., Duke, R. C., & Miller, G. J. 1999. Three-dimensional spheroid cultures of human prostate cancer cell lines. *Prostate*, **41**(3), 154–165.

[Helling, 2006] Helling, Thomas S. 2006. Liver failure following partial hepatectomy. *HPB (Oxford)*, **8**(3), 165–174.

[Helmlinger *et al.*, 1997] Helmlinger, G., Netti, P.A., Lichtenfeld, H.C., Melder, R.J., & Jain, R.K. 1997. Solid stress inhibits the growth of multicellular tumor spheroids. *Nat Biotech*, **15**(8), 778–783.

[Hendry & Kinnison, 1999] Hendry, A.P., & Kinnison, M.T. 1999. The pace of modern life: measuring rates of contemporary microevolution. *Evolution*, **53**, 1637–1653.

[Hengstler, 2008] Hengstler, Jan. 2008. Private communication.

[Hengstler *et al.*, 2005] Hengstler, Jan G, Brulport, Marc, Schormann, Wiebke, Bauer, Alexander, Hermes, Matthias, Nussler, Andreas K, Fandrich, Fred, Ruhnke, Maren, Ungefroren, Hendrik, Griffin, Louise, Bockamp, Ernesto, Oesch, Franz, & von Mach, Marc-Alexander. 2005. Generation of human hepatocytes by stem cell technology: definition of the hepatocyte. *Expert Opin Drug Metab Toxicol*, **1**(1), 61–74.

[Hengstler, 2007] Hengstler, J.G. 2007. (unpublished).

[Hertz, 1882] Hertz, H. 1882. Über die Berührung fester elastischer Körper (On the contact of elastic solids). *J. Reine Angewandte Math.*, **92**, 156–171.

[Hesiod, 700 BCE] Hesiod. 700 BCE. Theogony. Lines 507–616. http://www.sacred-texts.com/cla/hesiod/theogony.htm.

[Hoehme, 2007] Hoehme, S. 2007. (unpublished). Image taken using a bright field microscope. 31 individual images were registered to create a comprehensive view of the cell population.

[Hoehme & Drasdo, 2009a] Hoehme, S., & Drasdo, D. 2009a. Biomechanical versus nutrient control: what determines the growth dynamics of mammalian cell populations ? *Mathematical Population Studies.*

[Hoehme & Drasdo, 2009b] Hoehme, S., & Drasdo, D. 2009b. Simulating growing multi-cellular aggregates in tissue-like environments by agent-based single-cell models. *(unpublished)*.

[Hoehme *et al.*, 2007] Hoehme, S., Hengstler, J.G., Brulport, M., Schäfer, M., Bauer, A., Gebhardt, R., & Drasdo, D. 2007. Mathematical modelling of liver regeneration after intoxication with CCl4. *Chem Biol Interact*, **168**(1), 74–93.

[Hoehme *et al.*, 2008] Hoehme, S., Hengstler, J.G., Brulport, M., Bauer, A., & Drasdo, D. 2008. Towards modeling liver lobule regeneration in 3D. *Computational Systems Biology Conference 2008 Proceedings*.

[Hoehme *et al.*, 2009] Hoehme, Stefan, Brulport, Marc, Bauer, Alexander, Bedawy, Essam, Schormann, Wiebke, Gebhardt, Rolf, Zellmer, Sebastian, Schwarz, Michael, Bockamp, Ernesto, Timmel, Tobias, Hengstler, Jan G., & Drasdo, Dirk. 2009. Order principles to restore tissue architecture during liver regeneration: from experiment to virtual tissues and back. *(submitted)*.

[Hogeweg, 2000] Hogeweg, P. 2000. Evolving Mechanisms of Morphogenesis: on the Interplay between Differential Adhesion and Cell Differentiation. *J. Theor. Biol.*, **203**, 317–333.

[Holtfreter, 1944] Holtfreter, J. 1944. A study of the mechanics of gastrulation. *J Exp Zool*, **95**, 171–212.

[Hooke, 1665] Hooke, Robert. 1665. *Micrographia: or, Some physiological descriptions of minute bodies made by magnifying glasses*. London: J. Martyn and J. Allestry.

[Horb & Slack, 2000] Horb, L. D., & Slack, J. M. 2000. Role of cell division in branching morphogenesis and differentiation of the embryonic pancreas. *Int. J. Dev. Biol.*, **44**, 791– 796.

[Horwitz & Parsons, 1999] Horwitz, A. R., & Parsons, J. T. 1999. Cell migration–movin' on. *Science*, **286**(5442), 1102–1103.

[Horwitz & Webb, 2003] Horwitz, Rick, & Webb, Donna. 2003. Cell migration. *Curr Biol*, **13**(19), R756–R759.

[Huang & Ingber, 1999] Huang, S., & Ingber, D.E. 1999. The structural and mechanical complexity of cell-growth control. *Nature Cell Biol.*, **1**, E131–E138.

[Hui & Bhatia, 2007] Hui, Elliot E, & Bhatia, Sangeeta N. 2007. Micromechanical control of cell-cell interactions. *Proc Natl Acad Sci*, **104**(14), 5722–5726.

[Indovina *et al.*, 2006] Indovina, Paola, Ferrante, Antonella, Rainaldi, Gabriella, & Santini, Maria Teresa. 2006. Hypoxia and ionizing radiation: changes in adhesive properties and cell adhesion molecule expression in MG-63 three-dimensional tumor spheroids. *Cell Commun Adhes*, **13**(3), 185–198.

[Ingber, 2005] Ingber, D.E. 2005. Mechanical control of tissue growth: function follows form. *Proc. Natl. Acad. Sci. (USA)*, **102**(33), 11571–11572.

[Ingber, 2006] Ingber, D.E. 2006. Mechanical control of tissue morphogenesis during embryological development. *Int J Dev Biol.*, **50**(2 - 3), 255–66.

[Iyer & Saksena, 1970] Iyer, K. S., & Saksena, V. N. 1970. A stochastic model for the growth of cells in cancer. *Biometrics*, **26**(3), 401–410.

[Jennings, 2000] Jennings, R.N. 2000. On agent-based software engineering. *Artificial Intelligence*, **117**, 277–296.

[Jensen, 2001] Jensen, Henrik Wann. 2001. *Realistic Image Synthesis Using Photon Mapping*. AK Peters.

[Jensen & Christensen, 1995] Jensen, Henrik Wann, & Christensen, Niels Jørgen. 1995. Photon Maps in Bidirectional Monte Carlo Ray Tracing of Complex Objects. *Computers and Graphics*, **19**(2), 215–224.

[Jiang *et al.*, 2005] Jiang, Y, Pjesivac-Grbovic, J., Cantrell, C., & Freyer, JP. 2005. A multiscale model for avascular tumor growth. *Biophys. J.*, **89**(6), 3884–94.

[Johansson & Granéli, 1999] Johansson, N., & Granéli, E. 1999. Influence of different nutrient conditions on cell density, chemical composition and toxicity of Prymnesium parvum (Haptophyta) in semi-continuous cultures. *Journal of Experimental Marine Biology and Ecology*, **239**, 243–258.

[Johnson, 1985] Johnson, K.L. 1985. *Contact Mechanics*. Cambridge University Press.

[Johnson *et al.*, 1971] Johnson, K.L., Kendall, K., & Roberts, A.D. 1971. Surface Energy and the Contact of Elastic Solids. *Proc. Roc. Soc. A*, **324**, 301 – 313.

[Jones *et al.*, 2000] Jones, A.F., Byrne, H.M., Gibson, J.S., & Dold, J.W. 2000. A mathematical model of the stress induced during avascular tumour growth. *J. Math. Biol.*, **40**, 473–499.

[Junqueira & Carneiro, 2005] Junqueira, L.C., & Carneiro, J. 2005. *Basic Histology*. McGraw Hill.

[Juskeviciute *et al.*, 2008] Juskeviciute, Egle, Vadigepalli, Rajanikanth, & Hoek, Jan B. 2008. Temporal and functional profile of the transcriptional regulatory network in the early regenerative response to partial hepatectomy in the rat. *BMC Genomics*, **9**, 527.

[Kajiya, 1986] Kajiya, James. 1986. The Rendering Equation. *ACM SIGGRAPH Computer Graphics*, **20**(4), 143–150.

[Kanduc *et al.*, 2002] Kanduc, Darja, Mittelman, Abraham, Serpico, Rosario, Sinigaglia, Eberta, Sinha, Animesh A, Natale, Costanzo, Santacroce, Raffaella, Corcia, M. Grazia Di, Lucchese, Alberta, Dini, Luciana, Pani, Paolo, Santacroce,

Salvatore, Simone, Simone, Bucci, Romano, & Farber, Emanuel. 2002. Cell death: apoptosis versus necrosis (review). *Int J Oncol*, **21**(1), 165–170.

[Kay, 1993] Kay, A. C. 1993. The early history of Smalltalk. *The Second ACM SIGPLAN Conference on History of Programming Languages*, 69–95.

[Kay *et al.*, 1996] Kay, P.A., Robb, R.A., Bostwick, D.G., & Camp, J.J. 1996. *Robust 3-D reconstruction and analysis of microstructures from serial histologic sections, with emphasis on microvessels in prostate cancer*. Springer Berlin / Heidelberg.

[Keen, 1899] Keen, W. 1899. Report of a case of resection of the liver for the removal of a neoplasm, with a table of seventy-six cases of resection of the liver for hepatic tumors. *Ann Surg*, **30**, 267–283.

[Kellendonk *et al.*, 2000] Kellendonk, C., Opherk, C., Anlag, K., Schütz, G., & Tronche, F. 2000. Hepatocyte-specific expression of Cre recombinase. *Genesis*, **26**(2), 151–153.

[Kiernan, 1833] Kiernan, F. 1833. The anatomy and physiology of the liver. *Philos. Trans. R. Soc. Lond*, **123**, 711–770.

[Kilgard, 1996] Kilgard, M.J. 1996. *OpenGL programming for the X Window System*. Addison-Wesley Developers Press.

[Kim *et al.*, 2001] Kim, J.Y., Kim, L.S., & Hwang, S.H. 2001. An Advanced Contrast Enhancement Using Partially Overlapped Sub-Block Histogram Equalization. *IEEE Transactions on Circuits and Systems for Video Technology*, **11**(4), 475–484.

[Kitano, 2002a] Kitano, Hiroaki. 2002a. Computational systems biology. *Nature*, **420**(6912), 206–210.

[Kitano, 2002b] Kitano, Hiroaki. 2002b. Systems biology: a brief overview. *Science*, **295**(5560), 1662–1664.

[Klein, 2005] Klein, R. 2005. *Algorithmische Geometrie*. Springer Verlag.

[Klekotka *et al.*, 2001] Klekotka, P.A., Santoro, S.A., Ho, A., Dowdy, S.F., & Zutter, M.M. 2001. Mammary epithelial cell-cycle progression via the α2β1-integrin. *Am. J. Path*, **159**, 983–992.

[Klingmüller *et al.*, 2006] Klingmüller, U., Bauer, A., Bohl, S., Nickel, P. J., Breitkopf, K., Dooley, S., Zellmer, S., Kern, C., Merfort, I., Sparna, T., Donauer, J., Walz, G., Geyer, M., Kreutz, C., Hermes, M., Götschel, F., Hecht, A., Walter, D., Egger, L., Neubert, K., Borner, C., Brulport, M., Schormann, W., Sauer, C., Baumann, F., Preiss, R., MacNelly, S., Godoy, P., Wiercinska, E., Ciuclan, L., Edelmann, J., Zeilinger, K., Heinrich, M., Zanger, U. M., Gebhardt, R., Maiwald, T.,

Heinrich, R., Timmer, J., von Weizsäcker, F., & Hengstler, J. G. 2006. Primary mouse hepatocytes for systems biology approaches: a standardized in vitro system for modelling of signal transduction pathways. *Syst Biol (Stevenage)*, **153**(6), 433–447.

[Kourtis & Tavernarakis, 2009] Kourtis, N., & Tavernarakis, N. 2009. Autophagy and cell death in model organisms. *Cell Death Differ*, **16**(1), 21–30.

[Krause, 2003] Krause, L.; Lehman, L.; Wheeler A. 2003. A family of agent based models. *Integration of Knowledge Intensive Multi-Agent Systems, International Conference on*, **30**, 312–317.

[Kruger & Westermann, 2003] Kruger, J., & Westermann, R. 2003. Acceleration techniques for GPU-based volume rendering. *IEEE Visualization, 2003*, **24**(24), 287–292.

[Kuntz & Kuntz, 2008] Kuntz, E., & Kuntz, H.D. 2008. *Hepatology Textbook and Atlas: History, Morphology, Biochemistry, Diagnostics, Clinic, Therapy*. Springer, Berlin.

[Kunz-Schughart, 1999] Kunz-Schughart, L. A. 1999. Multicellular tumor spheroids: intermediates between monolayer culture and in vivo tumor. *Cell Biol Int*, **23**(3), 157–161.

[Lachmann *et al.*, 1988] Lachmann, P., Benke, R., Schirrmacher, V., & Schlag, P. 1988. Cell adhesion and migration of different human colon cell lines and primary tumors. *J Cancer Res Clin Oncol*, **114**(5), 493–496.

[Lafdil *et al.*, 2006] Lafdil, Fouad, Chobert, Marie Noële, Couchie, Dominique, Brouillet, Arthur, Zafrani, Elie Serge, Mavier, Philippe, & Laperche, Yannick. 2006. Induction of Gas6 protein in CCl4-induced rat liver injury and anti-apoptotic effect on hepatic stellate cells. *Hepatology*, **44**(1), 228–239.

[Laforsch *et al.*, 2005] Laforsch, C., Ngwa, W., Grill, W., & Tollrian, R. 2005. An acoustic microscopy technique reveals hidden morphological defenses in Daphnia. *Proc. Natl. Acad. Sci. (USA)*, **101**(45), 15911–15914.

[Laird, 1964] Laird, A. K. 1964. Dynamics of tumor growth. *Br J Cancer*, **13**, 490–502.

[Lamers *et al.*, 1989a] Lamers, W. H., Hilberts, A., Furt, E., Smith, J., Jonges, G. N., van Noorden, C. J., Janzen, J. W., Charles, R., & Moorman, A. F. 1989a. Hepatic enzymic zonation: a reevaluation of the concept of the liver acinus. *Hepatology*, **10**(1), 72–76.

[Lamers *et al.*, 1989b] Lamers, W.H., Moorman, A.F.M., & Charles, R. 1989b. *The metabolic lobulus, a key to the architecture of the liver*. Berlin: Springer International.

[Landau, 1975] Landau, D. 1975. *Theory of Elasticity*. Pergamon.

[Lauffenburger & Horwitz, 1996] Lauffenburger, D. A., & Horwitz, A. F. 1996. Cell migration: a physically integrated molecular process. *Cell*, **84**(3), 359–369.

[LeCouter *et al.*, 2003] LeCouter, Jennifer, Moritz, Dirk R, Li, Bing, Phillips, Gail Lewis, Liang, Xiao Huan, Gerber, Hans-Peter, Hillan, Kenneth J, & Ferrara, Napoleone. 2003. Angiogenesis-independent endothelial protection of liver: role of VEGFR-1. *Science*, **299**(5608), 890–893.

[Lee & Rieger, 2006] Lee, D.S., & Rieger, H. 2006. Flow Correlated Percolation during Vascular Remodeling in Growing Tumors. *Phys. Rev. Lett.*, **96**(5), 4.

[Lekka *et al.*, 1999] Lekka, M., Laidler, P., Gil, D., Lekki, J., Stachura, Z., & Hrynkiewicz, A.Z. 1999. Elasticity of normal and cancerous human bladder cells studied by scanning force microscopy. *European Biophysics Journal*, **28**(4), 312–316.

[Levinthal & Ware, 1972] Levinthal, C., & Ware, R. 1972. Three Dimensional Reconstruction from Serial Sections. *Nature*, **236**, 207–210.

[Levoy, 1988] Levoy, Marc. 1988. Display of Surfaces from Volume Data. *IEEE CG&A*.

[Li *et al.*, 2003] Li, Laiji, Backer, Jody, Wong, Annisa S K, Schwanke, Erin L, Stewart, Brian G, & Pasdar, Manijeh. 2003. Bcl-2 expression decreases cadherin-mediated cell-cell adhesion. *J Cell Sci*, **116**(18), 3687–3700.

[Lichtenbelt *et al.*, 1998] Lichtenbelt, Barthold, Crane, Randy, & Naqvi, Shaz. 1998. *Introduction to Volume Rendering*. Hewlett-Packard Professional Books.

[Lippens *et al.*, 2009] Lippens, Saskia, Hoste, Esther, Vandenabeele, Peter, Agostinis, Patrizia, & Declercq, Wim. 2009. Cell death in the skin. *Apoptosis*, **14**(4), 549–569.

[Liu & Layland, 1973] Liu, C., & Layland, J. 1973. Scheduling Algorithms for Multiprogramming in a Hard Real-time Environment. *Journal of the ACM*, **20**(1), 46–61.

[Lodish *et al.*, 2004] Lodish, H., Berk, A., Matsudaria, P., Kaiser, C.A., Krieger, M., Scott, M.P., Zipursky, S.L., & Darnell, J. 2004. *Molecular Cell Biology*. Freeman.

[Lorensen & Cline, 1987] Lorensen, W.E., & Cline, H.E. 1987. Marching Cubes: A high resolution 3D surface construction algorithm. *Computer Graphics*, **21**(4), 163–169.

[Lu *et al.*, 1995] Lu, P.J., Lu, Q.L., Rughetti, A., & Taylor-Papadimitriou, J. 1995. bcl-2 Overexpression Inhibits Cell Death and Promotes the Morphogenesis, but not Tumorigenesis of Human Mammary Epithelial Cells. *J. Cell Biol.*, **129**(5), 1363–1378.

[Lum *et al.*, 2004] Lum, E., Wilson, B., & Ma, K. 2004. High-Quality Lighting and Efficient Pre-Integration for Volume Rendering. *Eurographics/IEEE Symposium on Visualization*.

[Macklin & Lowengrub, 2007] Macklin, Paul, & Lowengrub, John. 2007. Nonlinear simulation of the effect of microenvironment on tumor growth. *J Theor Biol*, **245**(4), 677–704.

[Macleod & Langdon, 2004] Macleod, K. G., & Langdon, S. P. 2004. *Essential Techniques of Cancer Cell Culture*. Vol. 88. Humana Press.

[Madsen & Moller-Pedersen, 1988] Madsen, O.L., & Moller-Pedersen, B. 1988. What Object-Oriented Programming May Be and What It Does Not Have to Be. *Lecture Notes in Computer Science*, **322**, 1–20.

[Mahaffy *et al.*, 2000] Mahaffy, R. E., Shih, C. K., MacKintosh, F. C., & Käs, J. 2000. Scanning probe-based frequency-dependent microrheology of polymer gels and biological cells. *Phys Rev Lett*, **85**(4), 880–883.

[Maher, 1993] Maher, J. J. 1993. Cell-specific expression of hepatocyte growth factor in liver. Upregulation in sinusoidal endothelial cells after carbon tetrachloride. *J Clin Invest*, **91**(5), 2244–2252.

[Maler, 2008] Maler, Oded. 2008. On Computer Science in Systems Biology. http://chess.eecs.berkeley.edu/pubs/479.html.

[Malik *et al.*, 2002] Malik, Raza, Selden, Clare, & Hodgson, Humphrey. 2002. The role of non-parenchymal cells in liver growth. *Semin Cell Dev Biol*, **13**(6), 425–431.

[Mall, 1906] Mall, F.P. 1906. A study of the structural units of the liver. *Am J Anat*, **5**, 227–308.

[Manoussaki, 2006] Manoussaki, E. 2006. Cancer Research Projects funded under FP6. *European Commission EUR 22051*.

[Marcus, 2008] Marcus, F. 2008. *Bioinformatics and Systems Biology: Collaborative Research and Resources, Chapter 8 Cancer.* Springer-Verlag, Heidelberg.

[Martinez-Hernandez & Amenta, 1995] Martinez-Hernandez, A., & Amenta, P. S. 1995. The extracellular matrix in hepatic regeneration. *FASEB J*, **9**(14), 1401–1410.

[Marusic *et al.*, 1994] Marusic, M., Bajzer, Z., Freyer, J.P., & Vuk-Pavlovic, S. 1994. Analysis of growth of multicellular tumor spheroids by mathematical models. *Cell Prolif.*, **27**, 73–94.

[Marx-Stoelting *et al.*, 2008] Marx-Stoelting, Philip, Mahr, Johanna, Knorpp, Thomas, Schreiber, Sandra, Templin, Markus F, Ott, Thomas, Buchmann, Albrecht, & Schwarz, Michael. 2008. Tumor promotion in liver of mice with a conditional Cx26 knockout. *Toxicol Sci*, **103**(2), 260–267.

[Maton *et al.*, 1997] Maton, A., Hopkins, J., Johnson, S., LaHart, D., Quon, W.D., Maryanna, W., & Jill, D. 1997. *Cells Building Blocks of Life*. New Jersey: Prentice Hall.

[Matsumoto *et al.*, 1979] Matsumoto, R., Komori, R., & Magara, T. 1979. A study on the normal structure of human liver, with special reference to its angioarchitecture. *Jikeikai Med J*, **26**, 1–40.

[Matsumoto & Kawakami, 1982] Matsumoto, T., & Kawakami, M. 1982. The unit-concept of hepatic parenchyma–a re-examination based on angioarchitectural studies. *Acta Pathol Jpn*, **32**(2), 285–314.

[Maurice *et al.*, 1994] Maurice, M., Schell, M. J., Lardeux, B., & Hubbard, A. L. 1994. Biosynthesis and intracellular transport of a bile canalicular plasma membrane protein: studies in vivo and in the perfused rat liver. *Hepatology*, **19**(3), 648–655.

[Meineke *et al.*, 2001] Meineke, F.A., Potten, C.S., & Loeffler, M. 2001. Cell migration and organziation in the intestinal crypt using a lattice-free model. *Cell Prolif.*, **34**, 253 – 266.

[Merks & Glazier, 2005] Merks, R.M.H., & Glazier, J.A. 2005. A cell-centered approach to developmental biology. *Physica A*, **352**, 113–130.

[Michalopoulos, 2007] Michalopoulos, G.K. 2007. Liver regeneration. *J Cell Physiol*, **213**(2), 286–300.

[Michalopoulos & DeFrances, 1997] Michalopoulos, G.K., & DeFrances, M. 1997. Liver regeneration. *Science*, **276**(5309), 60–66.

[Michalopoulos & DeFrances, 2005] Michalopoulos, G.K., & DeFrances, M. 2005. Liver regeneration. *Adv Biochem Eng Biotechnol*, **93**, 101–134.

[Mombach & Glazier, 1996] Mombach, J.C., & Glazier, J.A. 1996. Single cell motion in aggregates of embryonic cells. *Phys. Rev. Lett.*, **76**(16), 3032–3035.

[Montani *et al.*, 1994]Montani, C., Scateni, R., & Scopigno, R. 1994. Discretized Marching Cubes. *Visualization '94 Proceedings, IEEE Computer Society Press*, 281–287.

[Moore, 1965]Moore, Gordon E. 1965. Cramming more Components onto Integrated Circuits. *Electronics*, **38**(8).

[Moreira & Deutsch, 2002] Moreira, J., & Deutsch, A. 2002. Cellular automata models of tumour development - a critical review. *Adv. in Complex Syst.*, **5**, 247–267.

[Moscona, 1952] Moscona, A. 1952. Cell suspensions from organ rudiments of chick embryos. *Exp Cell Res*, **3**, 535–539.

[Moy *et al.*, 1994] Moy, V.T., Florin, E.L., & Gaub, H.E. 1994. Intermolecular Forces and Energies between Ligands and Receptors. *Science*, **266**, 257–259.

[Mueller-Klieser, 1997] Mueller-Klieser, W. 1997. Three-dimensional cell cultures: from molecular mechanisms to clinical applications. *Am J Physiol*, **273**(4), C1109–C1123.

[Mueller-Klieser, 2000] Mueller-Klieser, W.J. 2000. Tumor biology and experimental therapeutics. *Critical Reviews in Oncology/Hematology*, **36**, 123–139.

[Nagino *et al.*, 2001] Nagino, M., Kamiya, J., Uesaka, K., Sano, T., Yamamoto, H., Hayakawa, N., Kanai, M., & Nimura, Y. 2001. Complications of hepatectomy for hilar cholangiocarcinoma. *World J Surg*, **25**(10), 1277–1283.

[Nathan, 1970] Nathan, R. 1970. *Spatial Frequency Filtering in Picture Processing and Psychopictorics*. Academic Press, New York.

[Neagu *et al.*, 2005] Neagu, A., Jakab, K., Jamison, R., & Forgacs, G. 2005. Role of physical mechanisms in biological self-organization. *Phys. Rev. Lett.*, **95**, 178104.

[Nelson *et al.*, 2005] Nelson, C.M., Jean, R.P., Tan, J.L., Liu, W.F., Sniadecki, N.J., Spector, A.A., & Chen, C.S. 2005. Mechanical control of tissue growth: function follows form. *Proc. Natl. Acad. Sci. (USA)*, **102**(9).

[Newman, 2005] Newman, T. 2005. Modeling Multi-cellular Systems Using Sub-cellular Elements. *Math. Biosci. Eng.*, **2**, 613–624.

[Nobuoka *et al.*, 2006] Nobuoka, T., Mizuguchi, T., Oshima, H., Shibata, T., Kimura, Y., Mitaka, T., Katsuramaki, T., & Hirata, K. 2006. Portal blood flow regulates volume recovery of the rat liver after partial hepatectomy: molecular evaluation. *Eur Surg Res*, **38**(6), 522–532.

[Noguchi *et al.*, 1979] Noguchi, P., Wallace, R., Johnson, J., Earley, E. M., O'Brien, S., Ferrone, S., Pellegrino, M. A., Milstien, J., Needy, C., Browne, W., &

Petricciani, J. 1979. Characterization of the WIDR: a human colon carcinoma cell line. *In Vitro*, **15**(6), 401–408.

[Nussler *et al.*, 2006] Nussler, Andreas, Konig, Sarah, Ott, Michael, Sokal, Etienne, Christ, Bruno, Thasler, Wolfgang, Brulport, Marc, Gabelein, Geredn, Schormann, Wiebke, Schulze, Maren, Ellis, Ewa, Kraemer, Matthias, Nocken, Frank, Fleig, Wolfgang, Manns, Michael, Strom, Steven C, & Hengstler, Jan G. 2006. Present status and perspectives of cell-based therapies for liver diseases. *J Hepatol*, **45**(1), 144–159.

[Nygaard, 1986] Nygaard, K. 1986. Basic Concepts in Object Oriented Programming. *ACM SIGPLAN Notices*, **21**(10), 128–132.

[Okabe *et al.*, 2000] Okabe, A., Boots, B., & Sugihara, K. 2000. *Spatial Tessellations: Concepts and Applications of Voronoi Diagrams*. Wiley.

[Orford *et al.*, 1999] Orford, K., Orford, C.C., & Byers, S. W. 1999. Exogenous Expression of β - Catenin Regulates Contact Inhibition, Anchorage-independent Growth, Anoikis, and Radiation-induced Cell Cycle Arrest. *J. Cell Biol.*, **146**(4), 855–867.

[Orrenius *et al.*, 2003] Orrenius, Sten, Zhivotovsky, Boris, & Nicotera, Pierluigi. 2003. Regulation of cell death: the calcium-apoptosis link. *Nat Rev Mol Cell Biol*, **4**(7), 552–565.

[Osterod *et al.*, 2001] Osterod, M., Hollenbach, S., Hengstler, J. G., Barnes, D. E., Lindahl, T., & Epe, B. 2001. Age-related and tissue-specific accumulation of oxidative DNA base damage in 7,8-dihydro-8-oxoguanine-DNA glycosylase (Ogg1) deficient mice. *Carcinogenesis*, **22**(9), 1459–1463.

[Osterod *et al.*, 2002] Osterod, Marcel, Larsen, Elisabeth, Page, Florence Le, Hengstler, Jan G, Horst, Gijsbertus T J Van Der, Boiteux, Serge, Klungland, Arne, & Epe, Bernd. 2002. A global DNA repair mechanism involving the Cockayne syndrome B (CSB) gene product can prevent the in vivo accumulation of endogenous oxidative DNA base damage. *Oncogene*, **21**(54), 8232–8239.

[Padera *et al.*, 2004] Padera, Timothy P, Stoll, Brian R, Tooredman, Jessica B, Capen, Diane, di Tomaso, Emmanuelle, & Jain, Rakesh K. 2004. Pathology: cancer cells compress intratumour vessels. *Nature*, **427**(6976), 695.

[Pahlavan *et al.*, 2006] Pahlavan, Payam Samareh, Feldmann, Robert E, Zavos, Christos, & Kountouras, Jannis. 2006. Prometheus' challenge: molecular, cellular and systemic aspects of liver regeneration. *J Surg Res*, **134**(2), 238–251.

[Palsson & Othmer, 2000] Palsson, E., & Othmer, H.G. 2000. A model for individual and collective cell movement in Dictyostelium discoideum. *Proc. Natl. Acad. Sci. USA*, **12**(18), 10448–10453.

[Ping *et al.*, 2006] Ping, Chen, Xiaoling, Dong, Jin, Zhu, Jiahong, Dong, Jiming, Ding, & Lin, Zhang. 2006. Hepatic sinusoidal endothelial cells promote hepatocyte proliferation early after partial hepatectomy in rats. *Arch Med Res*, **37**(5), 576–583.

[Piper *et al.*, 1998] Piper, J.W., Swerlick, R.A., & Zhu, C. 1998. Determining force dependence of two-dimensional receptor-ligand binding affinity by centrifugation. *Biophys. J.*, **74**, 492 – 513.

[Pizer *et al.*, 1987] Pizer, Stephen M., Amburn, E. Philip, Austin, John D., Cromartie, Robert, Geselowitz, Ari, Greer, Trey, Romeny, Bart Ter Haar, & Zimmerman, John B. 1987. Adaptive histogram equalization and its variations. *Comput. Vision Graph. Image Process.*, **39**(3), 355–368.

[Posch *et al.*, 2007] Posch, T., Birken, K., & Gerdom, M. 2007. *Basiswissen Softwarearchitektur*. Dpunkt Verlag.

[Pratt, 2007] Pratt, W.K. 2007. *Digital Image Processing*. Wiley-Interscience (4th edition).

[Press & Vetterling, 1992] Press, W. H.; Flannery, B. P.; Teukolsky S.A.;, & Vetterling, W.T. 1992. *Numerical Recipes in FORTRAN: The Art of Scientific Computing*. Cambridge, England: Cambridge University Press.

[Quinn, 2004] Quinn, M. J. 2004. *Parallel Programming in C with MPI and OpenMP*. McGraw-Hill Inc.

[Radszuweit *et al.*, 2009] Radszuweit, M., Block, M., Hengstler, J. G., Schöll, E., & Drasdo, D. 2009. Comparing the growth kinetics of cell populations in two and three dimensions. *Phys Rev E Stat Nonlin Soft Matter Phys*, **79**(5 Pt 1), 051907.

[Ramis-Conde *et al.*, 2008] Ramis-Conde, Ignacio, Drasdo, Dirk, Anderson, Alexander R A, & Chaplain, Mark A J. 2008. Modeling the influence of the E-cadherin-beta-catenin pathway in cancer cell invasion: a multiscale approach. *Biophys J*, **95**(1), 155–165.

[Ramis-Conde *et al.*, 2009] Ramis-Conde, Ignacio, Chaplain, Mark A J, Anderson, Alexander R A, & Drasdo, Dirk. 2009. Multi-scale modelling of cancer cell intravasation: the role of cadherins in metastasis. *Phys Biol*, **6**(1), 16008.

[Rappaport *et al.*, 1954] Rappaport, A. M., Borowy, Z. J., Lougheed, W. M., & Lotto, W. N. 1954. Subdivision of hexagonal liver lobules into a structural and functional unit; role in hepatic physiology and pathology. *Anat Rec*, **119**(1), 11–33.

[Reder-Hilz *et al.*, 2004] Reder-Hilz, B., Ullrich, M., Ringel, M., Hewitt, N., Utesch, D., Oesch, F., & Hengstler, J. G. 2004. Metabolism of propafenone and verapamil by cryopreserved human, rat, mouse and dog hepatocytes: comparison with metabolism in vivo. *Naunyn Schmiedebergs Arch Pharmacol*, **369**(4), 408–417.

[Reeves *et al.*, 1987] Reeves, William, Salesin, David, & Cook, Robert. 1987. Rendering antialiased shadows with depth maps. *SIGGRAPH 87*.

[Rivet & Boon, 2001] Rivet, J.P, & Boon, J.P. 2001. *Lattice Gas Hydrodynamics*. Cambridge University Press.

[Rode *et al.*, 2004] Rode, Hans-Jürgen, Eisel, Doris, & Frost, Inge. 2004. *Apoptosis, Cell Death and Cell Proliferation*. Roche Applied Science.

[Rosen & Misfeldt, 1980] Rosen, P., & Misfeldt, D.S. 1980. Cell Density Determines Epithelial Migration in Culture. *Proc. Natl. Acad. Sci.*, **77**(8), 4760–4763.

[Rosenfeld *et al.*, 1969] Rosenfeld, A., Park, C.M., & Strong, J.P. 1969. Noise Cleaning in Digital Pictures. *Proc. EASCON Convention Record*, 264–273.

[Rumbaugh *et al.*, 1991] Rumbaugh, J., Blaha, M., Premerlani, W., Eddy, F., & Lorensen, W. 1991. *Object-Oriented Modeling and Design*. Englewood Cliffs, New Jersey: Prentice Hall.

[Saam & Gordon, 1999] Saam, J. R., & Gordon, J. I. 1999. Inducible gene knockouts in the small intestinal and colonic epithelium. *J Biol Chem*, **274**(53), 38071–38082.

[Saffman & Taylor, 1958] Saffman, P.G., & Taylor, G.I. 1958. The penetration of a fluid into a porous medium or Hele-Shaw cell containing a more viscous liquid. *Proc. R. Soc. Lond.*, **245**, 312–329.

[Safran *et al.*, 2005] Safran, S.A., Gov, N., Nicolas, A., Schwarz, U.S., & Tlusty, T. 2005. Physics of cell elasticity, shape and adhesion. *Physica A*, **352**, 171–201.

[Saharinen *et al.*, 2008] Saharinen, Pipsa, Eklund, Lauri, Miettinen, Juho, Wirkkala, Riikka, Anisimov, Andrey, Winderlich, Mark, Nottebaum, Astrid, Vestweber, Dietmar, Deutsch, Urban, Koh, Gou Young, Olsen, Bjorn R, & Alitalo, Kari. 2008. Angiopoietins assemble distinct Tie2 signalling complexes in endothelial cell-cell and cell-matrix contacts. *Nat Cell Biol*, **10**(5), 527–537.

[Salazar-Ciudad *et al.*, 2003] Salazar-Ciudad, I., Jernvall, J., & Newman, S. A. 2003. Mechanisms of pattern formation in development and evolution. *Development*, **130**, 2027–2037.

[Santini *et al.*, 1987] Santini, M. T., Indovina, P. L., & Hausman, R. E. 1987. Changes in myoblast membrane order during differentiation as measured by EPR. *Biochim Biophys Acta*, **896**(1), 19–25.

[Santini & Rainaldi, 1999] Santini, M.T., & Rainaldi, G. 1999. Three-Dimensional Spheroid Model in Tumor Biology. *Pathobiology*, **67**, 148–157.

[Santini *et al.*, 1999] Santini, M.T., Rainaldi, G., & Indovina, P.L. 1999. Multicellular tumour spheroids in radiation biology. *Int. J. Radiat. Biol.*, **75**(7), 787–799.

[Santini *et al.*, 2000] Santini, M.T., Rainaldi, G., & Indovina, P.L. 2000. Apoptosis, cell adhesion and the extracellular matrix in the three-dimensional growth of multicellular tumor spheroids. *Crit. Reviews in Oncology/Hematology*, **36**, 75–87.

[Sato *et al.*, 1982] Sato, G.H., Pardee, A.B:, & Sirbasku, D.A. 1982. *Growth of Cells in Hormonally Defined Media*. Cold Spring Harbour Laboratory.

[Sato *et al.*, 1999] Sato, Y., Tsukada, K., & Hatakeyama, K. 1999. Role of shear stress and immune responses in liver regeneration after a partial hepatectomy. *Surg Today*, **29**(1), 1–9.

[Saucedo & Edgar, 2002] Saucedo, Leslie J, & Edgar, Bruce A. 2002. Why size matters: altering cell size. *Curr Opin Genet Dev*, **12**(5), 565–571.

[Sauer *et al.*, 2007] Sauer, Uwe, Heinemann, Matthias, & Zamboni, Nicola. 2007. Genetics. Getting closer to the whole picture. *Science*, **316**(5824), 550–551.

[Sayan *et al.*, 2001] Sayan, B.S., Ince, G., Sayan, A.E., & Ozturk, M. 2001. NAPO as a novel apoptosis marker. *J. Cell Biol.*, **155**, 719–724.

[Schaller & Meyer-Hermann, 2005] Schaller, G., & Meyer-Hermann, M. 2005. Multicellular tumor spheroid in an off-lattice Voronoi-Delaunay cell model. *Phys. Rev. E*, **71**(5), 1–16.

[Schienbein *et al.*, 1994] Schienbein, M., Franke, K., & Gruler, H. 1994. Random walk and directed movement: comparison between inert particles and self-organized molecular machines. *Phys. Rev. E*, **49**(6), 5462–5471.

[Schiffer *et al.*, 2003] Schiffer, I.B., Gebhard, S., Heimerdinger, C.K., Heling, A., Hast, J., Wollscheid, U., Seliger, B., Tanner, B., Gilbert, S., Beckers, T., Baasner, S., Brenner, W., Spangenberg, C., Prawitt, D., Trost, T., Schreiber, W.G., Zabel, B., Thelen, M., Lehr, H.A., Oesch, F., & Hengstler, J.G. 2003. Switching off HER-2/neu in a tetracycline-controlled mouse tumor model leads to apoptosis and tumor-size-dependent remission. *Cancer Res.*, **63**, 7221–7231.

[Schleich, 1967] Schleich, A. 1967. Studies on aggregation of human ascites tumor cells. *Eur J Cancer*, **3**(4), 243–246.

[Schroeder, 1992] Schroeder, M. 1992. *Fractals, Chaos, Power Laws: Minutes from an Infinite Paradise*. W. H. Freeman.

[Schwann, 1839] Schwann, T. 1839. *Mikroskopische Untersuchungen über die Übereinstimmung in der Struktur und dem Wachstum der Thiere und Pflanzen*. Vdm Verlag Dr. Mueller.

[Schwarz *et al.*, 2002] Schwarz, U.S., Balaban, N.Q., Riveline, D., Bershadsky, A., Geiger, B., & Safran, S.A. 2002. Calculation of Forces at Focal Adhesions from Elastic Substrate Data: The Effect of Localized Force and the Need for Regularization. *Biophys. J*, **83**, 1380 – 1394.

[Segal, 1992] Segal, Mark. 1992. Fast Shadows and Lighting Effects Using Texture Mapping. *SIGGRAPH 92*.

[Shapiro & Stockman, 2001] Shapiro, L.G., & Stockman, G.C. 2001. *Computer Vision*. Prentice-Hall New Jersey.

[Shirley & Morley, 2001] Shirley, P., & Morley, R.K. 2001. *Realistic Ray Tracing*. A.K. Peters.

[Shneiderman & Plaisant, 2004] Shneiderman, Ben, & Plaisant, Cahterine. 2004. *Designing the User Interface: Strategies for Effective Human-Computer Interaction*. Allyn & Bacon.

[Shraiman, 2005] Shraiman, B.I. 2005. Mechanical feedback as a possible regulator of tissue growth. *Proc Natl Acad Sci (USA)*, **102**(9), 3318–23.

[Snoep & Westerhoff, 2005] Snoep, J.L., & Westerhoff, H.V. 2005. *From isolation to integration, a systems biology approach for building the Silicon Cell in Systems Biology: Definitions and Perspectives:*. Springer-Verlag.

[Sparkman *et al.*, 2009] Sparkman, Amanda M, Vleck, Carol M, & Bronikowski, Anne M. 2009. Evolutionary ecology of endocrine-mediated life-history variation in the garter snake Thamnophis elegans. *Ecology*, **90**(3), 720–728.

[Stark & Fitzgerald, 1996] Stark, J. A., & Fitzgerald, W.J. 1996. An Alternative Algorithm for Adaptive Histogram Equalization. *Graphical Models And Image Processing*, **58**(2), 180–185.

[Stegmaier *et al.*, 2005] Stegmaier, S., Strengert, M., Klein, T., & Ertl, T. 2005. A Simple and Flexible Volume Rendering Framework for Graphics-Hardware-based Raycasting. *Proceedings of Volume Graphics 2005, Stony Brook, New York, USA*, 187–195.

[Stott *et al.*, 1999] Stott, E.L., Britton, N.F., Glazier, J.A., & Zajac, M. 1999. Stochastic Simulation of Benign Avascular Tumor Growth Using the Potts Model. *Math. Comput. Model.*, **30**, 183–198.

[Stroustrup, 1988] Stroustrup, B. 1988. What is object-oriented programming? *Software, IEEE*, **5**(3), 10–20.

[Stroustrup, 2000] Stroustrup, B. 2000. *Die C++ Programmiersprache*. Addison-Wesley München.

[Stupack & Cheresh, 2002] Stupack, D.G., & Cheresh, D.A. 2002. Get a ligand, get a life: integrins, signaling and cell survival. *J. Cell Science*, **115**, 3729–3738.

[Sutherland & Harris, 2002] Sutherland, Francis, & Harris, Julie. 2002. Claude Couinaud: a passion for the liver. *Arch Surg*, **137**(11), 1305–1310.

[Sutherland *et al.*, 1986] Sutherland, R., Freyer, J., Mueller-Klieser, W., Wilson, R., Heacock, C., Sciandra, J., & Sordat, B. 1986. Cellular growth and metabolic adaptations to nutrient stress environments in tumor microregions. *Int J Radiat Oncol Biol Phys*, **12**(4), 611–615.

[Sutherland, 1988] Sutherland, R. M. 1988. Cell and environment interactions in tumor microregions: the multicell spheroid model. *Science*, **240**(4849), 177–184.

[Sutherland & Durand, 1984] Sutherland, R. M., & Durand, R. E. 1984. Growth and cellular characteristics of multicell spheroids. *Recent Results Cancer Res*, **95**, 24–49.

[Sutherland *et al.*, 1971] Sutherland, R. M., McCredie, J. A., & Inch, W. R. 1971. Growth of multicell spheroids in tissue culture as a model of nodular carcinomas. *J Natl Cancer Inst*, **46**(1), 113–120.

[Swanson *et al.*, 2000] Swanson, K. R., Alvord, E. C., & Murray, J. D. 2000. A quantitative model for differential motility of gliomas in grey and white matter. *Cell Prolif*, **33**(5), 317–329.

[Takeichi, 1987] Takeichi, M. 1987. Cellular and molecular basis for tissue construction: role of cadherins in selective cell adhesion. *Seikagaku*, **59**(1), 1–9.

[Taub, 2004] Taub, Rebecca. 2004. Liver regeneration: from myth to mechanism. *Nat Rev Mol Cell Biol*, **5**(10), 836–847.

[Thomlinson & Gray, 1955] Thomlinson, R. H., & Gray, L. H. 1955. The histological structure of some human lung cancers and the possible implications for radiotherapy. *Br J Cancer*, **9**(4), 539–549.

[Thorne *et al.*, 2007] Thorne, B.C., Bailey, A.M., DeSimone, D.W., & Peirce, S.M. 2007. Agent-based modeling of multicell morphogenic processes during development. *Birth Defects Res C Embryo Today*, **81**(4), 344–353.

[Tom & Wolfe, 1982] Tom, V. T., & Wolfe, G. J. 1982. Adaptive histogram equalization and its applications. *SPIE Appl. Digital Image Process. IV*, **359**, 204–209.

[Tschumperlin, 2004] Tschumperlin, D. J. 2004. EGFR autocrine signaling in a compliant interstitial space: mechanotransduction from the outside in. *Cell Cycle*, **3**, 996.

[Tukey, 1971] Tukey, J.W. 1971. *Exploratory Data Analysis*. Addison-Wesley.

[Vaage, 1992] Vaage, J. 1992. Fibrosis in immune control of mammary-tumor growth. *Int J Cancer*, **51**(2), 325–328.

[van der Linden, 1996] van der Linden, P. J. 1996. Cell adhesion, cell adhesion molecules and their functional role in the human endometrium. *Early Pregnancy*, **2**(1), 5–14.

[Veach & Guibas, 1997] Veach, E., & Guibas, L.J. 1997. Metropolis Light Transport. *SIGGRAPH '97 Proceedings*, 65–76.

[Venit & Bishop, 1996] Venit, Stewart, & Bishop, Wayne. 1996. *Elementary Linear Algebra*. International Thompson Publishing (4th edition).

[Vintermyr & Døskeland, 1987] Vintermyr, O. K., & Døskeland, S. O. 1987. Cell cycle parameters of adult rat hepatocytes in a defined medium. A note on the timing of nucleolar DNA replication. *J Cell Physiol*, **132**(1), 12–21.

[Virchow, 1858] Virchow, Rudolf. 1858. *Die Cellularpathologie in ihrer Begründung auf physiologische und pathologische Gewebelehre*. Verlag von August Hirschwald.

[von Mach *et al.*, 2004] von Mach, Marc-Alexander, Hengstler, Jan Georg, Brulport, Marc, Eberhardt, Michael, Schormann, Wiebke, Hermes, Matthias, Prawitt, Dirk, Zabel, Bernhard, Grosche, Jens, Reichenbach, Andreas, Müller, Beat, Weilemann, Ludwig Sacha, & Zulewski, Henryk. 2004. In vitro cultured islet-derived progenitor cells of human origin express human albumin in severe combined immunodeficiency mouse liver in vivo. *Stem Cells*, **22**(7), 1134–1141.

[Walsh & Young, 2008] Walsh, J:E., & Young, M.R. 2008. Phosphatase regulation of cellular motility in the tumor microenvironment. *The FASEB J*, **22**(1029.9).

[Wang & Tao, 2006] Wang, Z.H., & Tao, J. 2006. A Fast Implementation of Adaptive Histogram Equalization. *8th International Conference on Signal Processing*, **2**, 16–20.

[Warchol, 2002] Warchol, M.E. 2002. Cell Density and N-cadherin Interaction Regulates Cell Proliferation in the Sensory Epithelia of the Inner Ear. *J. Neurosci.*, **22**(7), 2607–2616.

[Webb *et al.*, 2005] Webb, Donna J, Zhang, Huaye, & Horwitz, Alan F. 2005. Cell migration: an overview. *Methods Mol Biol*, **294**, 3–11.

[Wegner, 1987] Wegner, P. 1987. Dimensions of Object-Based Language Design. *ACM SIGPLAN Notices*, **22**(12), 168–182.

[Weinberg, 2007] Weinberg, R.A. 2007. *The Biology of Cancer*. New York and Oxford: Garland Science.

[Weiss, 2006] Weiss, Ben. 2006. Fast Median and Bilateral Filtering. *ACM Transactions of Graphics Proceedings of the ACM SIGGRAPH'06 Conference*.

[Werner & Noé, 1993] Werner, R. G., & Noé, W. 1993. Mammalian cell cultures. Part I: Characterization, morphology and metabolism. *Arzneimittelforschung*, **43**(10), 1134–1139.

[Wiegers, 2003] Wiegers, Karl E. 2003. *Software Requirements*. Microsoft Press (2nd edition).

[Wiener, 1948] Wiener, Norbert. 1948. *Cybernetics: or the Control and Communication in the Animal and the Machine*. The MIT Press.

[Williams, 1978] Williams, Lance. 1978. Casting curved shadows on curved surfaces. *In Proceedings of SIGGRAPH '78*, 270–274.

[Wintrebert, 1931] Wintrebert, P. 1931. La rotation immediate de l-Oeuf pondu et al rotation d'activation chez Discoglassus picus. *Orth Compres Rend Soc Biol*, **106**, 439–42.

[www, 01] shootout.alioth.debian.org.

[www, 03] Programming languages – C++, ISO/IEC 14882:2003: http://www.iso.org/iso/catalogue_detail.htm?csnumber=38110.

[www, 04] Autodesk Homepage: www.autodesk.com.

[www, 05] CompuCell: www.compucell3d.org.

[www, 06] Institute for Advanced Biosciences in Tsuruoka, Japan: www.e-cell.org.

[www, 07] GLUI: http://glui.sourceforge.net.

[www, 08] http://www.pathology.med.umich.edu/-greensonlab/etohmal.jpeg.

[www, 09] http://dir.niehs.nih.gov/-dirlep/liverpath/images/large/AdA3.jpg.

[www, 10] http://www.mc.vanderbilt.edu.

[www, 11] NRCAM (National Resource for Cell Analysis and Modeling): www.nrcam.uchc.edu.

[www, 12] Nvidia Homepage: www.nvidia.com.

[www, 13] Unified Modeling Language (UML) Specification: Infrastructure: http://www.omg.org/.

[www, 14] Poyray Homepage: http://povray.org/.

[www, 15] Rayshade Homepage: http://www-graphics.stanford.edu/ cek/rayshade.

[www, 16] World Health Organization: Cancer (2006): http://www.who.int/mediacentre/factsheets/fs297/en/.

[www, 17] Interpolation methods (Paul Bourke): http://local.wasp.uwa.edu.au/ pbourke/other/interpolation/index.html.

[www, 18] http://srab.cancer.gov/devcan/.

[Xin, 2000] Xin, J. 2000. Front Propagation in Heterogeneous Media. *Siam Review*, **42**(2), 161–230.

[Yan *et al.*, 1997] Yan, Z., Chen, M., Perucho, M., & Friedman, E. 1997. Oncogenic Ki-ras but Not Oncogenic Ha-ras Blocks Integrin ?1-Chain Maturation in Colon Epithelial Cells. *J. Biol. Chem.*, **272**(49), 2607–2616.

[Yin *et al.*, 1996] Yin, L., Yang, R., Gabbouj, M., & Neuvo, Y. 1996. Weighted Median Filters: A Tutorial. *IEEE Trans. on Circuits and Systems*, **43**(3), 157–192.

[Yu *et al.*, n.d.] Yu, P., Mustata, G., Nolte, D. D., Turek, J. J., & Frenc, P. M. W. *3D video holography through biological tissue*. See: http://www.vet.purdue.edu/cristal/oci-info.htm.

[Zhang *et al.*, 2004] Zhang, X., Chen, A., Leon, D.D., Li, H., Noiri, E., Moy, V.T., & Goligorsky, M.S. 2004. Atomic force microscopy measurement of leukocyte-endothelial interaction. *Am J. Physiol. Heart Circ. Physiol.*, **286**, H359–H367.

[Zhivotovsky, 2004] Zhivotovsky, Boris. 2004. Apoptosis, necrosis and between. *Cell Cycle*, **3**(1), 64–66.